Dissertation zur Erlangung des Doktorgrades der Fakultät für Chemie und Pharmazie der Ludwig-Maximilians-Universität München

Immune Cell Proteomes

Jan Christoph Rieckmann

aus

Frankfurt a.M., Germany

2021

Erklärung

Diese Dissertation wurde im Sinne von §7 der Promotionsordnung vom 28. November 2011 von Herrn Prof. Dr. Matthias Mann betreut.

Eidesstattliche Versicherung

Diese Dissertation wurde eigenständig und ohne unerlaubte Hilfe von mir erbracht.

München, 06.12.2021

Jan Christoph Rieckmann

Dissertation eingereicht am 06.09.2021

1. Gutachter: Prof. Dr. Matthias Mann

2. Gutachter: Prof. Dr. Felix Meissner

Mündliche Prüfung am 24.11.2021

Summary

The immune system is unique in its dynamic interplay, and highly specialized cell types execute its diverse functions. A major goal of immunology research is to elucidate how the context-dependent crosstalk between different cell types and the orchestration of their functions enable protection against disease. Due to the plasticity of immune responses and their context-dependent pathophysiological states, interpreting them is inherently challenging. Thus, the immune system has been studied at various hierarchical levels - genomic, transcriptional, translational, cellular signaling process, cell heterogeneity, spatial, intercellular, and organismal - each of which forms its own specialized networks. The advancement of large-scale omics-technologies and automated bioinformatic analysis pipelines increased the number of high-throughput experiments, resulting in diverse datasets suitable for studying the immune system from a network perspective. As such, the versatile toolbox of mass spectrometry-based proteomics has become an integral part of modern systems immunology research enabling the analysis of expression levels of thousands of proteins within immune cells, their interaction partners, post-translational modifications, and localization.

This thesis objectives were twofold: to advance the journey towards complete, accurate, and ubiquitous cell proteomes and to identify novel network connections that contribute to the understanding of immune responses.

This thesis demonstrates that proteomics can generate high-quality and comprehensive proteome profiles not only form individual immune cell types but also from time-resolved immune responses as well as multicellular immune systems derived from primary human samples. The optimized quantitative shotgun proteomics workflow with three-hour gradients achieved an average of 7,500 quantified proteins per measurement. In total, this thesis provides over 200 immune cell proteomes, that collectively cover 70% of all immune-relevant signaling molecules, including transcription factors, adaptor molecules, cell surface receptors, and secreted molecules, making this the most comprehensive immune proteome resource to date. From this data, I constructed three different immune networks - (1) a functional intracellular transcriptome and proteome network of murine CD8 memory T cells, (2) an intracellular and time-resolved proteome and metabolome network of the human CD4 T cell immune response, and (3) an intra- and intercellular proteome and secretome network of the human hematopoietic system. Cell surface markers from these networks resulted in a new

functional classification of memory T cells that could potentially be used to evaluate vaccination studies. Furthermore, the metabolome-proteome network identified L-arginine as a critical metabolite during T cell activation, enhancing T cell survival and anti-tumor activity. This discovery may be used to boost the efficacy of adoptive T cell therapies. Finally, the hematopoietic cell-cell communication network revealed novel intercellular connections and serves as a healthy state reference map for future studies aimed at identifying activation and disease-specific extracellular signaling pathways that can be targeted by immunotherapies.

Together, this thesis expanded the frontiers of quantitative mass spectrometry-based proteomics from few immune cell proteomes to system-wide protein-centric immune cell networks and provided the basis to understanding basic principles of intercellular signaling and devising novel immunotherapeutic strategies.

Table of Contents

1 Introduction

1.1 The immune system

1.1.1 Introduction to the immune system

Immunology emerged from medical microbiology in the last quarter of the nineteenth century to a well established field in both basic and clinical research today[1]. Louis Pasteur's germ theory and Robert Koch's studies on infectious diseases introduced a paradigm shift that diseases not only arise from dysfunctional body cells but can also be caused by exogenous pathogens. It took another two major discoveries that coined the birth of immunology. Elias Metchnikoff found that white blood cells can engulf and destroy invading pathogens[2], by a process called phagocytosis (Nobel Prize in Physiology or Medicine 1908) and Emil von Behring demonstrated that serum from infected animals can protect another animal from that disease (Nobel Prize in Physiology or Medicine 1901). These findings laid the basis for innate and acquired as well as cellular and humoral immunity, respectively. This two-class separation of the immune system was soon relaxed by Jules Bordet's work on the interaction of complement and antibodies (Nobel Prize in Physiology or Medicine 1919), as well as the experiments of Almroth Wright[3], who observed that antibodies can specifically facilitate phagocytosis of bacteria supporting the concept that the two arms of the immune system are highly intertwined. Furthermore, Paul Ehrlich's proposed "horror autotoxicus" theory was questioned, and it became clear that aberrant antibody responses could lead to hypersensitivity reactions[4], shown for example by Charles Richet's research on anaphylaxis (Nobel Prize in 1913). During that time, other clinical immunology contributions such as the discovery of the ABO major blood group system[5] (Landsteiner Nobel Prize in 1930) as well as immunochemistry discoveries such as the chemical structure of antibodies[6,7] (Rodney Porter and Gerald Edelman Nobel Prize in 1972) lead to a deeper understanding of the immune system. Then the area of immunobiology started with the discovery of antibody-producing B lymphocytes and immune regulating T lymphocytes[8], which soon became established as responsible cells of acquired cellular and humoral immunity, respectively[1]. In parallel, the major histocompatibility complex (MHC) was discovered to be accountable for transplant rejections[9] (Snell, Dausset and Benacerraf the Nobel Prize in 1980). These findings converged with the demonstration by Doherty and Zinkernagel that MHC molecules, besides transplant rejection, are also responsible for T-cell recognition of any type of antigen (Nobel

Prize in 1996). Many more important discoveries were made during that period that still shape our understanding of cellular immunity today. Besides cellular immunity, other eminent immunological questions were answered. For instance, Frank Macarlane Burnet and Peter Brian Medawar shed light on the immunological tolerance[10,11] (Nobel Prize in 1960) and Susumu Tonegawa explained the mechanisms under

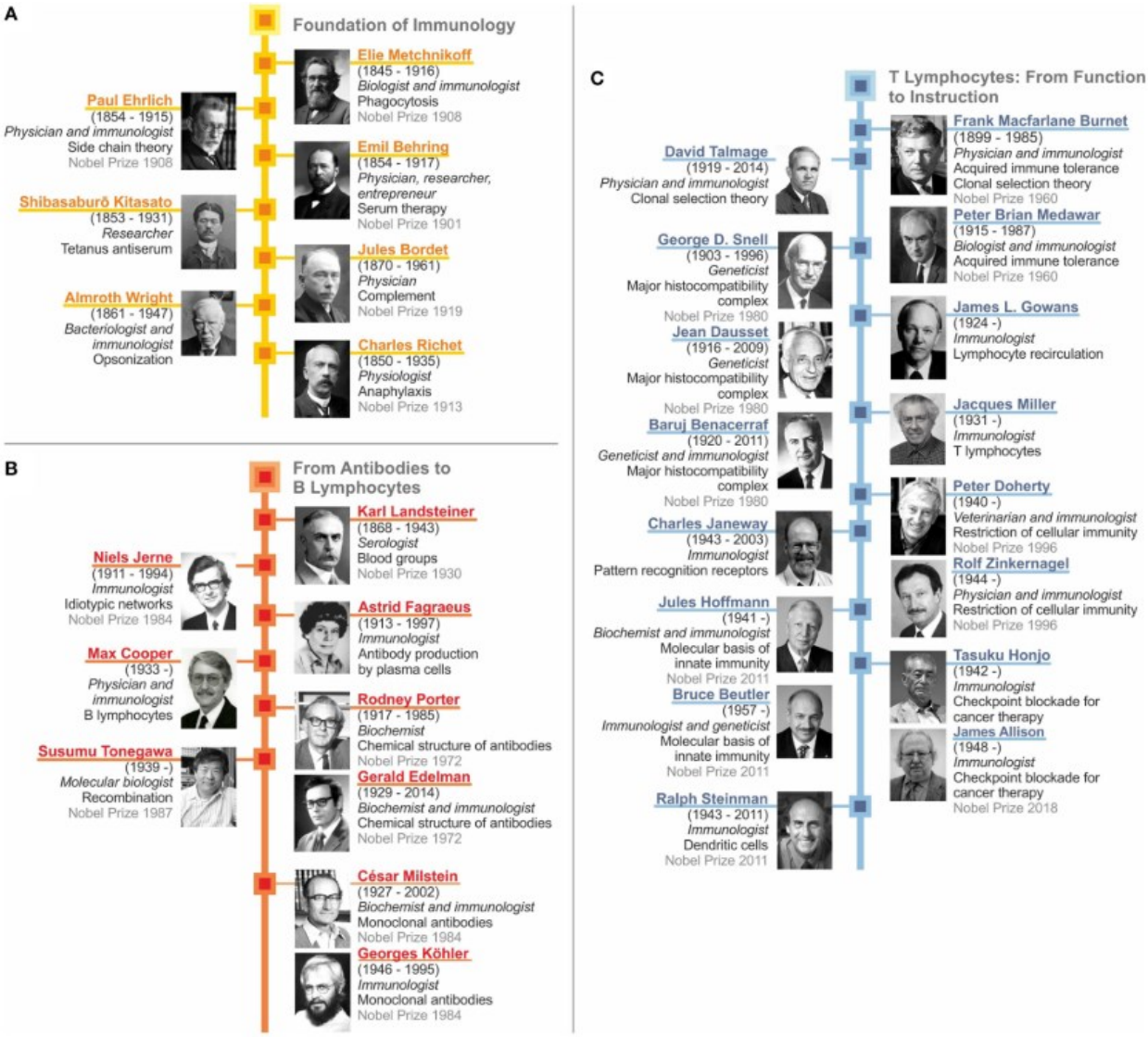

Figure 1: History of immunology form serum therapy to checkpoint control (adapted from[1]).

lying the huge diversity of antibody specificities[12] (the Nobel Prize in 1987). The acquired immune response dominated immunobiology in the second half of the twentieth century, but this changed with the discoveries of pattern recognition receptors[13,14] (Bruce Beutler and Jules Hoffmann Nobel Prize in 2011) and the major T cell instructor the dendritic cell[15] (Ralph Steinman Nobel Prize in 2011). Their work showed that innate immunity serves the immune

response from beginning to the end by first stimulating T cells through antigen presentation and second acting as professional phagocytes to clear invading pathogens. The extensive knowledge accumulated by basic immunology research was and is tightly linked to clinical applications. This can be seen by the first Nobel Prize for serum therapy awarded to Emil Behring, or by the production of monoclonal antibodies (Nobel Prize in 1984) that paved the way for cytokine-blocking immunotherapies against chronic inflammatory diseases[16], or by the latest Nobel Prize in 2018 for the discovery of cancer therapy by inhibition of negative immune regulation (Figure 1)[17].

This short historical summary highlights some of the major findings in immunology and furthermore illustrates the fast-paced environment and continuous discoveries that led to a research area of computational and systems immunology. With the technical advancements in omic technologies and machine learning algorithms it is now possible to study the immune responses at multiple levels with the promise to move from descriptive to predictive models of human diseases[18,19]. This thesis is a descriptive systems immunology approach with the primary objective of creating a protein landscape of the hematopoietic system. Secondary, the proteomic toolbox was used to identify novel immune response mechanisms that enabled the development of novel immunotherapeutic strategies.

The following section provides an overview of the immune system's major components, with an emphasis on T lymphocytes. The final chapter highlights proteomic strategies for studying the immune system and concludes with a summary of available immune networks.

Organs of the immune system

The network of immune organs facilitates a regulated immune response allowing the rapid production of a large number of immune cells and molecules, which can penetrate almost any tissue throughout the body[20]. Most immune cells arise from the bone marrow and then reside in the blood or tissues. For example, T and B lymphocytes mature in the primary immune organs (thymus or bone marrow, respectively), where they recombine their immune receptors[21]. Afterwards they migrate to the secondary immune organs, including lymph nodes, spleen, Peyer’s patches, the appendix, tonsils, adenoids, and other lymphatic tissue. Because of that these cells are often referred to as lymphocytes[20].

Immune cells constantly scan the body for pathogens using the blood and lymphatic system as means of transportation. The lymphatic system is a complex network dispersed throughout the

whole body, including the central nervous systems[22]. It consists of thin-walled lymph capillaries, which lead to afferent lymph vessels, which in turn connect to the lymph nodes. Its vessels are filled with lymph, a clear protein-containing fluid, which is passively moved unidirectional by skeletal muscle contractions towards the heart and eventually reenters the bloodstream at the junction of the internal jugular and subclavian veins at the base of the right side of the neck[23]. Together with the blood system, the lymphatic system forms an important meeting ground for immune cells to initialize an immune response[24].

Cells of the immune system

The cells of the immune system can be roughly categorized into innate or adaptive immune cells (Figure 2). While first react more quickly, latter can take a few days to fully develop an immune response against an invading pathogen[20].

Mast cells, granulocytes, macrophages, monocytes, dendritic cells and natural killer cells form the innate arm of the immune system[25]. Mast cells are involved in allergic reactions and can release granules of histamine and heparin upon pathogen encounter. They also play an important role in inflammation and wound healing. Granulocytes are divided into three subgroups based on their granule content (neutrophils, basophils, and eosinophils). They are relatively short lived and play an important role in the early defense against parasites and extracellular bacteria. Their ability to phagocytose invading bacteria induces the release of inflammatory cytokines, which causes adjacent blood vessels to dilate and other immune cells to migrate towards the inflammation point. In particular, Neutrophils can undergo a suicidal extrusion called neutrophil extracellular traps, which create a physical barrier preventing pathogens from spreading[26]. Macrophages (MQ) comprise another phagocytic cells type that produce inflammatory cytokines, but unlike neutrophils reside in the tissue and are relatively long-lived[27].

Dendritic cells (DCs) are also capable of phagocytosis, but more importantly like MQ can activate cells of the adaptive immune system by presenting pathogen peptides on their cell surface. Hence, DCs and MQ are called antigen presenting cells (APCs)[28]. In detail, upon encounter of a pathogen, APCs internalize the microbe or its debris and generate peptide fragments via the proteasome. These fragments are then shuttled to the cell surface being bound to a receptor complex called major histocompatibility complex II (MHC-II). APCs are divided into two subclasses. DCs and MQ are professional APCs[29]. They express co-stimulatory molecules on their cell surface (e.g. CD80, CD86, and CD40) and, together with

the MHC-II can activate naïve T lymphocytes by forming an immunological synapse. Non-professional APCs like fibroblasts or vascular endothelial cells lack those co-stimulatory receptors and can only reactivate memory T lymphocytes[30].

Natural killer (NK) cells form another innate immune cell type but interestingly are more closely related to the adaptive immune lymphocytes. Through their specialized receptors, they scan the body for infected or tumor cells and once identified release cytotoxic granules that kill the target cell. Recent evidence revealed that specific NK subsets can acquire long-lived and highly specific memory of a variety of viral and hapten-based antigens[20], linking the innate arm to the adaptive immune cells[31].

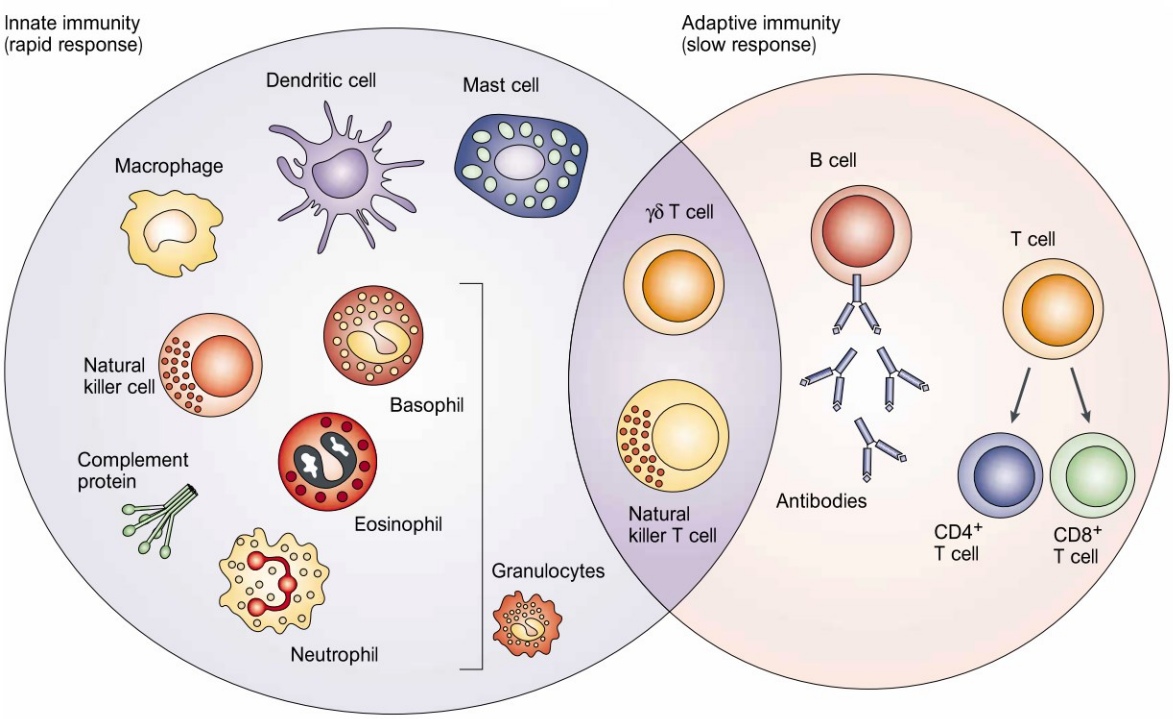

Figure 2: Innate and adaptive immune cell types. The rapid innate immune response consisting of soluble factors (complement proteins) and cellular components (granulocytes, mast cells, macrophages, dendritic cells, and natural killer cells) form the first line of defense against pathogens. In contrast the slower developing adaptive immune response consists of antibodies, B cells, and CD4 and CD8 T lymphocytes. Natural killer T cells and gamma-delta T cells straddle the interface of innate and adaptive immunity, as illustrated by the overlap of the two circles (adapted from[25]).

T and B lymphocytes form the adaptive arm of the immune system. T lymphocytes are broadly classified based on their CD8 or CD4 receptor expression in two cytotoxic or helper cells, respectively. Upon activation CD8 T lymphocytes secrete cytotoxic granules containing granzymes and perforin which induce apoptosis in the target cell[32]. In contrast, CD4 T

lymphocytes upon activation release cytokines that either drive cell-mediated immunity by MQs and CD8 T cells or humoral immunity by B lymphocytes. Thus, they are called T helper (Th) cells and, depending on their secretory profile, are classified into four major subclasses Th1 (IFNg, TNFb), Th2 (IL-4, IL-5, IL-13), Th17 (IL-17), and regulatory T cells (IL-10)[33].
B lymphocytes fight pathogens by secreting large amounts of antibodies after their activation. For example, antibody opsonization, where antibodies mark pathogens by binding to a specific antigen on their surface, mediates phagocytosis by MQ or neutrophils. Based on their location and function, B cells are broadly classified in B1 and B2 lymphocytes. B1 cells are the main producers of natural antibodies and can be found in the pleural and peritoneal cavities. B2 cells are further divided into marginal zone B cells (MZ B) and conventional follicular B cells (FO B)[20]. While MZ B cells are located in the marginal zone of the spleen and take part in the innate immune response, FO B cells reside in the lymphoid follicles of secondary lymph organs and play a role in the adaptive immune response[34].
The diversity and hetrogeniety of immune cell subsets is constantly evolving, in particular due to high-resolving and single cell technologies. Here, we briefly described only on the main subsets, however, due to discoveries of novel secreted molecules or receptors and the use of novel technologies the categorization of immune subsets will continue to grow in a dynamic manner[35].

Cytokines

Immune cells use diverse molecules – and in particular cytokines – to communicate with each other. They are important messengers involved in autocrine, paracrine, and endocrine signaling. Classically, they act on cells by binding to their corresponding extracellular receptor thereby regulating maturation, growth, and responsiveness of immune cells and their surrounding tissue. Besides immune cells, cytokines can also be secreted by other cells of the body like endothelial cells. Typically, cytokines are small proteins of 5-20 kDa in size and can be divided into four structural families. First, the four-α-helix bundle family containing the interleukin (IL) 2 subfamily, the interferon (IFN) subfamily, and IL-10 subfamily, second the IL-1 family, third the IL-17 family, and last the cysteine-knot family[36].
Although the functional categorization of cytokines is challenging as new properties of known cytokines are constantly being uncovered, they can be broadly grouped into ILs, lymphokines, chemokines, IFNs, and tumor necrosis factor family members[20]. ILs form the broadest and biggest group of cytokines and as the name suggest contains cytokines that act between

leukocytes. Lymphokines are produced by lymphocytes. Chemokines are involved in cell trafficking and are responsible in attracting cells to the inflammation site. IFNs are classified into two groups, type I (IFNa and IFNb) and type II (IFNg), and play a pivotal role in the combat of a viral infection or cancer[37]. Tumor necrosis factor family members are transmembrane proteins that are released through proteolytic cleavage and can act as cytokines. Their name originates from their ability to inhibit tumor genesis.
Taken together, cytokines control complex communication networks that play an important role in orchestrating innate and adaptive immunity. Due to their potent nature they are promising therapeutic targets and have been used in the treatment of cancer and autoimmunity[38].

Inflammation and the Innate Response

The first line of defense against invading pathogens is the skin and mucosal membranes, which form a physical barrier. In case a pathogen can pass this layer - for example through a lesion - the innate immune response gets activated. Here, the complement system starts a series of proteolytic cleavages when bound to the pathogen[39]. It thereby covers the pathogen with complement proteins that form multimeric complexes, which in turn kills the pathogen by disrupting their membrane.
In addition, innate immune cells such as MQ, DCs, and neutrophils contribute to the innate immune response by continuously scanning their local environment for invading pathogen and clearing them by phagocytosis. With their receptors, they can sense pathogen associated molecular patterns (PAMPs), like lipopolysaccharide (LPS), single stranded RNA, or unmethylated CpG[20]. Upon binding to PAMPs innate immune cells get activated and start to secrete proinflammatory cytokines and IFNs, which attracts more immune cells to the inflammation site and also makes nearby cells more resistant to infections[40]. Besides, PAMPs, a second class of intracellular molecules called damage associated molecular patterns can activated innate immune cells when released into the extracellular environment[41].
Sometimes pathogens are killed by the instant actions of the innate immune response, however often the response is not strong enough to clear the invading pathogen. In order to activate the adaptive immune response, APC transport phagocytosed pathogen debris to the lymph node, where they present those pathogen fragments to T and B lymphocytes. Once an antigen specific lymphocyte recognizes a specific antigen and receives additional signals

through secreted molecules, they become activated and start to proliferate. This marks the beginning of the slower but targeted adaptive immune response[37].

Immune Activation and the Acquired Response

While innate immune cells have a broad specificity towards pathogens, adaptive immune cells are antigen specific - meaning that only a few cells are specific for any given pathogen protein. In order to increase the chance of an APC to interact with its few antigen specific T or B lymphocytes, these cells continuously circulate throughout the lymphoid organs. When the antigen presenting cell and T cell interact and receive the correct co-stimulatory signals, they form an immunological synapse[20].

As previously mentioned, APC break down phagocytosed debris into peptides, which they present at their cell surface to T lymphocytes via MHC molecules. There are two different types of MHC receptors. While intracellular pathogens are presented through MHC-I, extracellular derived proteins will be bound to MHC-II receptors[37]. DCs are considered the most potent cell type for activating naïve T and B cells, because they secret co-stimulatory molecules and in addition migrate more efficiently through the lymphatic system. With their T cell receptor (TCR), T cells scan the surface of APC. However, the majority of TCR/MHC interactions will be of low affinity and will not lead to the activation of the T cell[20]. Only when the TCR-MHC complex forms a stable interaction, which is supported by co receptor-ligand interactions as well as activation signals from inflammatory cytokines, T cells start their activation program. This is marked by the rapid clonal proliferation as well as IL-2 secretion, which further promotes the proliferation process. As a next step, T cells undergo differentiation and depending on which T cell subtype they belong to perform different functions to enhance the immune response. CD8 T lymphocytes scan the periphery for infected cells by interacting with MHC-I receptors. In case the peptide bound to the MHC-I receptor causes a tight interaction with the TCR of the CD8 T cell, it will release cytolytic granules that penetrate the target cell[32]. This strategy clears intracellular pathogens by killing infected cells. CD4 T cells, also called helper cells, depending on their activation can differentiate into different effector cells. Usually caused by intracellular infections such as viruses, APC secrete cytokines like IL-12 and INFg, inducing a type-I T-helper (Th1) cell specific response. These helper cells aid in the clearance of a pathogen by activation of CD8 T cells. In the presence of IL-4, CD4 T cells activate B cells and induce type-II T helper (Th2) responses[42]. B cells present antigens from digested pathogens at their surface through MHC-II

receptors. Once the B cell forms a synapse with an activated CD4 T cell with its cognate T cell receptor, it becomes activated and undergoes massive expansion and differentiation. At the end the B cell will become a plasma cell that produces a large amount of antibodies that are released into the blood stream where they can opsonize invading extracellular pathogens[43]. B cell can further improve the affinity of their immune receptors through selection and mutation. Those B cell that carry a BCR with higher affinity to their target pathogen will also more efficiently recruit T helper cells and thus receive stronger activation signals. With successive rounds of target binding, activation, and mutation, the B cells with higher affinity will be selected[20,44].

After pathogens are neutralized by activated lymphocytes, the majority of them will perish and only a small proportion will form immunological memory. These memory cells reside within in the lymph node and can survive there for many years. Once an infection reoccurs, these memory cells react more quickly and can yield protective responses within few days[45]. Due to its huge receptor diversity the adaptive immune system can in principle mount an immune response to any possible chemical entity. Intrinsic (clonal deletion and anergy) and extrinsic (competitive deletion, immunogenic costimuli) cellular strategy are in place to control their activity against components of our own body. However, in few cases the tightly regulated development of T and B lymphocytes can lead to self-reactive receptors that cause uncontrolled and harmful immune responses known as autoimmune diseases[46,47].

1.1.2 T lymphocytes

T lymphocytes are required for the establishment and maintenance of immune response, homeostasis, and memory. With their ability to recognize a wide variety of antigens form pathogens, tumor, and the environment, they preserve immunological memory and self-tolerance. They derive from bone marrow progenitors that move to the thymus for maturation, selection, and finally circulate the body through the lymphatic system. They are broadly classified into three subsets: naive T cells, which can respond to novel antigens, memory T cells, which are generated through antigen encounter and maintain long-term immunity, and regulatory T cells, which regulate self-tolerance[48]. Understanding how immunological memory is formed is not only important for vaccine development, but also relevant for the treatment of many other infectious and autoimmune diseases[49] as well as cancer immunotherapies[50].

1.1.2.1 Memory T lymphocytes

We are constantly exposed to pathogens. The skin and mucosae are the primary entry points for pathogens. These either directly drain to local lymph nodes, where they are captured by macrophages (MQs) or are taken up by dendritic cells (DCs) and then move to secondary lymphoid organs[51]. DCs activate T cells in secondary lymphoid organs through antigen presentation, which triggers their proliferation and differentiation into pathogen dependent effector cell populations. In the T cell zone, DCs from a close association with the stromal cells of secondary lymphoid organs, such as fibroblastic reticular cells (FRCs)[52]. FRC promote the interaction of T cells with DCs by secreting CCL19 and CCL2[53]. In addition, CCL3 and CCL4 produced by activated DCs aids in the attraction of antigen-specific T cells[54]. Once the interactions between DCs and T cells stabilize and T cells receive their activating signals, T cells gradually alter their expression of various homing receptors that promote the migration to inflamed tissue sites. After pathogen clearance, only an exceedingly small fraction of the heterogenous pool of memory cells survives. These memory T cells are classified into two distinct subsets[55] - central memory T cells (TCM) expressing CCR7 and CD62L, and effector memory T cells (TEM) lacking these molecules. TCM can produce IL-2 and proliferate rapidly, while TEM are less proliferative and contain effector cytokines such as IFNg[56]. TCM predominate in secondary lymphoid organs, while TEM reside preferentially in peripheral compartments[57,58]. Surface molecules further elucidate the functional heterogeneity of the memory T cell subsets. For instance, with the chemokine receptors CXCR6, CCR3, CRTh2, CXCR3, and CCR4 the TCM and TEM pool can be subdivided into Th1 and Th2 cell characteristics[59]. Memory T cells also differ in their migratory or effector functions. For instance, tissue resident memory T cells form another subset that describes memory T cells that permanently reside in peripheral tissues after pathogen clearance[60,61]. The diversity of immune cells is important for orchestrating effective defense mechanisms. Unconstrained memory T cell trafficking in the peripheral tissues is one important factor to protect from reinfections. However, long lived memory T cells often fade over time and understanding the mechanisms for protective T cell immunity remains important for better vaccine development.

T cell priming and memory generation

During an infection, naive T cells rapidly proliferate, forming an enormous pool of antigen and pathogen-specific cells[62]. T cell expansion is often proportional to the initial frequency of

naive T cell precursors[63]. However, besides precursor frequency, multiple factors influence the production of effector and memory T cells – pathogen type, recruiting of naive T cells[64], T cell migration, T cell receptor stimulation[65] including antigens, enzymes, cytokines and chemokines. These factors not only determine cell numbers but also regulate the generation of effector versus memory cell populations[66,67]. For instance, chronic infections with high antigen and inflammation levels favor short-lived effector cells than memory cells[68]. Interleukins, such as IL-12 and IL-2, have been shown to promote effector T cell production[69,70], while IL-10 signaling facilitates memory development[71]. Expression of transcription factors T-bet and Blimp1 lead to an effector type, while Bcl6, Id2, and Id3 is required for memory formation[72]. In addition, metabolic pathways, and nutrient composition influence the development of memory T cells (discussed in the next chapter). Together, complex signaling networks decide the fate of T cells at different stages during the immune response forming different pools of memory T cells.

T cell migration

T cells are actively migrating through the body. Both, naive T cells and TCM readily migrate to lymph nodes searching for antigen before returning to circulation[73]. Antigens, chemokines, and adhesion molecules on high endothelial venules (HEVs), as well as DC-derived signals facilitate effector and memory T cell entry into lymph nodes. The initial tethering and rolling of cells on the lymph node endothelium is mediated by T cell receptors such as CD62L and PSGL-1 binding to peripheral lymph node addressin and P-selectin, respectively[56]. Chemokines, such as CCL21 binding to the T cell receptor CCR7, direct the migration of T cells through the endothelium. These interactions activate integrins and allows for firm arrest and subsequent diapedesis through HEVs[74].

In non-lymphoid tissues, the vascular endothelium produces a diverse variety of adhesion molecules and chemokines that primarily targets effector cells and TEM. Effector T cells can migrate into inflamed tissues by downregulating CD62L and CCR7 and upregulating other chemokine receptors and adhesion molecules. T cell recruitment to the skin is driven by numerous chemokine receptors, including CCR4, CCR10, CCR6, and CCR8[75], and upregulation of E-selectin ligands on T cells that promotes the binding to skin endothelium[76]. In mucosal tissues, such as the small intestine and Peyer's patches, T cells up upregulate integrin alpha4beta7 that binds to mucosal addressin cell adhesion molecule-1[77]. In the lung, integrin VLA-1 and the chemokine receptors CXCR3 and CCR5 play a critical role in T cell

trafficking critical for lung[78]. Many other chemokine receptors expressed on effector T cells (e.g., CXCR6, CCR1, CCR2, and CCR3) probably also play critical roles in tissue-specific homing and microenvironmental trafficking inside tissues[79]. Nonetheless, more research is needed to understand the complex network of chemokine receptor, integrin, and selectin expression on memory T cells that determine the trafficking into specific tissues[56].

1.1.2.2 T lymphocyte metabolism

The availability of nutrients, growth factor cytokines, as well as key receptor signaling pathways control metabolic reprogramming inside the cell. These metabolic pathways affect cell differentiation and function[80]. During development and quiescence, T cells cycle through different metabolic states. For instance, activation of the receptor Notch1 maintains cell survival and promotes linage commitment[81], while T cells migrate from the bone marrow to the lymph node, where they rearrange their antigen receptor gene loci to produce functional T cell receptors[80]. Together with CXCR4, phosphatidylinositol 3-kinase (PI3K) gets activated to stimulate anabolic metabolism[82]. Later in the development stage, glucose transporter expression increases and through the activation of the mechanistic target of rapamycin (mTOR) via PI3K-Akt signaling, glycolytic metabolism is augmented that supports cell growth and proliferation[83,84]. Furthermore, the cytokine IL-7 induces the expression of antiapoptotic factor Bcl-2[85] and therefore also plays an important role in the maintenance of survival and linage commitment[86]. To generate ATP, quiescent T cell primarily consume pyruvate via oxidative phosphorylation (OXPHOS) or use fatty acid oxidation (FAO)[87]. All these signals are essential to work in concert to sustain homeostatic proliferation of naive T cells[88].

Metabolic reprogramming during the life cycle of T cells

Once naive T cell encounter their specific antigen and co-stimulatory signals are in place, they get activated and proliferate in an explosive manner. To accumulate the required biomass, their metabolic pathways switch to aerobic glycolysis (Figure 3). Although less efficient than OXPHOS in generating ATP, it produces important metabolic intermediates for cell growth and proliferation[89]. For instance, pentose phosphate and serine biosynthesis pathways use glucose-6-phosphate or 3-phosphoglycerate to produce precursors for nucleotide and amino acid synthesis[90]. This process is coordinated by several transcription factors and signaling pathways. IL-2 and other growth factors promote the switch to glycolysis via nutrient

transporter expression and activation of the key metabolic regulator mTOR[91,92]. In addition, transcription factors, c-Myc, estrogen-regulated receptor alpha, and hypoxia inducible factor-1 alpha induce the expression of genes involved in intermediary metabolism that stimulate the clonal expansion of T lymphocytes[93–95]. Furthermore, different metabolic pathways also promote the differentiation of CD4 T lymphocytes. For instance, suppression of mTOR augments the production of Tregs upon activation[96]. While Tregs depend more on the oxidation of lipids, Th1, Th2, or Th17 exhibit a strong glycolytic profile via the mTOR pathway[97]. In addition, the two different mTOR complexes regulate the development Th1 and Th2 subsets[80,98].

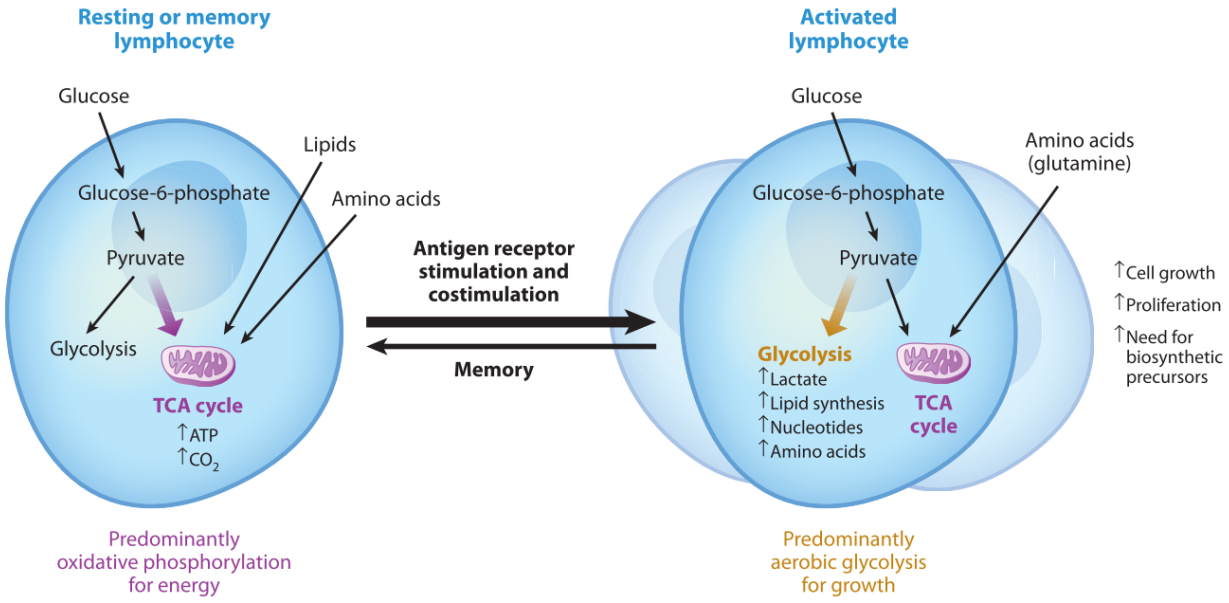

Figure 3: T cell metabolic programs in resting and activated state. While resting T cells predominately rely on oxidative phosphorylation for energy, activated T cells downregulate lipid oxidation and increase and glycolysis to produce sufficient biomass for rapid cell growth and proliferation. After the immune response, activated T cells metabolically revert and form a small pool of memory T cells (adapted from[99]).

After pathogen clearance, effector T cells undergo apoptosis and form a small population of long-lived memory T cells. This memory formation is also driven by different metabolic mechanisms. For instance, metformin promotes the generation of memory T cells after infection by activating adenosine monophosphate-activated protein kinase (AMPK)[100]. AMPK suppresses mTOR and thereby promotes FAO[101] and the generation of memory T cells. Also inhibiting mTOR directly with Rapamycin boots the memory development[102]. A second central characteristic of efficient memory formation is FAO[100]. It has been shown that the number of CD8 memory T cells increases when FAO is enhanced via carnitine

palmitoyltransferase 1a[103]. Together with IL-15 and IL-7, these signals support catabolic metabolism and promote mitochondrial biogenesis, giving memory T cell a greater respiratory capacity compared to naive or effector T cells. This bioenergetic surplus allows memory T cells for a stronger response to secondary infections[103,104]. However, it remains not completely understood what specific role FAO has in the development of memory T cells.

Key metabolic substrates

As mentioned before, glucose is an important metabolite for T cells[80]. It is a relevant energy source for the generation of biomass and production of activation markers required for proliferating T cells[105]. T cells show impaired cell activation, clonal expansion, and survival when deprived from glucose[106] or when their glucose transporter Glut1 is deleted[107].
Amino acids are an alternative class of metabolic substrates. Depending on their metabolic requirements, T cells harbor different amino acid concentration during their activation cycle[108,109]. Many different amino acid transports as well as catabolizing enzymes are being discovered that regulate T cell metabolism and function. For instance, the glutamine transporter or the transporter Slc7a5, which transports neutral amino acids such as leucine, play an important role in effector T cell generation[110,111]. On the molecular level, leucine can activate mTOR via leucyl-tRNA synthetase and consequently, impaired uptake inhibits mTOR[112,113]. Studies suggest that leucine deficiency has also additional effects on the metabolic transcription factor c-Myc[109]. The importance of leucine in T cell activation was further studied by manipulating the cytosolic branched chain aminotransferase, an enzyme that can control intracellular leucine concentration[114]. Furthermore, the alanine serine and cysteine transporter system (ASCT2/Slc1a5), is another important glutamine carrier during T cell activation. When depleted, glutamine levels are decreased, disbalancing the OXPHOS and glucose metabolism[115]. Arginine metabolism has a well-established role in MQ polarization[116] and several studies support that extracellular arginine concentrations can also influence T cell activation. For instance, depleting arginine impairs aerobic glycolysis[117].
Since substrate availability has a great influence on T cell response, studies have shown that antigen presenting cells can regulate extracellular concentrations of amino acids to control T cell activation. For instance, DCs can either express multiple amino acid transporters to deplete and impair T cell proliferation[118], or can release amino acids to foster T cell proliferation[119].

Lipids and fatty acids are other critical substrates in T cell growth, activation, and effector function - vital for cell membrane synthesis, energy consumption, and cell signaling. After activation, the cellular demand for fatty acids increases and FAO shifts to FAS[120]. As described earlier, mTOR and c-Myc are key coordinators[93], but also liver X receptors (LXR) and sterol regulatory element-binding proteins (SREBP) are critical to facilitating this metabolic shift[121]. After antigen stimulation, T cells decrease LXR activity and increase the SREBPs[122]. This leads to reduced cholesterol efflux and increased de novo synthesis of fatty acids and cholesterol[123]. Pharmacological interventions in the lipid and cholesterol homeostasis of T cells can heavily influence their proliferation capacities[121,122]. In addition, lipid metabolism also plays an important role in T cell differentiation and effector function. By inhibiting FAS via acetyl-CoA carboxylase 1, the generation of Th17 is reduced and Tregs increased. Furthermore, this inhibition also impaired Th1 and Th2 development[124].
The connection between metabolism and gene regulation in T cells is overly complex[125]. As indicated by the many studies mentioned above, the continuous increase in knowledge of metabolic regulation in T cells holds the promise to conceptualize new therapeutic approaches[126].

1.1.3 Cancer immunotherapy

The idea to exploit the immune system to treat cancer dates back decades [127,128] and found its recent peak by the award of the Nobel Prize in 2018 for the discovery of cancer therapy by inhibition of negative immune regulation. Cancer is characterized by dysregulation of cellular processes and accumulation of genetic alterations. Such events can cause the expression of mutated self-proteins, called neo-antigens, which in turn can lead to their presentation on the surface of cancer cells. Thus, cancers can be recognized by the immune system as foreign and be targeted by cytotoxic T cells. However, tumors have developed multiple resistance mechanism to evade such T cell responses. The delicate balance between the recognition of non-self and the prevention of autoimmunity is the current challenge in novel cancer immunotherapy strategies[129].

The Cancer-Immunity cycle

The effective killing of tumor cells by the immune system requires distinct checkpoints[130]. First, antigen presenting cells like dendritic cells (DCs) capture neoantigens created by

oncogenesis and present these through MHCI or MHCII receptor molecules on their surface. To trigger an effective anticancer T cell response, secondary signals such as proinflammatory cytokines must be released promoting the presentation of these foreign antigens. T cells get activated when they encounter their corresponding cancer-specific antigen. Eventually, activated effector T cells traffic and infiltrate the tumor bed and through their T cell receptor-MHCI-antigen complex specifically recognize and kill cancer cells. This leads to the release of more cancer antigens and increases the magnitude of the anti-cancer response in successive cycles. In cancer patients, this cancer-immunity cycle is apprehended by different means.

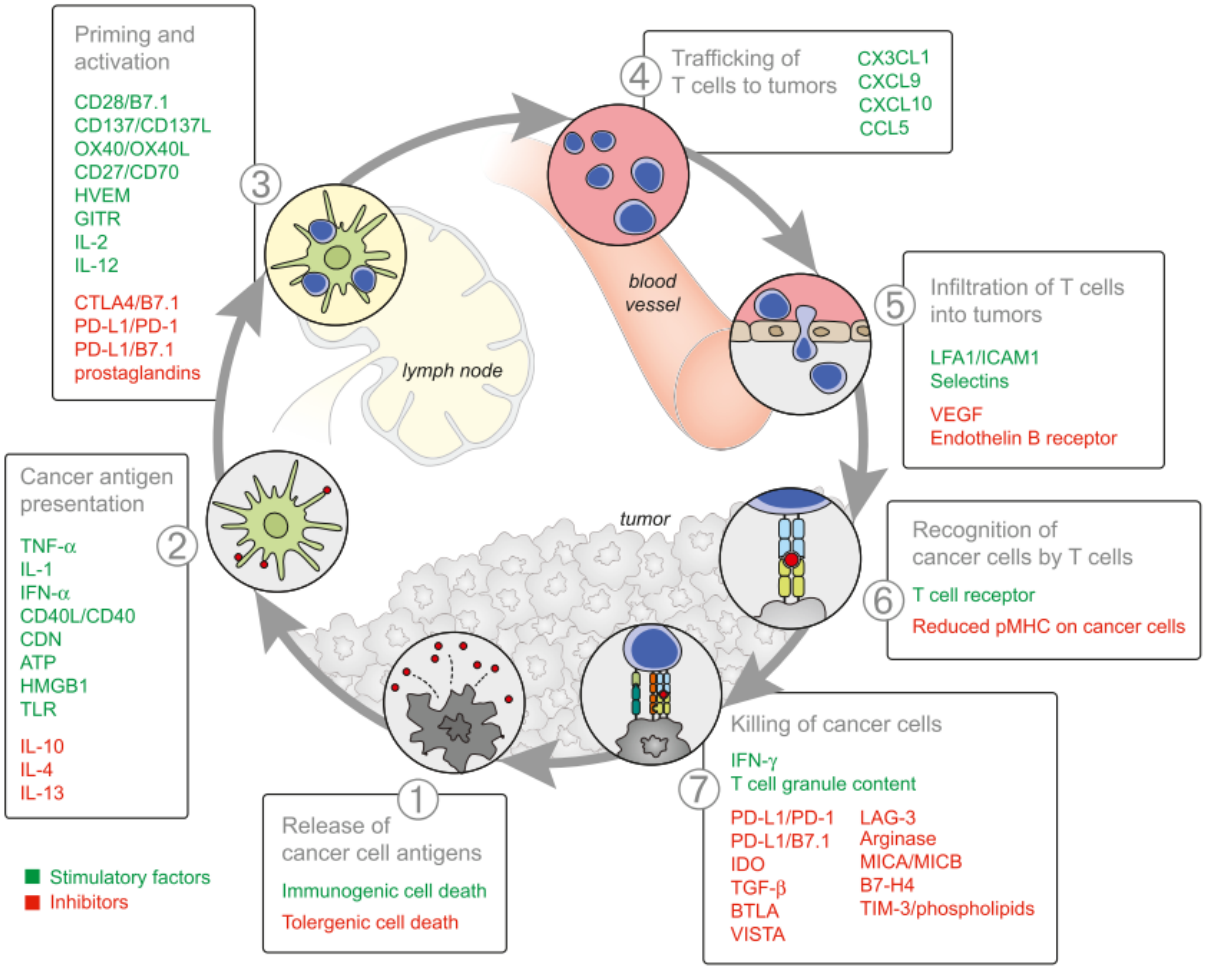

Figure 4: Stimulatory and Inhibitory Factors in the Cancer-Immunity Cycle. The different steps from antigen release, antigen presentation, priming and activation, immune cell trafficking, tumor infiltration, cancer cell recognition, and cancer cell killing are illustrated and for each step inhibitory (red) and stimulatory (green) factors are highlighted (adapted from[130]).

Either antigens are not detected, antigens are tolerated, T cell do not traffic to the tumor, the tumor is not accessible to T cells, or the tumor microenvironment suppresses the effector

cells[131]. Cancer immunotherapy's main aim is to reinitiate a self-sustaining cycle of cancer immunity, without triggering an autoimmune inflammatory response. Thus, it needs finetuned treatment strategy to overcome the negative feedback mechanisms of the immune system. Ideal treatment strategies are therefore patient-specific and identify the rate-limiting step to selectively target the appropriate checkpoints in the cancer-immunity cycle (Figure 4).

Cancer Vaccines

Like traditional vaccines against viruses, it is possible to immunize patients against cancer via tumor antigens[132]. However, in contrast to vaccines against infectious agents, cancer vaccines must, besides other challenges, also break immune tolerance acquired by the tumor to be effective[133]. Accordingly, several hurdles must be overcome to develop a cancer vaccine that achieves a potent cytotoxic T cell response. First, appropriate tumor antigens need to be identified. To avoid tolerance through antigenic drift, multivalent vaccines need to be designed. Sequencing data from tumor tissues can identify mutations or translocation fusions and thus predict potential antigens. However, patient and tumor heterogeneity and the mechanism that only certain peptides are presented on the surface of DCs, makes such predictions difficult[134]. Affinity purification mass spectrometry techniques[135] further improve the selection of antigen peptide targets, but even with the correct antigens in hand, the optimal delivery to patients remains unknown. To bypass this hurdle, DCs can be targeted directly. Because of their professional antigen presentation capabilities, they are also called nature's adjuvants[136] and can effectively initiate a T cell immune response. In this strategy, DCs are isolated from peripheral blood, loaded with tumor antigens, and then reinfused into the patient[129,133]. These DC-based vaccines have shown initial promise for the treatment of castration-resistant prostate cancer[137]. Even if the ideal vaccine can trigger the maturation of DCs and promotes the production of tumor specific cytotoxic T cells, numerous mechanisms of immune evasion by the tumor might compromise its effectiveness. Hence, cancer vaccines might not be administered alone but in combination with other immunotherapy approaches.

Adoptive cell therapy

This type of immunotherapy is based on the antitumor properties of lymphocytes to eradicate tumor cells. Briefly, lymphocytes are isolated from patient's blood, lymph node, or tumor tissue. Then they are expanded ex vivo and finally reinfused into the patient[129]. This approach produces a large amount of effector cells and thereby circumvents the initial steps in the

cancer-immunity cycle. One version of this approach employs T cells only from resected tumor tissue sites. This mixture of CD4 and CD8 positive T cells, also called tumor-infiltrating lymphocytes, are tumor-specific and when expanded with a cocktail of cytokines prior to reinfusion show an increased anti-tumor activity[138]. A modification to this method depletes the host's lymphocytes prior to the infusion of tumor-infiltrating lymphocytes. As a result, immunosuppressive cells, such as Tregs and myeloid-derived suppressor cells, are eliminated in the tumor microenvironment and homeostatic cytokine level increased[139]. This approach has been very successful in the treatment of melanoma patients[140]. However, adoptive cell therapies have obvious disadvantages. For instance, cultivation and expansion of tumor-specific lymphocytes is time and cost intensive[141]. Also, this approach has only shown to be effective in the treatment of melanoma patients, explained by the high tumor mutation burden in melanomas compared to other cancer types[142]. In addition, the treatment is perceived with safety concerns. Although lymphodepletion enhances the efficacy, it can be life-threatening and patient selection is not optimized[143]. To overcome these limitation two major genetic T cell engineering approaches have been developed. First, using viral vector-based expression systems, T cells are transfected to express T cell receptors specific to tumor-associated antigens. This approach profits from key improvements in gene transfer efficiency, T cell receptor design, and target antigen identification selective for tumor cells[144]. However, the clinical use has been limited due to significant secondary destruction of healthy tissues expressing the same target antigen. The second approach fuses an Ig variable domain to a T cell receptor constant domain[129]. These chimeric antigen receptors omit the need for tumor cells to carry a specific antigen, as such engineered T cells can potentially target any surface protein through their Ig antibody domain[145]. This approach is most developed in the treatment of B cell malignancies, where the chimeric antigen receptor is targeting the B cell linage marker, CD19[146]. New approaches are being developed to extended to other cancers than hematologic malignancies and further to address the toxicity and safety issues.

Immune checkpoint blockade

As briefly mentioned before, tumors can induce immune tolerance through the expression of ligands in the tumor microenvironment that bind to T cells and thereby inhibit their function. In general, targeting negative T cell regulators is another immunotherapy approach[147]. For instance, cytotoxic T-lymphocyte-associated protein 4 (CTLA-4) is a receptor expressed on T cells that down-regulates initial stages of T cell activation when interacting with its ligands

B7.1 and B7.2 expressed on DCs[148]. Ipilimumab, an antibody against CTLA-4 blocks this interaction leading to an increased pool of activated T cells. This approach had been approved by the FDA as first-line therapy for melanoma patients with metastatic disease[149]. However, the lack of selectivity regulating T cell activation led to a high percentage of immune related adverse events in treated patients[150]. Nevertheless, this initial success in clinical response coined the way to new targets, such as programmed cell death protein 1 (PD-1) signaling[151]. Once PD-1 expressed on T cells interacts with its ligand, programmed death-ligand 1 (PD-L1), expressed on tumor cells, it inhibits the antitumor response of antigen stimulated T cells by blocking the secretion or production of proinflammatory proteins, such as IFNg[152]. Inhibiting the interaction of PD-1 and PD-L1 with antibodies enhanced the T cell response and mediated anti-tumor activity[153]. This approach generated promising results in a variety of cancer types[154]. This suggest, that for many cancers the cancer-immunity cycle is intact until the step seven of killing cancer cells. The inhibition by PD-1 seems to be rapidly reversible, allowing preexisting anticancer T cells to regain their effector function. In comparison to non-specific activation of the immune system by CTLA-4, PD-1 inhibition shows favorable toxicity and safety profiles[155] with significant response rates[156]. Unfortunately, only a minority of patients do respond to PD-1 inhibitors, pointing to multiple other mechanism of immunosuppression[157,158].

Combination therapies

As outlined above the cancer-immunity cycle can be inhibited or stimulated at different steps. However, single therapy approaches are not as effective as combination therapies that also take the patient's cancer immunological state into account[159,160]. For instance, disabling the immune inhibition in the tumor microenvironment, e.g. using an PD-L1 inhibitor, could benefit vaccines that target earlier stages in the cancer-immunity cycle. However, PD-L1 inhibition might not be the right therapy approach for patients with immune deserted tumors[161]. Approaches that show promising results combine CTLA-4 with PD-1 inhibitors. While CTLA-4 enhances the priming and activation of T cells, blocking PD-1 removes the inhibition of cancer killing T cells inside the tumor. This two-step approach showed rapid and deep response in melanoma patients [162]. Furthermore, anti-PD-1 in combination with vaccination[163,164] or with agents enhancing T cell trafficking and infiltration into the tumor bed[131,165] emerge as promising strategies for the treatment of cancer. Furthermore, conventional therapies such as chemotherapy or radiotherapy, although harmful to the

immune system, also benefit antitumor responses by releasing multiple tumor neoantigens[166]. Cyclophosphamide know to deplete Tregs[167] or paclitaxel know to eliminate MDSCs[168], counter immunosuppressive activities.

Biomarkers

Although immunotherapy has greatly improved therapy options for certain cancer types and its development is progressing at an enormous pace, not all patients respond to these novel strategies. Patient selection based on molecular tumor characterization is crucial for treatment benefit and to avoid treatment-related toxicity. Therefore reliable biomarkers that are able to predict the clinical benefit are needed[169]. For instance, the mutational tumor frequency correlates with the clinical response to anti-CTLA-4 therapy in melanoma[170] or to PD-1 inhibitor in NSCLC[171] and colon cancer[172]. In general, it is hypothesized that high mutational burden is associated with positive response to immune check point inhibitors for certain cancers[142,173]. In addition, the expression levels of PD-L1 on tumor cells serves as a useful biomarker to identify patients that could benefit from such targeted therapies[153]. However, this biomarker is controversially discussed in the literature. It has been shown that patients with low PD-L1 expression might still benefit from anti-PD-L1 antibodies[162], while patients with high PD-L1 expression do not [174]. Furthermore, other biomarkers are explored that could predict the treatment response to immunotherapy, e.g. tumor infiltrating lymphocytes[175], T cell exhaustion markers[157], or genetic profiles of the tumor microenvironment[176]. Overall, more data from human tumors are necessary to further understand the cancer-immunity cycle and to improve cancer therapy response rates. More specific biomarkers will improve clinical decisions on treatment strategies allowing to lower the immune-related toxicities.

1.2 Immunoproteomics

1.2.1 Proteomic strategies to study the immune system

Studying the immune system on the level of proteins, requires the measurement of many proteins at the same time. Omics-technologies such as mass spectrometry (MS)-based proteomics not only allows the characterization of the expression levels of thousands of proteins inside immune cells, but also their interaction partners, post-translational modifications, and localization[177]. This versatile toolbox has become an essential part of modern systems immunology research and has contributed to many novel mechanisms of the immune system[178].

Affinity purification combined with quantitative mass spectrometry-based proteomics (AP-MS) is a widely used strategy to study protein complexes of signaling pathways or to create protein interaction maps of complete cellular proteomes[179]. Usually, the protein of interest serves as bait and through immunoprecipitation interaction partner are retrieved[180]. This strategy has been applied to many immunological research questions. To highlight a few, with AP-MS novel components and regulators of inflammasomes have been discovered. For instance, gasderminD[181] or NIMA-related kinase 7[182] were identified as an important mediators in NLRP3 activation. Furthermore, post translational modifications play a pivotal role in cellular signaling pathways. Phospho-peptide enrichment methods, such as titanium dioxide or immobilized metal ion affinity chromatography, together with tailored peptide identification and quantification methods have allowed immunologist to study phosphorylation sites on thousands of proteins from small sample amounts[183,184]. One of the most unique affinity MS-based strategy in immunology is the characterization of peptides bound to MHC molecules. In this two-step approach, MHC-peptide complexes are isolated via immunoaffinity purification and then the bound peptides are eluted for mass spectrometer (MS) analysis[185,186]. This approach has increased the understanding of the immunopeptidome dramatically by identifying neoepitopes from primary tumor material[187], post translational modifications[188], and proteasome-generated spliced peptides[189].

MS-based imaging strategies allow the study of cell and protein localizations in complex tissue samples. Different imaging methods have been developed that differ in labelling, scan mode, and resolution[190]. While matrix-assisted laser desorption ionization mass spectrometry imaging (MALDI-MSI) does not require any antibodies for detection it has the lowest resolution compared to other used methods[191]. Imaging mass cytometry (IMC) analyses metal-conjugated antibody-stained tissue samples[192]. This technique measures up to 50

antibodies simultaneously by raster scanning the tissue at 1 μm^2 spatial resolution[193]. The third and newest methods, multiplexed ion beam imaging (MIBI), also uses antibodies for protein quantification, but due to its novel ion beam can scan the tissue samples multiple times with a resolution of 10 nm[194]. These imaging strategies have been applied to many different clinical tissue samples and created astonishing pictures of the heterogeneity of the tumor environment[192]. As imaging is mainly based on static tissue samples, it does not capture protein localization dynamics. In addition, image-free proteomics approach have been developed to create organellar maps, which can characterize the protein composition of all major organelles and can study translocation events of proteins after stimulation[195].
Subcellular proteome analysis is a another commonly used proteomics strategy to study the immune system. For instance, intercellular immune cell communication pathways have been studied with traditional antibody-based methods such as ELISA focusing on few secreted proteins. In contrast, with MS-based proteomic approaches unbiased global secretion patterns can be analyzed. This strategy allows the time-resolved investigation of hundreds of secreted proteins from primary immune cells[196]. Furthermore, unconventionally protein section through extracellular vesicles, including exosomes, are another subcellular structure ideal for proteomic analysis[197]. These protein-cargo structures are typically isolated via centrifugation, affinity purification or filtration-based methods. Using proteomics many different EVs have been characterized[198] and new protein biomarkers discovered[199].
Cellular and tissue proteomics has been extensively applied to primary immune cells as well as diverse cancer tissue samples. Many different methodologies to analyze complete cell lysates have matured over the last decades and the common shotgun workflow is discussed in the next section. This quantitative proteomic strategy has revealed subset specific pattern recognition pathways in mouse dendritic cells (DCs)[200]. In human DCs, proteome profiling found that plasmacytoid DCs only express inflammatory-related proteins at low levels, thus unable to secrete pro-inflammatory cytokines[201]. Not only innate, but also adaptive immune cells have been characterized with this strategy. For instance, proteomic analysis revealed cytotoxic protein abundance difference in human CD4 T cell subsets[202] and the metabolic mTOR signaling pathways have been studied in cytotoxic T cells under different inhibitory conditions at a depth of almost 7,000 proteins[203]. Besides cell type resolved complete proteome analysis, this workflow has also been successfully applied to cancer tissues for biomarker discovery[204,205].
Together, these proteomic strategies have made major contrition to our understanding of the immune system. Novel proteomic technologies are on the horizon that will generate more

detailed insights of immune cell subsets and their functional difference. However, seamless integration with other omic-technologies will play a crucial role to generate even more comprehensive pictures of the complex interplay of the different immune cells in time, spatial and context-specific manner[206].

1.2.2 Quantitative shotgun proteomics workflow

Quantitative shotgun or bottom-up proteomics describes the quantification of proteins from their proteolytic digested peptides. The workflow is divided in several steps from protein extraction, digestion, peptide purification, peptide ionization, peptide mass analysis through fragmentation, peptide identification and protein quantification (Figure 5).

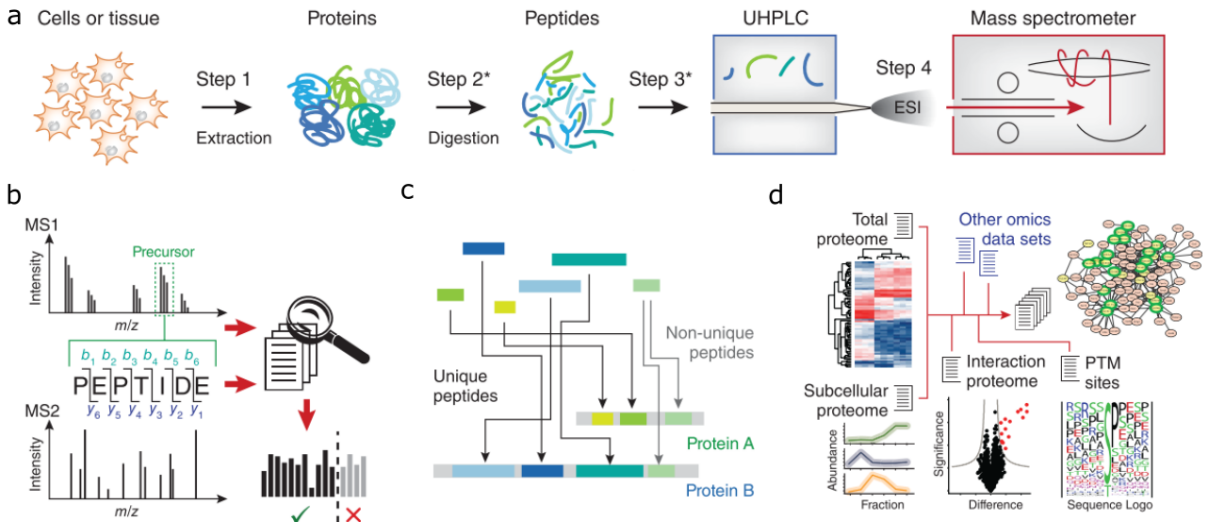

Figure 5: The quantitative shotgun proteomics workflow. a) The different steps from protein extraction, digestion, peptide purification, peptide ionization, and peptide mass analysis are displayed. b-c) The peptide and subsequent protein identification process is illustrated. d) Quantitative protein abundances derived from peptide intensity spectra are used for different data analysis pipelines (adapted from[207]).

First, proteins are extracted using a lysis buffer that typically contains detergents, followed by mechanical breakdowns steps such as sonification. Protease inhibitors are added to protect from unspecific proteolysis and cysteine oxidation is avoided by reducing and subsequent alkylating substances. The proteins are then digested using proteases with specific cleavage motifs. Most commonly, Trypsin and LysC are used for this step, resulting in peptides with terminal arginine or lysine amino acids. Finally, the peptide mixtures are cleaned for the subsequent MS analysis. Therefore, detergents and other MS interfering substances are often removed via filter aided devices[208,209]. When digesting complex samples such as immune

cells, the resulting peptide mixtures are too complex to be directly analyzed by MS. Proteomes from these cells can contain more than 100,000 unique peptides[210]. With reverse-phase ultrahigh-pressure liquid chromatography the peptides are gradually eluted from the hydrophobic column thereby reducing the complexity of the sample. The chromatographic resolution is a key element in the shotgun workflow and many parameters, such as column material, length, diameter, and temperature, have been optimized to achieve robust and reproducible elution profiles[211–213]. Next, the eluting peptides are ionized and thereby sprayed into the mass analyzer via the soft ionization method - electrospray ionization[214]. This method applies high voltage between the column tip and the inlet of the MS, leading to the evaporation of the solvent and subsequent release of charged peptide ions into the gas phase[215]. These ions are then analyzed by the mass analyzer. The different analyzers can be broadly classified into trap (Ion traps, linear ion trap quadrupole, Fourier transform ion cyclotrons, Orbitrap) and beam-based mass analyzer (triple quadrupole, time of flight (TOF)). Each of them has their different strengths and weaknesses based on mass resolution, mass accuracy, dynamic range, and scan speed[216–218]. Continuous improvements have made the Orbitrap, first introduced in 2000[219], a common mass analyzer for analyzing complex peptides mixtures from cell lysates[220–222]. Ions are injected off-center and trapped around a cone shaped electrode. By circulating around the central electrode on stable trajectories and oscillating along the z-axis, the trapped ions induce an alternating image current that is deconvoluted by Fourier transformation to obtain peptide mass spectra[223,224]. In order to clearly identify the different peptide sequences, the peptides are further fragmented. Peptide dissociation is induced by collision with an inert gas, which eventually breaks the peptide bond. To ensure the efficient fragmentation of the different eluting peptides the collisional energy is optimized for a specific peptide charges and mass ranges. In the shotgun proteomic workflow two different fragmentation methods are frequently used, higher energy C-trap dissociation and collision-induced dissociation, generating addition sequence information of the peptide[225,226]. While many peptides with different amino acid sequence have the same MS1 mass, they generate sequence specific MS2 spectra. With the combined information of the parent-ion mass (MS1) and its mass fragments (MS2), peptides from complex protein mixtures can be accurately identified[227]. Although current mass spectrometers have an extremely high scan speed, the selection and fragmentation of all eluting peptides at a given time point is not possible. Therefore, different data acquisition strategies have been developed to maximize peptide identification rates[228]. Single or multi reaction monitoring analyses a pre-selected specific set of precursor ions. Usually run on triple quadrupole instrument, this

targeted approach has a high sensitivity, but is not suitable for complete proteome analysis[229]. Data independent acquisition methods, such as SWATH MS, cycle through the total mass range with a specific small mass window and fragmentation all precursor ions. In this approach, the direct link between the precursor ion and its fragment ions is lost. The resulting complex MS2 spectra are deconvoluted with sample specific peptide fragmentation libraries. This approach requires extremely fast scan speeds and therefore is often applied with quadrupole TOF instruments[230]. In contrast, data dependent acquisition (DDA) methods first select precursor ions in a survey scan and then select the most abundant peptides for fragmentation. Therefore, extensive peptide fragment libraries are not needed, as each precursor ion is clearly linked to it MS2 spectra. However, in complex samples not every peptide will be selected for fragmentation, leading to higher missing peptide quantifications as compared to DDA methods. In the Q Exactive HF, a typical acquisition cycle of one MS1 and 10 MS2 scans takes only one second[221]. As the average peptide elution time is greater than one second, this approach allows the fragmentation of most peptides.

Protein identification

One central aspect of the computational proteomics workflow is the identification of proteins from the acquired peptide mass spectra. Ideally in DDA, each precursor ion can be precisely selected without interference of similar peptides and each fragmentation spectrum is sufficiently complete to allow the determination of the exact peptide sequence. In practice, however, the interpretation of the mass spectra can be challenging, due to contamination from co-isolating precursors or incomplete fragmentation spectra. These challenges are ameliorated by statistical algorithms. First, recorded MS2 spectra are matched against theoretical spectra derived from a sequence data base of in-silico digested proteins. For instance, the search engine Andromeda evaluates the match results with a probability-based scoring model. It calculates a probability that the observed number of matches between the calculated and measured fragment masses could have occurred by chance[231]. Although, the matching performance depends on robust and high-resolution mass analyzers, computational approaches can help to improve the peptide identification rate. To avoid high numbers of false positive hits, usually a false discovery rate of 1% is applied that is derived from reversed amino acid sequences[232]. In the final step of protein identification, the peptides are mapped to protein sequences. Because of protein splice variants or related protein sequences, some identified peptides can be assigned to multiple proteins. One commonly used approach

addresses this issue by assigning ambiguous peptides to proteins with the most evidence. Furthermore, based on the identified peptides certain proteins cannot be distinguished and are therefore grouped. As peptide identification, protein identification typically is also controlled by a 1% false discovery rate[232,233].

Protein quantification

To determine the concentration of proteins expressed in the cell, they first need to be identified and then quantified. In proteomics different relative and absolute quantification methods have been developed. While the former compares protein abundances across samples, absolute quantification allows comparisons of protein abundances within a given sample. All methods have their strengths and weaknesses[234]. In the following, label-free relative quantification and copy number quantification strategies are further discussed[235]. Relative quantification methods come in two flavors labeled or label-free. For instance, labeling approaches incorporate stable-isotope versions of essential amino acids in reference cell populations. While not changing the chemical structure or elution profile of peptides, it causes a mass shift that can be detected by the mass analyzer. Common labelling approaches include, stable amino acid labeling in cell culture[236], isotope-coded affinity tags[237], and tandem mass tags[238]. Although, such approaches are usually more accurate, label free approaches can be applied to any sample and do not suffer from increased sample complexity[235]. In the beginning, label-free approaches made use of the correlation between number of detected mass spectra and protein abundance. For instance, spectral counting estimates the abundance of a given protein by the number of recorded MS2 spectra[239]. Another approach uses the number of identified unique peptides, normalized by the theoretical observable peptides[240]. While these methods are relatively easy to implement their accuracy does not reach the same level of labeled approaches. More recent label-free approaches utilize the high resolution MS1 spectra and consider the intensities profiles of all identified peptides to quantify the proteins in a sample. For example, the MaxLFQ algorithms overcome many challenges of label free quantification. By introducing “delayed normalization” and by extracting the maximum ratio information from peptide signals, these algorithms archive protein quantification accuracies comparable to labeled approaches[241]. Absolute quantification approaches offer protein estimates to the level of copy numbers per cell. This accurate quantification is often achieve using isotopically labeled spike-in standards with known quantities[242–244]. As these approaches are very cost and labor intensive, other less

accurate methods have been developed. For example, the total protein abundance approach (TPA) does not require any spike-in standard but estimates protein copy numbers only based on peptide intensities, the molecular mass, and the protein amount of the cell[245].

1.2.3 Networks of the immune system

The immune systems can be studied on many different hierarchical levels – genomic, transcriptional, translational, cellular signaling process, cell heterogeneity, spatial, intercellular, and organismal - each of which forms their own networks. These networks can be classified by their types of macromolecules and nature of interactions into genetic, gene regulatory, protein-protein interaction, metabolic, and signaling networks. Advances in large-scale omics-technologies and automated bioinformatic analysis pipelines increased the number of high-throughput experiments, creating a wide variety of dataset suitable for studying the immune system from a network perspective[246]. As described in the first chapter, depending on the disease context the immune response triggers a dynamic and complex set of networks from different hierarchies involving hundreds to thousands different molecular players. Although, these networks can be analyzed in increasing detail, deriving biological functional conclusions form such large-scale networks remains challenging[247].

Intracellular signaling networks

Transcriptional networks, generated from yeast one-hybrid assays, chromatin immunoprecipitation experiments, or transcriptomic measurements, are typically analyzed to identify new transcription factors or to predict potential target genes[248,249]. In the immunological context they have been widely applied to decipher the transcriptional circuits of innate immune sensors and their ligands. In particular, microarray-based transcriptome studies identified ATF3 as a negative regulator in TLR-4-stimulated MQs[250] or created time-resolved functional modules in blood leukocytes during systemic inflammation[251]. Furthermore, by means of RNAi knockdowns, a time-resolved transcriptional network revealed the function of 125 transcription factors and divided the pathogen response of DCs into inflammatory and antiviral programs[252]. In addition, gene regulatory networks have been used to characterized cell fate and diversity. Network analysis showed that the transcription factors, PU.1 and Gfi1, orchestrate innate and adaptive immune cell fates[253] and the variety of existing macrophage (MQ) activation states, illustrated by more than 200 transcriptome profiles, challenged the M1/M2 polarization model[254]. Together, network analysis of

transcriptional and chromatin immunoprecipitation data has identified many fundamental gene-regulatory networks that orchestrate the immune response. Signaling networks in immune systems typically represent the information flow from an extracellular receptor down to its transcription factor or gene target. Besides proteins, also small chemical compounds can transmit signals along signaling cascade. Therefore, their network analysis requires the integration of multiple molecular networks, such as gene-regulatory and protein-protein interaction networks as well as their perturbations. Often signaling networks are analyzed by overlaying experimental perturbation data on existing global molecular networks, identifying active or suppressed nodes in the network[247]. MS-based proteomics has emerged as an ideal method for studying signaling networks, as it allows to quantify protein abundances, their post-translational modifications, interactions partners, and translation rates[177]. Integrative approaches, combing transcriptomics and proteomics as well as functional perturbation assays, have created diverse immune cell signaling networks, from TLR signaling in DCs[255,256] to viral DNA sensing[257], providing immunologist with rich resources for further discovery projects. Spatial networks investigate the dynamic relocation of proteins during signal transduction. Many innate sensors, such as NLRP3, move to specific compartments inside the cell to assemble to new complexes or to bind to effector molecules[258]. Organellar structure as well as protein movement adds another important level to the complex network of immune responses. Most described networks so far have analyzed immune cells in response to single or few purified receptor ligands. However, functional networks try to capture the crosstalk between multiple signaling pathways, that are activated during a natural infection. For instance, synergistic inflammatory responses have been discovered in TLR ligand-stimulated human innate immune cells[259]. Furthermore, sequential triggering of signaling pathways, such as LPS priming for inflammasome activation in MQs[260], provides the immune system with additional layers of immune regulation . These examples illustrate the importance to incorporate multiple levels into immune network analytics.

Intercellular networks

Effective pathogen eradication requires several different immune cell types to act in concert, including cells from other parts of the body. Rather than being isolated entities, immune cells maintain a continuous exchange with their surrounding environment, using paracrine and endocrine signaling pathways[261]. These highly coordinated and dynamic intercellular immune cell networks add another level of complexity to the numerous intracellular networks of the

immune system. Although new single-cell technologies, such as single cell transcriptomics[262], mass cytometry[263] or live cell imaging[264], have created maps of immune cell plasticity at exceptional depth, the integrated analysis of inter- and intracellular networks monitoring cells and their expressed proteins remains challenging and usually focus only on a few network levels and cell types. For instance, the immune-body cytokine network, derived from publicly available databases, identified a greater interconnectivity between immune cells as compared to non-immune cells and linked its three-cell cytokine motif architecture to those of social networks[265]. Using curated receptor-ligand databases combined with transcriptomic data, a cell-cell communication map containing 144 human primary cells underlined the highly connected and redundant ligand-receptor paths and revealed novel interacting cell type pairs[266]. As with protein localization in intracellular networks, the spatial location of cells in intercellular networks promotes effective immune responses. Using sophisticated live cell imaging methods to explore the cellular positioning and local intercellular communication within murine lymph nodes, identified diverse lymphoid cells in close proximity to MQs allowing for a rapid antimicrobial immune response[267]. A subclass of intercellular networks form host-pathogen interaction networks. Several such interaction networks have been created and collected in diverse databases[268,269]. Those networks have shown that both bacteria and viruses preferentially target host networks nodes with high connectivity and centrality involved in immune defense mechanisms[270].

While we are still a long way from developing detailed multi-layered predictive network models of the immune response to complex perturbations such as pathogens, the described examples illustrate the great potential systems immunology holds for disease understanding[271] as well as identification of novel actionable drug targets[272].

2 Results

2.1 Social network architecture of human immune cells unveiled by quantitative proteomics

2.1.1 Summary

The immune system is unique in its dynamic interplay and its diverse functions are executed by highly specialized cell types. A major goal of immunology research is to understand how the context-dependent crosstalk of different cell types and the orchestration of their functions enable protection against disease[247,261,273,274]. The interpretation of immune responses is inherently challenging due to its plasticity and its context dependent pathophysiological states (Figure **6**). At the molecular level, intercellular signals are mostly communicated through proteins produced by sending cells that act on receptors of receiving cells. Current approaches mainly focused on the characterization of interactions between individual cell types or cytokines, which neglect a systemic view of the immune response and hence architecture and syntax by which biological messages are exchanged between sometimes distant and mobile cell types remain incompletely understood[265,275].

In this study, high-resolution mass-spectrometry- based proteomics was used to characterize 28 primary human hematopoietic cell populations in steady and activated states at a depth of >10,000 proteins in total. This unbiases rich proteome resource recapitulates many well-known immune cell type functions, but also points to novel cell surface markers that could be used for staining and flow sorting. Together with selected secretome measurements and a newly developed bioinformatic framework, fundamental intercellular communication structures and previously unknown connections between immune cell types were discovered. For example, less related lineages tend to have more interactions, than close related lineages or antigen presenting cells increased their ligand repertoire once activated moving to the top of the intercellular signaling cascade. Together, the findings define a social network architecture of immune cells and provide a systems biology reference framework of intercellular signaling. The quantitative, high-resolution proteomics immune cell compendium, including protein copy numbers, assignments of cell-type-resolved functions, intercellular communication structures and pairwise cell- type comparisons, is available via MaxQB[276] and an interactive online database (http://www.immprot.org/).

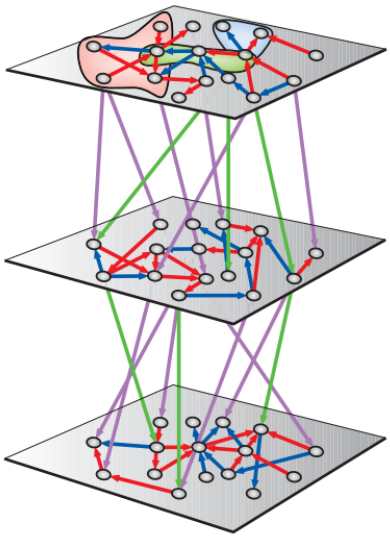

Network component	Social network	Immune system
Actors	Members of society	Immune-cell types
Roles	Same profession; similar age; shared interests	Shared function—e.g., early defense mechanisms; humoral immunity
Context	Family; professional; spare time	Organ; tissue; activation status
Intra-layer communication	Personal communication; e-mails; phone calls	Direct cell–cell interactions; receptor–ligand interactions
Inter-layer communication	Similar to intra-layer communication	Signaling across organs, tissues

Figure 6. The immune system as a multi-layered social network. Immune cells need to fulfill many different functions within the body. To successful coordinate their abilities, they need to interacted not only with each other but also with any other tissue type of the body. This complex interplay resembles in many ways a social network. Novel omic-technologies provide new understandings into the basic architecture of these sophisticated communication networks among immune cells (adapted from[277]).

2.1.2 Contribution

In this collaborative study with the research group of Prof. Lanzavecchia, I performed the immune cell type purification as well as the in vitro assays. David Jarrosay conducted the flow sorting of the different cell types. I conducted the mass spectrometry analysis of their proteomes and secretomes. I completed the RNA extraction and transcriptome analysis. The bioinformatic scripts and analysis were written and run by me. The online R shiny application was developed by Daniel Hornburg. The manuscript was written by Felix Meissner, Matthias Mann, and me. I prepared all figures and tables for the manuscript, except supplementary figure 1.

2.1.3 Publication

This work was published in the journal Nature Immunology in 2017.

Social network architecture of human immune cells unveiled by quantitative proteomics

Jan C Rieckmann, Roger Geiger, Daniel Hornburg, Tobias Wolf, Ksenya Kveler, David Jarrossay, Federica Sallusto, Shai S Shen-Orr, Antonio Lanzavecchia, Matthias Mann & Felix Meissner

Nat Immunol. 2017 May;18(5):583-593. doi: 10.1038/ni.3693. Epub 2017 Mar 6.

RESOURCE

nature immunology

Social network architecture of human immune cells unveiled by quantitative proteomics

Jan C Rieckmann[1], Roger Geiger[2,3], Daniel Hornburg[1], Tobias Wolf[2,3], Ksenya Kveler[4], David Jarrossay[2], Federica Sallusto[2], Shai S Shen-Orr[4], Antonio Lanzavecchia[2,3], Matthias Mann[5] & Felix Meissner[1]

The immune system is unique in its dynamic interplay between numerous cell types. However, a system-wide view of how immune cells communicate to protect against disease has not yet been established. We applied high-resolution mass-spectrometry-based proteomics to characterize 28 primary human hematopoietic cell populations in steady and activated states at a depth of >10,000 proteins in total. Protein copy numbers revealed a specialization of immune cells for ligand and receptor expression, thereby connecting distinct immune functions. By integrating total and secreted proteomes, we discovered fundamental intercellular communication structures and previously unknown connections between cell types. Our publicly accessible (http://www.immprot.org/) proteomic resource provides a framework for the orchestration of cellular interplay and a reference for altered communication associated with pathology.

Distinct immune functions are executed by highly specialized cell types. The coordinated action of the immune system resembles a social network, which enables complex immunological tasks beyond the sum of the functions of individual isolated cell types. A major goal of immunology research is to understand how the context-dependent crosstalk of different cell types and the orchestration of their functions enable protection against disease[1–4]. However, the architecture and syntax by which biological messages, such as cytokines with pleiotropic functions, are exchanged between sometimes distant and mobile cell types is a central feature of the immune system that remains incompletely understood[5,6]. Moreover, the functions of transmitted messages vary depending on the cellular sender, receiver and pathophysiological state, making the interpretation of immune responses inherently challenging.

At the molecular level, intercellular signals are mostly communicated through proteins produced by sending cells that act on receptors of receiving cells. Current approaches focus on the characterization of interactions between individual cell types or cytokines, but new proteomics technologies promise to capture the complexity of intercellular communication comprehensively at the protein level. However, this promise has been challenging to fulfil because of the scarcity of certain subtypes of immune cells, the large dynamic range of the cellular proteome (>6 orders of magnitude) and the low concentration of secreted factors. Important insights into immune cell type composition and intracellular signaling networks have been gained by system-wide transcriptional approaches and antibody-based technologies[7–11]. Although relative measurements of transcripts can be very comprehensive, the correlation between mRNA and protein copy numbers can vary widely[12,13], especially for proteins with roles in intercellular crosstalk[14]. Quantitative, high-resolution mass spectrometry (MS)-based proteomics has developed rapidly and has now matured into a powerful technology that provides a unique opportunity for the system-wide characterization of cellular senders and receivers as well as the accurate quantification of transmitted messages[15–17].

To unravel the complex interactions between immune cells at the protein level, we combined advanced MS approaches developed in our laboratories and characterized 28 hematopoietic cell types that we sorted by flow cytometry from human donors. We accommodated the limited amount of rare immune cells by employing a single-run MS analysis approach[18] while keeping the greatest possible proteome depth. To interpret the dynamic cellular proteomes and secretomes, we developed a bioinformatics framework to assign cell-type-resolved immune functions and connect these via transmitted biological messages. This yielded a network topology from which we could deduce the intercellular information exchange in the immune system. By comparing with the current literature, we discovered systematically understudied intercellular connections and biological messages. Our results highlight different communication structures for myeloid and lymphoid immune cells, as well as on the level of individual proteins for messages with distinct paracrine functions. Exemplified by the cell-type- and context-dependent secretion of innate immune cells, our results provide a holistic picture of unique and shared biological messages with their associated inter- and intracellular information flow. Together, our findings define the social network architecture of immune cells and provide a systems biology reference framework of intercellular signaling. The quantitative, high-resolution proteomics immune cell compendium,

[1]Experimental Systems Immunology, Max Planck Institute of Biochemistry, Bayern, Germany. [2]Institute for Research in Biomedicine, Università della Svizzera italiana, Bellinzona, Switzerland. [3]Institute of Microbiology, ETH Zürich, Zürich, Switzerland. [4]Department of Immunology, Faculty of Medicine, Technion-Israel Institute of Technology, Haifa, Israel. [5]Department of Proteomics and Signal Transduction, Max Planck Institute of Biochemistry, Bayern, Germany. Correspondence should be addressed to F.M. (meissner@biochem.mpg.de) or M.M. (mmann@biochem.mpg.de).

Received 31 August 2016; accepted 26 January 2017; published online 22 March 2017; doi:10.1038/ni.3693

including protein copy numbers, assignments of cell-type-resolved functions, intercellular communication structures and pairwise cell-type comparisons, is freely available via MaxQB[19] and an interactive online database (http://www.immprot.org/).

RESULTS

Proteome atlas of 28 distinct human hematopoietic cell types

We sorted 28 distinct human hematopoietic cell types from peripheral blood of healthy donors by flow cytometry (**Supplementary Fig. 1** and **Supplementary Table 1**). These comprised cells from seven major lineages, including granulocytes (GN), monocytes (MO), dendritic cells (DC), natural killer (NK), B cells (B), CD4 (T4) and CD8 (T8) lymphocytes, as well as erythrocytes and platelets. The two latter cell types were excluded from further analysis, as their proteomes differed markedly from all other proteomes because of their very specialized functions and lack of a nucleus (**Fig. 1a** and Online Methods). We analyzed the cellular proteomes in their steady state and for a subset (17 cell types) in activated states (**Supplementary Table 2**) in single runs by high-resolution MS using a quadrupole Orbitrap instrument[20] (Online Methods). Each proteome state was measured from three to four donors, generating a total of 175 immune cell proteomes. At a peptide and protein false discovery rate (FDR) of 1%, we identified more than 10,000 different proteins with an average of 7,500 proteins per measurement and 8,700 proteins per quadruplicate. For each major immune cell lineage, we identified an average of 9,500 proteins (**Fig. 1b**, **Supplementary Fig. 2a,b** and **Supplementary Table 3**). We performed quantification in a label-free format using the MaxQuant algorithms and the resulting intensity values served as the basis for relative and absolute proteome determination[21,22]. This demonstrated high inter-donor correlation for cell types ($r^2 > 0.97$) (**Supplementary Fig. 2c**).

Gene ontology (GO) category analysis revealed >80% coverage of proteins with known immune-related functions (**Fig. 1c** and **Supplementary Fig. 2d**). In comparison, two previous large-scale human immune cell type cataloguing efforts only covered about 60% of immune annotated and identified approximately 8,000 proteins or genes in total[8,23] (**Fig. 1c,d** and **Supplementary Fig. 2d**). Furthermore, the global proteome profiles are consistent with established cellular functional relationships[24] (**Supplementary Fig. 2e**). All marker proteins used for cell sorting were identified, except for the chemokine (C-C motif) receptor 4 (CCR4), and showed the expected expression profiles (**Supplementary Fig. 2f**).

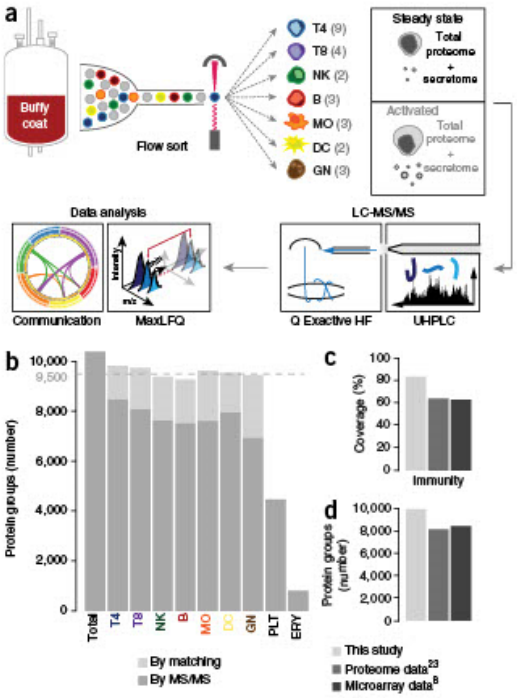

Figure 1 Comprehensive proteome atlas of 28 hematopoietic cell types by single shot LC-MS/MS analysis. (a) Schematic of experimental design and proteomics workflow. GNs, MOs, DCs, NK cells, B cells, and T4 and T8 lymphocytes were isolated by flow cytometry and analyzed by LC-MS/MS in steady and activated states. Numbers in brackets indicate the quantity of individual cell types of the indicated cellular lineage (for example, NK: $CD56^{bright}$ and $CD56^{dim}$ NK cells). ERY, erythrocytes; PLT, platelets. (b) Number of identified protein groups for each major cell lineage. MS/MS-based identifications and those transferred by 'match-between runs' are indicated in dark and light gray, respectively. (c,d) Comparison to proteome[23] and microarray data[8]. (c) Relative coverage of proteins with known immune function. (d) Comparison of the number of protein and gene identifications.

Immune-cell-type-resolved protein expression patterns

Principal component analysis (PCA) to compare the proteomes of the different immune cell types found a clear distinction between lymphoid and myeloid immune cell functions in the first principal component (PC1) (**Fig. 2a**). Bioinformatic enrichment analysis of functional GO terms along this axis[25] revealed that this separation could be attributed to 'T-cell regulation' versus 'early defense mechanisms' (**Supplementary Table 4** and Online Methods). The second dimension (PC2) differentiates 'microbial defense mechanisms' versus 'humoral immunity'.

T lymphocytes and NK cells formed a dense cluster, clearly revealing their close functional relationship. An independent PCA of T and NK cell types (**Fig. 2a**) resolved the effector classes from helper to cytotoxic in PC1 and lineage differentiation from naive to central or effector memory in PC2. Thus, the closest neighbors of NK cells are CD8 T effector memory (T_{EM}) cells, which both target virus-infected cells[26,27].

We selected the top differentially expressed proteins using the seven major lineages described above as labels in a supervised clustering analysis, which confirmed known lineage-specific marker proteins (**Fig. 2b**). These signature proteins were enriched for biological processes according to the functional attributes of the lineages, as expected (**Supplementary Table 5**), with some of these proteins being expressed more than 100-fold higher in particular cell types, such as CD3δ in T cells, CD79A in B cells and Toll-like receptor 2 (TLR2) in monocytes (**Supplementary Fig. 3a–c**). We used the fixed ratio between the total histone signal and cellular DNA to calculate protein copy numbers for the identified proteins[28] (**Supplementary Table 6**). Housekeeping proteins such as GAPDH or ACTB are present at between 10–50 million copies in immune cells, at the top of the ranked expression order (**Fig. 2c**). Lineage markers such as CD14 in classical monocytes or FCGR3B in neutrophils also reach high expression levels of 1–5 million copies. Other important lineage receptors, such as CD4 (T4), CD8A (T8) and CD79A (B cells), have copy numbers between 200,000 and 1 million (**Fig. 2c,d**). Although we found that some transcription factors were present in less than a 100 copies per cell, transcription factors as

a whole had a median of 10,000 copies. At the top of the distribution, IRF7 and IRF8, key transcriptional regulators of type I interferons, were quantified in plasmacytoid DCs (pDCs) with 200,000 and 1 million copies, respectively.

Cell types are commonly defined by exclusive or combinatorial expression of cell surface markers. We applied Lasso regression analysis[29] to investigate previously unknown cell surface receptor combinations for cell lineages as well as for individual cell types. This revealed

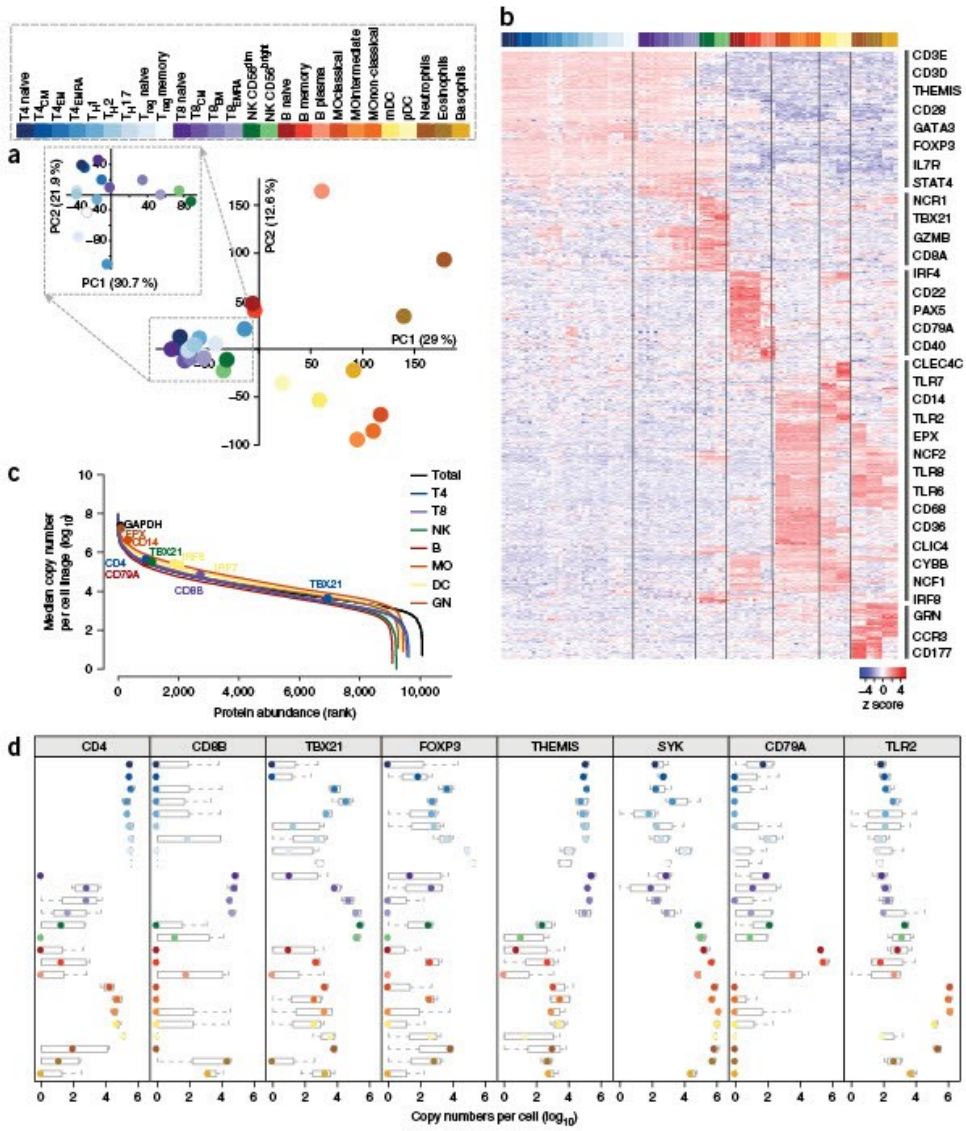

Figure 2 Immune cell relationships are defined by lineage-specific signature proteins. (a) Principal component analysis (PCA) of median protein abundances (ANOVA, Benjamini-Hochberg (BH) $P < 0.01$, df1 = 25, df2 = 78) for different immune cell types. Inset, PCA of T lymphocytes (T4 and T8) and NK cells. Different cell types are indicated by colors in the legend. (b) Heat map with the top 100 significantly differentially expressed proteins for each cell lineage (T4, T8, NK, B, MO, DC and GN) (two-tailed Welch's *t* test, FDR < 1%, $S_0 = 1$, $n = 4$ from independent donors). Rows were clustered using complete linkage with Euclidean distance and columns were ordered by lineage as shown in the legend. Protein names are examples of proteins present in the indicated clusters. (c) Dynamic range of the proteomes of measured cell lineages, based on median estimated copy numbers. (d) Copy number profiles of representative lineage marker proteins. Box-plot elements: center point, median; box limits, first to third quartile (Q1 to Q3); whiskers, from Q1–1.5 × interquartile range (IQR) to Q3+1.5 × IQR.

RESOURCE

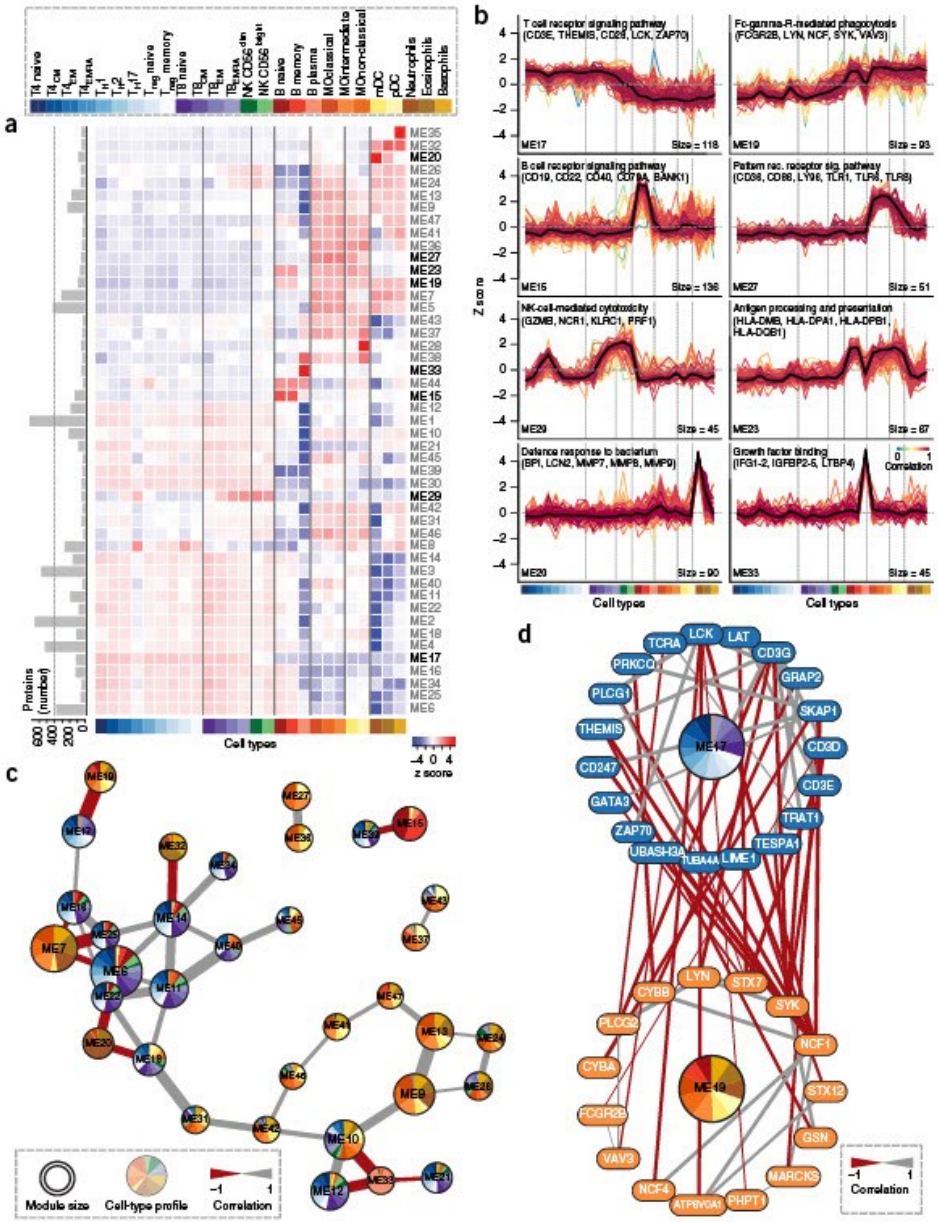

Figure 3 Functional modules of the immune system. (a) Average expression levels of 47 modules (ME1–47) defined by weighted gene cluster network analysis (WGCNA) across cell types. Bars on the left indicate the number of proteins in each module. Modules listed in bold are depicted in b. (b) Protein expression profiles of selected modules across cell types. Each line represents one protein. Average profile is shown in black. Module sizes are indicated at the bottom right. Specific functions of each module assigned by annotation enrichment analysis (Fisher exact test, BH FDR < 5%; **Supplementary Table 7**). (c) Immune system module network. Edges represent Pearson correlation coefficients. Only edges with absolute Pearson correlation > 0.8 are shown. Modules 1–5 and modules with no connecting edges are not shown. Pie chart colors correspond to cell types and the size of the slices corresponds to the module protein expression profile. Module size is represented by node size. (d) Network of proteins in module 17 (ME17, blue) and 19 (ME19, orange) annotated for the enrichment terms 'T cell receptor signaling pathway' and 'Fc-gamma-R-mediated phagocytosis', respectively. Edges represent Pearson correlation coefficient for each protein pair.

the chemokine receptor CX3CR1, identified on T cells with low proliferation, but high cytotoxic capacity[30], to be an lineage receptor for CD8 CD45RA+ effector memory (T_{EMRA}) cells (**Supplementary Fig. 3d**). For rare cell populations, exclusive markers are advantageous for staining and sorting; we identified plasmalemma vesicle-associated protein (PLVAP) and multiple epidermal growth factor-like domains protein 10 (MEGF10) to be such unique cell surface markers for B cell plasma blasts (**Supplementary Fig. 3d**), and confirmed PLVAP expression by flow cytometry (**Supplementary Fig. 3e**).

Functional modules of the immune system

We defined cell-type-resolved functions of the immune system in an unbiased clustering approach[31] by grouping proteins with correlating expression patterns and assigning their functional properties by GO enrichment analysis (**Fig. 3a,b** and **Supplementary Table 7**). Among the 47 resulting functional modules (ME), module ME27 contains the TLR proteins TLR1, TLR6 and TLR8 and is enriched for 'inflammatory response' and 'pattern recognition receptors signaling pathway'. These properties are characteristic of monocytes and

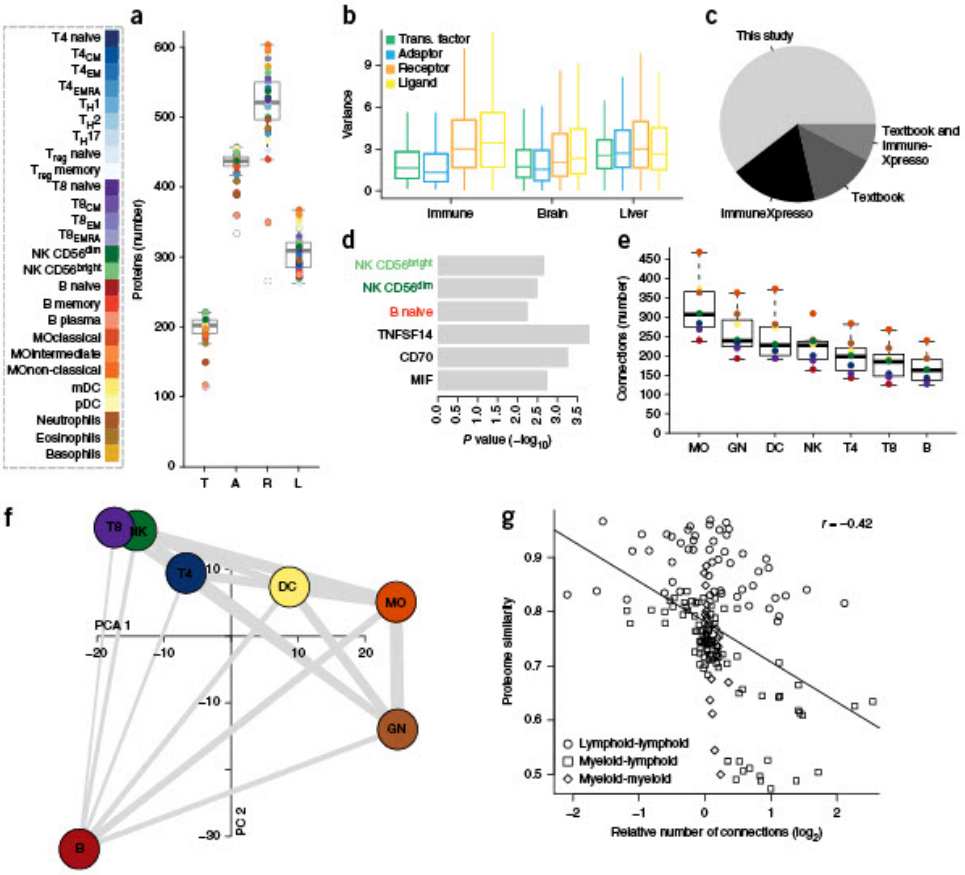

Figure 4 Communication network of immune cells. (**a**) Number of detected transcription factors (T), adaptor molecules (A), receptors (R) and ligands (L) per cell type. (**b**) Expression variances of all immune cell types according to the categories in **a** in steady state compared with cell-type-resolved brain and liver proteomes[38,39]. The variance for each protein was calculated from expression values across all cell types. Activated immune cell states as well as immune cell types from brain (microglia) and liver (Kupffer cells) were excluded from the analysis. Box-plot outliers are not shown in this panel. (**c**) Outgoing connections in our study compared with Textbook and ImmuneXpresso (Online Methods). The pie chart represents all outgoing connections from our study with connections already captured by the two different data sets indicated in slices. (**d**) Understudied cell types and cytokines from outgoing connections. Significantly enriched cell types and cytokines in our study compared to Textbook and ImmuneXpresso identified by Fisher's exact test with BH FDR < 5%. (**e**) Number of intercellular connections between cells of each lineage with all other lineages. (**f**) Immune cell lineage connectivity network. PCA of immune cell lineages proteomes filtered for receptors and ligands. Connecting line strength indicates the number of intercellular connections between lineages. (**g**) Pearson correlation coefficient of cell type median expression values and relative number of intercellular connections of cell type pairs in steady state. The number of interactions between each cell type pair was normalized by the number of receptor and ligand expressed on both cell types. Cell type pairs of the same lineage were excluded. Linear fit (solid line) and Pearson correlation (*r*) are shown (top right). Box-plot elements: center line, median; box limits, first to third quartile (Q1 to Q3); whiskers, from Q1−1.5 × IQR to Q3+1.5 × IQR; points, outliers.

dendritic cells, which specialize in sensing microbial- and danger-associated molecular patterns[32].

Other important modules include ME17, which is described by 'T cell receptor signaling pathway' and includes T-cell-specific proteins such as CD3ε and THEMIS. The specialized function of B lymphocytes, DCs and monocytes to present antigens to T lymphocytes is captured in ME23, which is highly enriched for MHC class II proteins. Module ME29 contains proteins that are highly abundant in NK, CD8 T effector memory (T_{EM}), T_{EMRA} and CD4 T_{EMRA} cells. Cytolytic proteins, such as granzyme B and perforin, are enriched in this module, suggesting that cytotoxic CD4 T cells belong to the CCR7-CD45RA+ memory compartment of CD4 T lymphocytes (**Supplementary Fig. 4a**). Low expression of CD27 and CD28 protein, characteristic of the CD4 T cell cytotoxic phenotype[33], support this finding. The transcription factors TBX21, EOMES, and HOPX are also present in ME29. Although the first two have been reported to be essential for the development of NK cells[34,35], the latter—already linked to T cell effector memory formation[36,37]—might also be involved in NK development or cytolytic immune function. Taken together, our proteome resource and assignment of proteins to functional modules recapitulates many known relationships of the immune system and holds the potential for the generation of new hypotheses.

All of the modules clustered in four groups, reflecting their functional lineage relationships (**Supplementary Fig. 4b**). T and NK cell modules, as well as monocyte and dendritic cell modules, overlapped, indicating shared functionalities; however, each lineage has its unique modules. Anti-correlated modules point toward unique and mutually exclusive cellular functions. For instance, ME20 in neutrophils and ME33 in plasma blasts are clusters that are not shared with any other cell type that are enriched for proteins in 'defense response to bacterium' or 'growth factor binding', respectively (**Fig. 3c**). The highest anti-correlating modules are ME17, representing proteins with adaptive immune functions enriched for 'T cell receptor signaling pathway' and 'lymphocyte differentiation' versus ME19, with proteins involved in innate immune functions such as 'phagocytosis' or 'response to fungus' (**Supplementary Fig. 4c,d**). These two arms of the immune system are also captured in ME25 versus ME7. Module-level anticorrelation could further be resolved at the protein level, and this showed near mutual exclusivity of cellular receptors (CD3ε versus CYBB), adaptors (LCK versus SYK) and transcription factors (STAT4 versus SPI1) (ME19 and ME17; **Fig. 3d**).

Architecture of intercellular communication

To assess which level of cellular signal transduction contributes most to cell-type specificity, we categorized proteins as transcription factors, adaptor molecules, receptors and secreted molecules and investigated how their expression differed between cell types (**Fig. 4a** and **Supplementary Fig. 5a**). The average expression variances of receptors and secreted ligands were nearly twice those of adaptors and transcription factors. These findings indicate that immune cells are more specialized intercellularly than intracellularly. This appears to be a special feature of the immune system, as we did not observe it in the cell-type-resolved proteomes of the brain and the liver[38,39] (**Fig. 4b**).

To further characterize the architecture of intercellular crosstalk, we compared the number of connections established by receptor-receptor or ligand-receptor interactions between cell types. Potential interactions recorded in the STRING database[40] are not cell-type resolved and would be compatible with a network of more than 4×10^5 connections between the 460 receptors and 300 secreted ligands identified in our study, counting interactions as different if they occurred between different cell types. On the basis of the proteomics

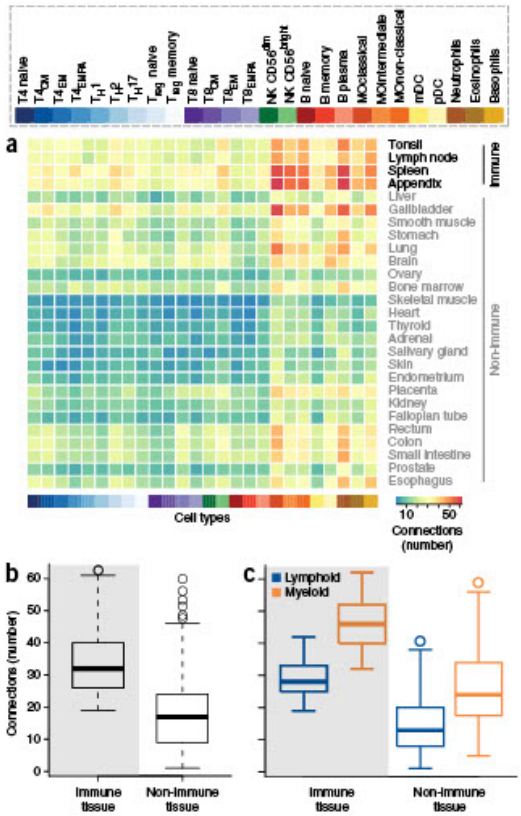

Figure 5 Intercellular connections between immune cells and tissues. (a) Number of intercellular receptor-receptor connections between human immune cell types and tissues. Tissue RNA sequencing data were retrieved from ref. 42. (b) Number of connections to immune or non-immune tissues from a. (c) Comparison of lymphoid and myeloid immune cell connections to tissues. Box-plot elements: center line, median; box limits, first to third quartile (Q1 to Q3); whiskers, from Q1–1.5 × IQR to Q3+1.5 × IQR; points, outliers.

data, we prioritized intercellular connections formed by proteins with high and reproducibly measured expression in the respective cell types. We further considered 'Textbook' knowledge[41] derived from a sophisticated analysis of current literature (Online Methods) to reduce our communication network to the 180,000 most confident connections of protein pairs in different cell types (**Supplementary Fig. 5b,c** and Online Methods). This analysis revealed a plethora of previously unknown cell-type-specific interactions for major cytokines (**Fig. 4c** and **Supplementary Fig. 5d**), as compared with those reported in 1.3 million published PubMed abstracts (ImmuneXpresso, Online Methods). Overrepresented in our communication network were outgoing connections in which NK and naive B cells function as senders as well as those involving tumor necrosis factor (TNF) family members TNFSF14 and TNFSF7 (CD70) and macrophage migration inhibitory factor (MIF) (**Fig. 4d** and **Supplementary Fig. 5e**). We validated one out-going and one in-going intercellular connection that are not described in the current literature. First, we found Resistin

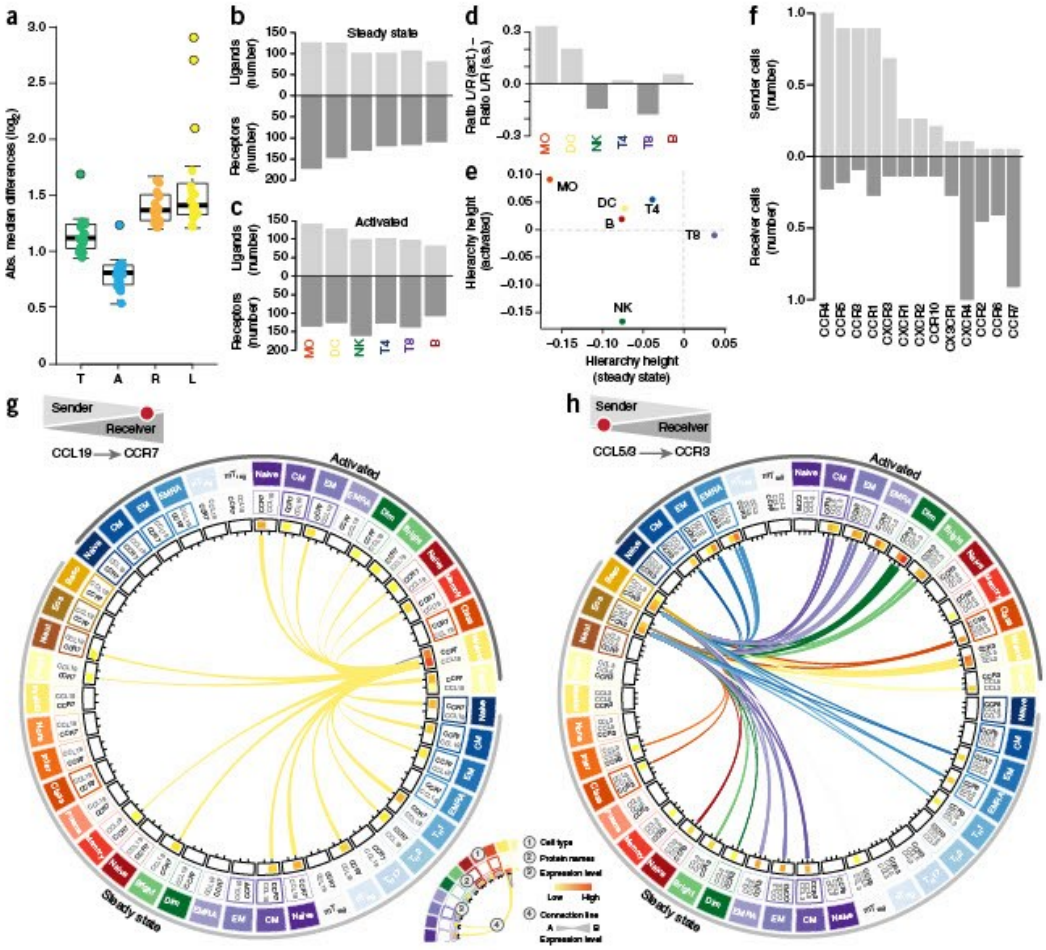

Figure 6 Dynamics of senders and receivers of biological information. (a) Absolute median *t* test expression differences for transcription factors (T), adaptor molecules (A), receptors (R) and ligands (L) between cells in steady and activated states. (b) Receptor and ligand count for the indicated cell types in steady state. (c) Receptor and ligand count for the indicated cell types in activated state. (d) Activation induced change of cellular sending and receiving capacity. Ratio of R/L (act., activated state) to R/L (s.s., steady state) are displayed. (e) In-out degree hierarchy height (h = (O – I) / (O + I)) of immune cell lineages in steady and activated state. (f) Number of cellular senders and receivers for all quantified chemokine receptors. The total numbers are divided by the maximum sender or receiver number, respectively. (g,h) Intercellular communication structures for chemokine receptors (CCRs) and their ligands (CCLs): CCR7-CCL19 (g) and CCR3-CCL5/CCL3 (h). Outer circle, cell types; middle circle, receptor and ligand gene names; inner circle, expression levels. Connecting lines indicate biological information flow with the line color corresponding to the cellular sender. Box-plot elements: center line, median; box limits, first to third quartile (Q1 to Q3); whiskers, from Q1–1.5 × IQR to Q3+1.5 × IQR; points, outliers.

(RETN), which is known to be secreted by monocytes, to also be secreted by activated memory B cells and confirmed this finding by ELISA (**Supplementary Fig. 5f**). Second, we found that the receptor CSF1R, which is known to be expressed on CD4 T cells, was also activated by IL-34 on CD4 memory T cells (**Supplementary Fig. 5g**). In comparison with RNAseq (**Supplementary Table 8**) and microarray data, we observed median correlation of approximately 0.5 for matched cell types and protein profiles (**Supplementary Fig. 6a–d** and **Supplementary Table 9**). Notably, proteome- and transcriptome-based intercellular communication networks were similar in size, but only shared 50% of their connections (**Supplementary Fig. 6e**). We conclude that the current knowledge on immune cell interplay is still incomplete, and our analysis revealed systematically understudied intercellular immune cell signaling paths.

Focusing on the major cell lineages (T4, T8, NK, B, MO, DC, GN), we observed that myeloid immune cells had more connections than lymphoid immune cells (**Fig. 4e,f**). Monocytes establish on average 300 connections with other immune cells, compared with T lymphocytes, which on average establish only 200 connections. Analyzing all cell types in this way established the general trend that

RESOURCE

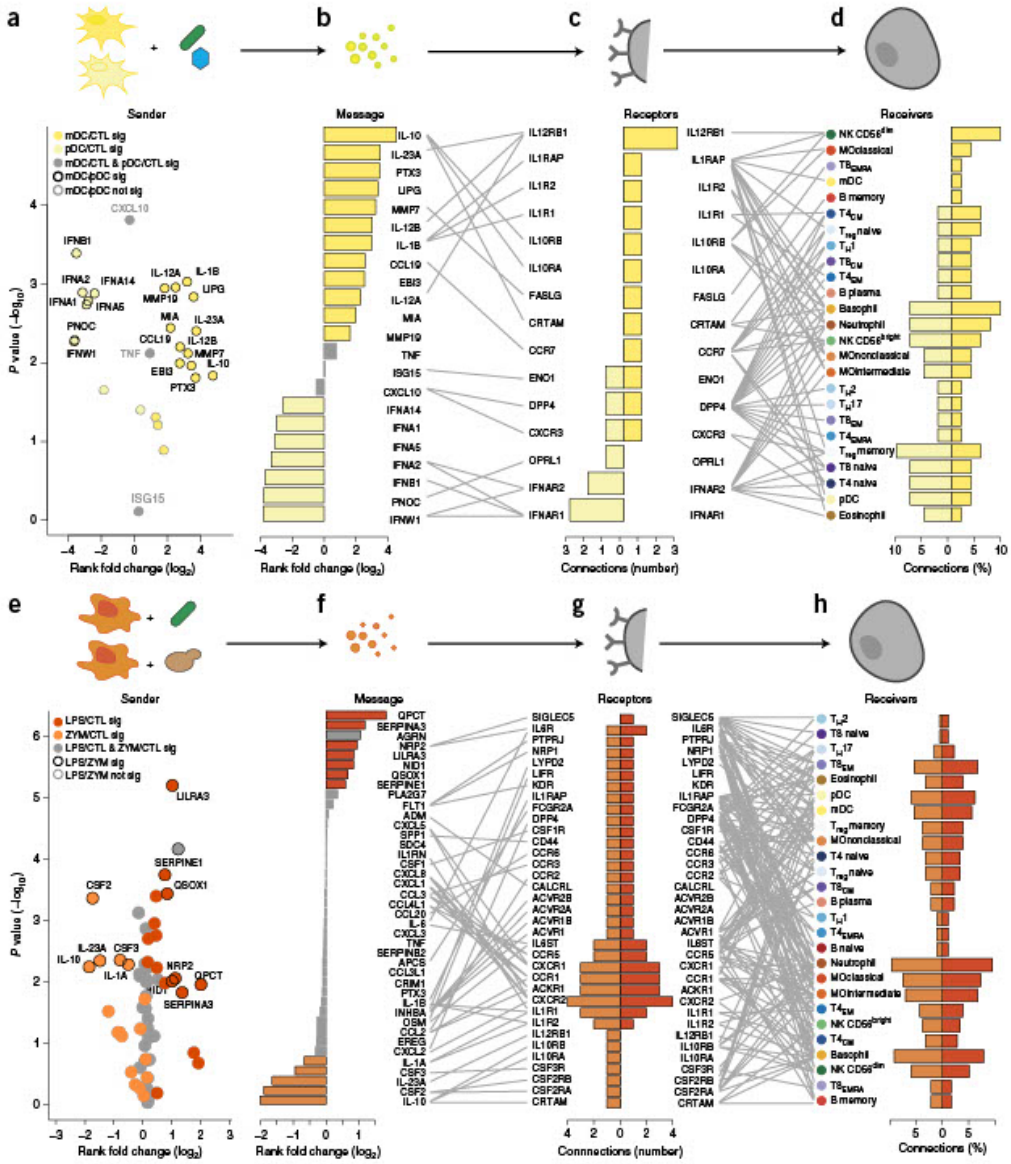

Figure 7 Cell-type- and context-dependent communication. (a) Significantly (two-tailed Welch's *t* test, FDR<5%, $S_0 = 1$, $n = 4$ independent donors) secreted proteins from activated mDCs versus pDCs plotted by rank of secretion. Only significantly secreted proteins compared with unstimulated cells and those proteins annotated as ligand are shown. (b) Same as in a ordered by rank. (c) Receptors interacting with the significantly secreted proteins from mDCs or pDCs. Receptors are ordered by number of ligands and cell-type specificity. Ligand-receptor pairs are connected with a gray line (StringDB score > 0.7). (d) Relative count of connections between secreted molecules from mDCs or pDCs with other immune cell types in their steady state. Receptor expression on receiving cell types are indicated with a connecting gray line. (e) Significantly (two-tailed Welch's *t* test, FDR < 5%, $S_0 = 1$, $n = 5$ independent donors) secreted proteins from cMOs activated either with LPS or ZYM plotted by rank of secretion. Only significantly secreted proteins compared to unstimulated cells and those proteins annotated as ligand are shown. (f) Data are presented as in d ordered by rank. (g) Receptors interacting with the significantly secreted proteins from cMO stimulated with LPS or ZYM. Receptors are ordered by number of ligands and cell-type specificity. Ligand-receptor pairs are connected with a gray line (StringDB score > 0.7). (h) Relative count of connections between cMOs and other immune cell types following either LPS or ZYM activation. Receptor expression on receiving cell types are indicated with a connecting gray line.

less-related cell types (as determined by proteome correlation), such as neutrophils to naive B cells, are more highly connected (**Fig. 4f,g**). Thus, the immune system links distinct cell-type-resolved functions via strong communication structures.

To further elucidate how immune cells connect with organs and tissues, we expanded our network using an atlas of 32 different human organs and tissues[42], focusing only on receptor-receptor intercellular interactions (Online Methods). Immune cells had significantly more connections to tissues related to the immune system (for example, lymph node, spleen, tonsil, and appendix) than to non-lymphoid tissues ($P < 10^{-15}$; **Fig. 5a,b**). Furthermore, myeloid immune cells established more connections with non-immune tissues than lymphoid immune cells (**Fig. 5c**). This presumably reflects cellular preference for tissue residence as phagocytic cells, which scan almost the entire body for foreign or altered self and T lymphocytes, reside primarily in the lymphatic system.

Dynamics of senders and receivers of biological information

Biological messages are dynamic and depend on cell type as well as context, and this is captured in our data set by the dynamic changes of immune cell proteomes following activation. We observed dominant changes at the level of receptors and ligands, which is the level that determines context-dependent adaptation of cellular communication behavior (**Fig. 6a** and Online Methods). To systematically evaluate cellular sender or receiver roles, we assessed the expression and secretion of protein ligands (out degree, O) as well as the expression of the corresponding receptors (in degree, I), respectively. Our analysis highlights the degree to which myeloid cells engage in intercellular communication, as these cells expressed more receptors and ligands than lymphoid cells (**Fig. 6b,c**). Following activation, MO and DCs showed an increase in their ligand-receptor ratio (L/R), whereas the ratio for cytolytic cell types (NK, T8) decreased (**Fig. 6d**). Thus, immune cells seem to employ distinct communication strategies: antigen-presenting cells (MO and DC) changed both quantity and diversity of their ligands and reduce their receptor diversity, whereas cytolytic cell types changed only the quantity of their ligands and increased their receptor diversity (**Fig. 6a–d**). We compared the hierarchy height ($h = (O - I) / (O + I)$)[43] of intercellular signal transduction before and after activation, where senders have $h > 0$ and receivers $h < 0$ (**Fig. 6e**). Following activation, antigen-presenting cells increased their hierarchy height. In particular, MO showed the most prominent change by being at the bottom in steady state, but then move to the top of the hierarchy after activation. Together with the functional module analysis described above, our proteomic analysis sheds light on the dynamic cellular properties of antigen-presenting cells that enable them to alert surrounding cells after sensing microbes or danger.

Apart from the global analysis of communication networks, our data allow the deduction of sender and receiver patterns with different biological functions. Using the established framework at the level of individual proteins, we observed two general types of communication structures for chemokine receptors and their ligands. Broadly expressed receptors, such as CCR7, received information from few sending cells, whereas receptors with cell-type-specific expression patterns, such as CCR3, received information from many cell types (**Fig. 6f–h**). These opposing communication structures are associated with different paracrine functions of transmitted messages. For example, diverse recipient cells expressing CCR7 are attracted to lymph nodes[44], whereas receptor ligation of CCR3 exclusively recruits polymorphonuclear phagocytes to inflamed areas[45]. Thus, our analysis establishes on a global scale that chemokines require specificity either on the sending or receiving end, a principle of directed asymmetric information exchange.

Cell-type- and context-resolved communication structures

To learn more about the syntax of intercellular communication, we compared cell-type- and context-dependent innate immune responses employing in depth and quantitative secretome measurements[14]. We analyzed the outcome of the biological messages by tracing the paracrine intercellular information flow of the secreted proteins. Using dendritic cells as an example for cell-type specificity, we found that, following broad TLR activation, myeloid DCs (mDCs) secreted many different inflammatory cytokines, whereas pDCs secreted primarily type I interferons (**Fig. 7a,b**, **Supplementary Fig. 7a,b** and **Supplementary Table 10**). Using our communication framework, we established that mDCs target numerous receptors and form an intercellular connection network with multiple channels to diverse recipient cells (**Fig. 7c,d**). Intracellularly, the targeted signaling pathways in recipient cells amplified the primary pro-inflammatory signature originating from mDCs by intracellular signal integration and converted it into a defined secondary signature by employing distinct JAK-STAT signaling pathways (**Supplementary Fig. 7c**). By contrast, pDCs fostered a defined single-layer antiviral response in recipient cells by engaging mainly with the interferon alpha receptor (**Fig. 7c,d** and **Supplementary Fig. 7c**).

To dissect context-dependent paracrine responses, we further compared responses of classical monocytes (cMOs, $CD14^{+}CD16^{-}$) to challenges that require distinct actions, such as fungal (zymosan, ZYM) versus bacterial (lipopolysaccharide, LPS) encounters. Key cytokines secreted following ZYM exposure included members of the colony-stimulating factor (CSF) and the anti-inflammatory IL-10 families that connect cMOs with myeloid cells, stimulating a strong intracellular NF-kB signature (**Fig. 7e,f**, **Supplementary Fig. 7d,e** and **Supplementary Table 11**). Conversely, LPS activation released serine protease inhibitors associated with tissue remodeling as well as cell-matrix interactions (**Fig. 7e,f**). Both activation events elicited a strong shared secretory program comprising almost 20 pro-inflammatory proteins, including interleukins, chemokines and TNF family members such as IL-6, CXCL8 or TNF (**Fig. 7e,f**). Based on the targeted receptors and their cell-type-specific expression, the shared pro-inflammatory program conveyed immune instructions directed toward multiple cellular recipients (**Fig. 7g,h**). It converged intracellularly with pleiotropic properties ranging from pro-inflammatory over chemoattractant to cell-death-inducing functions (**Supplementary Fig. 7f**).

DISCUSSION

Intercellular communication between diverse cell types orchestrates a plethora of physiological functions. However, a system-wide view of how cells exchange information had not been established because of technological limitations. We attempted to globally assess the dynamic communication structures of the immune system. We successfully measured the proteomes of all major human immune cell types present in the blood in steady and selected activation states at great sensitivity and quantitative depths. With more than 80% coverage of immune-system-annotated proteins and around 70% coverage for immune-relevant signaling molecules such as transcription factors, adaptor molecules, cell surface receptors and secreted molecules, we provide the most comprehensive cell-type-resolved human proteome resource to date. Some of the remaining proteins appear to be confined to non-circulating immune cells or to immune states that were not sampled. The immune system displays an almost infinite diversity in cell types and activation states, and achieving completeness in both dimensions is particularly challenging for human cells[46].

RESOURCE

By combining total proteome with secretome measurements and a bioinformatics framework, we constructed a social network of human immune cells and deduced the logic of immune cell interplay. This enabled the discovery of potential new cell type markers, protein associations to functional modules and intercellular connections. As a result of the imperfect correlation of proteome to transcriptome, communication networks constructed from RNA data may insufficiently capture intercellular signaling on the level of proteins. Our proteomics-based analysis revealed that the immune cell communication network is more complex than what is captured by the current literature. Common messages are used between many more cell types, highlighting promising research directions, such as NK cells, which appear to have additional functions in orchestrating immune responses. As examples for the discovery potential of our analysis, we validated one previously unknown outgoing connection (B cells → RETN) and one ingoing connection (IL-34 → T4 memory cells). However, as a result of the automated extraction of intercellular connections from the current literature (Online Methods) and its mapping to our proteomics communication network, inaccuracies in total as well as individual understudied connections can be expected. Given that connections in our network are defined by annotated evidence (Online Methods), individual pairwise interactions may not be captured correctly. Although false positives may derive from incorrect or outdated annotations, false negatives may derive from not discovered or not deposited interactions as well as by undetected proteins. To avoid overestimation, we discarded 50% of the possible interactions of the communication network and report only those with high confidence using 'Textbook' knowledge as reference. To evaluate the probability of individual intercellular connections, however, further information on cell type abundance and tissue distributions could be considered in the future.

Our results demonstrate that immune cell signaling is more diverse inter- than intracellularly in comparison with other organs such as brain and liver. To adapt to extracellular cues, intercellular immune signaling is further specifically tuned by the regulation of ligand and receptor expression. Thus, proteomics highlight how immune cell diversity and plasticity together shape protective immunity. We found that antigen-presenting cells increased their capacity to send information in response to changing conditions, forming the top of the intercellular signaling hierarchy. In contrast, cells with cytotoxic functions decreased their hierarchy height. Dependent on the biological messages that are sent, however, different communication structures are employed: as a general underlying principle, we found that communication was restricted to a limited number of sending or receiving cell types for any given cytokine, presumably to achieve specificity in intercellular signal transduction at a minimum cost of resources. On the level of individual cells, intercellular communication structures may differ from those obtained from sorted cell populations. Single-cell technologies to study cell-to-cell crosstalk on the protein level may further increase our understanding of communication diversity and heterogeneity in the future.

According to our data and analysis, the current classification of immune cell identity based on expression of lineage markers, mainly transcription factors and cell surface receptors, would gain resolution by including secreted ligands and corresponding intercellular connections. Moreover, the interpretation of biological messages transmitted during disease, that is, cocktails of cytokines in case of complex immune responses, could be improved by integrating information on targeted cell types and their activated intracellular signaling programs. Current experimental approaches are largely focused on a single or a few different proteins, which makes it challenging to dissect the logic of inflammatory programs in redundant versus cooperative immunological signals. By contrast, the proteomics approach naturally deals with these challenges and provides a systems-wide, interconnected network of healthy immune functions, representing a reference to identify deviating communication patterns associated with pathology.

The immune system's diversity of cellular components and complementation of cell-type-resolved competences comprises features immanent to social communities. Considering heterogeneity, plasticity and networking of cell types, the immune system is tremendously complex. Given the mobility of the cellular players, it presents an ideal example for studying how physiological functions are orchestrated by intercellular communication. Our analysis reveals some of the concepts that are shared between the immune system and other types of social networks. These include communication structures between individual players with defined hierarchy and logic aimed at achieving complex tasks.

Our study should be considered a starting point for the investigation of intercellular information exchange at higher cellular and contextual resolution. An expansion of the communication network to tissue resident immune cells and their direct interactions would be particularly exciting, although accessibility and the number of cells obtainable from healthy human donors remain a challenge. Future studies should evaluate whether the sender-receiver principles of cellular communication deduced here can be extended to other organs and multicellular organisms. The availability of further system-wide information that can also be gained by proteomics, such as extracellular protein-protein interactions or post-translational modifications in intracellular signaling networks, could further refine the architecture of our communication network.

In conclusion, our findings establish a social immune cell network on the level of proteins and provides an experimental and conceptual framework to deduce fundamental communications structures and interpret context and cell-type-dependent immune dynamics.

METHODS

Methods, including statements of data availability and any associated accession codes and references, are available in the online version of the paper.

Note: Any Supplementary Information and Source Data files are available in the online version of the paper.

ACKNOWLEDGMENTS

We thank R. Scheltema for MS assistance, K. Mayr, I. Paron, S. Gabriele, S. Dewitz and M. Dodel for technical assistance, M. Wierer and P. Sinitcyn for support with RNAseq analysis, M. Oroshi and C. Schaab for computer and database support, A. Zychlinsky for critical review of the manuscript, and J. Geddes, A. Frauenstein, M. Phulphagar and L. Kühn for helpful discussions. The work was funded by the Max Planck Society for the Advancement of Science. R.G. was supported by a grant from the Swiss SystemsX.ch initiative, evaluated by the Swiss National Science Foundation. A.L. is supported by the Helmut Horten Foundation.

AUTHOR CONTRIBUTIONS

J.C.R., R.G., D.J. and T.W. performed flow and cell culture experiments. J.C.R. developed and implemented the bioinformatics methods. J.C.R. and F.M. conceived the data analysis and interpreted the data. D.H. assisted in data analysis and implemented the website. S.S.S. and K.K. assisted in data analysis and provided the Textbook and ImmuneXpresso data sets. F.M. and M.M. conceived the study. F.M., A.L. and F.S. supervised the experiments. F.M., J.C.R. and M.M. wrote the manuscript.

COMPETING FINANCIAL INTERESTS

The authors declare no competing financial interests.

1. Subramanian, N., Torabi-Parizi, P., Gottschalk, R.A., Germain, R.N. & Dutta, B. Network representations of immune system complexity. *Wiley Interdiscip. Rev. Syst. Biol. Med.* **7**, 13–38 (2015).
2. Rivera, A., Siracusa, M.C., Yap, G.S. & Gause, W.C. Innate cell communication kick-starts pathogen-specific immunity. *Nat. Immunol.* **17**, 356–363 (2016).
3. Hotson, A.N. *et al.* Coordinate actions of innate immune responses oppose those of the adaptive immune system during Salmonella infection of mice. *Sci. Signal.* **9**, ra4 (2016).
4. Dobrin, R. *et al.* Multi-tissue coexpression networks reveal unexpected subnetworks associated with disease. *Genome Biol.* **10**, R55 (2009).
5. Frankenstein, Z., Alon, U. & Cohen, I.R. The immune-body cytokine network defines a social architecture of cell interactions. *Biol. Direct* **1**, 32 (2006).
6. Shen-Orr, S.S. *et al.* Towards a cytokine-cell interaction knowledgebase of the adaptive immune system. *Pac. Symp. Biocomput.* **2009**, 439–450 (2009).
7. Heng, T.S., Painter, M.W. & Immunological Genome Project, C. The Immunological Genome Project: networks of gene expression in immune cells. *Nat. Immunol.* **9**, 1091–1094 (2008).
8. Novershtern, N. *et al.* Densely interconnected transcriptional circuits control cell states in human hematopoiesis. *Cell* **144**, 296–309 (2011).
9. Bendall, S.C. *et al.* Single-cell mass cytometry of differential immune and drug responses across a human hematopoietic continuum. *Science* **332**, 687–696 (2011).
10. Parnas, O. *et al.* A genome-wide CRISPR screen in primary immune cells to dissect regulatory networks. *Cell* **162**, 675–686 (2015).
11. Paul, F. *et al.* Transcriptional heterogeneity and lineage commitment in myeloid progenitors. *Cell* **163**, 1663–1677 (2015).
12. Schwanhausser, B. *et al.* Global quantification of mammalian gene expression control. *Nature* **473**, 337–342 (2011).
13. Jovanovic, M. *et al.* Immunogenetics. Dynamic profiling of the protein life cycle in response to pathogens. *Science* **347**, 1259038 (2015).
14. Meissner, F., Scheltema, R.A., Mollenkopf, H.J. & Mann, M. Direct proteomic quantification of the secretome of activated immune cells. *Science* **340**, 475–478 (2013).
15. Altelaar, A.F., Munoz, J. & Heck, A.J. Next-generation proteomics: towards an integrative view of proteome dynamics. *Nat. Rev. Genet.* **14**, 35–48 (2013).
16. Aebersold, R. & Mann, M. Mass-spectrometric exploration of proteome structure and function. *Nature* **537**, 347–355 (2016).
17. Meissner, F. & Mann, M. Quantitative shotgun proteomics: considerations for a high-quality workflow in immunology. *Nat. Immunol.* **15**, 112–117 (2014).
18. Nagaraj, N. *et al.* System-wide perturbation analysis with nearly complete coverage of the yeast proteome by single-shot ultra HPLC runs on a bench top Orbitrap. *Mol. Cell Proteomics* **11**, M111 013722 (2012).
19. Schaab, C., Geiger, T., Stoehr, G., Cox, J. & Mann, M. Analysis of high accuracy, quantitative proteomics data in the MaxQB database. *Mol. Cell Proteomics* **11**, M111 014068 (2012).
20. Scheltema, R.A. *et al.* The Q Exactive HF, a Benchtop mass spectrometer with a pre-filter, high-performance quadrupole and an ultra-high-field Orbitrap analyzer. *Mol. Cell. Proteomics* **13**, 3698–3708 (2014).
21. Cox, J. & Mann, M. MaxQuant enables high peptide identification rates, individualized p.p.b.-range mass accuracies and proteome-wide protein quantification. *Nat. Biotechnol.* **26**, 1367–1372 (2008).
22. Cox, J. *et al.* Accurate proteome-wide label-free quantification by delayed normalization and maximal peptide ratio extraction, termed MaxLFQ. *Mol. Cell. Proteomics* **13**, 2513–2526 (2014).
23. Kim, M.S. *et al.* A draft map of the human proteome. *Nature* **509**, 575–581 (2014).
24. Jojic, V. *et al.* Identification of transcriptional regulators in the mouse immune system. *Nat. Immunol.* **14**, 633–643 (2013).
25. Cox, J. & Mann, M. 1D and 2D annotation enrichment: a statistical method integrating quantitative proteomics with complementary high-throughput data. *BMC Bioinformatics* **13** (Suppl. 16), S12 (2012).
26. Vivier, E., Tomasello, E., Baratin, M., Walzer, T. & Ugolini, S. Functions of natural killer cells. *Nat. Immunol.* **9**, 503–510 (2008).
27. Zhang, N. & Bevan, M.J. CD8(+) T cells: foot soldiers of the immune system. *Immunity* **35**, 161–168 (2011).
28. Wisniewski, J.R., Hein, M.Y., Cox, J. & Mann, M. A 'proteomic ruler' for protein copy number and concentration estimation without spike-in standards. *Mol. Cell. Proteomics* **13**, 3497–3506 (2014).
29. Friedman, J., Hastie, T. & Tibshirani, R. Regularization paths for generalized linear models via coordinate descent. *J. Stat. Softw.* **33**, 1–22 (2010).
30. Bottcher, J.P. *et al.* Functional classification of memory CD8+ T cells by CX3CR1 expression. *Nat. Commun.* **6**, 8306 (2015).
31. Langfelder, P. & Horvath, S. WGCNA: an R package for weighted correlation network analysis. *BMC Bioinformatics* **9**, 559 (2008).
32. Bieber, K. & Autenrieth, S.E. Insights how monocytes and dendritic cells contribute and regulate immune defense against microbial pathogens. *Immunobiology* **220**, 215–226 (2015).
33. Appay, V. The physiological role of cytotoxic CD4+ T cells: the holy grail? *Clin. Exp. Immunol.* **138**, 10–13 (2004).
34. Gordon, S.M. *et al.* The transcription factors T-bet and Eomes control key checkpoints of natural killer cell maturation. *Immunity* **36**, 55–67 (2012).
35. Townsend, M.J. *et al.* T-bet regulates the terminal maturation and homeostasis of NK and Valpha14i NKT cells. *Immunity* **20**, 477–494 (2004).
36. Bezman, N.A. *et al.* Molecular definition of the identity and activation of natural killer cells. *Nat. Immunol.* **13**, 1000–1009 (2012).
37. Albrecht, I. *et al.* Persistence of effector memory Th1 cells is regulated by Hopx. *Eur. J. Immunol.* **40**, 2993–3006 (2010).
38. Sharma, K. *et al.* Cell-type- and brain-region-resolved mouse brain proteome. *Nat. Neurosci.* **18**, 1819–1831 (2015).
39. Azimifar, S.B., Nagaraj, N., Cox, J. & Mann, M. Cell-type-resolved quantitative proteomics of murine liver. *Cell Metab.* **20**, 1076–1087 (2014).
40. Szklarczyk, D. *et al.* STRING v10: protein-protein interaction networks, integrated over the tree of life. *Nucleic Acids Res.* **43**, D447–D452 (2015).
41. Dembic, Z. *The Cytokines of the Immune System: The Role of Cytokines in Disease Related to Immune Response* (Elsevier Science, 2015).
42. Uhlen, M. *et al.* Proteomics. Tissue-based map of the human proteome. *Science* **347**, 1260419 (2015).
43. Gerstein, M.B. *et al.* Architecture of the human regulatory network derived from ENCODE data. *Nature* **489**, 91–100 (2012).
44. Forster, R., Davalos-Misslitz, A.C. & Rot, A. CCR7 and its ligands: balancing immunity and tolerance. *Nat. Rev. Immunol.* **8**, 362–371 (2008).
45. Ponath, P.D. *et al.* Molecular cloning and characterization of a human eotaxin receptor expressed selectively on eosinophils. *J. Exp. Med.* **183**, 2437–2448 (1996).
46. Kim, C.C. & Lanier, L.L. Beyond the transcriptome: completion of act one of the Immunological Genome Project. *Curr. Opin. Immunol.* **25**, 593–597 (2013).

ONLINE METHODS

Blood samples and cell sorting. Blood from healthy donors (~450 ml) was obtained from the Swiss Blood Donation Center of Basel and Lugano, and used in compliance with the Federal Office of Public Health (Authorization no. A000197/2 to F.S.). Peripheral blood mononuclear cells (PBMC) were isolated using Ficoll-Plaque Plus (GE Healthcare) sedimentation. Cells were positively selected using magnetic microbeads (Miltenyi Biotec). Sorting was performed with a FACSAria flow cytometer (BD Biosciences) and cell types were sorted to >98% purity (**Supplementary Fig. 1** and **Supplementary Tables 1** and **12**). Cells were either collected in complete medium or for proteome measurement washed in PBS, snap frozen and stored at −80 °C. Erythrocytes were isolated by removing the fraction with lower density as previously described[47]. The erythrocyte packed phase at the bottom after the density centrifugation was washed twice with ice cold PBS, snap frozen and then stored at −80 °C until further use. Platelets were isolated by OptiPrep density gradient purification[48]. 3 ml whole blood was layered over 5 ml of the density solution (5 ml of 1.320 g/ml 60% iodixanol stock solution; OptiPrep density gradient medium, Sigma-Aldrich) and mixed with 22 ml diluent (0.85% NaCl, 20 mM HEPES-NaOH, pH 7.4, 1 mM EDTA). The sample was centrifuged at 350 *g* for 15 min at 20 °C in a swinging bucket rotor with the brake switched off. Platelets were harvested from the broad turbid band below the interface. Platelets were washed twice with PBS and stored at −80 °C until further use.

***In vitro* activation assays.** Flow sorted cells were cultured in RPMI-1640 medium supplemented with 2 mM glutamine, non-essential amino acids (0.1 mM of each amino acid), 1 mM sodium pyruvate, penicillin (50 U/ml), streptomycin (50 µg/ml; all from Invitrogen) and 5% (v/v) human serum (Swiss Blood Center). T lymphocytes were stimulated for 48h with plate-bound anti-CD3 (5µg/ml, clone TR66) and anti-CD28 (1µg/ml CD28.2, BD Biosciences) and expanded for 48 h with IL-2 (500 U/ml). NK cells were stimulated with the NK Cell Activation/Expansion Kit, according to the manufacturer's instructions (130094483, Miltenyi). In brief, NK cells were co-cultured in the presents of CD2 and CD355 (NKp46) coated beads together with IL-2 (500 U/ml) for up to 14 d. B cells were stimulated using a cocktail of Goat F(ab')2 anti-human Lambda/Kappa (each 2 µg/ml), F(ab')2 Goat anti-mouse IgG Fc (3 µg/ml), CpG (100ng/ml), anti-CD40 (6µg/ml), for 96h. Monocytes and dendritic cells were stimulated with the TLR4 agonist lipopolysaccharide (LPS, 100ng/ml) and TLR7/8 agonist Resiquimod (R848, 2.5 µg/ml) for 12 h (activation conditions are summarized in **Supplementary Table 2**). After stimulation, cells were washed with PBS and shock frozen until further use. For secretome measurements, cells were cultured as described above, with the adjustment of exchanging the complete medium after 2 h of priming with medium lacking serum and phenol red. Our data show that with this strategy we also capture proteins that are released early (such as many chemokines or TNF) while maintaining optimal cell viability. Cells were pelleted at 3,000 rpm for 5 min. Supernatants were removed carefully while leaving ¼ culture medium surplus to reduce cell contamination. Cell debris were removed by an additional centrifugation step at full speed for 10 min. Supernatants were shock frozen and stored at −80 °C until further use.

Cytokine analysis. Secretion of resistin (RETN) was measured in culture supernatants using the human resistin ELISA kit from Sigma Aldrich.

CD4 T cell activation with IL-34. Total CD4 memory T cells were flow sorted ($CD4^+CD45RA^+$) and activated as described above with the alteration that IL-34 was added to the culture medium (1, 10, 100 ng/ml). After 96 h cells were washed twice with PBS, shock frozen and subjected to total proteome analysis.

Sample preparation for MS analysis. Cell pellets and supernatants were lysed in 8 M urea and 2 M urea, respectively, 10 mM HEPES (pH 8), 10 mM DTT and sonicated at 4 °C for 15 min (level 5, Bioruptor, Diagenode). Alkylation of reduced cysteines was performed in the dark for 30 min with 55 mM iodacetamide (IAA) followed by a two-step proteolytic digestion. Samples were digested at 21–24 °C with LysC (1:50, w/w, Wako) for 3 h. Cell lysates were adjusted to 2 M Urea with 50 mM ammoniumbicarbonate and then both cell lysates and supernatants were digested with trypsin (1:50, w/w, Promega) at 21–24 °C overnight. The resulting peptide mixtures were acidified and loaded on C18 StageTips (EmporeTM, IVA-Analysentechnik). Peptides were eluted with 80% acetonitrile (ACN), dried using a SpeedVac centrifuge, and resuspended in 2% ACN, 0.1% trifluoroacetic acid (TFA), and 0.5% acetic acid. For MACS enriched cell pellets lysis was performed in 4% SDS, 10 mM HEPES (pH 8, Biomol), 10 mM DTT. Cells were heated at 95 °C for 10 min and sonicated at 4 °C for 15 min (level 5, Bioruptor, Diagenode). Proteins were precipitated with acetone at −20 °C overnight and resuspended the next day in 8 M urea, 10 mM Hepes (pH 8). Proteolytic digestion was carried out as described above. Chemicals were purchased from Sigma-Aldrich unless stated otherwise.

LC-MS/MS. Peptides were separated on an EASY-nLC 1000 HPLC system (Thermo Fisher Scientific) coupled online to the Q Exactive HF mass spectrometer via a nanoelectrospray source (Thermo Fisher Scientific)[20]. Peptides were loaded in buffer A (0.5% formic acid) on in house packed columns (75-µm inner diameter, 50 cm length, and 1.9 µm C18 particles from Dr. Maisch GmbH, Germany). Peptides were eluted with a nonlinear 180-min gradient of 5–60% buffer B (80% ACN, 0.5% formic acid) at a flow rate of 250 nl/min and a column temperature of 55 °C. Operational parameters were real-time monitored by the SprayQC software[49]. The Q Exactive HF was operated in a data dependent mode with a survey scan range of 300–1,650 m/z and a resolution of 60,000 to 120,000 at m/z 200. Up to the ten most abundant isotope patterns with a charge >1 were isolated with a 1.8 Thomson (Th) isolation window and subjected to higher-energy collisional dissociation (HCD) fragmentation at a normalized collision energy of 26. Fragmentation spectra were acquired with a resolution of 15,000 at m/z 200. Dynamic exclusion of sequenced peptides was set to 30 s to reduce repeated peptide sequencing. Thresholds for ion injection time and ion target values were set to 20 ms and 3E6 for the survey scans and 55 ms and 1E5 for the MS/MS scans, respectively. Data were acquired using the Xcalibur software (Thermo Scientific).

LC-MS/MS data analysis. MaxQuant software (version 1.5.3.2) was used to analyze MS raw files[21]. MS/MS spectra were searched against the human Uniprot FASTA database (Version May 2013, 90,507 entries) and a common contaminants database (247 entries) by the Andromeda search engine[50]. Cysteine carbamidomethylation was applied as fixed and N-terminal acetylation, deamidation at NQ, and methionine oxidation as variable modifications. Enzyme specificity was set to trypsin with a maximum of 2 missed cleavages and a minimum peptide length of 7 amino acids. A false discovery rate (FDR) of 1% was applied at the peptide and protein level. Peptide identification was performed with an allowed initial precursor mass deviation of up to 7 ppm and an allowed fragment mass deviation of 20 ppm. Nonlinear retention time alignment of all measured samples was performed in MaxQuant. Peptide identifications were matched across all samples within a time window of 1 min of the aligned retention times[51]. A library for 'match between runs' in MaxQuant was built from duplicate and additional single shot MS runs from MACS enriched cell types. Protein identification required at least 1 'razor peptide' in MaxQuant. A minimum ratio count of 1 was required for valid quantification events via MaxQuant's Label Free Quantification algorithm (MaxLFQ)[22]. We enabled FastLFQ with a minimum of three and an average of six neighbors. Data were filtered for common contaminants and peptides only identified by side modification were excluded from further analysis. We observed lower identification rates for plasma blasts and neutrophils compared to all other cell types. In the case of plasma blasts the lower identification rate derives from the low cell count. Neutrophil identification rates are below average because 1) neutrophils contain many proteases and as a result peptides are cleaved at different positions than arginine or lysine (the expected residues from tryptic digestions) and 2) have high abundant proteins that result in unusually broad peptide peak widths, interfering with the detection of other ions.

Transcription profiling. Total RNA was isolated from flow sorted cell types (as described in Blood samples and cell sorting) using the RNeasy Plus Mini Kit from Qiagen. RNA samples from four donors were pooled. RNA was analyzed using an Agilent 2100 Bioanalyzer system (Agilent Biotechnologies). Only samples with RIN > 8 were subjected to sequencing at the Genomics Core Facility (GeneCore), Heidelberg using an Illumina Hiseq2000 sequencer. Processed reads were mapped to the human genome (GRCh37) using the

doi:10.1038/ni.3693

PERSEUS software (v. 1.5.5.5). RPKM values were calculated by normalizing to the maximum gene length. A cutoff value of 1 RPKM was used as a limit for detection.

Data filtering, imputation of missing values and copy number estimation. Data analysis and visualization was performed using the Perseus software[52] and the R statistical framework[53,54]. Before imputing missing values, protein identifications were required to have more than 50% valid values in at least one group of replicates. The remaining missing values were imputed by a normal distribution with a s.d. of 30% in comparison to the deviation of the measured values and a down-shift of the mean by 2.2 s.d. to simulate the distribution of low abundant proteins. Copy numbers were estimated using the proteomic ruler approach by using the fixed ratio between the total histone signal and cellular DNA mass[28].

Comparison to proteome and microarray data. Microarray data were retrieved from http://www.broadinstitute.org/dmap/home[8]. We employed the R Bioconductor package 'mygene' to match Uniprot identifier to the provided Entrez identifier[55]. Raw files from[23] were processed with MaxQuant applying identical cut offs for protein identifications as stated above. Only MACS enriched immune cell protein identifications were used for comparison. The total number of identifications and coverage of immune system relevant annotations was determined by matching all three data sets to a human reference genome (20,591 entries, Perseus v1.5.2.12) based on Uniprot identifiers (**Fig. 1c,d**).

Lineage-specific protein signatures and cell-type marker selection. Proteomes were compared by three different groupings: (1) pairwise, (2) cell lineage (T4, T8, NK, B, MO, DC, and GN) versus rest, (3) and individual cell types versus all other proteomes. Proteomes of activated cell types were excluded from cell lineage comparisons and platelets and erythrocytes from all comparisons. Proteins that significantly differed in abundance were identified by a parametric two-tailed Welch's *t*-test with a permutation-based false discovery rate (FDR) of 5% and a S_0 parameter of 1 (ref. 56), if not stated otherwise (**Fig. 2b**). In addition, we employed Lasso regression analysis[29] to identify cell-type-specific markers for cell sorting (**Supplementary Fig. 3d**). The pool of proteins was reduced to cell surface receptors.

Assignment of functional modules. Proteins were clustered to functional modules using weighted gene co-expression network analysis (WGCNA)[31]. The proteome data was reduced to proteomes of cell types in their steady state and selected for proteins with a significantly different abundance pattern between cell types (ANOVA, Benjamini-Hochberg (BH) FDR $P < 5 \times 10^{-5}$, df1 = 25, df2 = 78). Standard parameters were changed to a power of 14, 'signed' network, average clustering, and a minimum module size of 20. The algorithm assigned the 6,982 proteins to 47 modules containing 23–725 proteins.

Annotation enrichment analysis. Protein modules, cell type signatures as well as selected principal components were functionally characterized by annotation enrichment analysis. For all three cases we used proteins annotations form the Gene Ontology (GO)[57], KEGG[58], and Uniprot Keywords[59] databases. For the first two cases, enrichment scores were determined using Fisher exact test and in the latter 1D annotation enrichment analysis was performed[25]. Both tests we corrected for multiple hypotheses using a Benjamini-Hochberg false discovery rate of 5%, if not stated otherwise.

Categorization of intracellular signaling levels. Based on protein annotations combinations, we defined four levels of signal transduction: transcription factor (T), adaptor molecule (A), receptor (R) and secreted molecules/ligands (L). 'T' were characterized by being localized in the nucleus (GOCC: 'nucleus', 'nuclear part'), DNA binders (GOMF: 'DNA binding') and transcription regulators (GOMF: 'transcription regulatory region DNA binding', 'sequence-specific DNA binding transcription factor activity'), but at the same time were not involved in DNA repair (GOMF: 'damaged DNA binding'; GOBP 'DNA repair'). 'A' were required to interact with at least one receptor (StringDB score > 0.4). In addition, they had to be localized in the cytoplasm (GOCC: ('cytoplasm', 'cytosol', 'cytoplasmic part') and involved in cell signaling (GOBP: 'signaling', 'signal transduction'). 'R' were defined solely by UniProt sequence features. Proteins were required to have either an' extracellular' or 'GPI-anchor' topology domain. 'L' were required to be secreted (Keywords: 'Secreted', 'Signal') or interact with a receptor (StringDB score > 0.4) and be localized in the extracellular region (GOCC: 'extracellular space', 'extracellular region'). Furthermore, for 'R' such as TNF, we define a specific category. 'R' with cytokine activity (GOMF: 'cytokine activity', 'chemokine activity', 'growth factor activity', 'hormone activity'; UniProt Keywords: 'Cytokine', 'Hormone', 'Growthfactor') were assigned 'L'.

Intercellular interaction network. To define intercellular connections we retrieved protein interaction data from the String database[40]. From the different score levels available we selected only interactions with experimental evidence and a score greater than 0.4. In addition, we established a twofold ranking for pairwise intercellular protein interactions using our proteome data. First, individual protein expressions were divided by their maximum expression level in order to weigh protein expression across all cell types independent of their abundance. Second, we computed a significance score by counting how often a protein was significantly (FDR 5%) more abundant in one cell type compared to all other cell types and normalized it by the maximum count. The product of normalized expression and normalized significance was used to compute connection ranks for all proteins. The final intercellular connection score between protein pairs was calculated as the mean of the individual connection ranks of the two proteins. We excluded self-loops as well as L-L interactions. To avoid intercellular connection between proteins of the same receptor complex, we annotated receptor complexes using GOCC terms and the protein complex database PCDq[60] and merged proteins of the same complex to one entity. This resulted in a network of about 4×10^5 possible receptor-ligand or receptor-receptor connection between the 26 different cell types in their steady and activated states. We evaluated our intercellular connection scores by comparing their distribution to a manually annotated immune cell-cytokine connection network 'Textbook' (http://www.immunexpresso.org/, see below). We observed that with increasing intercellular connection score the number of connections covered by the textbook fits a sigmoid curve and set intercellular interaction score cutoff at the inflection point (0.47) (**Supplementary Fig. 5b,c**). Together, this resulted in a high confidence immune cell communication network comprising approximately 180,000 interactions, containing roughly 80,000 R-R and 100,000 R-L interactions. The networks were visualized with the R package 'circlize'[61]. Furthermore, we extend our interaction network by applying the described interaction framework features to body tissues[42]. For the transcriptomes, we applied the same scoring but restricted the network to receptor-receptor interactions.

Transcriptome-proteome correlation and module analysis. Data sets were filtered for cell types present in both data sets (T4.naive - TCELLA6, T4.CM - TCELLA8, T4.EM - TCELLA7, T8.naive - TCELLA2, T8.CM - TCELLA4, T8.EM - TCELLA3, T8.EMRA - TCELLA1, NK.bright - NKA2, NK.dim - NKA3, B.memory - BCELLA2, B.naive - BCELLA1, MO.classical - MONO2, mDC - DENDA2, pDC - DENDA1, Neutrophil - GRAN3, Eosinophil - EOS2, Basophil - BASO1). We calculated Pearson correlation coefficients for protein profiles across all matched cell types. WGCNA was performed with ANOVA significant proteins (Benjamini-Hochberg (BH) FDR $P < 5 \times 10^{-5}$). Standard parameters were changed to a power of 14, 'signed' network, average clustering, and a minimum module size of 20. Highly correlating modules were merged at a cutHeight of 0.2 or 0.3 for the microarray and proteome data set, respectively. This assigned the 5,782 genes of the microarray data set to 18 modules and 5,974 proteins of the proteome data set to also 18 modules. Module similarity was determined by two measures: Pearson correlation of the module Eigengenes and relative gene overlap between the modules. Intercellular communication network for both data set were constructed as described above but restricting the networks to shared cell types only.

Comparison to Textbook and ImmuneXpresso. To identify novel connections between immune cell pairs, we compared our intercellular interaction network to a comprehensive literature-based interaction network (http://www.immunexpresso.org/). This literature-based network consists of two data sets 'Textbook' (1) and 'ImmuneXpresso' (2). The 'Textbook' contains semi-manual annotated cell-cytokine or cytokine-cell interactions retrieved from[41].

doi:10.1038/ni.3693

'ImmuneXpresso' has an identical data structure, but the interactions are automatically extracted from PubMed abstracts by a Natural Language Processing engine. For comparisons, the data sets were matched by gene names and cell types. In case cell types were not identical, the parent cell types were matched.

Intracellular interaction network. We used the bioinformatics framework described above in 'Intercellular interaction network' to construct intracellular protein signaling networks for each immune cell type. To this end, we assigned to each receptor the closest adaptors (path length = 1, degree > 10) and the closest transcription factors (path length < 3, degree > 5). We grouped receptors according to their downstream signaling molecules to identify at which layer of signal transduction input signals from ligands present in secretomes converge (**Supplementary Fig. 7c,f**).

Secretome analysis. iBAQ intensity values[12] were median normalized and missing values imputed as described in 'Data filtering, imputation of missing values and copy number estimation'. Significant secreted proteins were identified by two-tailed Welch's *t* test comparing stimulated with unstimulated cells with a permutation-based false discovery rate (FDR) of 1% and a S_0 parameter of 1 for monocytes (**Supplementary Fig. 7d,e**). For mDC the FDR was set to 5% and for pDC to 15% (**Supplementary Fig. 7a,b**). To compare the context depended activations, significant secreted proteins were ranked to account for abundance biases due to different agonists or cell types. For example, TNF is one of the most abundant proteins secreted from monocytes after ZYM and LPS stimulation. However, ZYM treated monocytes secrete significantly more TNF than LPS treated monocytes. However, this abundance difference might be minor at different time points or LPS concentrations. Therefore, secretome results are presented as rank-based secretion (**Fig. 7a,b,e,f**)

Data availability. All data generated during this study are included in this published article and deposited online (ProteomeXchange Consortium, data set identifier PXD004352). Detailed descriptions for all submitted data tables can be found in **Supplementary Note 1**. The data is publicly accessible under http://www.immprot.org or MaxQB (http://maxqb.biochem.mpg.de/mxdb/). Additional published data include, microarray data of immune cells (http://www.broadinstitute.org/dmap/home), transcriptome data of tissues and organs (10.1126/science.1260419), protein interaction data (http://string-db.org/, version 10.0), and protein complex annotations (http://h-invitational.jp/hinv/pcdq/). Raw data and the MaxQuant output tables have been deposited to the ProteomeXchange Consortium via the PRIDE[62] partner repository with the data set identifier PXD004352 (https://www.ebi.ac.uk/pride/archive/projects/PXD004352). The data is publicly accessible under http://www.immprot.org/. The data that support the findings of this study are either available in a public repository, attached as supplementary tables or can be requested from the corresponding authors.

47. Brosseron, F. *et al.* Stepwise isolation of human peripheral erythrocytes, T lymphocytes, and monocytes for blood cell proteomics. *Proteomics Clin. Appl.* **6**, 497–501 (2012).
48. Trichler, S.A., Bulla, S.C., Thomason, J., Lunsford, K.V. & Bulla, C. Ultra-pure platelet isolation from canine whole blood. *BMC Vet. Res.* **9**, 144 (2013).
49. Scheltema, R.A. & Mann, M. SprayQc: a real-time LC-MS/MS quality monitoring system to maximize uptime using off the shelf components. *J. Proteome Res.* **11**, 3458–3466 (2012).
50. Cox, J. *et al.* Andromeda: a peptide search engine integrated into the MaxQuant environment. *J. Proteome Res.* **10**, 1794–1805 (2011).
51. Tyanova, S., Temu, T. & Cox, J. The MaxQuant computational platform for mass spectrometry-based shotgun proteomics. *Nat. Protoc.* **11**, 2301–2319 (2016).
52. Tyanova, S. *et al.* The Perseus computational platform for comprehensive analysis of (prote)omics data. *Nat. Methods* **13**, 731–740 (2016).
53. RStudio, I. *Shiny: Easy web applications in R* (2014).
54. Team, R.D.C. *R: a Language and Environment for Statistical Computing* (2008).
55. Gentleman, R.C. *et al.* Bioconductor: open software development for computational biology and bioinformatics. *Genome Biol.* **5**, R80 (2004).
56. Tusher, V.G., Tibshirani, R. & Chu, G. Significance analysis of microarrays applied to the ionizing radiation response. *Proc. Natl. Acad. Sci. USA* **98**, 5116–5121 (2001).
57. Ashburner, M. *et al.* Gene ontology: tool for the unification of biology. The Gene Ontology Consortium. *Nat. Genet.* **25**, 25–29 (2000).
58. Kanehisa, M., Goto, S., Sato, Y., Furumichi, M. & Tanabe, M. KEGG for integration and interpretation of large-scale molecular data sets. *Nucleic Acids Res.* **40**, D109–D114 (2012).
59. Magrane, M. & UniProt, C. UniProt Knowledgebase: a hub of integrated protein data. *Database (Oxford)* **2011**, bar009 (2011).
60. Kikugawa, S. *et al.* PCDq: human protein complex database with quality index which summarizes different levels of evidences of protein complexes predicted from h-invitational protein-protein interactions integrative dataset. *BMC Syst. Biol.* **6** (Suppl, 2), S7 (2012).
61. Gu, Z., Gu, L., Eils, R., Schlesner, M. & Brors, B. circlize Implements and enhances circular visualization in R. *Bioinformatics* **30**, 2811–2812 (2014).
62. Vizcaino, J.A. *et al.* The PRoteomics IDEntifications (PRIDE) database and associated tools: status in 2013. *Nucleic Acids Res.* **41**, D1063–D1069 (2013).

doi:10.1038/ni.3693

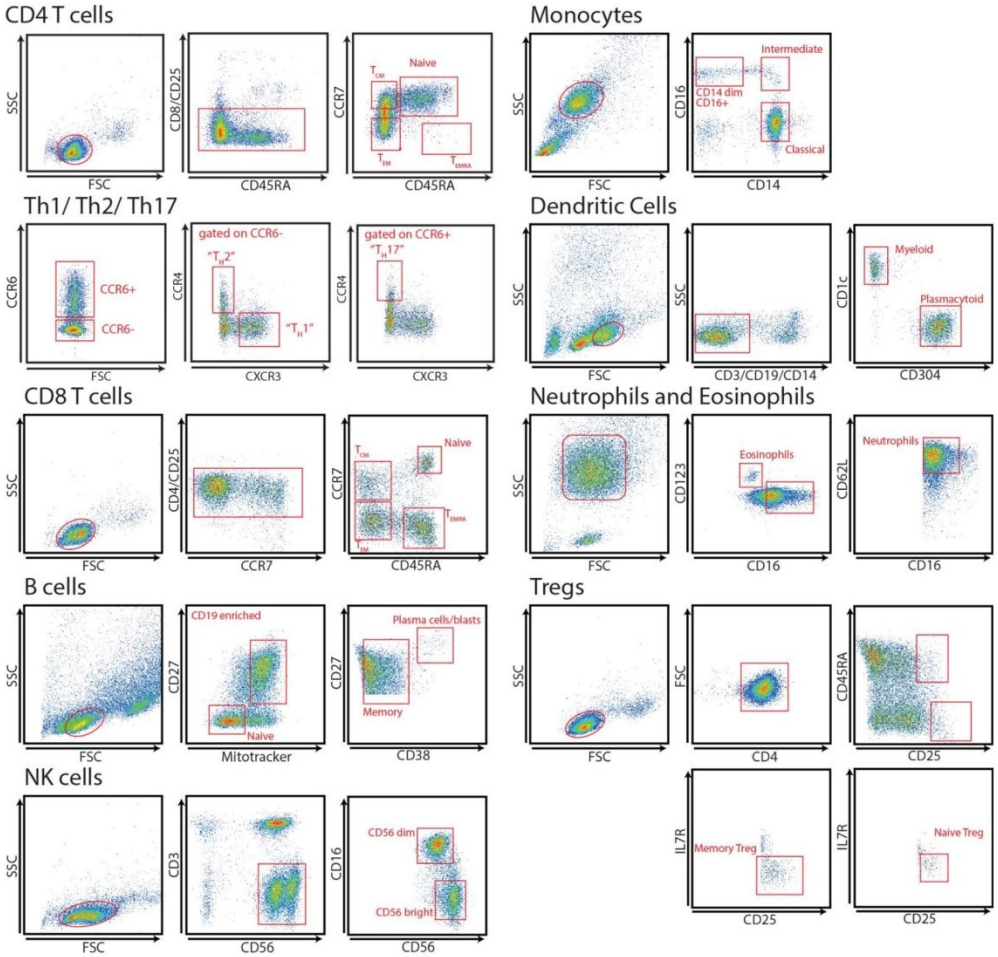

Supplementary Figure 1

Representative flow cytometry scatter plots of the sorting panels for each immune cell population measured by LC-MS/MS.

Total CD4 T cells, Tregs, T_H1, T_H2 and T_H17 were enriched with anti-CD4 coated magnetic beads; CD8 T cells with anti-CD8 coated beads, dendritic cells with anti-CD1c and anti-CD304 coated beads, B cells with anti-CD19 coated beads and NK cells with anti-CD56 coated beads.

Nature Immunology: doi:10.1038/ni.3693

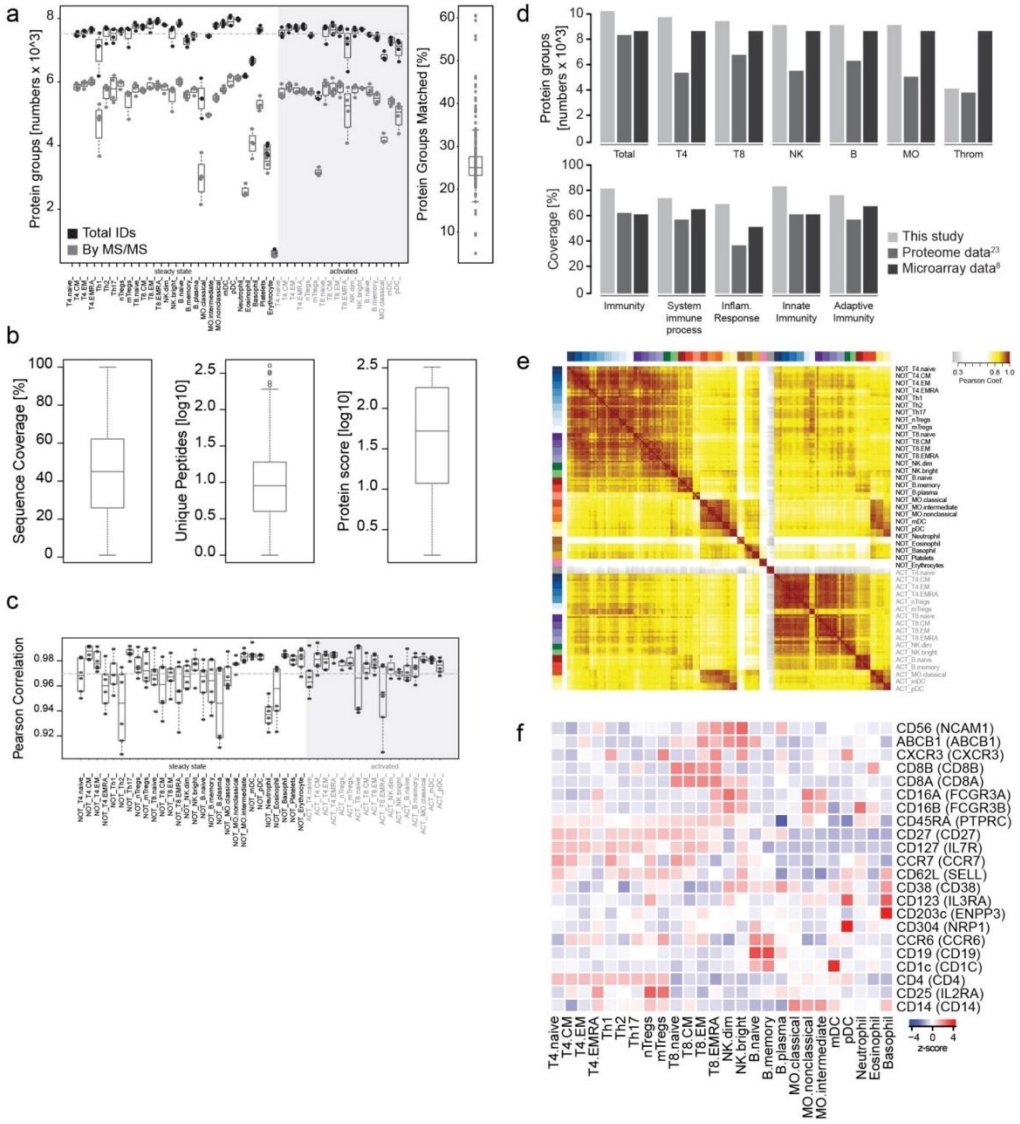

Supplementary Figure 2

Quality measures of proteome data set.

(a) Left: Number of identified protein groups for each cell type. Total identification is displayed in black, solely MS/MS based identification is displayed in grey (NOT: steady state, ACT: activated). Right: Percent transferred identifications from other MS/MS measurements.
(b) Sequence coverage, unique peptides and protein score for all identified protein group.
(c) Pearson correlation coefficients between cell types replicates.

Nature Immunology: doi:10.1038/ni.3693

(d) Comparison of protein identifications for individual cell lineages and relative coverage of relevant immune processes. Reference datasets are indicated.
(e) Pearson correlation coefficients of all total proteome measurements. Samples are arranged according to their lineage relationship.
(f) Heat map of protein markers used for cell sorting. Gene names are indicated in parentheses.

Nature Immunology: doi:10.1038/ni.3693

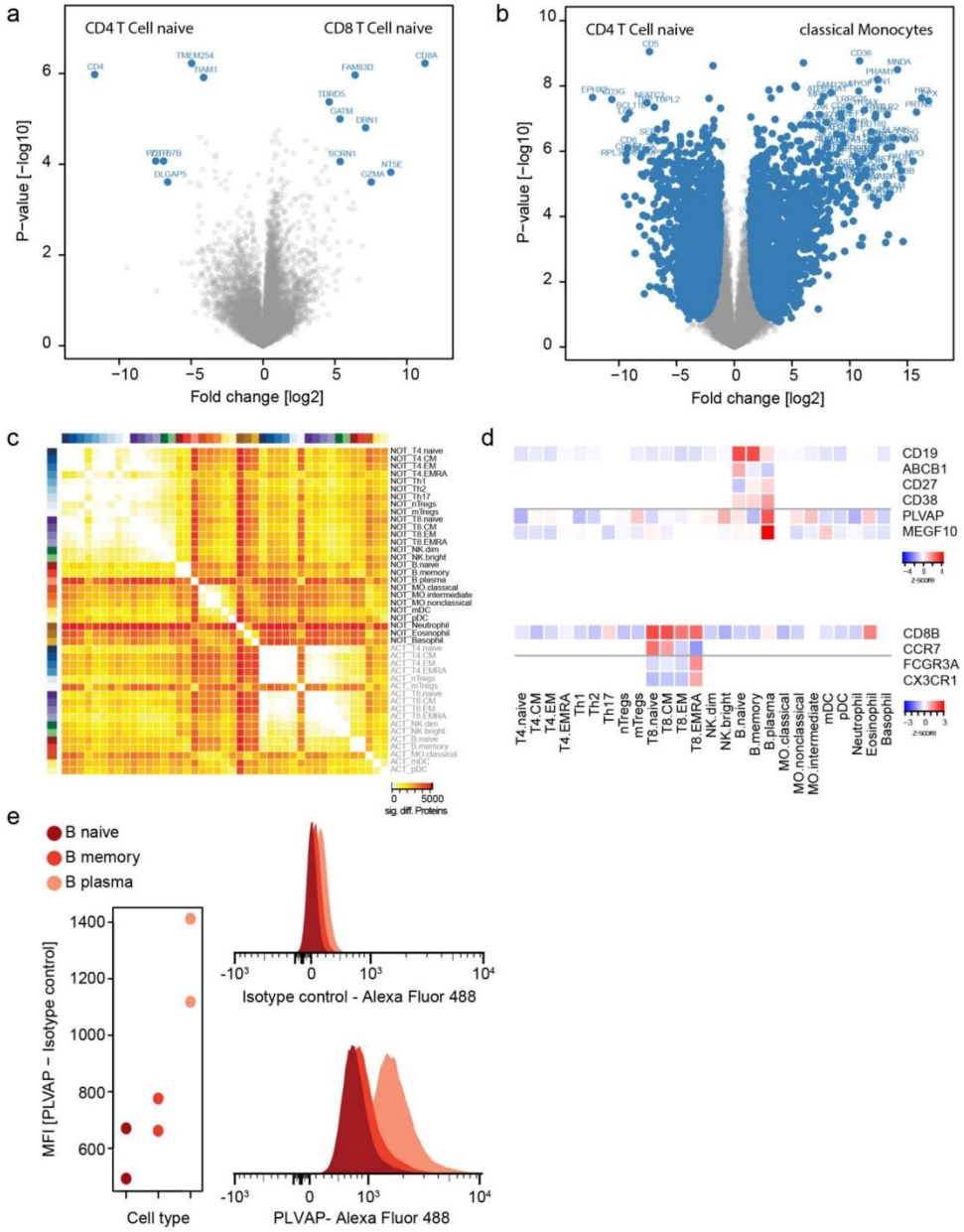

Supplementary Figure 3

Nature Immunology: doi:10.1038/ni.3693

Proteome differences and marker proteins.

(a) Proteome comparison of naive CD4 with naive CD8 T cells (Welch's t-test, FDR<5%, S_0=1). Significant proteins are marked in blue containing the lineage markers CD4 and CD8A.
(b) Proteome comparison of naive CD4 with classical monocytes, respectively (Welch's t-test, FDR<5%, S_0=1). Significant proteins are marked in blue and the top 50 differentially abundant proteins are named.
(c) Number of significantly (Welch's t-test, FDR<5%, S_0=1) different proteins by pairwise proteome comparison (NOT: steady state, ACT: activated).
(d) Expression comparison (z-scored MaxLFQ values) of marker proteins for B cell plasma blasts (top) and for CD8 T_{EMRA} cells (bottom). Potential unique marker proteins are indicated below the grey horizontal line. For clarity z-score values of other cell lineages were removed except for cell lineage markers (CD19, CD8B) and potential exclusive cell type markers. The isoforms of CD45 could not be resolved from the proteome analysis, therefore CD45RO and CD45RA are not included in the plot.
(e) Median fluorescence intensity (MFI) of PLVAP (intracellular staining) in B cells determined by flow cytometry and normalized by isotype control MFI (n=2, two independent donors, left). Representative histograms of fluorescence intensities of isotype control and PLVAP (right).

Nature Immunology: doi:10.1038/ni.3693

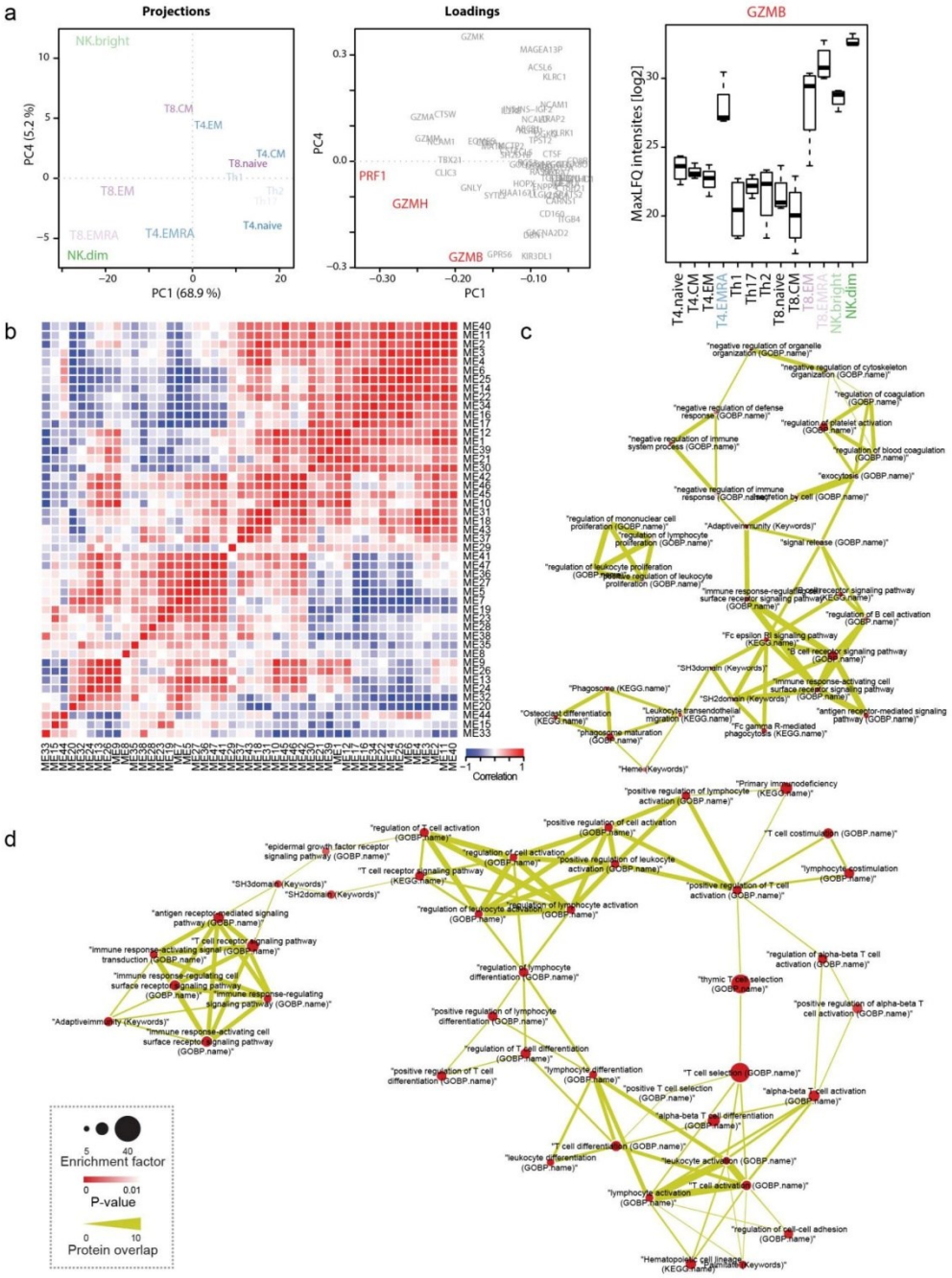

Nature Immunology: doi:10.1038/ni.3693

Supplementary Figure 4

Module relationship, annotation enrichment maps and CD4 T_{EMRA} cytotoxicity.

(a) PCA of proteins in module 29 and its representative cell types. Projections and loadings are displayed. Cell types are color-coded as in Fig. 1. Cytolytic proteins shared between CD4 T_{EMRA}, NK and CD8 T cells are labelled in red. Expression profile of GZMB is displayed as an example.
(b) Heat map of module correlation coefficients.
(c) Enrichment map of module 17. Nodes are annotation terms, edges represent gene overlap between terms. Node size represent annotation enrichment, fill color indicates adjusted p value.
(d) Enrichment map of module 19. Labels as in panel B.

Nature Immunology: doi:10.1038/ni.3693

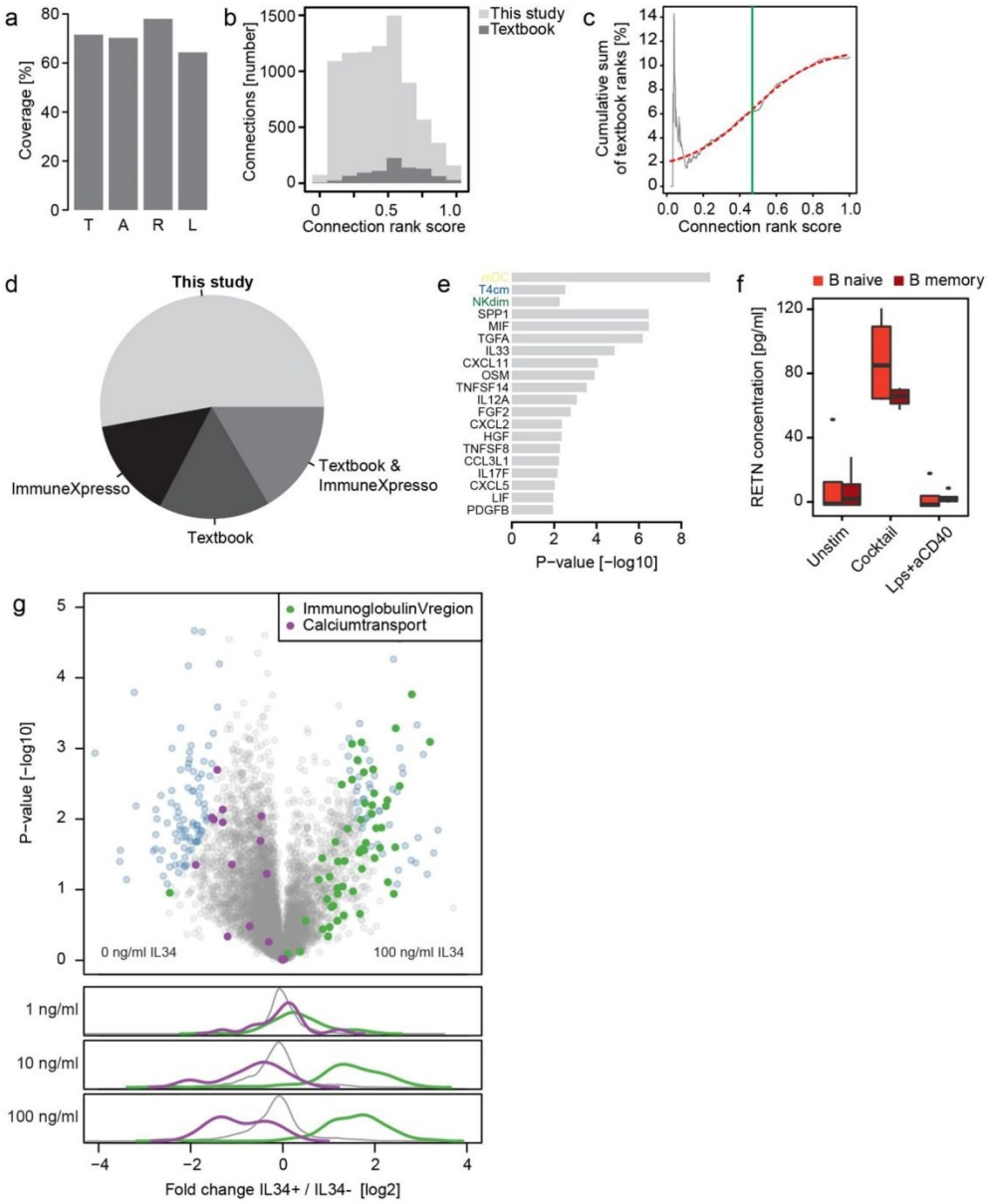

Supplementary Figure 5

Communication network assembly and validation of novel connections.

(a) Relative coverage of immune annotated transcription factors (T), adaptor molecules (A), receptors (R), and ligands (L).

Nature Immunology: doi:10.1038/ni.3693

(b) Histogram of intercellular interaction scores. Intercellular interaction scores of our study were reduced to cell types and cytokines identified in the textbook (light grey). Intercellular interaction scores covered by the textbook are displayed in (dark grey).
(c) Intercellular interaction score cutoff (Online Methods).
(d) Percentage of ingoing connections for cytokines in our study compared to 'Textbook' and 'ImmuneXpresso'.
(e) Understudied cell types and cytokines from ingoing connections. Significantly enriched cell types and cytokines in our study compared to 'Textbook' and 'ImmuneXpresso' were identified by Fisher's exact test with BH FDR of 5%.
(f) Resistin (RETN) secretion of B cells. B cells were stimulated with a cocktail (Goat F(ab')2 anti-human Lambda/Kappa, F(ab')2 Goat anti-mouse IgG Fc, CpG, anti-CD40) or LPS and anti-CD40 for 4 days and the resistin concentration in the supernatant was determined by ELISA (n=4, cell culture replicates from 2 independent donors).
(g) T4 memory cells respond to IL-34 by total proteome changes. T4 memory cells were activated with aCD3/aCD28 for 2 days and then cultured for another 2 days with IL-2 in the presence of different amounts of IL-34 (0, 1, 10, or 100 ng/ml). The volcano plot (top) shows the protein differences between T4 memory cells treated with 0 ng/ml and 100 ng/ml IL-34 (significantly changed proteins are shown in blue, S_0=1, FDR < 5%, n=4, cell culture replicates from 2 independent donors). Examples for significantly shifted Keyword annotations (determined by 1D annotation enrichment, BH FDR < 1%) are highlighted in violet (calcium transport) or green (immunglobulinVregion). Density distribution (bottom) show the shift of the Keyword annotations in dependency of IL-34 concentration.

Nature Immunology: doi:10.1038/ni.3693

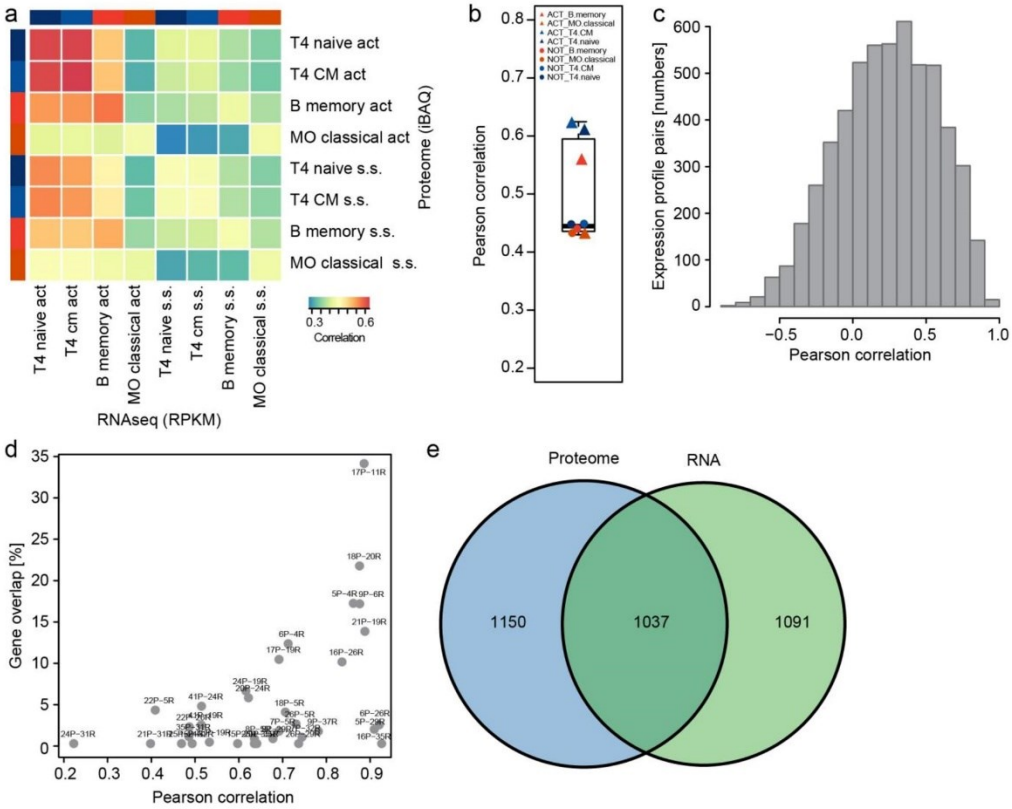

Supplementary Figure 6

Transcriptome to proteome comparison.

(a) Pearson correlation coefficients of comparable cell types from RNAseq (columns) and proteome (rows) measurements. Correlation coefficients were computed from RPKM and iBAQ values (s.s.: steady state, act: activated).
(b) Pearson correlation coefficients (RNAseq vs Proteome) of only matched cell type pairs.
(c) Pearson correlation coefficients (Microarray vs Proteome) of protein-gene expression profiles.
(d) Comparison of WGCNA modules from microarray and proteome data. Modules were matched by Pearson correlation of their module eigengenes and the best two correlating microarray (R) modules for each proteome (P) module are displayed and plotted against their gene overlap. The gene overlap represents the percentage of genes in the proteome module covered by the corresponding microarray module.
(e) Comparison of intercellular receptor-ligand connections in proteome (blue) and microarray (green) data. For this comparison the intercellular signaling networks were constructed by only shared cell types.

Nature Immunology: doi:10.1038/ni.3693

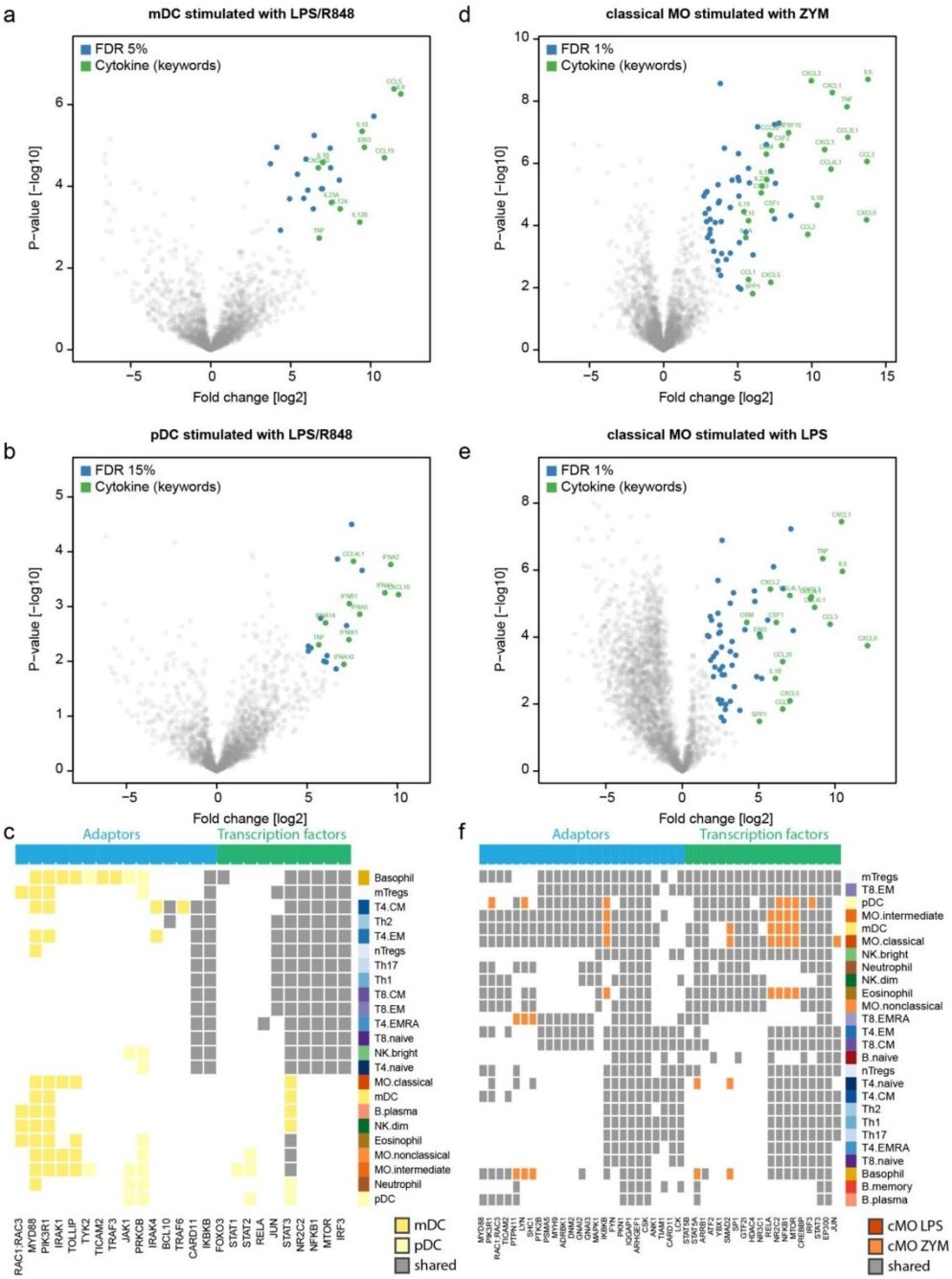

Nature Immunology: doi:10.1038/ni.3693

Supplementary Figure 7

Differential protein secretion patterns and intracellular signaling networks.

(a, b) Volcano plots of secreted proteins from mDCs (a) and pDCs (b). Significantly secreted proteins are colored in blue (FDR 0.05, S_0=1, n=4 from independent donors). Known cytokines are labelled in green.
(c) Intracellular signaling adaptors and transcription factors (columns) for each cell type (rows) that propagate intercellular signals upon receptor ligation by proteins secreted by mDCs and pDCs.
(d, e) Volcano plots of secreted proteins from classical monocytes activated with lipopolysaccharide (LPS) (d) or zymosan (ZYM) (e). Significantly secreted proteins are colored in blue (FDR 0.01, S_0=1, n=5 from independent donors). Known cytokines are labelled in green.
(f) Intracellular signaling adaptors and transcription factors (columns) for each cell type (rows) that propagate intercellular signals upon receptor ligation by proteins secreted by cMO.

Nature Immunology: doi:10.1038/ni.3693

Supplementary Table 1 Cell type sorting panels.

Cell type	Sorting panel	Antibody colors	Cells [Mio/Buffy]
T4 naive	$CD4^+CCR7^+CD45RA^+$	anti-CD4 beads, CCR7-PB, CD45RA-PE, CD4-APC, CD8/CD25/CD19-FITC	3.0
T4 T_{CM}	$CD4^+CCR7^+CD45RA^-$	anti-CD4 beads, CCR7-PB, CD45RA-PE, CD4-APC, CD8/CD25/CD19-FITC	3.5
T4 T_{EM}	$CD4^+CCR7^-CD45RA^-$	anti-CD4 beads, CCR7-PB, CD45RA-PE, CD4-APC, CD8/CD25/CD19-FITC	1.7
T4 T_{EMRA}	$CD4^+CCR7^-CD45RA^+$	anti-CD4 beads, CCR7-PB, CD45RA-PE, CD4-APC, CD8/CD25/CD19-FITC	0.2
T_{reg} naive	$CD4^+$ $CCR7^+CD45RA^+$ $CD25^+CD127^-$	CD4beads, CD4-APC, CD25-PE, CD45RA-PC7, CCR7-BV421, CD127-FITC	0.4
T_{reg} memory	$CD4^+$ $CCR7^+CD45RA^-$ $CD25^+CD127^-$	CD4beads, CD4-APC, CD25-PE, CD45RA-PC7, CCR7-BV421, CD127-FITC	1.1
T4 T_H1	$CD4^+CCR7^+CD45RA^-$ $CCR6^-CCR4^-CXCR3^+$	anti-CD4 beads, CCR7-BV, CCR6-PE, CCR4-PECy7, CXCR3-APC, CD45RA-PECy5, CD8/CD25-FITC	2.4
T4 T_H2	$CD4^+CCR7^+CD45RA^-$ $CCR6^-CCR4^+CXCR3^-$	anti-CD4 beads, CCR7-BV, CCR6-PE, CCR4-PECy7, CXCR3-APC, CD45RA-PECy5, CD8/CD25-FITC	1.5
T4 T_H17	$CD4^+CCR7^+CD45RA^-$ $CCR6^+CCR4^+CXCR3^-$	anti-CD4 beads, CCR7-BV, CCR6-PE, CCR4-PECy7, CXCR3-APC, CD45RA-PECy5, CD8/CD25-FITC	1.4
T8 naive	$CD8^+CCR7^+CD45RA^+$	CD8 beads, CD8-APC, CCR7-PB, CD45RA-PE, CD25/CD4-FITC	2.5
T8 T_{CM}	$CD8^+CCR7^+CD45RA^-$	CD8 beads, CD8-APC, CCR7-PB, CD45RA-PE, CD25/CD4-FITC	2.1
T8 T_{EM}	$CD8^+CCR7^-CD45RA^-$	CD8 beads, CD8-APC, CCR7-PB, CD45RA-PE, CD25/CD4-FITC	2.3
T8 T_{EMRA}	$CD8^+CCR7^-CD45RA^+$	CD8 beads, CD8-APC, CCR7-PB, CD45RA-PE, CD25/CD4-FITC	1.6
NK $CD56^{bright}$	$CD56^{bright}CD16^-$	CD56-PE, anti-PE beads, CD16-FITC, CD3-PC5	1.6
NK $CD56^{dim}$	$CD56^{dim}CD16^+$	CD56-PE, anti-PE beads, CD16-FITC, CD3-PC5	2.3
B naive	$CD19^+$MitroTrackerGreen$^-$ $CD27^-$	anti-CD19 beads, MitoTrackerGreen, CD38-APC, CD27-PE, CD19-PECy7	2.4
B memory	$CD19^+$MitroTrackerGreen$^+$ $CD27^+$ $CD38^-$	anti-CD19 beads, MitoTrackerGreen, CD38-APC, CD27-PE, CD19-PECy7	2.0
B plasma	$CD19^+$MitroTrackerGreen$^+$ $CD27^+CD38^+$	anti-CD19 beads, MitoTrackerGreen, CD38-APC, CD27-PE, CD19-PECy7	0.03
MO classical	$CD14^+CD16^-$	negative selection kit (19058, Stem Cell), CD14-APC, CD16-FITC	3.3
MO non-classical	$CD14^{dim}CD16^+$	negative selection kit (19058, Stem Cell), CD14-APC, CD16-FITC	1.1
MO intermediate	$CD14^+CD16^+$	negative selection kit (19058, Stem Cell), CD14-APC, CD16-FITC	0.5
DC CD1c	$CD1c^+CD304^-CD19^-CD14^-$ $CD3^-$	CD304-PE, CD1c-FITC, anti-PE/anti-FITC beads, CD14/CD19/CD3-PC5	0.3
DC CD304	$CD1c^-CD304^+CD19^-CD14^-$ $CD3^-$	CD304-PE, CD1c-FITC, anti-PE/anti-FITC beads, CD14/CD19/CD3-PC5	0.7
Neutrophils	$SSC^{high}CD16^+CD123^-$ $CD62L^+$	SSChigh, CD16-FITC, CD62L-PE-Cy5(PC5), CD123-biotin/strep-PB	4.0
Eosinophils	$SSC^{high}CD16^{dim}CD123^+$	SSChigh, CD16-FITC, CD62L-PE-Cy5(PC5), CD123-biotin/strep-PB	0.8
Basophil	$SSC^{high}CD203c^+$	97A6-PE, PE-beads	1.0

Nature Immunology: doi:10.1038/ni.3693

Supplementary Table 2 *In vitro* activation conditions

Cell type	Stimulus	Concentration	Time [h]
T4 and T8 cell activation	anit-CD3 and anti-CD28, plate bound	5 µg/ml and 1µg/ml	48
T4 and T8 cell expansion	IL-2	500 U/ml	48
NK cells	CD2 and CD355 coated beads, IL-2	1 bead per 2 cells, 500 U/ml	96
B cells	Goat F(ab')2 anti-human (1) Lambda and (2) Kappa, (3) F(ab')2 Goat anti-mouse IgG Fc, (4) CpG, (5) anti-CD40	(1) and (2) 2µg/ml, (3) 3µg/ml, (4) 100 ng/ml, (5) 6µg/ml	96
Monocytes	LPS	100 ng/ml	12
Monocytes	ZYM	2 µg/ml	12
Dendritic cells	LPS and R848	100 ng/ml and 2.5 µg/ml	12

Nature Immunology: doi:10.1038/ni.3693

Supplementary Table 12 Antibodies used for cell sorting.

Name	Conjugate/Tag	Clone	Cat#	Company
anti-hCCR7		150503	MAB197	R&D Systems
CCR4	PE Cy7	1G1	557864	BD
CCR6	PE	11A9	559562	BD
CCR7	BV421	G043H7	353208	BioLegend
CD123	Biotin	9F5	33332D	BD
CD127	FITC	HIL-7R-M21	560549	BD
CD14	APC	RMO52	IM2580	Beckman Coulter
CD14	PC5	RMO52	A07765	Beckman Coulter
CD16	FITC	3G8	IM0814U	Beckman Coulter
CD19	FITC	HIB19	555412	BD
CD19	PE Cy7	SJ25C1	25-0198-42	eBioscience
CD19	PC5	J3-119	A07771	Beckman Coulter
CD1c	FITC	AD5-8E7	130-090-507	Miltenyi
CD203c	PE	97A6	IM3575	Beckman Coulter
CD25	FITC	B1.49.9	IM0478U	Beckman Coulter
CD25	PC5	B1.49.9	IM2646	Beckman Coulter
CD25	PE	M-A251	555432	BD
CD27	PE	L128	340425	BD
CD3	PC5	UCHT1	A07749	Beckman Coulter
CD304	PE	AD5-17F6	130-090-533	Miltenyi
CD38	APC	HIT2	555462	BD
CD4	FITC	13B8.2	A07750	Beckman Coulter
CD4	APC	13B8.2	IM2468	Beckman Coulter
CD45RA	PE	ALB11	IM1834U	Beckman Coulter
CD45RA	QD655	MEM-56	Q10069	Invitrogen
CD45RA	PE Cy5	HI100	555490	BD
CD45RA	PE Cy7	HI100	25-0458-41	eBioscience
CD56	PE	N901	A07788	Beckman Coulter
CD62L	PC5	DREG56	IM2655U	Beckman Coulter
CD8	APC	B9.11	IM2469	Beckman Coulter
CD8	FITC	B9.11	A07756	Beckman Coulter
CXCR3	APC	1C6	550967	BD
IgG2a Biotin	Biotin		1080-08	SouthernBiotech
Mito Tracker	Green FM		M-7514	Invitrogen
Streptavidin	PB		S11222	Invitrogen

Nature Immunology: doi:10.1038/ni.3693

Supplementary Note 1

Supplementary table descriptions

Supplementary Table 3: Quantitative proteomics data of total proteomes.
List of protein identifications, including Intensity, iBAQ, LFQ, and imputed values as well as annotations, module assignment, unique peptides, sequence coverage, protein score, gene names, protein names, and protein ids.

Column	Name	Description
1	Majority Protein IDs	UniProt identifier separated by semicolon.
2	Gene names	Gene names
3	Protein names	Copy number for each measurement (CopyNumber_CelltypeX_ReplicateX_steady-state/activated).
4	WGCNA module	Module numbers of the WGCNA
5	Signal category	Proteins assigned to the following categories: Transcription factor (T), Adaptor (A), Receptor (R), Ligand (L)
6-180	Intensity values	Intensity values are summed up peptide intensities for each protein.
181-355	iBAQ value	iBAQ (intensity based absolute quantification): Intensity values are normalized by the number of theoretically observable peptides of the protein.
356-530	LFQ intensity values	LFQ (label-free quantification) intensity values.
531-705	LFQ intensity imputed	LFQ (label-free quantification) intensity values. Missing values are imputed. For more information see supplementary information section 'Data filtering, imputation of missing values and copy number estimation'.
706	GOBP name	Gene Ontology Biological Process
707	GOMF name	Gene Ontology Molecular Function
708	GOCC name	Gene Ontology Cellular Component
709	KEGG name	Kyoto Encyclopedia of Genes and Genomes
710	Keywords	Uniprot Keywords
711	Unique peptides	The total number of unique peptides associated with the protein group (i.e. these peptides are not shared with another protein group).
712	Sequence coverage [%]	Percentage of the sequence that is covered by the identified peptides of the best protein sequence contained in the protein group.
713	Score	Andromeda score for the best identified among the associated MS/MS spectra.

Supplementary Table 4: Annotation enrichment analysis of principal components.
1D annotation enrichment analysis of the principal components shown in Fig. 2.

Column	Name	Description
1	Principal component	Number of principal component
2	Reference	Reference annotation (e.g. KEGG)
3	Annotation	Specific annotation name (e.g. DNA excision)
4	Size	Number of proteins with this annotation
5	Score	Normalized score from -1 to 1 indicating the shift of the annotation along the distribution axis.
6	p-value	P-value
7	BH adj. p-value	Benjamini-Hochberg corrected p-value

Nature Immunology: doi:10.1038/ni.3693

Supplementary Table 5: Annotation enrichment analysis of lineage signature genes.

Column	Name	Description
1	Cell lineage	Cell lineage
2	Reference	Reference annotation (e.g. KEGG)
3	Annotation	Specific annotation name (e.g. DNA excision)
4	Total size	Total number of proteins in the data set
5	Selection size	Top 100 proteins sig. cell lineage specific proteins
6	Category size	Number of proteins with this annotation
7	Intersection size	Number of proteins in this module with this annotation
8	Enrichment	Fisher enrichment
9	p-value	P-value
10	BH adj. p-value	Benjamini-Hochberg corrected p-value

Supplementary Table 6: Protein copy numbers of immune cell types.

Column	Name	Description
1	Majority Protein IDs	UniProt identifier separated by semicolon.
2	Gene names	Gene names
3-169	CopyNumber	Copy number for each measurement (CopyNumber_CelltypeX_ReplicateX_steady-state/activated).

Supplementary Table 7: Annotation enrichment analysis of WGCNA modules.

Column	Name	Description
1	WGCNA module	Module numbers of the WGCNA
2	Reference	Reference annotation (e.g. KEGG)
3	Annotation	Specific annotation name (e.g. DNA excision)
4	Total size	Total number of proteins in the data set
5	Selection size	Number of proteins in this module
6	Category size	Number of proteins with this annotation
7	Intersection size	Number of proteins in this module with this annotation
8	Enrichment	Fisher enrichment
9	p-value	P-value
10	BH adj. p-value	Benjamini-Hochberg corrected p-value

Supplementary Table 8: RNAseq data of immune cell types.

Column	Name	Description
1	Gene names	Gene names
2-9	RPKM values	RPKM values of different immune cells
10	Gene id	Gene id
11	Transcript(Protein) ids	Transcript(Protein) ids
12	Ensembl Gene ID	Ensembl Gene ID
13	UniProt/SwissProt Accession	UniProt/SwissProt Accession

Supplementary Table 9: Annotation enrichement analysis of WGCNA modules microarray vs proteome.

Column	Name	Description
1	Dataset	Either Microarray or proteome
2	WGCNA module	Module numbers of the WGCNA
3	Reference	Reference annotation (e.g. KEGG)
4	Annotation	Specific annotation name (e.g. DNA excision)

Nature Immunology: doi:10.1038/ni.3693

5	Enrichment	Fisher enrichment
6	p-value	P-value
7	BH adj. p-value	Benjamini-Hochberg corrected p-value
8	Total size	Total number of proteins in the data set
9	Selection size	Number of proteins in this module
10	Category size	Number of proteins with this annotation
11	Intersection size	Number of proteins in this module with this annotation

Supplementary Table 10: Quantitative proteomics data of dendritic cell secreteomes.

Column	Name	Description
1	Majority Protein IDs	UniProt identifier separated by semicolon.
2	Gene names	Gene names
3	Protein names	Copy number for each measurement (CopyNumber_CelltypeX_ReplicateX_steady-state/activated).
4-19	iBAQ value	iBAQ (intensity based absolute quantification): Intensity values are normalized by the number of theoretically observable peptides of the protein.
20-35	LFQ intensity values	LFQ (label-free quantification) intensity values.
36	GOBP name	Gene Ontology Biological Process
37	GOMF name	Gene Ontology Molecular Function
38	GOCC name	Gene Ontology Cellular Component
39	KEGG name	Kyoto Encyclopedia of Genes and Genomes
40	Keywords	Uniprot Keywords
41	Signal category	Proteins assigned to the following categories: Transcription factor (T), Adaptor (A), Receptor (R), Ligand (L)

Supplementary Table 11: Quantitative proteomics data of classical monocyte secreteomes.

Column	Name	Description
1	Majority Protein IDs	UniProt identifier separated by semicolon.
2	Gene names	Gene names
3	Protein names	Copy number for each measurement (CopyNumber_CelltypeX_ReplicateX_steady-state/activated).
4-18	iBAQ value	iBAQ (intensity based absolute quantification): Intensity values are normalized by the number of theoretically observable peptides of the protein.
19-33	LFQ intensity values	LFQ (label-free quantification) intensity values.
34	GOBP name	Gene Ontology Biological Process
35	GOMF name	Gene Ontology Molecular Function
36	GOCC name	Gene Ontology Cellular Component
37	KEGG name	Kyoto Encyclopedia of Genes and Genomes
38	Keywords	Uniprot Keywords
39	Signal category	Proteins assigned to the following categories: Transcription factor (T), Adaptor (A), Receptor (R), Ligand (L)

Nature Immunology: doi:10.1038/ni.3693

2.2 L-arginine modulates T cell metabolism and enhances survival and anti-tumor activity

2.2.1 Summary

In light of the successful application of T cell-mediated anticancer therapies, the metabolic profiles of the heterogeneous T cell subpopulations have been linked to linage stability and functionality[278]. For instance, moderate glycolysis with increased usage of mitochondrial oxidative metabolism promotes cell longevity and supports effective T cell responses against pathogens and tumors, whereas T cells with heavy glycolytic metabolism show reduced longevity and decreased antitumor response[279,280]. In addition, nutrient composition can greatly influence the behavior of immune cells. In the tumor microenvironment, myeloid-derived suppressor cells can impair T cell responsiveness by degrading L-arginine[281]. In general, arginine metabolism is important for protein synthesis and produces precursors for many metabolites, such as polyamines and nitric oxide, which have strong immunomodulatory properties[282].

In this study, the metabolic and proteomic changes of activated naïve CD4 T cells over a period of 4 days was investigated with a multi-omic approach. The measurements showed that after T cell activation the intracellular L-arginine levels decreased while other downstream metabolites like ornithine were increased. When adding L-arginine to the culture medium the metabolic regulation of T cells changed, indicated by decreased expression of glycolytic enzymes and increased levels of TCA and serine biosynthesis pathway proteins (Figure 7). This metabolic shift was further observed through reduced glucose consumption rate and increased mitochondrial oxidative phosphorylation. In addition, the effector characteristics of T cells in L-arginine rich medium changed indicated by decreased INFg secretion and elevated expression of the lymph node homing factor receptor CCR7. Most striking, T cells in L-arginine rich medium showed increased survival rate in an IL-2 withdraw assay. Mechanistically, these changes were in part mediated by the nuclear proteins, BAZ1B, PSIP1, and TSN, as their deletion abrogated some of the arginine induced effects. These proteins could function as arginine sensors through conformational changes, however their functional role remained unclear. In a translational approach, tumor control and overall survival could be improved by transferring T cells cultured in medium supplemented with additional L-arginine. Moreover, oral administration of L-arginine enhanced T cell-mediated antitumor

activity. These findings indicated that L-arginine plays a pivotal role in T cell regulation and when available in access, promotes a central memory phenotype with increases T cell persistence. These characteristics showed beneficial in adoptive T cell therapy approaches. Together this study highlights the importance of metabolic pathways and illustrates that boosting T cell metabolism presents a great opportunity to increase effectiveness of antitumor therapies.

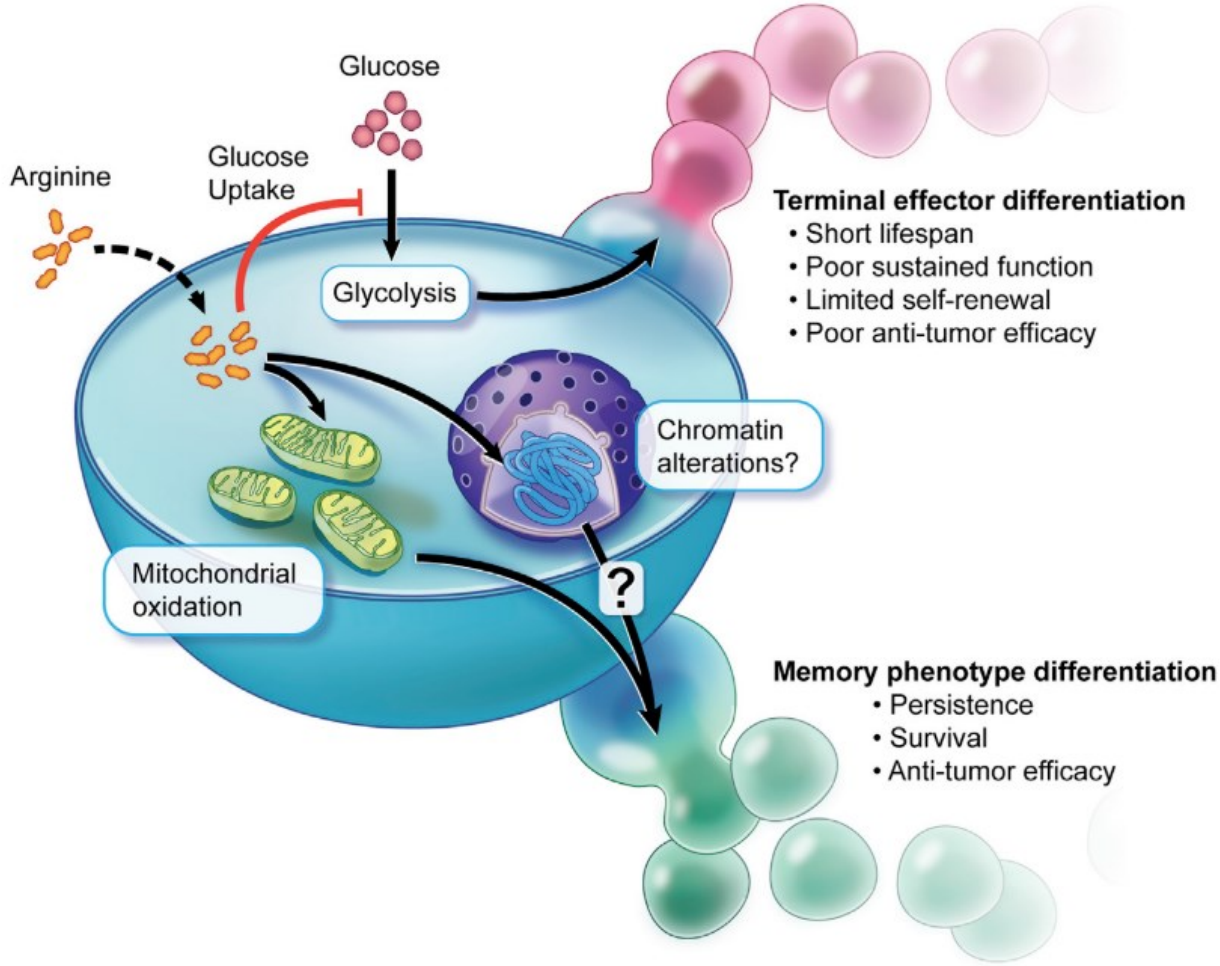

Figure 7. L-arginine promotes memory T cell formation and antitumor activity. Elevated arginine levels in T cells inhibit glucose uptake and promote mitochondrial oxidative metabolism. This metabolic change shifts the T cell differentiation towards a memory phenotype with higher survival and anti-tumor activity[283].

2.2.2 Contribution

In this collaborative study with the research group of Prof. Lanzavecchia, I performed the time series proteomic measurements and analysis of human CD4 T cells. I contributed to the analysis workflow with R programming scripts, e.g. enrichment analysis, protein copy number estimation, and differential expression analysis. In particular, Figure 1b, 2c,

Supplementary Figure 1a-d, and proteomic method sections. In addition, I performed measurements of proteomes of mouse CD4 T cell, proteomes of CD4 T cells without arginine and affinity purification mass spectrometry experiments which are not included in this manuscript.

2.2.3 Publication

This work was published in the journal Cell in 2016.

L-Arginine Modulates T Cell Metabolism and Enhances Survival and Anti-tumor Activity

Roger Geiger, Jan C Rieckmann, Tobias Wolf, Camilla Basso, Yuehan Feng, Tobias Fuhrer, Maria Kogadeeva, Paola Picotti, Felix Meissner, Matthias Mann, Nicola Zamboni, Federica Sallusto, Antonio Lanzavecchia

Cell. 2016 Oct 20;167(3):829-842.e13. doi: 10.1016/j.cell.2016.09.031. Epub 2016 Oct 13.

Article

Cell

L-Arginine Modulates T Cell Metabolism and Enhances Survival and Anti-tumor Activity

Graphical Abstract

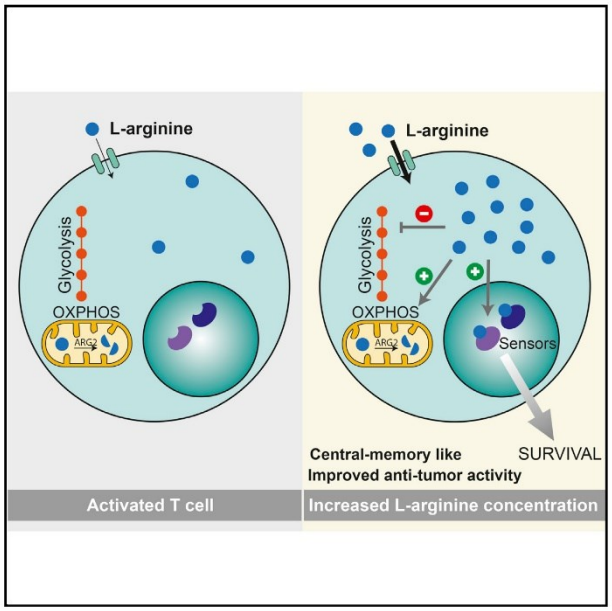

Authors

Roger Geiger, Jan C. Rieckmann, Tobias Wolf, ..., Nicola Zamboni, Federica Sallusto, Antonio Lanzavecchia

Correspondence

roger.geiger@irb.usi.ch (R.G.), lanzavecchia@irb.usi.ch (A.L.)

In Brief

Metabolomic and proteomic profiling unveil intracellular L-arginine as a crucial regulator of metabolic fitness, survival capacity, and anti-tumor activity of central memory T cells.

Highlights

- Dataset on dynamic metabolome/proteome profiles of activated human naive T cells
- Intracellular L-arginine levels regulate several metabolic pathways in T cells
- T cells with increased L-arginine display enhanced survival and anti-tumor activity
- LiP-MS identified proteins that are structurally modified by high L-arginine levels

Geiger et al., 2016, Cell *167*, 829–842
October 20, 2016
http://dx.doi.org/10.1016/j.cell.2016.09.031

CellPress

Article

Cell

L-Arginine Modulates T Cell Metabolism and Enhances Survival and Anti-tumor Activity

Roger Geiger,[1,2,*] Jan C. Rieckmann,[3] Tobias Wolf,[1,2] Camilla Basso,[1] Yuehan Feng,[4] Tobias Fuhrer,[5] Maria Kogadeeva,[5] Paola Picotti,[4] Felix Meissner,[3] Matthias Mann,[3] Nicola Zamboni,[5] Federica Sallusto,[1,6] and Antonio Lanzavecchia[1,2,7,*]
[1]Institute for Research in Biomedicine, Università della Svizzera italiana, Bellinzona 6500, Switzerland
[2]Institute of Microbiology, ETH Zurich, Zurich 8093, Switzerland
[3]Department of Proteomics and Signal Transduction, Max Planck Institute of Biochemistry, Martinsried 82152, Germany
[4]Institute of Biochemistry, ETH Zurich, Zurich 8093, Switzerland
[5]Institute of Molecular Systems Biology, ETH Zurich, Zurich 8093, Switzerland
[6]Center of Medical Immunology, Institute for Research in Biomedicine, Università della Svizzera italiana, Bellinzona 6500, Switzerland
[7]Lead Contact
*Correspondence: roger.geiger@irb.usi.ch (R.G.), lanzavecchia@irb.usi.ch (A.L.)
http://dx.doi.org/10.1016/j.cell.2016.09.031

SUMMARY

Metabolic activity is intimately linked to T cell fate and function. Using high-resolution mass spectrometry, we generated dynamic metabolome and proteome profiles of human primary naive T cells following activation. We discovered critical changes in the arginine metabolism that led to a drop in intracellular L-arginine concentration. Elevating L-arginine levels induced global metabolic changes including a shift from glycolysis to oxidative phosphorylation in activated T cells and promoted the generation of central memory-like cells endowed with higher survival capacity and, in a mouse model, anti-tumor activity. Proteome-wide probing of structural alterations, validated by the analysis of knockout T cell clones, identified three transcriptional regulators (BAZ1B, PSIP1, and TSN) that sensed L-arginine levels and promoted T cell survival. Thus, intracellular L-arginine concentrations directly impact the metabolic fitness and survival capacity of T cells that are crucial for anti-tumor responses.

INTRODUCTION

Upon antigenic stimulation, antigen-specific naive T cells proliferate extensively and acquire different types of effector functions. To support cell growth and proliferation, activated T cells adapt their metabolism to ensure the generation of sufficient biomass and energy (Fox et al., 2005). Unlike quiescent T cells, which require little nutrients and mostly use oxidative phosphorylation (OXPHOS) for their energy supply, activated T cells consume large amounts of glucose, amino acids, and fatty acids and adjust their metabolic pathways toward increased glycolytic and glutaminolytic activity (Blagih et al., 2015; Rolf et al., 2013; Sinclair et al., 2013; Wang et al., 2011).

At the end of the immune response, most T cells undergo apoptosis, while a few survive as memory T cells that confer long-term protection (Kaech and Cui, 2012; Sallusto et al., 2010). T cell survival is regulated by extrinsic and intrinsic factors. Prolonged or strong stimulation of the T cell receptor (TCR) of $CD4^+$ and $CD8^+$ T cells promotes "fitness" by enhancing survival and responsiveness to the homeostatic cytokines IL-7 and IL-15, which in turn sustain expression of anti-apoptotic proteins (Gett et al., 2003; Schluns and Lefrançois, 2003; Surh et al., 2006). Metabolic activity is also critical to determine T cell fate and memory formation (MacIver et al., 2013; Pearce et al., 2013; Wang and Green, 2012). For instance, triglyceride synthesis is central in IL-7-mediated survival of memory $CD8^+$ T cells (Cui et al., 2015), while increased mitochondrial capacity endows T cells with a bioenergetic advantage for survival and recall responses (van der Windt et al., 2012). Mitochondrial fatty acid oxidation is required for the generation of memory T cells (Pearce et al., 2009), while the mammalian target of rapamycin (mTOR), a central regulator of cell metabolism, has been shown to control T cell memory formation (Araki et al., 2009).

Metabolic fitness and T cell survival are particularly crucial in anti-tumor responses because nutrients are often scarce in the tumor microenvironment leading to T cell dysfunction (Chang et al., 2015; Ho et al., 2015), stress, and apoptosis (Alves et al., 2006; Maciver et al., 2008; Siska and Rathmell, 2015). Depletion of glucose may decrease production of interferon (IFN)-γ (Chang et al., 2013) and modulate the differentiation of regulatory T cells (De Rosa et al., 2015). In addition, degradation of L-arginine by myeloid-derived suppressor cells leads to reduced expression of the CD3ζ chain, resulting in impaired T cell responsiveness (Bronte and Zanovello, 2005; Rodriguez et al., 2007). L-arginine is a versatile amino acid that serves as a building block for protein synthesis and as a precursor for multiple metabolites, including, polyamines, and nitric oxide (NO) that have strong immunomodulatory properties (Grohmann and Bronte, 2010).

In this study, we took advantage of recent developments in mass spectrometry (Bensimon et al., 2012; Meissner and Mann, 2014; Zamboni et al., 2015) to obtain dynamic proteome and metabolome profiles of human primary naive T cells following activation and found several changes in metabolic pathways. In particular, we found that L-arginine controls

Cell 167, 829–842, October 20, 2016

Cell

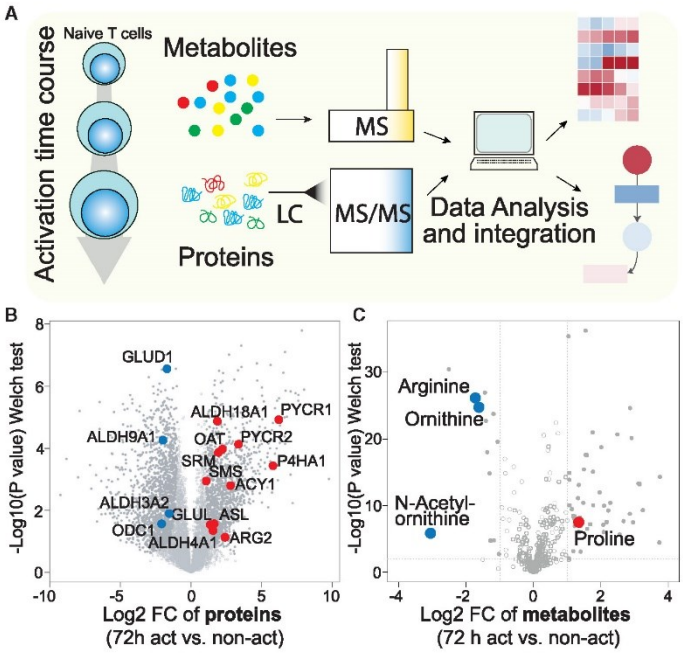

Figure 1. Metabolic and Proteomic Profiling Reveals Distinct Changes in L-Arginine Metabolism in Activated Human T Cells

(A) Schematic view of the experimental approach.

(B) Comparison of protein abundances between 72-hr-activated (CD3 + CD28 antibodies) and freshly isolated non-activated human naive CD4$^+$ T cells. Closed circles indicate proteins that changed significantly (FDR = 0.05, S_0 = 1). Colored dots are enzymes of the arginine and proline metabolism that changed significantly.

(C) Comparison of metabolite abundances in 72 hr-activated and freshly isolated non-activated human naive CD4$^+$ T cells. Closed circles indicate metabolites that changed significantly (|Log2 fc| > 1, $p < 0.01$). Colored dots are metabolites of the arginine and proline metabolism that changed significantly. Similar changes were observed when 72 hr-activated CD4$^+$ T cells were compared with naive CD4$^+$ T cells cultured overnight in the absence of TCR stimulation.

See also Figure S1 and Tables S1, S2, and S3.

glycolysis and mitochondrial activity and enhances T cell survival by interaction with transcriptional regulators. Moreover, L-arginine enhanced the generation of central memory-like T (Tcm) cells with enhanced anti-tumor activity in a mouse model.

RESULTS

Proteomic and Metabolomic Changes following Activation of Human Naive CD4$^+$ T Cells

To investigate the metabolic adaptations underlying T cell activation, we analyzed the cellular proteome and metabolome of human primary naive T cells using high-resolution mass spectrometry. Naive CD45RA$^+$ CCR7$^+$ CD4$^+$ T cells were sorted up to >98% purity from blood of healthy donors (Figure S1A) and either analyzed immediately after sorting or at different time points following activation with antibodies to CD3 and CD28. After cell lysis, proteins were digested and analyzed by liquid chromatography-coupled mass spectrometry (LC-MS) (Meissner and Mann, 2014; Nagaraj et al., 2011). In parallel, polar metabolites were extracted from cells at each time point and analyzed by non-targeted flow-injection metabolomics, a semi-quantitative method that allows rapid and deep profiling of metabolites, with the limitations that isobaric compounds cannot be discriminated and of possible in-source degradation (Fuhrer et al., 2011) (Figure 1A).

We identified a total of 9,718 proteins, quantified the abundance of 7,816 at each time point, and estimated their absolute copy numbers. Expression profiles of characteristic T cell proteins were in agreement with the literature and copy numbers of stable protein complexes had correct ratios (Figures S1B–S1G; Table S1). Non-targeted metabolomics led to the identification of 429 distinct ion species, which were putatively mapped to human metabolites (Table S2).

A comparative analysis of the proteome and metabolome of 72 hr activated and non-activated naive T cells identified 2,824 proteins whose relative expression changed significantly (Welch-test, false discovery rate [FDR] = 0.05, S_0 = 1), reflecting the fundamental morphological and functional alterations that T cells undergo upon activation (Figure 1B; Table S3). Upregulated proteins were enriched in enzymes of several metabolic pathways, including nucleotide synthesis, folate-mediated one-carbon metabolism, as well as arginine and proline metabolism. Out of 429 metabolites, 49 increased significantly (Log2 fold change [fc] > 1; $p < 0.01$), but only 14 were less abundant in activated T cells, of which three, arginine, ornithine, and N-acetylornithine, belonged to the same metabolic pathway (Figure 1C). Collectively, these data provide a comprehensive resource on the dynamics occurring in the proteome and metabolome of activated human primary naive CD4$^+$ T cells.

Intracellular L-Arginine Is Rapidly Metabolized in Activated T Cells

Based on the data obtained, we inspected the changes in the arginine metabolism more closely. The decrease in intracellular arginine occurred abruptly between 24 and 48 hr after T cell activation (Figure 2A). This finding was surprising in view of the high concentration of L-arginine in the medium (1 mM) and of the high uptake rate of ^{3}H-L-arginine in activated T cells, which exceeded

Cell

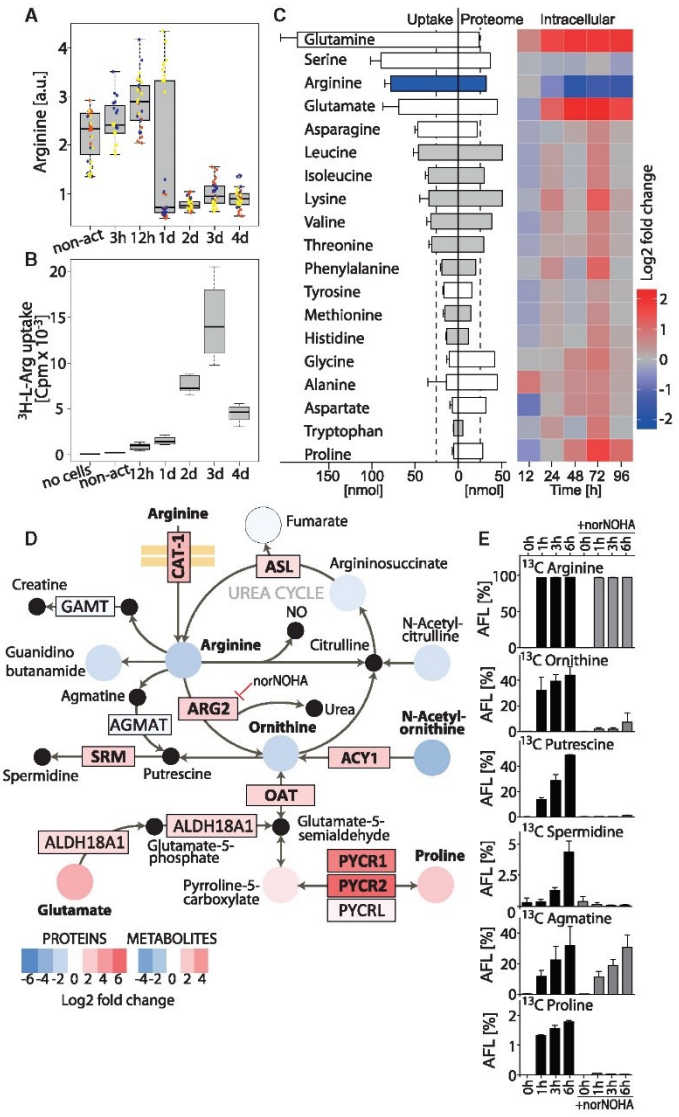

Figure 2. L-Arginine Is Rapidly Metabolized upon Activation

(A) Intracellular abundance of L-arginine in non-activated (non-act) and activated naive CD4$^+$ T cells (CD3 + CD28 antibodies). Boxplot, n = 30 from three donors, each in a different color.

(B) Kinetics of ^{3}H-L-arginine uptake during a 15-min pulse. Box plot, n = 5 from three donors.

(C) Uptake, proteome incorporation and intracellular abundance of the indicated amino acids. Barplot (left): 5 × 10^4 cells were activated for 4 days and consumption of amino acids from medium was analyzed. Essential amino acids are in gray; n = 4 from four donors, error bars represent SEM. Barplot (center): proteome incorporation of amino acids estimated from the copy numbers of each protein. Heat map (right): intracellular amino acid abundance relative to naive T cells over time as determined by mass spectrometry (MS) n = 30 from three donors. Leucine and isoleucine could not be distinguished as they have the same mass.

(D) Changes in the abundance of metabolites and proteins of the arginine and proline metabolism between non-activated and 72 hr-activated CD4$^+$ T cells. Log2 fold changes of proteins and metabolites are color-coded. Significant changes are in bold (FDR = 0.05, S_0 = 1 for proteins; and $p < 0.05$ [two-tailed unpaired Student's t test], |Log2 fc| > 1 for metabolites). Black dots are metabolites that were not detected by MS. Only enzymes that were detected by MS are shown.

(E) Metabolic tracing of L-arginine. Ninety-six hour-activated T cells were pulsed with $^{13}C_6$-L-arginine and the metabolic fate was analyzed by LC-MS/MS at different time points. AFL, apparent fractional labeling; n = 4 from two donors. ^{13}C Citrulline was not detected. Error bars represent SEM.

For (A) and (B), upper whisker = min(max(x), Q_3 + 1.5 * IQR) and lower whisker = max(min(x), Q_1 − 1.5 * IQR).

the requirement for protein synthesis by more than 2-fold (Figures 2C and 2B).

To gain insights into the metabolic fate of L-arginine, we analyzed the activation-induced changes in metabolites and proteins of the surrounding metabolic network (Figure 2D). While metabolites around the urea cycle were decreased, the arginine transporter cationic amino acid transporter 1 (CAT-1) and the enzymes arginase 2 (ARG2), ornithine aminotransferase (OAT), and spermidine synthase (SRM), which are required for the conversion of L-arginine into ornithine, L-proline, and spermidine, respectively, were upregulated. These findings suggest that L-arginine was rapidly converted into downstream metabolites. Indeed, ^{13}C-L-arginine tracing experiments showed an immediate and strong accumulation of ^{13}C in ornithine, putrescine, agmatine, and, to a lower extent, in spermidine and proline (Figure 2E). Addition of the arginase inhibitor norNOHA did not affect the conversion of L-arginine into agmatine, but markedly reduced the conversion into ornithine, putrescine, spermidine, and proline (Figure 2E). This indicated that in T cells L-arginine is mainly catabolized through arginase, likely through mitochondrial ARG2, because the cytosolic enzyme arginase 1 (ARG1) was not detected in T cells.

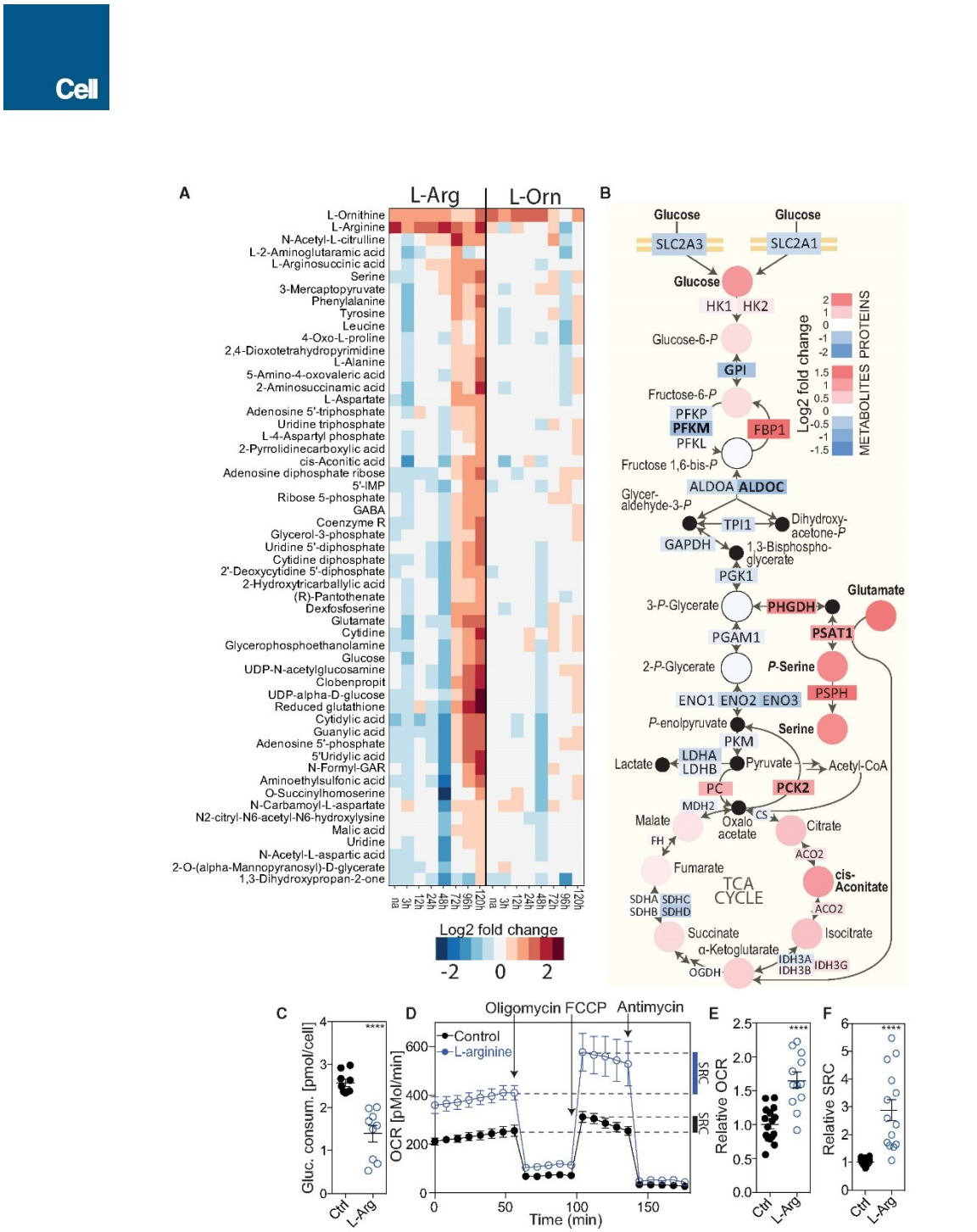

(legend on next page)

Cell

Collectively, these data show that L-arginine is avidly taken up by activated T cells in amounts exceeding the requirements for protein synthesis and can be rapidly converted by metabolic enzymes into downstream metabolites.

Elevated L-Arginine Levels Regulate Several Metabolic Pathways

Because activated T cells showed a drop in their intracellular arginine concentration—while all other amino acids either remained steady or increased—we assessed the consequences of increasing L-arginine availability on metabolism. We first performed a kinetic metabolome analysis of naive T cells activated in standard medium (containing 1 mM L-arginine) or in medium in which the concentration of L-arginine was increased 4-fold. Intracellular arginine and ornithine levels were increased 1.5- to 2.5-fold at all time points in T cells activated in L-arginine-supplemented medium as compared to controls (Figure 3A), while nitric oxide, which is generated from L-arginine by nitric oxide synthase (NOS), did not increase (Figure S2A). Notably, at late time points after activation (72–120 hr), several other metabolites, including intermediates of the urea cycle, nucleotides, sugar derivatives, and amino acids were increased (Figure 3A). In contrast, an increased availability of L-arginine's downstream metabolites L-ornithine or L-citrulline (added to the culture medium at the same concentration as L-arginine) only had minor effects on metabolism (Figures 3A and S2B). These findings suggest that L-arginine directly regulates several metabolic pathways in activated T cells.

A proteome analysis showed that the expression of 202 out of 7,243 proteins was significantly different in T cells activated in L-arginine-supplemented medium (Table S4, ANOVA, FDR = 0.005, $S_0 = 5$, $|\text{Log2 fc}| > 1$), indicating that T cells were reprogrammed under the influence of increased intracellular L-arginine levels. In particular, PC, PCK2, and FBP1, which promote gluconeogenesis, were increased, while glucose transporters and glycolytic enzymes were decreased (Figure 3B). Indeed, these T cells consumed less glucose (Figure 3C), indicating that the glycolytic flux was diminished by L-arginine supplementation. Moreover, the serine biosynthesis pathway that branches from glycolysis and several intermediates of the mitochondrial tricarboxylic acid (TCA) cycle were upregulated (Figure 3B). Consistent with the fact that the TCA cycle fuels OXPHOS, L-arginine supplementation increased oxygen consumption 1.7-fold and augmented the mitochondrial spare respiratory capacity (SRC) (Figures 3D–3F). Collectively, these data demonstrate that an increase in intracellular L-arginine levels skewed the metabolism in activated T cells from glycolysis toward mitochondrial OXPHOS.

L-Arginine Influences Human T Cell Proliferation, Differentiation, and Survival

Naive T cells start to divide after an initial period of growth that lasts 24–40 hr. Subsequently, they divide rapidly and differentiate into effector T cells that produce inflammatory cytokines, such as IFN-γ, and into memory T cells that survive through homeostatic mechanisms (Schluns and Lefrançois, 2003; Surh et al., 2006). We therefore asked whether elevated intracellular L-arginine concentrations affect the fate of activated T cells. Naive $CD4^+$ T cells activated in L-arginine-supplemented medium showed a slightly delayed onset of proliferation, but once proliferation started, doubling rates were comparable to controls (Figures S3A and S3B). The onset of proliferation was not affected by D-arginine or by addition of L-lysine (a competitive inhibitor of L-arginine uptake; Figure S3A) to L-arginine-supplemented cultures (Figure S3C). Importantly, T cells activated in L-arginine-supplemented medium secreted much less IFN-γ than T cells cultured in control medium (Figure 4A). However, when these cells were re-activated, they were able to secrete IFN-γ in comparable amounts (Figure 4B), indicating that T cells primed in the presence of high L-arginine concentrations retained the capacity to differentiate into Th1 effector cells upon secondary stimulation. Because low production of cytokines is characteristic of $CCR7^+$ lymph node-homing Tcm cells (Sallusto et al., 1999), we analyzed the expression of CCR7 on day 10 after activation and found a higher fraction of proliferating $CCR7^+$ T cells in L-arginine supplemented cultures than in control cultures (Figure 4C). Collectively, these data indicate that increased intracellular L-arginine levels limit T cell differentiation and maintain cells in a Tcm-like state.

To test whether L-arginine affects T cell survival, we activated human naive $CD4^+$ and $CD8^+$ T cells, expanded them in the presence of IL-2 or IL-15, and measured their viability upon cytokine withdrawal. Strikingly, L-arginine supplementation significantly increased the survival of activated $CD4^+$ and $CD8^+$ T cells when cultured in the absence of exogenous cytokines (Figures 4D and 4E). L-arginine was most effective when added during the first 48 hr following T cell activation (Figure 4F). Conversely, L-lysine or D-arginine, which both inhibit L-arginine uptake

Figure 3. L-Arginine Globally Influences Metabolism of Activated Human T Cells

(A) Human naive $CD4^+$ T cells were activated in control medium (Ctrl) or in medium supplemented with 3 mM L-arginine (L-Arg) or 3 mM L-ornithine (L-Orn) and harvested at different time points. The heat map shows the difference between the abundance of metabolites in T cells cultured in L-Arg or L-Orn-medium and controls. Shown are only metabolites with a Log2 fc > 1 and an adjusted p value of < 0.05; n = 12 from two donors.

(B) Differential analysis of the glycolytic pathway between naive $CD4^+$ T cells cultured in L-Arg medium or Ctrl medium, 96 hr after activation. Log2 fold changes of proteins and metabolites are color-coded. Proteins or metabolites whose abundance changed significantly are in bold (for proteins FDR = 0.005, $S_0 = 5$, $|\text{Log2 fc}| > 1$ and for metabolites $p < 0.05$ (Student's t test), $|\text{Log2 fc}| > 1$). 3-*P*-glycerate and 2-*P*-glycerate could not be distinguished as they have the same mass.

(C) Seventy-two hour-activated T cells were plated in fresh medium and glucose consumption was determined enzymatically after 24 hr; n = 9 from three donors. Error bars represent SEM.

(D) Seahorse experiment performed with activated (96 hr) T cells from one donor. Oligomycin was injected after 56 min, FCCP after 96 min, and antimycin (to inhibit the respiratory chain) after 136 min. Data are representative of five independent experiments with different donors; n = 4. Error bars represent SEM.

(E and F) Relative oxygen consumption rate (OCR) (E) and relative spare respiratory capacity (SRC) (F) of activated (96 hr) T cells; n = 12 from three donors. ****$p < 0.0001$ (Student's t test). Error bars represent SEM.

See also Figure S2 and Table S4.

Cell

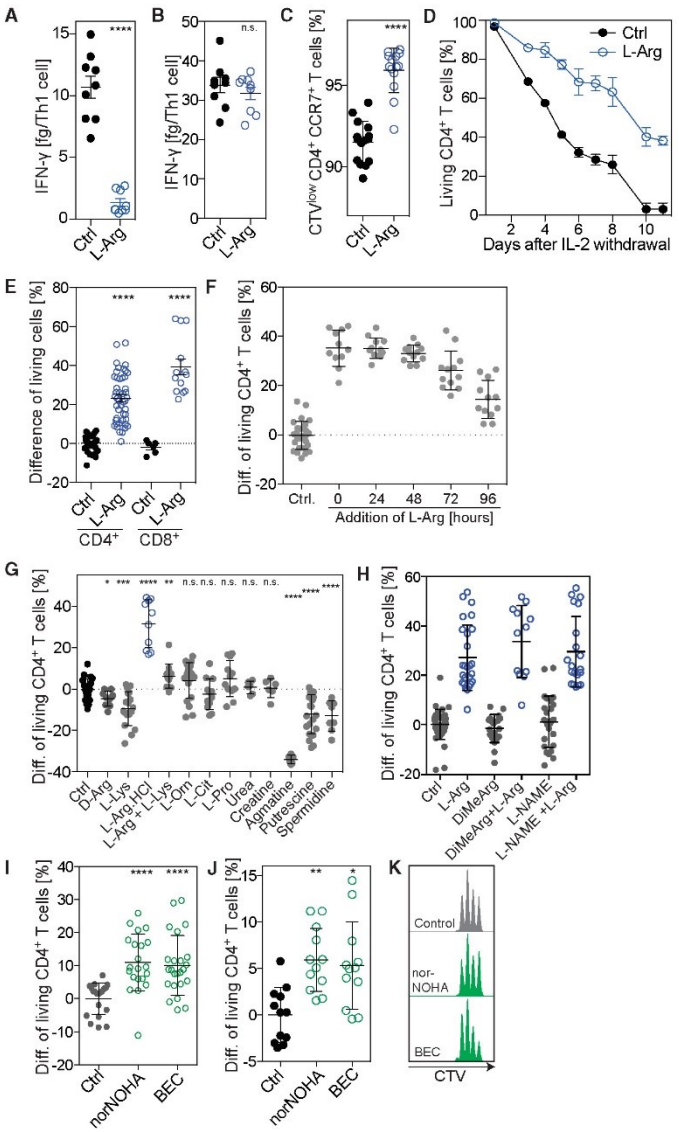

Figure 4. L-Arginine Limits Human T Cell Differentiation and Endows Cells with a High Survival Capacity In Vitro

(A and B) Human naive CD4+ T cells were activated in L-Arg medium or Ctrl medium in the presence of 10 ng/mL IL-12. IFN-γ was quantified in culture supernatants after 5 days (A) or after re-activation for 5 hr with PMA/ionomycin (B); n = 9 from three donors.

(C) Naive CD4+ T cells were labeled with CellTrace Violet (CTV) and activated in L-Arg medium or Ctrl medium. On day 10, proliferating CTV^0 T cells were stained with an antibody to CCR7 and analyzed by flow cytometry; n = 15 from three donors.

(D) Naive CD4+ T cells were activated for 5 days in L-Arg or Ctrl medium in the presence of exogenous IL-2, washed extensively, and cultured in Ctrl medium in the absence of IL-2. Shown is the percentage of living T cells as determined by Annexin V staining at different time points after IL-2 withdrawal. One representative experiment out of three performed.

(E) Same experiment as in (D). Shown is the difference of living activated CD4+ and CD8+ T cells 5 days after withdrawal of IL-2; n = 46, from 16 donors (CD4+ T cells); n = 13, from four donors (CD8+ T cells).

(F) Difference of living activated CD4+ T cells 5 days after IL-2 withdrawal. Naive CD4+ T cells were activated and L-Arg (3 mM) was added to the culture medium at the indicated time points; n = 12 from four donors.

(G) Difference of living activated CD4+ T cells 5 days after IL-2 withdrawal. Naive CD4+ T cells were activated in Ctrl medium or medium supplemented with the indicated metabolites (3 mM, except for spermidine 0.1 mM). Ctrl, n = 21; D-Arg, n = 9; L-lysine, n = 18; L-Arg-HCl, n = 10; L-Arg + L-Lys, n = 12; L-Orn, n = 20; L-Cit, L-Pro, n = 12; urea, creatine, agmatine, n = 6; putrescine, n = 18; spermidine, n = 8, from at least three donors.

(H) Difference of living activated CD4+ T cells 5 days after IL-2 withdrawal. Naive CD4+ T cells were activated in the presence or absence of nitric oxide synthase inhibitors dimethylarginine (DiMeArg) or L-NG-nitroarginine methyl ester (L-NAME), both used at 1 mM. Ctrl and L-Arg, n = 26; DiMeArg and L-NAME, n = 16; DiMeArg + L-Arg and L-NAME + L-Arg, n = 12, from at least three donors.

(I) Difference of living activated CD4+ T cells 5 days after IL-2 withdrawal. Naive CD4+ T cells were activated in absence (Ctrl) or presence of the arginase inhibitors N^ω-Hydroxy-nor-L-arginine (norNOHA, 300 μM) or S-(2-boronoethyl)-L-cysteine (BEC, 300 μM); n = 21, from seven donors.

(J) Same as in (I) but cultures were performed in medium containing 150 μM L-arginine.

(K) Effect of norNOHA and BEC on proliferation of CTV-labeled naive T cells measured 72 hr after activation. *p < 0.05, **p < 0.01, ***p < 0.001, ****p < 0.0001 (Student's t test).

(A–J) Error bars represent SEM throughout.

See also Figures S3 and S4.

Cell

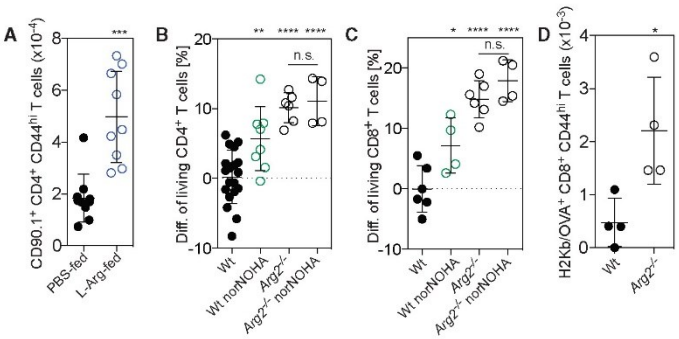

Figure 5. Increased Intracellular L-Arginine Levels Endow Mouse T Cells with a High Survival Capacity In Vitro and In Vivo

(A) BALB/c CD90.1$^+$ CD4$^+$ TCR transgenic T cells specific for the influenza $HA_{110-119}$ peptide were adoptively transferred into CD90.2$^-$ host mice that were then immunized subcutaneously (s.c.) with $HA_{110-119}$ in complete Freund's adjuvant (CFA). Mice were fed with L-arginine-HCl (1.5 mg/g body weight) or PBS, administrated daily starting 1 day before immunization. Fifteen days later, the amount of CD44^{hi} CD90.1$^+$ CD4$^+$ TCR transgenic T cells in draining lymph nodes was measured by fluorescence-activated cell sorting (FACS) analysis; n = 9 from two independent experiments.

(B and C) In vitro T cell survival experiment with C57BL/6 wild-type (WT) or *Arg2*$^{-/-}$ T cells. Naive CD62L^h CD44^o CD4$^+$ T cells and CD8$^+$ T cells were activated for 4 days in L-Arg or Ctrl medium in the absence or presence of the arginase inhibitor norNOHA (500 μM). On day 2 exogenous IL-2 was added to the cultures, on day 4 cells were washed extensively and cultured in medium without IL-2. Shown is the difference in the percentage of living CD4$^+$ (B) and CD8$^+$ (C) T cells relative to WT T cells as determined by Annexin V staining 2 days after IL-2 withdrawal. WT, n = 6-19; WT norNOHA, n = 6–8; *Arg2*$^{-/-}$, n = 4–6; *Arg2*$^{-/-}$ norNOHA, n = 4.

(D) Equal numbers of CD45.1$^+$ WT and CD45.2$^+$ CD90.2$^+$ *Arg2*$^{-/-}$ naive CD8$^+$ T cells were transferred into CD45.2$^+$ CD90.1$^+$ host mice. Mice were immunized with the $OVA_{257-264}$ peptide in CFA. Fifteen days after immunization, the amount of $OVA_{257-264}$-specific CD44^{hi} CD8$^+$ T cells was measured in draining lymph nodes by flow cytometry using $OVA_{257-264}$/H-2Kb multimers; n = 4. One representative experiment out of two performed. *$p < 0.05$, **$p < 0.01$, ***$p < 0.001$, ****$p < 0.0001$ (Student's t test).

Error bars represent SEM throughout.

See also Figure S5.

(Figure S3C), decreased T cell survival significantly (Figure 4G), indicating that reduced availability of intracellular L-arginine negatively affects T cell survival. L-arginine's downstream metabolites ornithine, citrulline, proline, urea, and creatine, as well as nitric oxide, had no effect, while agmatine, putrescine, or spermidine decreased T cell survival (Figure 4G and 4H). L-arginine-HCl enhanced T cell survival to a similar extent than free base L-arginine, ruling out a possible influence of pH. The increased T cell survival induced by elevated intracellular L-arginine concentration was independent of mTOR signaling (Araki et al., 2009), based on the finding that L-arginine supplementation did not change phosphorylation levels of two targets of mTOR (p70 S6K1 and 4E-BP) and inhibition of mTOR by rapamycin, although enhancing T cell survival, affected metabolism in an entirely different way than L-arginine (Figures S4A–S4D).

To further support the notion that L-arginine regulates T cell survival, we inhibited arginase (that converts L-arginine into L-ornithine) with norNOHA or BEC, which increase intracellular L-arginine levels (Monticelli et al., 2016). Inhibition of arginase significantly increased the survival capacity of activated CD4$^+$ T cells, even in medium containing physiological levels of L-arginine (150 μM) (Figures 4I and 4J). Inhibition of arginase did not affect proliferation (Figure 4K), indicating that polyamines can be synthesized from other sources than L-arginine, i.e., from L-glutamate (Wang et al., 2011), a finding that is consistent with the experiments showing that polyamine synthesis only partially depends on L-arginine (Figure 2E).

Collectively, these data indicate that elevated intracellular L-arginine levels directly induced metabolic changes and longevity of human CD4$^+$ and CD8$^+$ T cells, independently of mTOR signaling or downstream metabolites.

L-Arginine Influences Mouse T Cell Survival In Vivo

To address the impact of changes in intracellular L-arginine levels in vivo, we performed experiments in mice. Naive TCR transgenic CD4$^+$ T cells specific for a hemagglutinin peptide ($HA_{110-119}$) were adoptively transferred into BALB/c mice that received daily supplements of L-arginine (1.5 mg/g body weight) or PBS as a control. This amount of arginine doubled the daily dietary intake present in chow. Mice were immunized with $HA_{110-119}$ in CFA and the amount of transgenic T cells in draining lymph nodes was measured 15 days later. Three times more CD44^{hi} CD4$^+$ TCR transgenic T cells were recovered in mice fed with L-arginine compared to control mice (Figure 5A). In control experiments, we found that 30 min after oral administration, L-arginine levels in the serum increased from ~160 μM to 700 μM (Figure S5A) and intracellular L-arginine levels of CD44^{hi}-activated T cells increased ~2-fold (Figure S5B).

We then analyzed CD4$^+$ and CD8$^+$ T cells from *Arg2*-deficient mice. When compared to wild-type T cells, *Arg2*$^{-/-}$ T cells showed 20% higher baseline intracellular L-arginine levels (Figure S5C) and when stimulated in vitro with antibodies to CD3 and CD28, they survived significantly longer than wild-type T cells after IL-2 withdrawal (Figures 5B and 5C). Moreover, activation in the presence of the arginase inhibitor norNOHA, while increasing the survival of wild-type T cells, did not affect survival of *Arg2*$^{-/-}$ T cells (Figures 5B and 5C), indicating that in mouse T cells L-arginine degradation occurred mainly through ARG2. Finally, equal numbers of congenically marked wild-type and *Arg2*$^{-/-}$ CD8$^+$ T cells were co-transferred into wild-type mice that were immunized with the ovalbumin-peptide SIINFEKL ($OVA_{257-264}$) in CFA. Fifteen days after immunization, the number of MHC-I H-2K^b haplotype (Kb)-restricted $OVA_{257-264}$-specific CD44^{hi} CD8$^+$ T cells was measured in lymph nodes by multimer

Cell

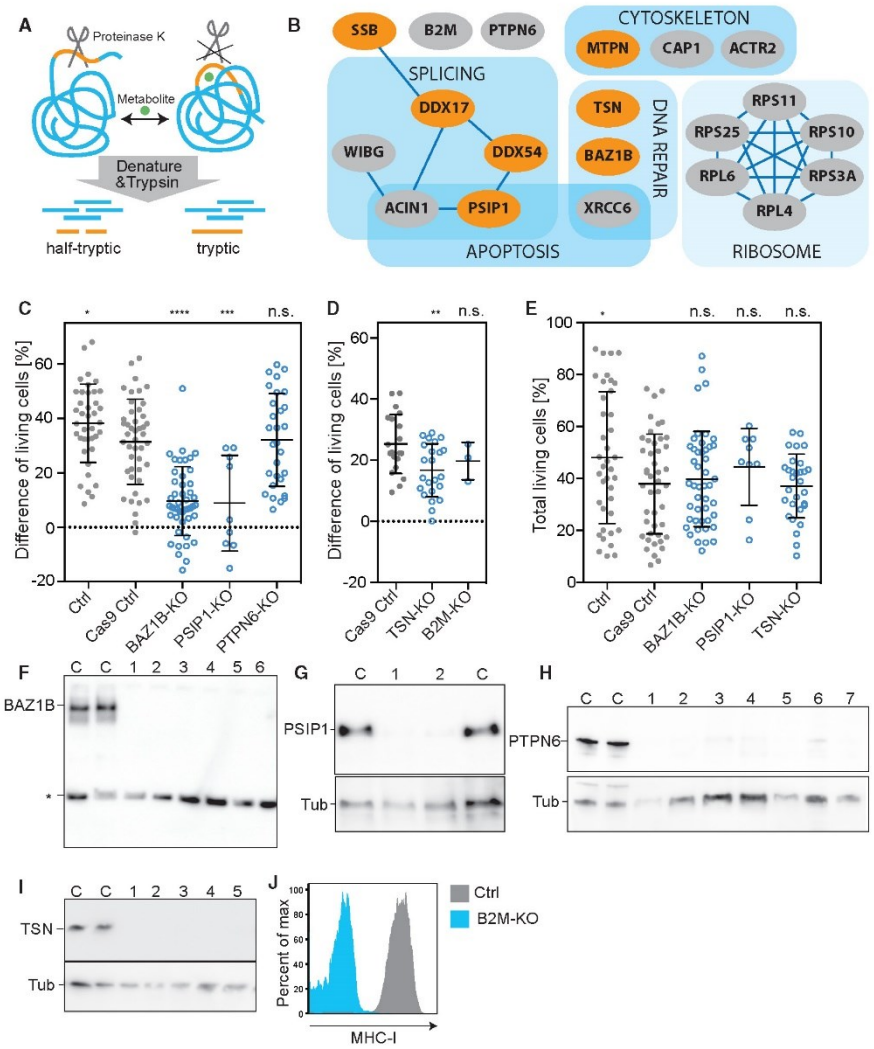

Figure 6. BAZ1B, PSIP1, and TSN Mediate the L-Arginine-Dependent Reprogramming of T Cells toward Increased Survival Capacity

(A) Scheme of the limited proteolysis workflow.

(B) Proteins that experience a structural change in response to 1 mM L-arginine but not to 1 mM D-arginine or L-ornithine. Transcriptional regulators are in orange, proteins are grouped according to their functions. Known interactions are indicated based on http://string-db.org/ and http://www.genemania.org/.

(C) Survival experiment with human $CD4^+$ T cell clones devoid of the indicated proteins. Control (Ctrl), n = 39; Cas9-transduced control (Cas9 Ctrl), n = 45; BAZ1B-KO, PSIP1-KO, and PTPN6-KO, n = 46, n = 9, and n = 29, respectively. Each T cell clone was analyzed in triplicate. Bars represent the mean ± SEM.

(D) Same as in (C). Cas9 Ctrl, n = 20; TSN-KO and B2M-KO, n = 23 and n = 3, respectively.

(E) Percentage of living cells after IL-2 withdrawal of T cells cultured in Ctrl medium. Ctrl, n = 39; Cas9 Ctrl, n = 45; BAZ1B-KO, PSIP1-KO, and TSN-KO, n = 46, n = 9, and n = 29, respectively.

(legend continued on next page)

Cell

staining. As shown in Figure 5D, OVA-specific *Arg2*$^{-/-}$ T cells were more numerous than OVA-specific wild-type T cells. Taken together, these findings provide evidence that intracellular L-arginine concentrations, which can be elevated by dietary supplementation, can increase the survival capacity of antigen-activated T cells in vivo.

Global Analysis of Structural Changes Identifies Putative L-Arginine Sensors

To elucidate the mechanism by which L-arginine promotes T cell survival, we first examined the list of differentially expressed proteins (Table S4) and found among the top hits Sirtuin-1, a histone deacetylase, which is known to increase the lifespan of different organisms (Tissenbaum and Guarente, 2001). However, a role for Sirtuin-1 was excluded based on the findings that human naive T cells activated in the presence of the Sirtuin-1 inhibitor Ex-527 and Sirtuin-1-deficient T cells generated using the CRISPR/Cas9 technology displayed a L-arginine-mediated increase in survival comparable to controls (Figure S6).

Given that L-arginine directly promotes T cell survival, we set out to identify putative protein interactors that may be modified by binding of L-arginine and initiate the pro-survival program. For this, we probed structural changes across the T cell proteome that occur in response to L-arginine following a recently developed workflow (Feng et al., 2014) (Figure 6A). T cells were homogenized and incubated in the absence or presence of 1 mM L-arginine, D-arginine, or L-ornithine. Subsequently, samples were subjected to limited proteolysis (LiP) with proteinase K, which preferentially cleaves flexible regions of a protein. After denaturation and trypsin digestion, peptide mixtures were analyzed by LC-MS. Because trypsin cleaves polypeptides specifically after lysine or arginine, cleavages after other amino acids were introduced by proteinase K, leading to half-tryptic peptides. Significant changes in the abundances of half-tryptic peptides (fc > 5, $p < 0.05$, > 2 peptides per protein) were used as readout for structural changes induced by the addition of metabolites.

Because L-arginine, but not D-arginine or L-ornithine, promoted T cell survival, we searched for proteins that were exclusively affected by L-arginine and were cleaved by proteinase K at identical sites in all samples from six donors. Out of 5,856 identified proteins, only 20 candidates fulfilled these stringent criteria (Figure 6B). These proteins differed widely in molecular weight and abundance (Table S5), excluding a bias toward large or abundant proteins. Most candidates were assigned to four functional groups: mRNA splicing, DNA repair, regulation of the cytoskeleton, and the ribosome, while seven were transcriptional regulators (in orange in Figure 6B). Thus, our global approach revealed several proteins with various functions that structurally respond to elevated intracellular L-arginine levels.

BAZ1B, PSIP1, and TSN Are Required for the L-Arginine-Mediated Effect on T Cell Survival

To test whether selected candidates identified through the structural analysis were involved in the L-arginine-mediated survival benefit, we generated gene knockout human T cell clones using the CRISPR/Cas9 system that were screened for loss of the corresponding protein by western blot or flow cytometry. Knockout of *PTPN6* (Shp-1) or *B2M* did not alter the effect of L-arginine on T cell survival (Figures 6C and 6D), while no viable clones were obtained after knockout of *XRCC6*, *ACIN1*, and *SSB* (not shown). Strikingly, knockout of the transcriptional regulators BAZ1B, PSIP1, and TSN significantly reduced L-arginine's beneficial effect on T cell survival (Figures 6C, 6D, and 6F–6J). Importantly, when cultured in control medium prior to the IL-2 withdrawal, T cell clones lacking these transcriptional regulators proliferated and survived like controls (Figure 6E), indicating that their viability was unaffected but they were unable to sense increased L-arginine levels and to induce the pro-survival program. Taken together, these data provide evidence that BAZ1B, PSIP1, and TSN interact with L-arginine and play a role in the reprograming of T cells toward increased survival capacity.

L-Arginine Improves Anti-tumor T Cell Response In Vivo

Because L-arginine increased the survival capacity of human and mouse T cells and favored the formation of Tcm-like cells that have been shown to be superior than effector memory T cells (Tem) in eradicating tumors in mouse models (Klebanoff et al., 2005), we reasoned that increased intracellular L-arginine levels might positively affect anti-tumor T cell responses in vivo. We stimulated naive TCR transgenic CD8$^+$ OT-I T cells specific for the $OVA_{257-264}$ peptide in control or L-arginine-supplemented medium for 4 days and measured their survival in vitro following IL-2 withdrawal and in vivo after adoptive transfer into lymphopenic *Cd3e*$^{-/-}$ mice. Consistent with our previous data, L-arginine endowed OT-I T cells with a higher survival capacity both in vitro and in vivo (Figures 7A and 7B). Moreover, these T cells maintained a Tcm-like state and secreted less IFN-γ than controls after in vitro priming but upon reactivation, they produced even more IFN-γ than controls (Figures 7C–7E). Remarkably, when adoptively transferred into wild-type mice bearing B16 melanoma tumors expressing the OVA antigen, L-arginine-treated OT-I T cells mounted a superior anti-tumor response, as measured by the reduction of tumor size and by the increased survival of mice (Figures 7F and 7G). Naive OT-I T cells primed in vivo by OVA + Alum immunization of tumor-bearing mice that were fed with L-arginine were also superior in mediating an anti-tumor response compared to OT-I T cells primed in mice fed with PBS (Figure 7H). Collectively, these data demonstrate that elevated L-arginine levels increased the survival capacity of CD8$^+$ T cells and their anti-tumor activity in vivo.

(F–I) Western blots or FACS analysis of T cell clones showing deletion of target proteins. C refers to Cas9 Ctrl clones. Unspecific bands are marked with asterisk. An antibody to tubulin (Tub) was used as a loading control. B2M-KO was verified by staining cells with an antibody against MHC-I. *$p < 0.05$, **$p < 0.01$, ***$p < 0.001$, ****$p < 0.0001$ (Student's t test).
(C–E) Error bars represent SEM throughout.
See also Figure S6 and Table S5.

Cell

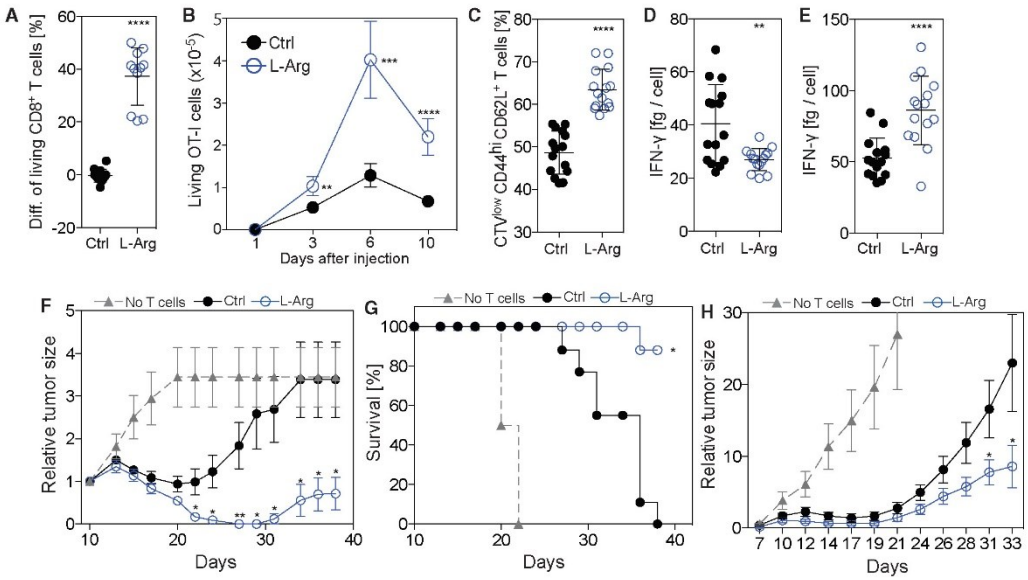

Figure 7. CD8⁺ T Cells with Increased L-Arginine Levels Display Improved Anti-tumor Activity In Vivo

(A) Survival of activated mouse CD8⁺ OT-I T cells (4 days) after IL-2 withdrawal. Data points represent the difference between the percentage of living T cells from cultures performed in L-Arg medium or Ctrl medium; n = 11.

(B) CD90.1⁺ CD45.1/2⁺ and CD90.1⁺ CD45.1⁺ naive CD8⁺ OT-I T cells were activated for 4 days in Ctrl medium or L-Arg medium, respectively. Equal numbers of the congenically marked activated OT-I cells were co-transferred into *Cd3e*$^{-/-}$ mouse and the number of living T cells was measured in pooled spleen and lymph nodes at the indicated time points; n = 3 at each time point.

(C) Naive CD8⁻ OT-I T cells were activated with CD3 + CD28 antibodies in L-Arg medium or Ctrl medium. Five days after activation, the percentage of Tcm-like cells (CD44^{hi}, CD62L⁺) was measured by flow cytometry; n = 15.

(D) Naive OT-I CD8⁺ T cells were activated in L-Arg medium or Ctrl medium and IFN-γ was quantified in culture supernatants after 5 days; n = 15.

(E) Same as in (D) but T cells were re-activated on day 5 day with PMA/Ionomycin; n = 15.

(F and G) B16.OVA melanoma cells were injected into C57BL/6 mice and tumors were allowed to grow for 10 days. Naive OT-I CD8⁺ T cells were activated in vitro in L-Arg medium or Ctrl medium and injected into tumor bearing mice. Tumor burden (F) and survival (G) were assessed over time. Data are representative of three independent experiments, each performed with seven to nine mice per group.

(H) B16.OVA melanoma cells were injected into C57BL/6 mice and tumors were allowed to grow for 6 days. At day 6, naive CD8⁺ OT-I T cells were transferred into tumor bearing mice and at day 7 mice were immunized with OVA peptide. Starting one day before the T cell transfer, PBS or L-arginine (1.5 mg/g body weight) was orally administered daily; n = 19 from three independent experiments. Bars represent the SEM. *$p < 0.05$, **$p < 0.01$, ***$p < 0.001$, ****$p < 0.0001$ (Student's t test). In (G), *$p < 0.05$ as determined by log-rank test comparison between curves.

Error bars represent SEM throughout.

DISCUSSION

Using proteomics, metabolomics, and functional approaches, we have shown that increased L-arginine levels can exert pleiotropic effects on T cell activation, differentiation, and function, ranging from increased bioenergetics and survival to in vivo anti-tumor activity.

We found that activated T cells heavily consume L-arginine and rapidly convert it into downstream metabolites, which lead to a marked decrease in intracellular levels after activation. Addition of exogenous L-arginine to the culture medium increased intracellular levels of free L-arginine and of several other metabolites and induced a metabolic switch from glycolysis to OXPHOS, thus counteracting the Warburg effect (Vander Heiden et al., 2009). While the mechanism by which L-arginine induces the broad metabolic changes remains elusive, a possible explanation for the switch toward OXPHOS is that increased L-arginine levels upregulate the serine biosynthesis pathway, which has been shown to fuel the TCA cycle and consequently OXPHOS (Possemato et al., 2011). Suggestive evidence for a link between L-arginine and the functionality of mitochondria has been provided by earlier observations; L-arginine improves mitochondrial function and reduces apoptosis of bronchial epithelial cells after injury induced by allergic airway inflammation (Mabalirajan et al., 2010) and had a beneficial effect for the treatment of patients with a mitochondrial disorder (Koga et al., 2010).

A striking finding is that a 2-fold increase in intracellular L-arginine concentrations induces human and mouse T cells to acquire

a Tcm-like phenotype with high expression of CCR7 and CD62L and a decreased production of IFN-γ. This may be a consequence of decreased glycolysis induced by L-arginine, as previous studies demonstrated that glycolytic activity supports IFN-γ mRNA translation (Chang et al., 2013). Although we observed a delayed onset of cell proliferation, L-arginine-treated T cells progressed through cell division in a way comparable to controls and readily proliferated and differentiated to effector cells upon secondary stimulation. Furthermore, inhibition of arginases in human T cells or deletion of ARG2 in mouse T cells did not affect cell proliferation, suggesting that the downstream fate of L-arginine is less important in T cells than the levels of free L-arginine. L-arginine may induce some of its pleiotropic effects through interfering with arginine methyltransferases, which can affect the functions of various proteins (Geoghegan et al., 2015).

Improved T cell survival is another striking effect induced by elevated intracellular L-arginine levels. Having excluded a role for L-arginine-derived nitric oxide and for the metabolic regulator Sirtuin-1 that has been shown to increase lifespan of lower eukaryotes (Tissenbaum and Guarente, 2001) and reduce glycolytic activity (Rodgers et al., 2005), which in T cells may enhance memory T cell formation and anti-tumor responses (Sukumar et al., 2013), we considered a direct effect of L-arginine on protein functions. Metabolite-protein interactions are more frequent than previously appreciated (Li et al., 2010), and in some cases, such interactions may have functional consequences. For instance, cholesterol binds to ~250 proteins (Hulce et al., 2013) and succinate, an intermediate of the TCA cycle, stabilizes HIF-1α in macrophages, leading to increased secretion of IL-1β (Tannahill et al., 2013). We took advantage of a novel method that allows proteome-wide probing of metabolite-protein interactions without modifying metabolites (Feng et al., 2014) and identified several proteins that changed their structure in the presence of L-arginine, which were likely sensors required to mediate the metabolic and functional response. We provide evidence that three nuclear proteins (BAZ1B, PSIP1, and TSN) were required in T cells for mediating L-arginine's effect on survival. BAZ1B is a transcriptional regulator containing a PHD domain that supposedly binds to methylated histones. PSIP1 is a transcriptional co-activator implicated in protection from apoptosis (Ganapathy et al., 2003). Interestingly, the structural changes induced by L-arginine affect the PHD domain of BAZ1B and the AT-hook DNA-binding domain of PSIP1, which may affect DNA binding and lead to the induction of the pro-survival program. Finally, TSN, a small DNA and RNA binding protein, has been implicated in DNA repair, regulation of mRNA expression, and RNAi (Jaendling and McFarlane, 2010) and can thus influence the cellular phenotype in various ways. The conclusion that these three proteins are involved in the pro-survival effect mediated by L-arginine is based on the analysis of several different knockout T cell clones. Yet, there was variability in the response to L-arginine, which may suggest compensatory mechanisms. This would be consistent with our finding that several independent proteins can sense L-arginine and contribute to the improved survival capacity. Future studies are needed to clarify the mechanism of how L-arginine affects the structure and functions of the identified sensors in vivo and how this translates into increased survival.

While in this study we addressed the response to elevated L-arginine levels, it is well established that T cells also sense L-arginine depletion, as it may occur in tumor microenvironments or when myeloid suppressor cells degrade L-arginine through ARG1 (Bronte and Zanovello, 2005). We have shown that moderately reduced uptake of L-arginine has a negative impact on T cell survival without affecting proliferation. However, when L-arginine was completely depleted from the culture medium, T cells no longer proliferated (data not shown and Rodriguez et al., 2007). Lack of L-arginine in T cells can be sensed by GCN2, leading to an amino acid starvation response (Rodriguez et al., 2007) and by SLC38A9, leading to inhibition of mTOR (Rebsamen et al., 2015; Wang et al., 2015), which in turn inhibits T cell growth and proliferation.

Our findings that T cells with increased L-arginine levels display improved anti-tumor activity may be due to a combination of phenotypic changes, including improved survival capacity, metabolic adaptations, and maintenance of a Tcm-like phenotype. L-arginine may also impact on other cell types in vivo, e.g., oral administration of L-arginine to healthy volunteers has been shown to enhance the numbers and activity of natural killer cells (Park et al., 1991). Future work is needed to address the exact mechanism by which L-arginine acts in vivo and favors memory T cell formation and anti-tumor responses.

Generally, metabolite levels can be influenced without genetic manipulations, offering the possibility for therapeutic applications. The beneficial effect of L-arginine on T cell survival and anti-tumor functionality may be exploited therapeutically, for instance to improve adoptive T cell therapies. Additionally, our dataset on the dynamics of the proteome and metabolome during the T cell response constitute a framework for future studies addressing the complex interplay between metabolism and cellular functions.

STAR★METHODS

Detailed methods are provided in the online version of this paper and include the following:

- KEY RESOURCES TABLE
- CONTACT FOR REAGENT AND RESOURCE SHARING
- EXPERIMENTAL MODEL AND SUBJECT DETAILS
  - Human Primary T Cells
  - Mice
- METHOD DETAILS
  - Isolation of Human T Cells
  - Cell Culture
  - Metabolomics
  - Metabolic Flux Experiments
  - Detection of Amino Acids and Polyamines by HILIC LC-MS/MS
  - Sample Preparation for Proteome MS Analysis
  - LC-MS/MS for Analysis of Proteome
  - Analysis of Proteomics Data
  - Limited Proteolysis and Mass Spectrometry
  - Quantitative Amino Acid Uptake and Calculation of Proteome Incorporation
  - ^{3}H-Arginine Uptake Assay

SUPPLEMENTAL INFORMATION

Supplemental Information includes six figures and six tables and can be found with this article online at http://dx.doi.org/10.1016/j.cell.2016.09.031.

AUTHOR CONTRIBUTIONS

R.G. conceived the project, designed and performed experiments, analyzed the data, and wrote the manuscript. T.W. designed and performed experiments and analyzed the data. J.R., R.G., and F.M. performed the proteomic experiments and analyzed the data. T.F., M.K., and N.Z. designed and performed metabolome and flux experiments and analyzed data. C.B. designed and performed mouse experiments. Y.F. and P.P. designed and performed limited proteolysis experiments. A.L., F.S., M.M., and N.Z. supervised the work and edited the manuscript.

ACKNOWLEDGMENTS

We thank Walter Reith, Isabelle Dunand-Sauthier, and Adria-Arnau Marti Lindez for providing the *Arg2*$^{-/-}$ mice, David Jarrossay for cell sorting, Luana Perlini for help with mouse experiments, Peter Mirtschink and Wilhelm Krek for providing access to the Seahorse analyzer, and members of the A.L., F.S., N.Z., and M.M. laboratories for discussions. This work was supported in part by the Swiss Vaccine Research Institute, the Swiss National Science Foundation (grant 149475 to A.L.), and the European Research Council (grant 323183 PREDICT to F.S.). R.G. was supported by a grant from the Swiss SystemsX.ch initiative, evaluated by the Swiss National Science Foundation. A.L. is supported by the Helmut Horten Foundation.

Received: February 3, 2016
Revised: March 18, 2016
Accepted: September 19, 2016
Published: October 13, 2016

REFERENCES

Alves, N.L., Derks, I.A., Berk, E., Spijker, R., van Lier, R.A., and Eldering, E. (2006). The Noxa/Mcl-1 axis regulates susceptibility to apoptosis under glucose limitation in dividing T cells. Immunity *24*, 703–716.

Araki, K., Turner, A.P., Shaffer, V.O., Gangappa, S., Keller, S.A., Bachmann, M.F., Larsen, C.P., and Ahmed, R. (2009). mTOR regulates memory CD8 T-cell differentiation. Nature *460*, 108–112.

Bellone, M., Cantarella, D., Castiglioni, P., Crosti, M.C., Ronchetti, A., Moro, M., Garancini, M.P., Casorati, G., and Dellabona, P. (2000). Relevance of the tumor antigen in the validation of three vaccination strategies for melanoma. J. Immunol. *165*, 2651–2656.

Bensimon, A., Heck, A.J., and Aebersold, R. (2012). Mass spectrometry-based proteomics and network biology. Annu. Rev. Biochem. *81*, 379–405.

Blagih, J., Coulombe, F., Vincent, E.E., Dupuy, F., Galicia-Vázquez, G., Yurchenko, E., Raissi, T.C., van der Windt, G.J., Viollet, B., Pearce, E.L., et al. (2015). The energy sensor AMPK regulates T cell metabolic adaptation and effector responses in vivo. Immunity *42*, 41–54.

Bronte, V., and Zanovello, P. (2005). Regulation of immune responses by L-arginine metabolism. Nat. Rev. Immunol. *5*, 641–654.

Carr, E.L., Kelman, A., Wu, G.S., Gopaul, R., Senkevitch, E., Aghvanyan, A., Turay, A.M., and Frauwirth, K.A. (2010). Glutamine uptake and metabolism are coordinately regulated by ERK/MAPK during T lymphocyte activation. J. Immunol. *185*, 1037–1044.

Chang, C.H., Curtis, J.D., Maggi, L.B., Jr., Faubert, B., Villarino, A.V., O'Sullivan, D., Huang, S.C., van der Windt, G.J., Blagih, J., Qiu, J., et al. (2013). Post-transcriptional control of T cell effector function by aerobic glycolysis. Cell *153*, 1239–1251.

Chang, C.H., Qiu, J., O'Sullivan, D., Buck, M.D., Noguchi, T., Curtis, J.D., Chen, Q., Gindin, M., Gubin, M.M., van der Windt, G.J., et al. (2015). Metabolic competition in the tumor microenvironment is a driver of cancer progression. Cell *162*, 1229–1241.

Cox, J., and Mann, M. (2008). MaxQuant enables high peptide identification rates, individualized p.p.b.-range mass accuracies and proteome-wide protein quantification. Nat. Biotechnol. *26*, 1367–1372.

Cox, J., and Mann, M. (2012). 1D and 2D annotation enrichment: a statistical method integrating quantitative proteomics with complementary high-throughput data. BMC Bioinformatics *13* (*Suppl 16*), S12.

Cox, J., Neuhauser, N., Michalski, A., Scheltema, R.A., Olsen, J.V., and Mann, M. (2011). Andromeda: a peptide search engine integrated into the MaxQuant environment. J. Proteome Res. *10*, 1794–1805.

Cui, G., Staron, M.M., Gray, S.M., Ho, P.C., Amezquita, R.A., Wu, J., and Kaech, S.M. (2015). IL-7-induced glycerol transport and TAG synthesis promotes memory CD8+ T cell longevity. Cell *161*, 750–761.

De Rosa, V., Galgani, M., Porcellini, A., Colamatteo, A., Santopaolo, M., Zuchegna, C., Romano, A., De Simone, S., Procaccini, C., La Rocca, C., et al. (2015). Glycolysis controls the induction of human regulatory T cells by modulating the expression of FOXP3 exon 2 splicing variants. Nat. Immunol. *16*, 1174–1184.

Feng, Y., De Franceschi, G., Kahraman, A., Soste, M., Melnik, A., Boersema, P.J., de Laureto, P.P., Nikolaev, Y., Oliveira, A.P., and Picotti, P. (2014). Global analysis of protein structural changes in complex proteomes. Nat. Biotechnol. *32*, 1036–1044.

Fox, C.J., Hammerman, P.S., and Thompson, C.B. (2005). Fuel feeds function: energy metabolism and the T-cell response. Nat. Rev. Immunol. *5*, 844–852.

Fuhrer, T., Heer, D., Begemann, B., and Zamboni, N. (2011). High-throughput, accurate mass metabolome profiling of cellular extracts by flow injection-time-of-flight mass spectrometry. Anal. Chem. *83*, 7074–7080.

Ganapathy, V., Daniels, T., and Casiano, C.A. (2003). LEDGF/p75: a novel nuclear autoantigen at the crossroads of cell survival and apoptosis. Autoimmun. Rev. *2*, 290–297.

Geoghegan, V., Guo, A., Trudgian, D., Thomas, B., and Acuto, O. (2015). Comprehensive identification of arginine methylation in primary T cells reveals regulatory roles in cell signalling. Nat. Commun. *6*, 6758.

Gett, A.V., Sallusto, F., Lanzavecchia, A., and Geginat, J. (2003). T cell fitness determined by signal strength. Nat. Immunol. *4*, 355–360.

Grohmann, U., and Bronte, V. (2010). Control of immune response by amino acid metabolism. Immunol. Rev. *236*, 243–264.

Ho, P.C., Bihuniak, J.D., Macintyre, A.N., Staron, M., Liu, X., Amezquita, R., Tsui, Y.C., Cui, G., Micevic, G., Perales, J.C., et al. (2015). Phosphoenolpyruvate is a metabolic checkpoint of anti-tumor T cell responses. Cell *162*, 1217–1228.

Hornburg, D., Drepper, C., Butter, F., Meissner, F., Sendtner, M., and Mann, M. (2014). Deep proteomic evaluation of primary and cell line motoneuron disease

models delineates major differences in neuronal characteristics. Mol. Cell. Proteomics *13*, 3410–3420.

Hubner, N.C., Ren, S., and Mann, M. (2008). Peptide separation with immobilized pI strips is an attractive alternative to in-gel protein digestion for proteome analysis. Proteomics *8*, 4862–4872.

Hubner, N.C., Bird, A.W., Cox, J., Splettstoesser, B., Bandilla, P., Poser, I., Hyman, A., and Mann, M. (2010). Quantitative proteomics combined with BAC TransgeneOmics reveals in vivo protein interactions. J. Cell Biol. *189*, 739–754.

Hulce, J.J., Cognetta, A.B., Niphakis, M.J., Tully, S.E., and Cravatt, B.F. (2013). Proteome-wide mapping of cholesterol-interacting proteins in mammalian cells. Nat. Methods *10*, 259–264.

Jaendling, A., and McFarlane, R.J. (2010). Biological roles of translin and translin-associated factor-X: RNA metabolism comes to the fore. Biochem. J. *429*, 225–234.

Kaech, S.M., and Cui, W. (2012). Transcriptional control of effector and memory CD8+ T cell differentiation. Nat. Rev. Immunol. *12*, 749–761.

Kirberg, J., Baron, A., Jakob, S., Rolink, A., Karjalainen, K., and von Boehmer, H. (1994). Thymic selection of CD8+ single positive cells with a class II major histocompatibility complex-restricted receptor. J. Exp. Med. *180*, 25–34.

Klebanoff, C.A., Gattinoni, L., Torabi-Parizi, P., Kerstann, K., Cardones, A.R., Finkelstein, S.E., Palmer, D.C., Antony, P.A., Hwang, S.T., Rosenberg, S.A., et al. (2005). Central memory self/tumor-reactive CD8+ T cells confer superior antitumor immunity compared with effector memory T cells. Proc. Natl. Acad. Sci. USA *102*, 9571–9576.

Koga, Y., Povalko, N., Nishioka, J., Katayama, K., Kakimoto, N., and Matsuishi, T. (2010). MELAS and L-arginine therapy: pathophysiology of stroke-like episodes. Ann. N Y Acad. Sci. *1201*, 104–110.

Lanzavecchia, A., and Scheidegger, D. (1987). The use of hybrid hybridomas to target human cytotoxic T lymphocytes. Eur. J. Immunol. *17*, 105–111.

Li, X., Gianoulis, T.A., Yip, K.Y., Gerstein, M., and Snyder, M. (2010). Extensive in vivo metabolite-protein interactions revealed by large-scale systematic analyses. Cell *143*, 639–650.

Link, H., Fuhrer, T., Gerosa, L., Zamboni, N., and Sauer, U. (2015). Real-time metabolome profiling of the metabolic switch between starvation and growth. Nat. Methods *12*, 1091–1097.

Luber, C.A., Cox, J., Lauterbach, H., Fancke, B., Selbach, M., Tschopp, J., Akira, S., Wiegand, M., Hochrein, H., O'Keeffe, M., and Mann, M. (2010). Quantitative proteomics reveals subset-specific viral recognition in dendritic cells. Immunity *32*, 279–289.

Mabalirajan, U., Ahmad, T., Leishangthem, G.D., Dinda, A.K., Agrawal, A., and Ghosh, B. (2010). L-arginine reduces mitochondrial dysfunction and airway injury in murine allergic airway inflammation. Int. Immunopharmacol. *10*, 1514–1519.

Maciver, N.J., Jacobs, S.R., Wieman, H.L., Wofford, J.A., Coloff, J.L., and Rathmell, J.C. (2008). Glucose metabolism in lymphocytes is a regulated process with significant effects on immune cell function and survival. J. Leukoc. Biol. *84*, 949–957.

MacIver, N.J., Michalek, R.D., and Rathmell, J.C. (2013). Metabolic regulation of T lymphocytes. Annu. Rev. Immunol. *31*, 259–283.

Malissen, M., Gillet, A., Ardouin, L., Bouvier, G., Trucy, J., Ferrier, P., Vivier, E., and Malissen, B. (1995). Altered T cell development in mice with a targeted mutation of the CD3-epsilon gene. EMBO J. *14*, 4641–4653.

Meissner, F., and Mann, M. (2014). Quantitative shotgun proteomics: considerations for a high-quality workflow in immunology. Nat. Immunol. *15*, 112–117.

Messi, M., Giacchetto, I., Nagata, K., Lanzavecchia, A., Natoli, G., and Sallusto, F. (2003). Memory and flexibility of cytokine gene expression as separable properties of human T(H)1 and T(H)2 lymphocytes. Nat. Immunol. *4*, 78–86.

Michalski, A., Damoc, E., Hauschild, J.P., Lange, O., Wieghaus, A., Makarov, A., Nagaraj, N., Cox, J., Mann, M., and Horning, S. (2011). Mass spectrometry-based proteomics using Q Exactive, a high-performance benchtop quadrupole Orbitrap mass spectrometer. Molecular & cellular proteomics : MCP *10*, M111 011015.

Monticelli, L.A., Buck, M.D., Flamar, A.L., Saenz, S.A., Tait Wojno, E.D., Yudanin, N.A., Osborne, L.C., Hepworth, M.R., Tran, S.V., Rodewald, H.R., et al. (2016). Arginase 1 is an innate lymphoid-cell-intrinsic metabolic checkpoint controlling type 2 inflammation. Nat. Immunol. *17*, 656–665.

Nagaraj, N., Wisniewski, J.R., Geiger, T., Cox, J., Kircher, M., Kelso, J., Pääbo, S., and Mann, M. (2011). Deep proteome and transcriptome mapping of a human cancer cell line. Mol. Syst. Biol. *7*, 548.

Olsen, J.V., Macek, B., Lange, O., Makarov, A., Horning, S., and Mann, M. (2007). Higher-energy C-trap dissociation for peptide modification analysis. Nat. Methods *4*, 709–712.

Ori, A., Banterle, N., Iskar, M., Andrés-Pons, A., Escher, C., Khanh Bui, H., Sparks, L., Solis-Mezarino, V., Rinner, O., Bork, P., et al. (2013). Cell type-specific nuclear pores: a case in point for context-dependent stoichiometry of molecular machines. Mol. Syst. Biol. *9*, 648.

Park, K.G., Hayes, P.D., Garlick, P.J., Sewell, H., and Eremin, O. (1991). Stimulation of lymphocyte natural cytotoxicity by L-arginine. Lancet *337*, 645–646.

Pearce, E.L., Walsh, M.C., Cejas, P.J., Harms, G.M., Shen, H., Wang, L.S., Jones, R.G., and Choi, Y. (2009). Enhancing CD8 T-cell memory by modulating fatty acid metabolism. Nature *460*, 103–107.

Pearce, E.L., Poffenberger, M.C., Chang, C.H., and Jones, R.G. (2013). Fueling immunity: insights into metabolism and lymphocyte function. Science *342*, 1242454.

Possemato, R., Marks, K.M., Shaul, Y.D., Pacold, M.E., Kim, D., Birsoy, K., Sethumadhavan, S., Woo, H.K., Jang, H.G., Jha, A.K., et al. (2011). Functional genomics reveal that the serine synthesis pathway is essential in breast cancer. Nature *476*, 346–350.

Rappsilber, J., Mann, M., and Ishihama, Y. (2007). Protocol for micro-purification, enrichment, pre-fractionation and storage of peptides for proteomics using StageTips. Nat. Protoc. *2*, 1896–1906.

Rebsamen, M., Pochini, L., Stasyk, T., de Araújo, M.E., Galluccio, M., Kandasamy, R.K., Snijder, B., Fauster, A., Rudashevskaya, E.L., Bruckner, M., et al. (2015). SLC38A9 is a component of the lysosomal amino acid sensing machinery that controls mTORC1. Nature *519*, 477–481.

Rodgers, J.T., Lerin, C., Haas, W., Gygi, S.P., Spiegelman, B.M., and Puigserver, P. (2005). Nutrient control of glucose homeostasis through a complex of PGC-1alpha and SIRT1. Nature *434*, 113–118.

Rodriguez, P.C., Quiceno, D.G., and Ochoa, A.C. (2007). L-arginine availability regulates T-lymphocyte cell-cycle progression. Blood *109*, 1568–1573.

Rolf, J., Zarrouk, M., Finlay, D.K., Foretz, M., Viollet, B., and Cantrell, D.A. (2013). AMPKα1: a glucose sensor that controls CD8 T-cell memory. Eur. J. Immunol. *43*, 889–896.

Sallusto, F., Lenig, D., Förster, R., Lipp, M., and Lanzavecchia, A. (1999). Two subsets of memory T lymphocytes with distinct homing potentials and effector functions. Nature *401*, 708–712.

Sallusto, F., Lanzavecchia, A., Araki, K., and Ahmed, R. (2010). From vaccines to memory and back. Immunity *33*, 451–463.

Sanjana, N.E., Shalem, O., and Zhang, F. (2014). Improved vectors and genome-wide libraries for CRISPR screening. Nat. Methods *11*, 783–784.

Scheltema, R.A., and Mann, M. (2012). SprayQc: a real-time LC-MS/MS quality monitoring system to maximize uptime using off the shelf components. J. Proteome Res. *11*, 3458–3466.

Schluns, K.S., and Lefrançois, L. (2003). Cytokine control of memory T-cell development and survival. Nat. Rev. Immunol. *3*, 269–279.

Shiow, L.R., Rosen, D.B., Brdicková, N., Xu, Y., An, J., Lanier, L.L., Cyster, J.G., and Matloubian, M. (2006). CD69 acts downstream of interferon-alpha/beta to inhibit S1P1 and lymphocyte egress from lymphoid organs. Nature *440*, 540–544.

Sinclair, L.V., Rolf, J., Emslie, E., Shi, Y.B., Taylor, P.M., and Cantrell, D.A. (2013). Control of amino-acid transport by antigen receptors coordinates the

metabolic reprogramming essential for T cell differentiation. Nat. Immunol. *14*, 500–508.

Siska, P.J., and Rathmell, J.C. (2015). T cell metabolic fitness in antitumor immunity. Trends Immunol. *36*, 257–264.

Subramanian, A., Tamayo, P., Mootha, V.K., Mukherjee, S., Ebert, B.L., Gillette, M.A., Paulovich, A., Pomeroy, S.L., Golub, T.R., Lander, E.S., and Mesirov, J.P. (2005). Gene set enrichment analysis: a knowledge-based approach for interpreting genome-wide expression profiles. Proc. Natl. Acad. Sci. USA *102*, 15545–15550.

Sukumar, M., Liu, J., Ji, Y., Subramanian, M., Crompton, J.G., Yu, Z., Roychoudhuri, R., Palmer, D.C., Muranski, P., Karoly, E.D., et al. (2013). Inhibiting glycolytic metabolism enhances CD8+ T cell memory and antitumor function. J. Clin. Invest. *123*, 4479–4488.

Surh, C.D., Boyman, O., Purton, J.F., and Sprent, J. (2006). Homeostasis of memory T cells. Immunol. Rev. *211*, 154–163.

Tannahill, G.M., Curtis, A.M., Adamik, J., Palsson-McDermott, E.M., McGettrick, A.F., Goel, G., Frezza, C., Bernard, N.J., Kelly, B., Foley, N.H., et al. (2013). Succinate is an inflammatory signal that induces IL-1β through HIF-1α. Nature *496*, 238–242.

Tissenbaum, H.A., and Guarente, L. (2001). Increased dosage of a sir-2 gene extends lifespan in Caenorhabditis elegans. Nature *410*, 227–230.

Tusher, V.G., Tibshirani, R., and Chu, G. (2001). Significance analysis of microarrays applied to the ionizing radiation response. Proc. Natl. Acad. Sci. USA *98*, 5116–5121.

van der Windt, G.J., Everts, B., Chang, C.H., Curtis, J.D., Freitas, T.C., Amiel, E., Pearce, E.J., and Pearce, E.L. (2012). Mitochondrial respiratory capacity is a critical regulator of CD8+ T cell memory development. Immunity *36*, 68–78.

Vander Heiden, M.G., Cantley, L.C., and Thompson, C.B. (2009). Understanding the Warburg effect: the metabolic requirements of cell proliferation. Science *324*, 1029–1033.

Wang, R., and Green, D.R. (2012). Metabolic checkpoints in activated T cells. Nat. Immunol. *13*, 907–915.

Wang, R., Dillon, C.P., Shi, L.Z., Milasta, S., Carter, R., Finkelstein, D., McCormick, L.L., Fitzgerald, P., Chi, H., Munger, J., and Green, D.R. (2011). The transcription factor Myc controls metabolic reprogramming upon T lymphocyte activation. Immunity *35*, 871–882.

Wang, S., Tsun, Z.Y., Wolfson, R.L., Shen, K., Wyant, G.A., Plovanich, M.E., Yuan, E.D., Jones, T.D., Chantranupong, L., Comb, W., et al. (2015). Metabolism. Lysosomal amino acid transporter SLC38A9 signals arginine sufficiency to mTORC1. Science *347*, 188–194.

Wiśniewski, J.R., Ostasiewicz, P., Duś, K., Zielińska, D.F., Gnad, F., and Mann, M. (2012). Extensive quantitative remodeling of the proteome between normal colon tissue and adenocarcinoma. Mol. Syst. Biol. *8*, 611.

Zamboni, N., Saghatelian, A., and Patti, G.J. (2015). Defining the metabolome: size, flux, and regulation. Mol. Cell *58*, 699–706.

Cell

STAR★METHODS

KEY RESOURCES TABLE

REAGENT or RESOURCE	SOURCE	IDENTIFIER
Antibodies		
Human CD4-APC (clone 13B8.2)	Beckman Coulter	Cat#IM2468; RRID: AB_130781
Human CD45RA-PE (clone ALB11)	Beckman Coulter	Cat#IM1834U
Human CCR7-BV421 (clone G043H7)	BioLegend	Cat#353208; RRID: AB_11203894
Human CCR7 (clone 15053)	R&D Systems	Cat#MAB197
Human CD25-FITC (clone B1.49.9)	Beckman Coulter	Cat#IM0478U; RRID: AB_130985
Human CD8-FITC (clone B9.11)	Beckman Coulter	Cat#A07756; RRID: AB_1575981
Human CD3 (clone TR66)	In house	Lanzavecchia and Scheidegger, 1987
Human CD28 (clone CD28.2)	BD Biosciences	Cat#555725; RRID: AB_396068
Human BAZ1B (WSTF) polyclonal	Abcam	Cat#AB50850; RRID: AB_870595
Human PSIP1 (LEDGF/p75) polyclonal	Bethyl laboratories	Cat#A300-848A
Human TSN polyclonal	Atlas antibodies/Sigma	Cat#HPA059561
Human PTPN6 (SH-PTP1, SHP-1) polyclonal	Santa Cruz	Cat#sc-287; RRID: AB_2173829
Human MHC-I (HLA-ABC) FITC (clone W6/32)	eBiosciences	Cat#11-9983-42
Human p70 S6 Kinase	Cell Signaling	Cat#9202; RRID: AB_331676
Human Phospho-p70 S6 Kinase (Thr389)	Cell Signaling	Cat#9205; RRID: AB_330944
Human 4E-BP1	Cell Signaling	Cat#9644; RRID: AB_2097841
Human Phospho-4EBP1 (Thr37/46)	Cell Signaling	Cat#2855; RRID: AB_560835
Anti-mouse CD4, Pacific Orange (clone RM4-5)	Invitrogen	Cat#MCD0430
Anti-mouse CD8a, Pacific Blue (clone 53-6.7)	Biolegend	Cat#100725; RRID: AB_493425
Anti-mouse/human CD44, APC/Cy7 (clone IM7)	Biolegend	Cat#103028; RRID: AB_830785
Anti-mouse/human CD44, FITC (clone IM7)	Biolegend	Cat#103022; RRID: AB_493685
Anti-mouse/human CD44, APC (clone IM7)	Biolegend	Cat#103012; RRID: AB_312963
Anti-mouse CD62L, PE/Cy7 (clone MEL-14)	Biolegend	Cat#104418; RRID: AB_313103
Anti-mouse 90.1, APC/Cy7 (clone OX-7)	Biolegend	Cat#202520; RRID: AB_2303153
LEAF purified anti-mouse CD3ε (clone 145-2C11)	Biolegend	Cat#100331; RRID: AB_1877073
Purified hamster anti-mouse CD28 (clone37.51)	BD Biosciences	Cat#553295; RRID: AB_394764
Chemicals, Peptides, and Recombinant Proteins		
L-arginine	Sigma	Cat#A5006
L-arginine monohydrochloride	Sigma	Cat#A4599
D-arginine	Sigma	Cat#A2646
L-Arginine-13C6 hydrochloride	Sigma	Cat#643440
L-[2,3,4-^{3}H]-arginine-monohydrochloride	Perkin Elmer	Cat#NET1123001MC
Annexin-V-FITC	Biolegend	Cat#640906
Cell-Tak	BD Biosciences	Cat#354240
Oligomycin	Sigma	Cat#75351
Carbonyl cyanide-4-(trifluoromethoxy) phenylhydrazone (FCCP)	Sigma	Cat#C2920
Antimycin	Sigma	Cat#A8674
Recombinant human interleukin-2	BD Biosciences	Cat#554603
Recombinant human interleukin-12	Biolegend	Cat#573002
Human recombinant interleukin-2 (transfected J588L cell supernatant)	In house	N/A
FlowCytomix basic kit	eBioscience	Cat#BMS8420FF
Flow Cytomix human Th1/Th2/Th9/Th17/Th22 13plex	eBioscience	Cat#BMS817FF

(*Continued on next page*)

Cell

Continued		
REAGENT or RESOURCE	SOURCE	IDENTIFIER
Phorbol 12-myristate 13-acetate (PMA)	Sigma	Cat#P1585
Ionomycin	Sigma	Cat#I0634
Rapamycin	Sigma	Cat#R8781
Proteinase K	Sigma	Cat#P2308
Critical Commercial Assays		
Glucose (GO) Assay Kit	Sigma	Cat#GAGO20-1KT
Experimental Models: Cell Lines		
Human: primary T lymphocytes	This paper	N/A
Mouse: primary T lymphocytes	This paper	N/A
HEK293T/17	ATCC	Cat#CRL-11268
B16.OVA	Matteo Bellone	Bellone et al., 2000
Experimental Models: Organisms/Strains		
Mouse: C57BL/6: (C57BL/6JOlaHsd)	Harlan	Cat#57
Mouse: BALB/c: (BALB/cOlaHsd)	Harlan	Cat#162
Mouse: *Cd3e*$^{-/-}$ C57BL/6	Malissen et al., 1995	N/A
Mouse: OT-I: (C57BL/6-Tg(TcraTcrb)1100Mjb/J)	The Jackson Laboratory	Cat#JAX003831
Mouse: *Rag1*$^{-/-}$: (B6.129S7-*Rag1*^{tm1Mom}/J)	The Jackson Laboratory	Cat#JAX002216
Mouse: *Arg2*$^{-/-}$: C57BL/6 (*Arg2*^{tm1Weo}/J)	The Jackson Laboratory	Cat#JAX020286
Mouse: Hemagglutinin (HA) TCR-transgenic (6.5) BALB/c	Kirberg et al., 1994	N/A
Recombinant DNA		
lentiCRISPR v2	Addgene	Cat#52961
psPAX	Addgene	Cat#12260
pMD2.G	Addgene	Cat#12259
Sequence-Based Reagents		
Short guide RNAs, see Table S6	This paper	N/A
Software and Algorithms		
MaxQuant	Cox and Mann, 2008	http://www.coxdocs.org/doku.php?id=maxquant:start
Perseus	Cox and Mann, 2012	http://www.coxdocs.org/doku.php?id=perseus:start
Progenesis-QI Version 2.0	Nonlinear Dynamics, Waters	http://www.nonlinear.com/progenesis/qi/
Proteome Discoverer 1.4 (SEQUEST HT search engine)	Thermo Fisher	https://www.thermofisher.com/order/catalog/product/IQLAAEGABSFAKJMAUH
R environment for statistical computing	N/A	https://www.r-project.org/

CONTACT FOR REAGENT AND RESOURCE SHARING

Further information and requests for reagents may be directed to, and will be fulfilled by the corresponding author Antonio Lanzavecchia (lanzavecchia@irb.usi.ch).

EXPERIMENTAL MODEL AND SUBJECT DETAILS

Human Primary T Cells

Blood from healthy male or female donors was obtained from the Swiss Blood Donation Center of Basel and Lugano, and used in compliance with the Federal Office of Public Health (authorization no. A000197/2 to F.S).

Mice

Wild-type (WT) C57BL/6J and BALB/c mice were obtained from Harlan (Italy). *Cd3e*$^{-/-}$ C57BL/6 mice, which lack all T cells but exhibit organized lymphoid organ structures and normal B cell development, have been described previously (Malissen et al., 1995). OT-I

(JAX 003831) mice were bred and maintained on a *Rag1*$^{-/-}$ (JAX 002216) background. WT C57BL/6 mice with different CD45 and CD90 alleles were bred in our facility, and crossed with *Rag1*$^{-/-}$ OT-I transgenic mice, to perform adoptive transfer experiments. *Arg2*$^{-/-}$ C57BL/6 (JAX 020286) mice were kindly provided by W. Reith. Hemagglutinin (HA) TCR-transgenic (6.5) BALB/c mice (Kirberg et al., 1994) specific for peptide 111-119 from influenza HA were kindly provided by J. Kirberg and bred in our facility. All mice were bred and maintained under specific pathogen-free conditions. Animals were treated in accordance with guidelines of the Swiss Federal Veterinary Office and experiments were approved by the Dipartimento della Sanità e Socialità of Canton Ticino.

METHOD DETAILS

Isolation of Human T Cells

Peripheral blood mononuclear cells (PBMCs) were isolated by Ficoll gradient centrifugation. CD4$^+$ T cells were enriched with magnetic microbeads (Miltenyi Biotec). Naive CD4$^+$ T cells were sorted as CD4$^+$ CCR7$^+$ CD45RA$^+$ CD25$^-$ CD8$^-$ on a FACS Aria III cell sorter (BD Biosciences). For cell staining, the following antibodies were used: anti-CD4-APC (allophycocyanin), clone 13B8.2; anti-CD8-APC, clone B9.11; anti-CD8-FITC (fluorescein isothiocyanate), clone B9.11; anti-CD4-FITC, clone 13B8.2; anti-CD45RA-PE (phycoerythrin), clone alb11; anti-CD25-FITC, clone B1.49.9 (all from Beckman Coulter); anti-CCR7-Brilliant Violet 421, clone G043H7 (Biolegend).

Cell Culture

Cells were cultured in RPMI-1640 medium supplemented with 2mM glutamine, 1% (v/v) non-essential amino acids, 1% (v/v) sodium pyruvate, penicillin (50 U ml^{-1}), streptomycin (50 μg ml^{-1}; all from Invitrogen), and 5% (v/v) human serum (Swiss Blood Center). Human T cells were activated with plate bound anti-CD3 (5 μg/ ml, clone TR66) and anti-CD28 (1 μg/ml, clone CD28.2, BD Biosciences) for 48 hr. Then, cells were cultured in IL-2 containing media (500 U/ml).

Metabolomics

Naive CD4$^+$ T cells were either analyzed directly after isolation or at different time points after activation with CD3 and CD28 antibodies. Cells were washed twice in 96-well plates with 75 mM ammonium carbonate at pH 7.4 and snap frozen in liquid nitrogen. Metabolites were extracted three times with hot (> 70°C) 70% ethanol. Extracts were analyzed by flow injection – time of flight mass spectrometry on an Agilent 6550 QTOF instrument operated in the negative mode, as described previously (Fuhrer et al., 2011). Typically 5,000-12,000 ions with distinct mass-to-charge (m/z) ratio could be identified in each batch of samples. Ions were putatively annotated by matching their measured mass to that of the compounds listed by the KEGG database for *Homo sapiens*, allowing a tolerance of 0.001 Da. Only deprotonated ions (without adducts) were considered in the analysis. In case of multiple matching, such as in the case of structural isomers, all candidates were retained.

Metabolic Flux Experiments

Naive CD4$^+$ T cells were activated and 4 days later extensively washed and pulsed with L-arginine free RPMI medium containing 1 mM [U-^{13}C]-L-Arginine hydrochloride (Sigma). After increasing pulse-times, cells were washed and snap frozen in liquid nitrogen. Metabolites were extracted and analyzed by HILIC LC-MS/MS.

Detection of Amino Acids and Polyamines by HILIC LC-MS/MS

Supernatants from extraction were dried at 0.12 mbar to complete dryness in a rotational vacuum concentrator setup (Christ, Osterode am Harz, Germany) and dried metabolite extracts were stored at −80°C. Dry metabolite extracts were resuspended in 100 μl water and 5 μl were injected on an Agilent HILIC Plus RRHD column (100 × 2.1mm × 1.8 μm; Agilent, Santa Clara, CA, USA). A gradient of mobile phase A (10 mM ammonium formate and 0.1% formic acid) and mobile phase B (acetonitrile with 0.1% formic acid) was used as described previously (Link et al., 2015). Flow rate was held constant at 400 μl/min and metabolites were detected on a 5500 QTRAP triple quadrupole mass spectrometer in positive MRM scan mode (SCIEX, Framingham, MA, USA).

Sample Preparation for Proteome MS Analysis

Samples were processed as described by (Hornburg et al., 2014). In brief, cell pellets were washed with PBS and lysed in 4% SDS, 10 mM HEPES (pH 8), 10 mM DTT. Cell pellets were heat-treated at 95°C for 10 min and sonicated at 4°C for 15 min (level 5, Bioruptor, Diagenode). Alkylation was performed in the dark for 30 min by adding 55 mM iodoacetamide (IAA). Proteins were precipitated overnight with acetone at −20°C and resuspended the next day in 8 M Urea, 10 mM HEPES (pH 8). A two-step proteolytic digestion was performed. First, samples were digested at room temperature (RT) with LysC (1:50, w/w) for 3h. Then, they were diluted 1:5 with 50 mM ammoniumbicarbonate (pH 8) and digested with trypsin (1:50, w/w) at RT overnight. The resulting peptide mixtures were acidified and loaded on C18 StageTips (Rappsilber et al., 2007). Peptides were eluted with 80% acetonitrile (ACN), dried using a SpeedVac centrifuge (Eppendorf, Concentrator plus, 5305 000.304), and resuspended in 2% ACN, 0.1% trifluoroacetic acid (TFA), and 0.5% acetic acid. For deeper proteome analysis a peptide library was built. For this, peptides from naive and activated T cells were separated according to their isoelectric point on dried gel strips with an immobilized pH gradient (SERVA IPG BlueStrips, 3-10 / 11 cm) into 12 fractions as described by Hubner et al., 2008 (Hubner et al., 2008).

Cell

LC-MS/MS for Analysis of Proteome

Peptides were separated on an EASY-nLC 1000 HPLC system (Thermo Fisher Scientific, Odense) coupled online to a Q Exactive mass spectrometer via a nanoelectrospray source (Thermo Fisher Scientific)(Michalski et al., 2011). Peptides were loaded in buffer A (0.5% formic acid) on in house packed columns (75 μm inner diameter, 50 cm length, and 1.9 μm C18 particles from Dr. Maisch GmbH). Peptides were eluted with a non-linear 270 min gradient of 5%–60% buffer B (80% ACN, 0.5% formic acid) at a flow rate of 250 nl/min and a column temperature of 50°C. Operational parameters were real-time monitored by the SprayQC software (Scheltema and Mann, 2012). The Q Exactive was operated in a data dependent mode with a survey scan range of 300-1750 m/z and a resolution of 70'000 at m/z 200. Up to 5 most abundant isotope patterns with a charge $\geq$ 2 were isolated with a 2.2 Th wide isolation window and subjected to higher-energy C-trap dissociation (HCD) fragmentation at a normalized collision energy of 25 (Olsen et al., 2007). Fragmentation spectra were acquired with a resolution of 17,500 at m/z 200. Dynamic exclusion of sequenced peptides was set to 45 s to reduce the number of repeated sequences. Thresholds for the ion injection time and ion target values were set to 20 ms and 3E6 for the survey scans and 120 ms and 1E5 for the MS/MS scans, respectively. Data were acquired using the Xcalibur software (Thermo Scientific).

Analysis of Proteomics Data

MaxQuant software (version 1.3.10.18) was used to analyze MS raw files (Cox and Mann, 2008). MS/MS spectra were searched against the human Uniprot FASTA database (Version May 2013, 88'847 entries) and a common contaminants database (247 entries) by the Andromeda search engine (Cox et al., 2011). Cysteine carbamidomethylation was applied as fixed and N-terminal acetylation and methionine oxidation as variable modification. Enzyme specificity was set to trypsin with a maximum of 2 missed cleavages and a minimum peptide length of 7 amino acids. A false discovery rate (FDR) of 1% was required for peptides and proteins. Peptide identification was performed with an allowed initial precursor mass deviation of up to 7 ppm and an allowed fragment mass deviation of 20 ppm. Nonlinear retention time alignment of all measured samples was performed in MaxQuant. Peptide identifications were matched across different replicates within a time window of 1 min of the aligned retention times. A library for 'match between runs' in MaxQuant was built from additional single shot analysis at various time points as well as from OFF gel fractionated peptides of naive and memory CD4 T cells. Protein identification required at least 1 razor peptide. A minimum ratio count of 1 was required for valid quantification events via MaxQuant's Label Free Quantification algorithm (MaxLFQ)(Cox and Mann, 2008; Luber et al., 2010). Data were filtered for common contaminants and peptides only identified by side modification were excluded from further analysis. In addition, it was required to have a minimum of two valid quantifications values in at least one group of replicates. Copy numbers were estimated based on the protein mass of cells (Wiśniewski et al., 2012). We set the protein mass of a naive T cell to 25 pg and of an activated T cell to 75 pg.

Limited Proteolysis and Mass Spectrometry

Naive $CD4^+$ T cells were washed twice with PBS and homogenized on ice under non-denaturing conditions (20 mM HEPES, 150 mM KCl and 10 mM $MgCl_2$ [pH 7.5]) using a tissue grinder (Wheaton, Millville, NJ, NSA). Homogenates were further passed several times through a syringe (0.45x12mm) on ice. Next, cell debris was removed by centrifugation and protein concentration of supernatants was determined by BCA assay (BCA Protein Assay Kit, Thermo Scientific, Rockford, IL, USA). L-arginine, D-arginine or L-ornithine was added to homogenates to a final concentration of 1 nmol per μg total protein, and incubated for 5 min at room temperature. As a control, samples without added metabolites were processed in parallel. Then, proteinase K from *Tritirachium album* (Sigma) was added at an enzyme to substrate ratio of 1:100, followed by an incubation of 5 min at room temperature. The digestion was stopped by boiling the reaction mixture for 3 min. Proteins were denatured by adding 10% sodium deoxycholate (DOC) solution (1:1, v/v) to the reaction mixture, followed by a second boiling step of 3 min. Disulfide bridges were reduced with 5 mM Tris(2-carboxyethyl)phosphine hydrochloride (Thermo Scientific) at 37°C for 30 min and subsequently free cysteines were alkylated with 40 mM IAA at 25°C for 30 min in the dark. DOC concentration of the mixture was diluted to 1% with 0.1 M ammonium bicarbonate (AmBiC) prior to a stepwise protein digestion with LysC (1:100, w/w) for 4 hr at 37°C and trypsin (1:100, w/w) overnight at 37°C. The resulting peptide mixture was acidified to pH < 2, loaded onto Sep-Pak tC18 cartridges (Waters, Milford, MA, USA), desalted and eluted with 80% acetonitrile. Peptide samples were dried using a vacuum centrifuge and resuspended in 0.1% formic acid for analysis by mass spectrometry.

Peptides were separated using an online EASY-nLC 1000 HPLC system (Thermo Fisher Scientific) operated with a 50 cm long in house packed reversed-phase analytical column (Reprosil Pur C18 Aq, Dr. Maisch, 1.9 μm) (Reprosil Pur C18 Aq, Dr. Maisch, 1.9 μm) before being measured on a Q-Exactive Plus (QE+) mass spectrometer. A linear gradient from 5%–25% acetonitrile in 240 min at a flowrate of 300 nl/min was used to elute the peptides from the column. Precursor ion scans were measured at a resolution of 70,000 at 200 m/z and 20 MS/MS spectra were acquired after higher-energy collision induced dissociation (HCD) in the Orbitrap at a resolution of 17,500 at 200 m/z per scan. The ion count threshold was set at 1,00 to trigger MS/MS, with a dynamic exclusion of 25 s. Raw data were searched against the *H. sapiens* Uniprot database using SEQUEST embedded in the Proteome Discoverer software (both Thermo Fisher Scientific). Digestion enzyme was set to trypsin, allowing up to two missed cleavages, one non-tryptic terminus and no cleavages at KP (lysine-proline) and RP (arginine-proline) sites. Precursor and fragment mass tolerance was set at 10 ppm and 0.02 Da, respectively. Carbamidomethylation of cysteines (+57.021 Da) was set as static modification whereas oxidation

(+15.995 Da) of methionine was set as dynamic modification. False discovery rate (FDR) was estimated by the Percolator (embedded in Proteome Discoverer) and the filtering threshold was set to 1%.

Label-free quantitation was performed using the Progenesis-QI Software (Nonlinear Dynamics, Waters). Raw data files were imported directly into Progenesis for analysis. MS1 feature identification was achieved by importing the filtered search results (as described above) from Proteome Discoverer into Progenesis to map the corresponding peptides based on their m/z and retention times. Annotated peptides were then quantified using the areas under their extracted ion chromatograms. Pairwise comparisons were performed with the untreated (no metabolite added) sample as a reference and peptide fold changes were calculated using three biological replicates per condition where the statistical significance was assessed with a two-tailed heteroscedastic Student's t test. A fold change was considered significant with an absolute change > 5 and a corresponding p value < 0.05. Only proteins with two or more peptides changing significantly (according to the aforementioned criteria) were taken into consideration.

Quantitative Amino Acid Uptake and Calculation of Proteome Incorporation

150,000 freshly isolated naive $CD4^+$ T cells were activated with plate bound CD3 and CD28 antibodies and cultured in the same medium for four days. As a control, medium without cells was co-cultured. Then cell supernatants and control media were analyzed by quantitative amino acid analysis (MassTrak, Waters) at the Functional Genomic Center in Zurich. Amino acid uptake was calculated as the difference between control media and cell supernatants. At the time of the measurement, we counted on average 1 Mio cells. We then calculated how much of each amino acid is incorporated into the proteome of 850,000 cells based on the amino acid sequences and copy numbers of each protein. Average copy numbers from the time point 72 hr were used.

^{3}H-Arginine Uptake Assay

Arginine uptake was measured as previously described for glutamine uptake (Carr et al., 2010). Briefly, resting or activated T cells were resuspended at a concentration of 1.5×10^7 cells/ml in serum-free RPMI 1640 lacking L-arginine. 50 μl 8% sucrose/20% perchloric acid were layered to the bottom of a 0.5 ml Eppendorf tube and 200 μl 1-bromododecane on top of it (middle layer), followed by 50 μl L-arginine-free medium containing 1.5 mCi L-[2,3,4-^{3}H]-arginine-monohydrochloride (Perkin Elmer). Then, 100 μl cell suspension was added to the top layer and cells were allowed to take up radiolabeled L-arginine for 15 min at room temperature. Cells were then spun through the bromododecane into the acid/sucrose. This stops the reaction and separates cells from unincorporated ^{3}H-L-arginine. The bottom layer containing the cells was carefully removed and analyzed by liquid scintillation. As controls cell-free media were used.

OCR Measurements

Measurements were performed using a Seahorse XF-24 extracellular flux analyzer (Seahorse Bioscience). Naive $CD4^+$ T cells were sorted and activated with plate-bound CD3 and CD28 antibodies in complete medium or medium supplemented with 3 mM L-arginine. Four days later (in the morning), cells were pooled, carefully count and plated (7×10^5 cells/well) in serum-free unbuffered RPMI-1640 medium (Sigma) onto Seahorse cell plates coated with Cell-Tak (BD Bioscience). The serum-free unbuffered medium was not supplemented with L-arginine. Oligomycin (1.4 μM, Sigma), Carbonyl cyanide-*4*-(trifluoromethoxy)phenylhydrazone (FCCP, 0.6 μM, Sigma) and antimycin (1.4 μM, Sigma) were injected.

IL-2 Withdrawal Assay

Naive CD4 T cells were activated with plate-bound CD3 and CD28 antibodies. 48 hr after activation IL-2 was added to culture media (500 U ml^{-1}). After a further 3 days of culturing, cells were washed, counted, and equal cell numbers were plated in medium devoid of IL-2. The withdrawal medium was no longer supplemented with e.g., L-arginine. Cell viability was assessed with annexin V.

Cytokine Analysis

10^5 naive T cells were stimulated with plate bound anti-CD3 (5μg/ml^{-1}) and anti-CD28 (1μg/ml^{-1}) in the presence of IL-12 (10 ng/ml, R&D Systems) to polarize cells toward a Th1 phenotype. After 48 hr, cells were transferred into U-bottom plates and IL-2 (10 ng/ml, R&D Systems) was added. Three days later, supernatants were collected and interferon-γ was quantified using FlowCytomix assays (eBioscience). Samples were analyzed on a BD LSR Fortessa FACS instrument and quantification was performed with the FlowCytomix Pro 3.0 software. For re-stimulation, cells were cultured for 5 hr in the presence of 0.2 μM phorbol 12-myristate 13-acetate (PMA) and 1 μg/ml ionomycin (both from Sigma).

Glucose Consumption Assay

The amount of glucose in media was determined using the Glucose (GO) Assay Kit from Sigma. Consumption was calculated as the difference between glucose content in reference medium (co-incubated medium without cells) and cell supernatants.

Analysis of Phosphorylation Levels of 4E-BP and S6K1

Naive $CD4^+$ T cells were activated with plate-bound antibodies to CD3 and CD28. Four days after activation, cells were lysed and analyzed by western blot with the following antibodies obtained from Cell Signaling Technology. Phospho-p70 S6K(Thr389) #9205; p70 S6 Kinase #9202; Phospho-4E-BP1 (Thr37/46) #2855; 4E-BP1 #9644. Rapamycin (Sigma) was used at 100 nM.

Cell

CRISPR/Cas9-Mediated Gene Disruption

Two to four short guide RNAs (sgRNAs) per gene (Table S6) were designed using the online tool provided by the Zhang laboratory (http://tools.genome-engineering.org). Oligonucleotide pairs with BsmBI-compatible overhangs were annealed and cloned into the lentiviral vector lentiCRISPR v2 (Addgene plasmid # 52961) (Sanjana et al., 2014). For virus production, HEK293T/17 cells were transfected with lentiCRISPR v2, psPAX2 (Addgene # 12260) and pMD2.G (Addgene plasmid # 12259) at a 8:4:1 ratio using polyethylenimine and cultured in Dulbecco's modified Eagle medium supplemented with 10% fetal bovine serum (FBS), 1% sodium pyruvate, 1% non-essential amino acids, 1% kanamycin, 50 units/ml penicilin/streptomycin and 50 μM β-mercaptoethanol. The medium was replaced 12 hr after transfection and after a further 48 hr virus was harvested from supernatant. Cell debris was removed by centrifugation (10 min at 2000 rpm followed) followed by ultra-centrifugation (2.5 hr at 24'000 rpm) through a sucrose cushion.

Freshly isolated naive $CD4^+$ T cells were lentivirally transduced and activated with plate-bound CD3 and CD28 antibodies. 48 hr after activation IL-2 was added to culture media (500 U/ml^{-1}). 6 days after activation, cells were cultured for 2 days in medium supplemented with 1 μg/ml puromycin to select for cells expressing the lentiCRISPR v2 vector. Subsequently, cells were cultured in normal medium followed by additional two days in medium containing puromycin for a second selection step. Then, single cell clones were generated by limiting dilution as described in (Messi et al., 2003).

To screen for clones with disrupted target genes, individual clones were lysed with sample buffer containing 80 mM Tris (pH 6.8), 10.5% glycerol, 2% SDS and 0.00004% Bromophenol blue. Lysate of 100'000 cells was separated by SDS-PAGE followed, blotted onto PVDF membranes and analyzed with antibodies to target proteins, Baz1B (Abcam, ab50850), PSIP1 (Bethyl, A300-848A), DDX17 (Abcam, ab180190), PTPN6 (Santa Cruz, sc-287) or TSN (Sigma, HPA059561). As loading control membranes were reprobed with an antibody to beta-tubulin (Sigma, T6074). To screen for clones with disrupted *B2M*, single cell clones were stained with an antibody to MHC-I (eBioscience, HLA-ABC-FITC) and analyzed by flow cytometry.

Isolation and Culturing of Mouse $CD8^+$ T Cells

Naive $CD8^+$ OT-I cells were isolated from *Rag1*$^{-/-}$ OT-I transgenic mice. Lymph nodes and spleens were harvested and homogenized using the rubber end of a syringe and cell suspensions were filtered through a fine mesh. Cells were first enriched with anti-CD8 magnetic microbeads (CD8a, Ly-2 microbeads, mouse, Miltenyi Biotec) and then sorted on a FACSAria III Cell Sorter (BD Biosciences) to obtain cells with a $CD44^{lo}$ $CD62L^{hi}$ $CD8^+$ phenotype. OT-I cells ($CD90.1^+$) were cultured for 2 days in αCD3/αCD28 (2μg/ml) bound to NUNC 96 well MicroWell MaxiSorp plates (Sigma-Aldrich M9410) in the presence or absence of 3 mM L-arginine in the culture medium. On day 2 cells were transferred to U-bottom plates and cultured for 2 additional days in the presence of IL-2 (500 U/ml).

Adoptive T Cell Transfers and Survival Experiments

$CD90.1^+$ $CD45.1/2^+$ OT-I T cells were activated with plate-bound antibodies to CD3 and CD28 in control medium. OT-I cells with a different congenic marker ($CD90.1^+$ $CD45.1^+$) were activated in L-arginine-supplemented medium. At day 4, equal cell numbers were injected into the tail vein of *Cd3e*$^{-/-}$ host mice. To study the expansion of OT-I effector cells, host mice were sacrificed after 1, 3, 6, and 10 days post transfer and $CD90.1^+$ OT-I T cells from lymphoid organs (spleen and lymph nodes) were enriched with anti-CD90.1 microbeads (Miltenyi Biotec), stained and analyzed by FACS. The following monoclonal antibodies were used α-CD8α (53-6.7), α-CD44 (IM7), α-CD62L (MEL-14), α-CD90.1 (OX-7), α-CD90.2 (30-H12), α-CD45.1 (A20), α-CD45.2 (104).

Tumor Experiments: In Vitro Activation of T Cells

B16-OVA melanoma cells were cultured in RPMI 1640 plus 10% FCS, 1% penicillin/streptomycin and 2 mM glutamine. Before injection into mice, cells were trypsinized and washed twice in PBS. Then, $5x10^5$ cells were subcutaneously injected in the dorsal region of WT C57BL/6 mice. Ten days post injection, $5x10^6$ OT-I cells, that have been activated in vitro as described above, were injected into the tail vein of tumor-bearing mice. The size of tumors was measured in a blinded fashion using calipers.

Tumor Experiments: In Vivo Priming of T Cells

B16-OVA melanoma cells were cultured and injected into WT C57BL/6 mice as described above. Five days post injection, when tumors were very small, mice were γ-irradiated (5 Gy) and 24 hr later they received $4x10^5$ OT-I cells intravenously (i.v.). The day after mice were immunized intraperitoneally (i.p.) with SIINFEKL peptide ($OVA_{257-264}$) in Imject Alum Adjuvant (Thermo Fisher Scientific). L-Arg (1.5 g/Kg body weight) or PBS, as control, was daily orally administrated, starting one day before T cell transfer and until the end of the experiment. The size of tumors was measured in a blinded fashion using calipers.

Experiments with *Arg2*$^{-/-}$ Mouse T Cells

For in vitro experiments, $5x10^4$ FACS-sorted naive T cells were activated with plate-bound antibodies to CD3 (2 μg/ml) and CD28 (2 μg/ml). Two days after activation, T cells were transferred into U-bottom plates and IL-2 was added to culture media. Four days after activation, cells were washed extensively and plated in medium devoid of IL-2. Cell viability was measured two days after IL-2 withdrawal by Annexin V staining. For in vivo experiments, 10^6 FACS-sorted WT $CD8^+$ naive T cells ($CD45.1^+$) were transferred together with 10^6 FACS-sorted *Arg2*$^{-/-}$ $CD8^+$ naive T cells ($CD45.2^+$, $CD90.2^+$), into slightly γ-irradiated (3 Gy) WT mice ($CD45.2^+$, $CD90.1^+$). The day after, host mice were immunized subcutaneously (s.c.) with MHC class-I binding peptide SIINFEKL (Chicken Ovalbumin, OVA, amino acids 257-264, 15 μg/mouse) emulsified in Complete Freund's Adjuvant, CFA. CFA was prepared by adding

Cell

4 mg/ml of *M. tuberculosis* H37RA (Difco) to Incomplete Freund's Adjuvant, IFA (BD Biosciences). SIINFEKL peptide ($OVA_{257-264}$) was obtained from Servei de Proteòmica, Pompeu Fabra University, Barcelona, Spain. On day 15 post immunization, mice were euthanized and draining lymph nodes were collected and analyzed by flow cytometry. Cells were counted according to the expression of congenic markers and by gating on live $CD44^{hi}$, H-2Kb/$OVA_{257-264}$ $multimer^{+}$, $CD8^{+}$ cells. The H-2Kb/$OVA_{257-264}$ multimers were purchased from TCMetrix.

Mouse Experiments with Dietary L-Arginine

$2x10^5$ $CD90.1^{+}$ $CD4^{+}$ HA TCR-transgenic T cells, on a BALB/c background, were adoptively transferred in WT $CD90.2^{+}$ BALB/c mice. The day after, host mice were immunized s.c. with influenza $HA_{110-119}$ peptide (purchased from Anaspec) emulsified in CFA. L-Arg (1.5 g/kg body weight) or PBS, as control, was daily orally administrated, starting 1 day before T cell transfer and until the end of the experiment. Draining lymph nodes were analyzed on day 15 post immunization for the presence of transferred transgenic memory $CD44^{hi}$ $CD90.1^{+}$ $CD4^{+}$ T cells. Sera were collected 30 min after oral L-arginine administration to mice and L-arginine and L-threonine concentrations in sera were measured on a MassTrak (Waters) instrument at the functional genomics center in Zurich. To determine intracellular L-arginine levels, activated T cells were isolated from draining lymph nodes 60 hr after activation and 30 min after the daily L-arginine administration. Metabolites were extracted with hot 70% ethanol and analyzed by HILIC LC-MS/MS.

QUANTIFICATION AND STATISTICAL ANALYSIS

Statistical parameters including the exact value of n, the definition of center, dispersion and precision measures (mean ± SEM) and statistical significance are reported in the Figures and Figure Legends. Data were judged to be statistically significant when $p < 0.05$ by two-tailed Student's t test. In figures, asterisks denote statistical significance as calculated by Student's t test (*, $p < 0.05$; **, $p < 0.01$; ***, $p < 0.001$; ****, $p < 0.0001$). Survival significance in adoptive cell transfer studies was determined by a Log-rank test. Statistical analysis was performed in R or GraphPad PRISM 6.

Proteome Data

Data analysis was performed using the Perseus software and the R statistical computing environment. Missing values were imputed with a normal distribution of 30% in comparison to the SD of measured values and a 1.8 SD down-shift of the mean to simulate the distribution of low signal values (Hubner et al., 2010). Statistical significance between time points was evaluated by one-way ANOVA for each proteinGroup using a FDR of 0.1% and S_0 of 2 (S_0 sets a threshold for minimum fold change), unless otherwise noted (Tusher et al., 2001). For pairwise comparison, t test statistic was applied with a permutation based FDR of 5% and S_0 of 1.

Enrichment Analysis

Univariate test was performed on either all proteins or metabolites by t test with unequal variance (Welch Test). The resulting *P*-values were adjusted using the Benjamini-Hochberg procedure. Enrichment analysis was performed as suggested by Subramanian et al. (Subramanian et al., 2005). Both for metabolomics and proteomics data, we applied a permissive filtering with adj. p value less or equal than 0.1 and absolute log2(fold-change) larger or equal than 0.5. Enrichment *P*-values were calculated by the Fisher's exact test for all incremental subsets of filtered features ranked by the p value. For the 261 pathways defined by KEGG, the lowest *P*-value was retained as a reflection of the best possible enrichment given by the data independently of hard cut-offs. Eventually, enrichment *P*-values were corrected for multiple testing by the Benjamini-Hochberg method. In general, enrichments with an adjusted *P*-value < 0.05 were considered significant. Pathway enrichments were calculated independently for proteomics and metabolomics data. For metabolome-based enrichments, structural isomers in pathway were condensed and counted only once to account for the fact that the employed technology cannot distinguish between metabolite with identical molecular weight.

DATA AND SOFTWARE AVAILABILITY

The metabolomics and proteomics data are available in Tables S1 and S2. All software is freely or commercially available and is listed in the STAR Methods.

Supplemental Figures

Cell

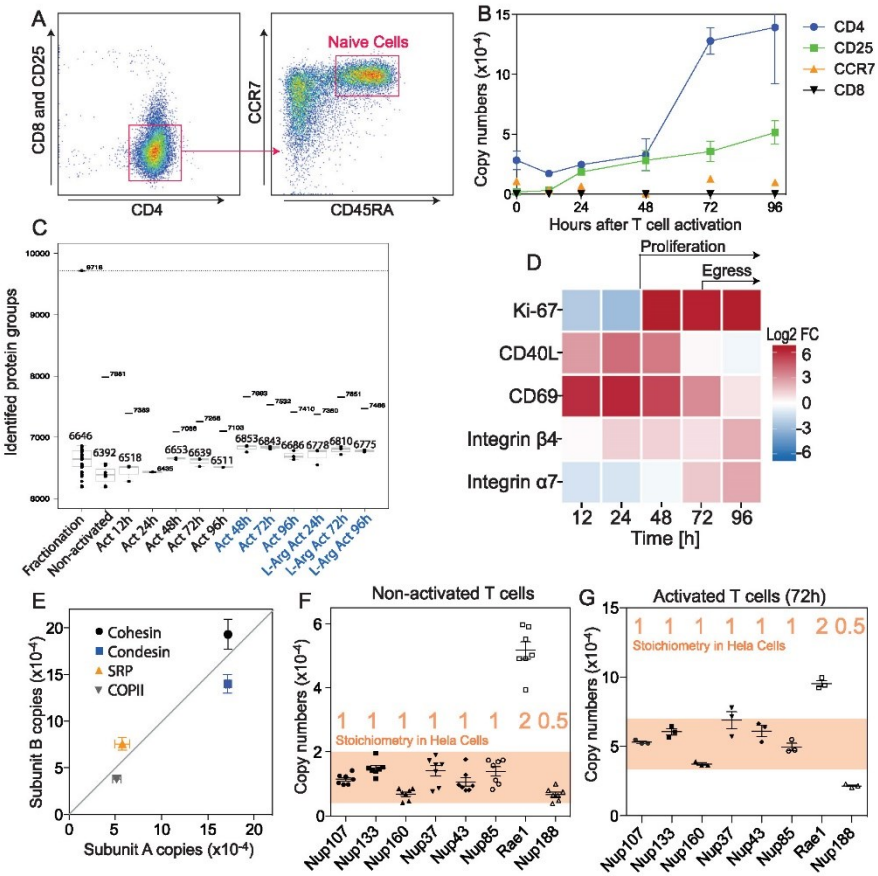

Figure S1. Quality Control of the Proteome Dataset, Related to Figure 1

(A) Sorting of human naive CD4⁺ T cells. Shown are FACS plots of cells after enrichment with anti-CD4 magnetic beads. Cells were sorted as CD4⁺ CCR7⁻ CD45RA⁺ and CD8⁻CD25⁻.

(B) Expression kinetics of indicated marker proteins. Bars represent the SEM of data from different donors, n = 7 (for resting cells), n = 3 (for 12h, 72h), n = 2 (for 96h, 48h), n = 1 (for 24h). CD25 and CD8 were not identified in resting cells. After activation, expression of CD25 increased whereas CD8 was never detected.

(C) Identified protein groups per condition. Taking all conditions together, a total of 9,718 proteins were identified. Per condition two numbers are indicated; the higher number indicates the total identifications and the lower number the mean of the single shots. Samples in blue were measured on a different instrument than samples in black. L-arg refers to 3 mM L-arginine.

(D) Relative protein abundance over time shown as a heat map. Log2 fold changes (FC) are relative to naive resting T cells. The marker for proliferating cells Ki-67 increased abruptly after 48h, when cells started to proliferate. CD40L expression increased immediately after activation and then decreased to initial levels. A similar expression pattern was observed for CD69, which inhibits egress from lymph nodes (Shiow et al., 2006). The expression of integrins α4 and β7 increased at later time points.

(E) Copy numbers of individual subunits of well-characterized protein complexes were plotted against each other. As the Sec23 subfamily includes Sec23A and Sec23B, their copy numbers were added up. The same was done for the subfamily members of Sec24 (A-D).

(F) Copy numbers of components of the nuclear pore complex (NPC). The stoichiometry of subunits measured using targeted quantitative proteomics (Ori et al., 2013) is indicated on the graph in red. Shown are copy numbers measured in naive resting T cells from seven donors.

(G) Same as in (F) but shown are copy numbers measured from activated cells (72h). n = 3 from three donors. Note that the numbers of Nup107 increased from 11,464 ± 1620 to 53,091 ± 1471. (A and E–G) Error bars represent SEM throughout.

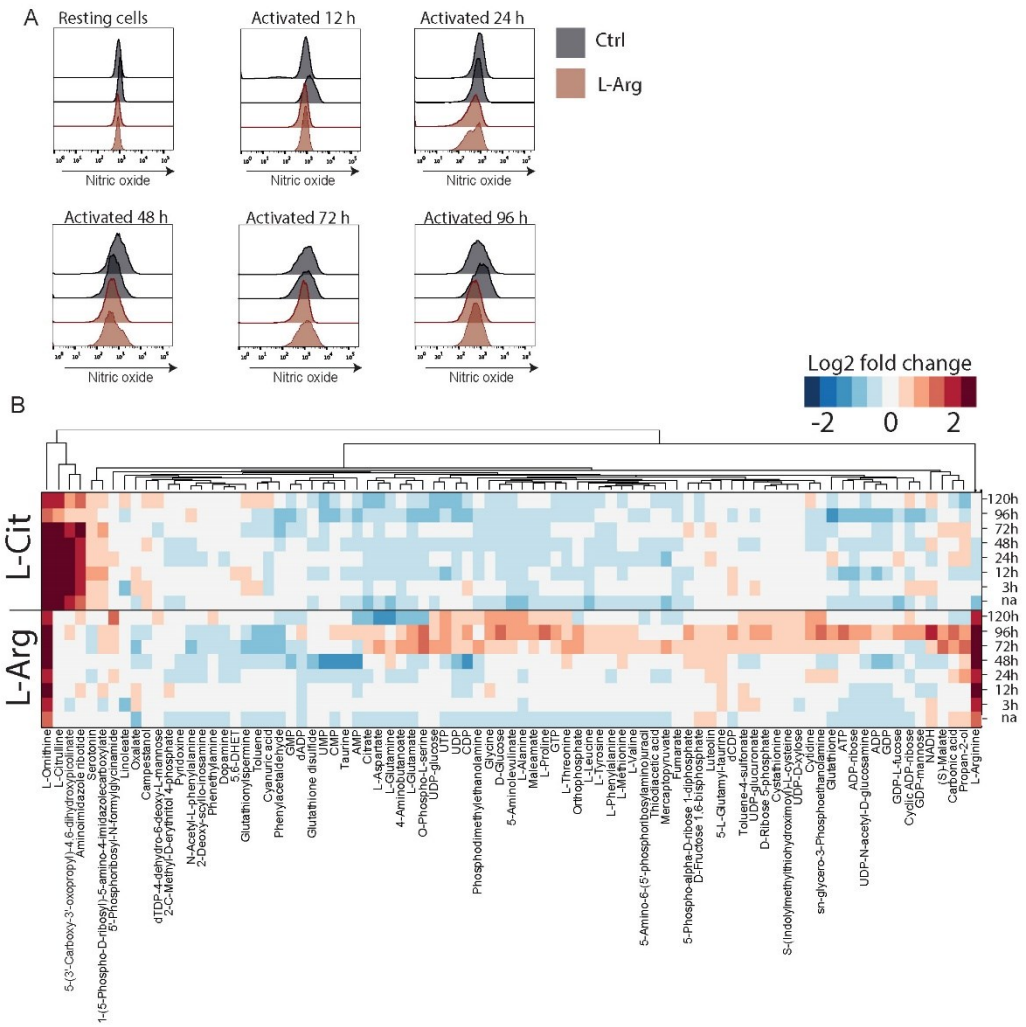

Figure S2. Impact of L-citrulline on Metabolism, Related to Figure 3

(A) Human naive CD4+ T cells were activated in normal medium or in L-Arg medium. Nitric oxide formation was measured using DAF-FM diacetate at different time points.

(B) T cells were activated in control medium (Ctrl, containing 1mM L-arginine), or in medium supplemented with 3mM L-arginine (L-Arg) or 3mM L-citrulline (L-Cit) and harvested at different time points. The heat map shows the difference in the abundance of metabolites in T cells cultured in L-Arg- or L-Cit-medium compared to controls. Shown are only metabolites with a log2 fold change > 1 and an adjusted p value of < 0.05. n = 6 from one donor.

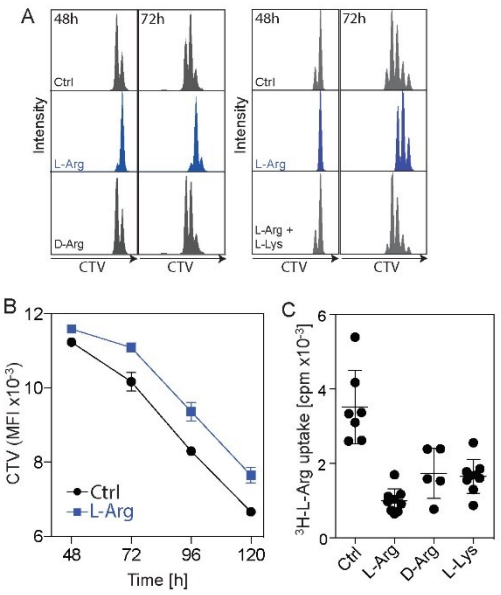

Figure S3. L-Arginine Delays the Onset of Proliferation, Related to Figure 4

(A) Kinetics of T cell proliferation. Human naive CD4+ T cells were labeled with CellTraceViolet (CTV) and activated in Ctrl medium or in L-Arg medium or in medium supplemented with 3 mM D-arginine or 3 mM L-arginine together with 3 mM L-lysine. Cell divisions were monitored at 48h and 72h by flow cytometry.

(B) CTV-labeled CD4+ T cells were activated in normal medium or L-Arg medium and the dilution of CTV was measured over time by flow cytometry. n = 5 from two donors.

(C) ^{3}H-L-arginine uptake by 3 day-activated CD4+ T cells during a 15 min pulse. Where indicated, 3 mM L-arginine, D-arginine or L-lysine was added to the culture medium as a competitive uptake inhibitor. n = 7 for control, n = 9 for L-Arg, n = 5 for D-Arg, and n = 9 for L-Lys. Error bars represent SEM throughout.

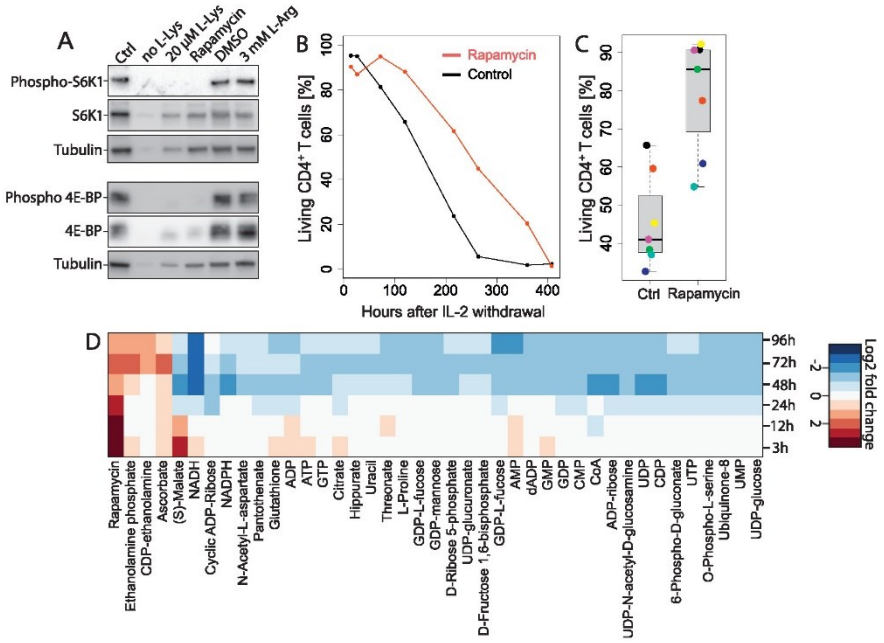

Figure S4. L-Arginine Increases the Survival of Activated T Cells Independent of mTOR Signaling, Related to Figure 4

(A) Human naive CD4+ T cells were activated for 4 days, lysed and the phosphorylation levels of S6K1 (pThr389) and 4E-BP (pThr37/46) were analyzed by western blot. Rapamycin inhibited the phosphorylation of the mTOR targets, while DMSO or supplementation of the culture medium with 3 mM L-arginine had no effect. T cells hardly proliferated upon activation in culture medium containing no or 20 µM L-lysine and therefore phosphorylation of the target proteins could not be assessed.

(B) T cell survival experiment. Human naive CD4+ T cells were activated in Ctrl medium or in medium containing 100 nM rapamycin. On day 5, cells were washed to withdraw IL-2 and cell survival was measured at different time points.

(C) Same as in (B) but cell survival was only measured 5 days after IL-2 withdrawal. n = 7 from seven donors. Boxplot. Same as in Figures 2A and 2B.

(D) Metabolic profiling of CD4+ T cells activated in medium containing 100 nM rapamycin. The heat map shows the difference of metabolite abundances between rapamycin-treated cells and controls. n = 10 from two donors.

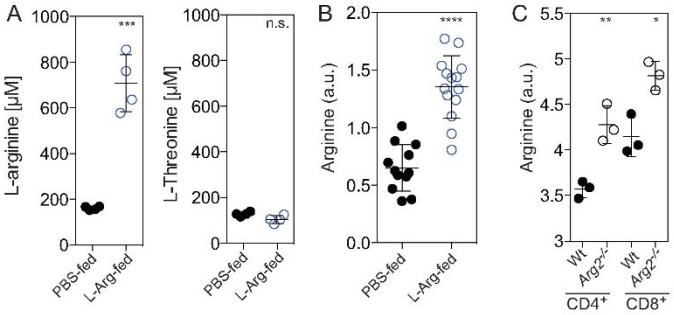

Figure S5. Oral Administration of L-Arginine Increases L-Arginine Levels in Mouse Sera and T Cells, Related to Figure 5

(A) BALB/c mice were administered L-arginine (1.5 mg/g body weight) and sera were collected after 30 min. L-arginine and, as a control, L-threonine concentrations were analyzed on a MassTrak amino acid analyzer. n = 4.

(B) BALB/c mice were immunized with ovalbumin in CFA. Sixty hours later, activated T cells from draining lymph nodes were enriched using magnetic beads coated with antibodies to CD44. Metabolites were extracted using hot 70% ethanol and L-arginine and L-glutamine levels (as an internal standard) were measured using LC-MS/MS. Shown is the ratio between L-arginine and L-glutamine intensities. n = 14.

(C) Intracellular L-arginine levels of wild-type and *Arg2*$^{-/-}$ CD4^{+} and CD8^{+} T cells 4 days after activation. n = 3. For statistical tests, a two-tailed unpaired Student's t test was used throughout, n.s. non significant; *$p < 0.05$; **$p < 0.005$; ***$p < 0.0005$; ****$p < 0.0001$. Error bars represent SEM throughout.

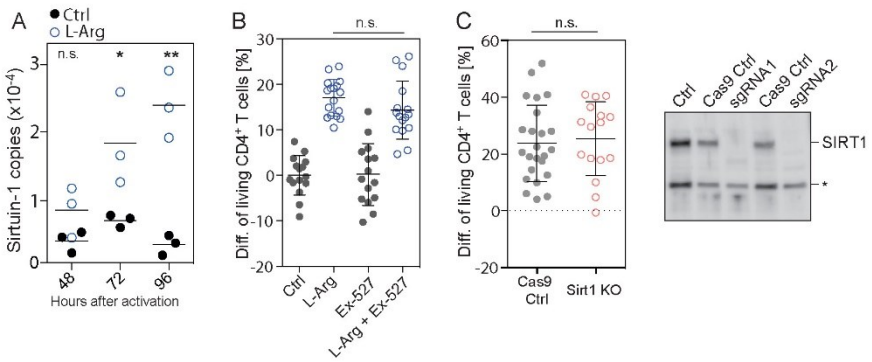

Figure S6. L-arginine Upregulates Sirtuin-1, Related to Figure 6

(A) Copy numbers of Sirtuin-1 (SIRT1) as determined by quantitative MS in human naive CD4⁺ T cells activated in normal medium or L-Arg-medium. n = 3 from three donors.

(B) T cell survival experiment. The Sirtuin-1 inhibitor Ex-527 was added at the time point of activation at a concentration of 5 μM. n = 16 from four donors.

(C) T cell survival experiments with clones expressing Cas9 only, or clones devoid of Sirtuin-1. n = 16 from 6 clones. Right panel: western blot of two different Sirtuin-1 knockout clones generated with different sgRNAs. * unspecific band. For statistical tests, a two-tailed unpaired Student's t test was used throughout, n.s. non significant; *p < 0.05; **p < 0.005; ***p < 0.0005; ****p < 0.0001. (B and C) Error bars represent SEM throughout.

2.3 Functional classification of memory CD8(+) T cells by CX3CR1 expression

2.3.1 Summary

CD8 T lymphocytes play a pivotal role in the clearance of intracellular microorganisms such as viruses and intracellular bacteria. To provide the host with long term protection against reinfections of the same pathogen, memory T lymphocytes are generated[284]. Depending on their functional, proliferative and trafficking characteristics, initially, memory T cell subpopulations were classified into central and effector memory T cells based on their lymphoid homing receptors (CD62L and CCR7) and their cytotoxic effector functions[55]. However, this view has been extended with tissue resident memory T cells that do not recirculate to the lymph node but possess both effector function and the capacity of self-renewal[285]. In addition, T cells with effector function are also required in the lymphoid tissue to protect for invading bacteria or viruses[267], leading to the question whether functionally distinct memory T-cell populations exist among CD62L+ central memory T cells in lymph nodes.

In this study, the fractalkine receptor CX3CR1 was identify as a surface marker that differentiates CD8+ T lymphocytes with cytotoxic effector function from those with proliferative potential both in human and mice. Using transcriptome and proteome-profiling a core gene and protein signature led to the identification of a CX3CR1+CD62Lhi memory T cell population with direct effector function. Furthermore, this population resides in the lymph node and locates to the subcapsular area where pathogens enter. In patients suffering from chronic viral infections, the number of CX3CR1+ memory T lymphocytes correlates with control of infection and response to immune therapy. CX3CR1-based functional classification of memory CD8+ T lymphocytes will help to resolve the principles of protective T-cell memory.

2.3.2 Contribution

In this collaborative effort our main contact partners were Percy Knolle, Jan Böttchner and Marc Beyer from the University in Bonn. I performed the proteomic measurements and analysis of four different CD8 T lymphocyte subpopulations. Together with Marc Beyer and Felix Meissner, I contributed to the integrative analysis of the RNASeq and proteomic data

sets. In particular, Figure 5 b-d, Supplementary Figure 5 a-b, and the proteomic method sections.

2.3.3 Publication

This work was published in the journal Nature Communications in 2015.

Functional classification of memory CD8(+) T cells by CX3CR1 expression

Jan P Böttcher , Marc Beyer , Felix Meissner , Zeinab Abdullah, Jil Sander, Bastian Höchst, Sarah Eickhoff, Jan C Rieckmann, Caroline Russo, Tanja Bauer, Tobias Flecken, Dominik Giesen, Daniel Engel, Steffen Jung, Dirk H Busch, Ulrike Protzer, Robert Thimme, Matthias Mann, Christian Kurts, Joachim L Schultze, Wolfgang Kastenmüller, Percy A Knolle

Nat Commun. 2015 Sep 25;6:8306. doi: 10.1038/ncomms9306.

nature COMMUNICATIONS

ARTICLE

Received 26 Apr 2015 | Accepted 6 Aug 2015 | Published 25 Sep 2015 DOI: 10.1038/ncomms9306 OPEN

Functional classification of memory CD8$^+$ T cells by CX_3CR1 expression

Jan P. Böttcher[1,†,*], Marc Beyer[2,*], Felix Meissner[3], Zeinab Abdullah[1], Jil Sander[2], Bastian Höchst[4], Sarah Eickhoff[1], Jan C. Rieckmann[3], Caroline Russo[5], Tanja Bauer[5], Tobias Flecken[6], Dominik Giesen[6], Daniel Engel[1], Steffen Jung[7], Dirk H. Busch[8], Ulrike Protzer[5], Robert Thimme[6], Matthias Mann[3], Christian Kurts[1], Joachim L. Schultze[2], Wolfgang Kastenmüller[1] & Percy A. Knolle[1,4]

Localization of memory CD8$^+$ T cells to lymphoid or peripheral tissues is believed to correlate with proliferative capacity or effector function. Here we demonstrate that the fractalkine-receptor/CX_3CR1 distinguishes memory CD8$^+$ T cells with cytotoxic effector function from those with proliferative capacity, independent of tissue-homing properties. CX_3CR1-based transcriptome and proteome-profiling defines a core signature of memory CD8$^+$ T cells with effector function. We find CD62L^{hi}CX_3CR1^+ memory T cells that reside within lymph nodes. This population shows distinct migration patterns and positioning in proximity to pathogen entry sites. Virus-specific CX_3CR1^+ memory CD8$^+$ T cells are scarce during chronic infection in humans and mice but increase when infection is controlled spontaneously or by therapeutic intervention. This CX_3CR1-based functional classification will help to resolve the principles of protective CD8$^+$ T-cell memory.

[1] Institute of Experimental Immunology, Universitätsklinikum Bonn, Sigmund-Freud-Street 25, Bonn 53105, Germany. [2] Genomics and Immunoregulation, LIMES-Institute, Universität Bonn, Carl-Troll-Street 31, Bonn 53115, Germany. [3] Max Planck Institute of Biochemistry, Am Klopferspitz 18, München 82152, Germany. [4] Institute of Molecular Immunology and Experimental Oncology, Technische Universität München, Ismaninger Street 22, München 81675, Germany. [5] Institute of Virology, Technische Universität München, Troger Street 30, München 81675, Germany. [6] Clinic for Internal Medicine II, Universitätsklinikum Freiburg, Hugstetter Street 55, Freiburg 79106, Germany. [7] Weizmann Institute of Science, Rehovot 76100, Israel. [8] Institute of Microbiology, Immunology and Hygiene, Technische Universität München, Troger Street 30, München 81675, Germany. † Present address: Immunobiology Laboratory, Francis Crick Institute, Lincoln's Inn Fields Laboratory, 44 Lincoln's Inn Fields, London WC2A 3LY, UK. * These authors contributed equally to this work. Correspondence and requests for materials should be addressed to P.A.K. (email: percy.knolle@tum.de)

Upon challenge with infectious intracellular microorganisms such as viruses and intracellular bacteria, the immune systems mounts a rapid and commensurate response characterized by an early innate inflammatory response that is followed by generation of pathogen-specific $CD8^+$ T-cell immunity. Such $CD8^+$ T-cell immunity is important to eliminate or at least contain infection with intracellular pathogens[1,2]. Memory $CD8^+$ T cells generated in response to the initial pathogen encounter survive in the absence of further antigen-specific stimulation[3] but also survive during chronic infection and continuous antigen challenge[4]. Memory $CD8^+$ T cells provide protection against re-infection with the same pathogen but may also contribute to long-term control of infection if the pathogen cannot be completely eliminated, such as during infection with herpes viruses or hepatitis viruses. Initially, two discrete memory $CD8^+$ T-cell populations were characterized by their distinct tissue localization that are believed to be linked to their functionality: central memory T cells (TCM) with proliferative potential that localize to lymphoid tissues and effector memory T cells (TEM) with direct cytotoxic effector functions that reside in peripheral tissues[5]. Consequently, TCM were distinguished from TEM by differential expression of the lymphoid-tissue homing receptors CD62L and CCR7 (ref. 5). Proliferation of memory T cells is required to generate sufficient numbers of effector T cells to control infection, whereas memory T cells with direct cytotoxic effector function are important to provide immediate protection in infected tissues[6].

However, this strict correlation between memory $CD8^+$ T-cell function and their localization was challenged by the finding that T cells with effector functions in the memory T-cell population directly mediate protective immunity[6] and the discovery of tissue-resident memory T cells (TRM) that possess effector function and have the capacity for self-renewal yet do not recirculate to lymphoid tissues[7]. Furthermore, invasion of lymphoid tissues by bacteria and viruses indicated the necessity of T cells with effector function to be present in lymphoid tissues[8], which cannot be explained by our current understanding. Rather than looking at bulk T-cell populations that localize to particular tissues, more sophisticated distinction via surface markers is necessary to better understand the mechanisms determining T-cell immunity. Attempts have been made to establish phenotypic markers that predict the functional properties of memory T cells[6,9]. Although distinct memory T-cell populations that differ in their functional, proliferative and trafficking characteristics have been recognized[10,11], it has not been investigated whether functionally distinct memory T-cell populations exist among $CD62L^+$ TCM in lymph nodes.

Here we report that the expression of the fractalkine receptor CX_3CR1 discriminates memory $CD8^+$ T cells with cytotoxic effector function from those with proliferative potential both in humans and mice. Using CX_3CR1 together with CD62L as markers, we determine a core gene and protein signature of memory $CD8^+$ T cells with cytotoxic effector functions. This allowed us to identify a $CX_3CR1^+CD62L^{hi}$ memory T-cell population with direct effector function. This population is stationary in the lymph node and locates to the subcapsular area where pathogens enter. We find low numbers of CX_3CR1^+ memory $CD8^+$ T cells with effector function in patients suffering from chronic viral infection and high numbers in patients who recovered from viral infection. Also in preclinical models of chronic viral infection, that is, lymphocytic choriomeningitis virus (LCMV) clone 13 infection, numbers of CX_3CR1^+ memory $CD8^+$ T cells correlate with control of infection and response to immune therapy.

Results

CX_3CR1 expression on memory $CD8^+$ T cells. We have previously reported a unique murine memory $CD8^+$ T-cell population with proliferative potential that is distinct from TCM and is induced by non-professional antigen-presenting cells in the liver but not lymphoid tissues[12]. We reassessed our previously published set of whole-genome transcriptome data utilizing an analysis of variance (ANOVA) model to detect differentially expressed genes as well as self-organizing-map analysis of gene expression profiles to identify genes specific for memory T cells[12]. We found the fractalkine receptor CX_3CR1 among genes coding for cell surface receptors that were most upregulated within a memory-specific cluster of genes (Fig. 1a and Supplementary Fig. 1A). CX_3CR1 has been reported to define subsets of myeloid cells, including monocytes and dendritic cells, in the blood and different tissues, such as the gut and lymph nodes[13–15]. So far, CX_3CR1 expression on a protein level was detected on $CD4^+$ T cells residing in the lung or skin[16,17]. However, to date, this was not analysed in detail for memory $CD8^+$ T cells, although published transcriptome analysis in memory $CD8^+$ T cells indicated the expression of the *Cx₃cr1* gene[18,19] and CX_3CR1 was detected on terminally differentiated cytotoxic effector T cells[20]. To analyse the expression pattern of CX_3CR1 in $CD8^+$ T cells during the course of infection and memory formation, we used $CX_3CR1^{+/GFP}$ reporter mice[13], in which GFP expression correlated with CX_3CR1 protein expression (Supplementary Fig. 1B).

In healthy mice, we observed GFP (CX_3CR1) expression on some antigen-experienced $CD44^+$ but not naive $CD44^{low}$ $CD8^+$ T cells (Fig. 1b). The frequency of CX_3CR1-expressing T cells among total $CD8^+$ T cells increased after adenoviral infection (d60) (Fig. 1b,c). Among $CD44^+$ T cells, CX_3CR1 expression was most prominent in $CD8^+$ T cells (Fig. 1d), prompting us to study CX_3CR1 expression on antigen-specific memory $CD8^+$ T cells in response to infection. After infection with a recombinant adenovirus coding for luciferase and ovalbumin (OVA), which results in hepatocyte infection that can be monitored by *in vivo* bioluminescence measurement[21], *in vivo* activation of ovalbumin-specific OT-$I^{CX3CR1\text{-}GFP}$ T cells was observed at 2 days post infection (d.p.i.) as demonstrated by increased CD44 expression. GFP (CX_3CR1) expression, however, was not detected before 5 d.p.i. when control over viral infection had been achieved (Fig. 1e), as determined by reduction of *in vivo* bioluminescence (Fig. 1f). The total numbers of GFP^+ (CX_3CR1^+) T cells were highest at 5 d.p.i. and then gradually decreased parallel to the total numbers of antigen-specific $CD8^+$ T cells (Supplementary Fig. 1C) consistent with contraction. Antigen-specific GFP^+ (CX_3CR1^+) and GFP^{neg} (CX_3CR1^{neg}) $CD8^+$ T cells were found in the lymphoid tissue like in the spleen but also in the blood and liver after viral infection (Supplementary Fig. 1D). The GFP (CX_3CR1) expression level per $CD8^+$ T cell increased during this time by one log (Fig. 1e and Supplementary Fig. 1E). These findings were corroborated studying CX_3CR1 expression on antigen-specific $CD8^+$ T cells generated from the endogenous T-cell repertoire. CX_3CR1^+ expression was observed after infection with adenovirus (AdOVA) or *Listeria monocytogenes* (*L.m.*-OVA) on OVA-specific memory $CD8^+$ T cells and after LCMV infection on LCMV-gp33-specific memory $CD8^+$ T cells (Supplementary Fig. 1F). At 60 d.p.i. of $CX_3CR1^{+/GFP}$ reporter mice, the majority of $CD8^+$ T cells in the blood and spleen, which were specific for OVA (after AdOVA or *L.m.*-OVA infection) or LCMV-gp33, showed GFP (CX_3CR1) expression (Fig. 1g and Supplementary Fig. 1G). A similar separation in CX_3CR1^+ and CX_3CR1^{neg} populations was observed in memory $CD8^+$ T cells generated from 500 adoptively transferred naive OT-$I^{CX3CR1\text{-}GFP}$ $CD8^+$ T cells (Supplementary Fig. 1H). Even >200 days after AdOVA infection, antigen-specific GFP^+ (CX_3CR1^+) and GFP^{neg} (CX_3CR1^{neg}) memory $CD8^+$ T cells were found

NATURE COMMUNICATIONS | DOI: 10.1038/ncomms9306

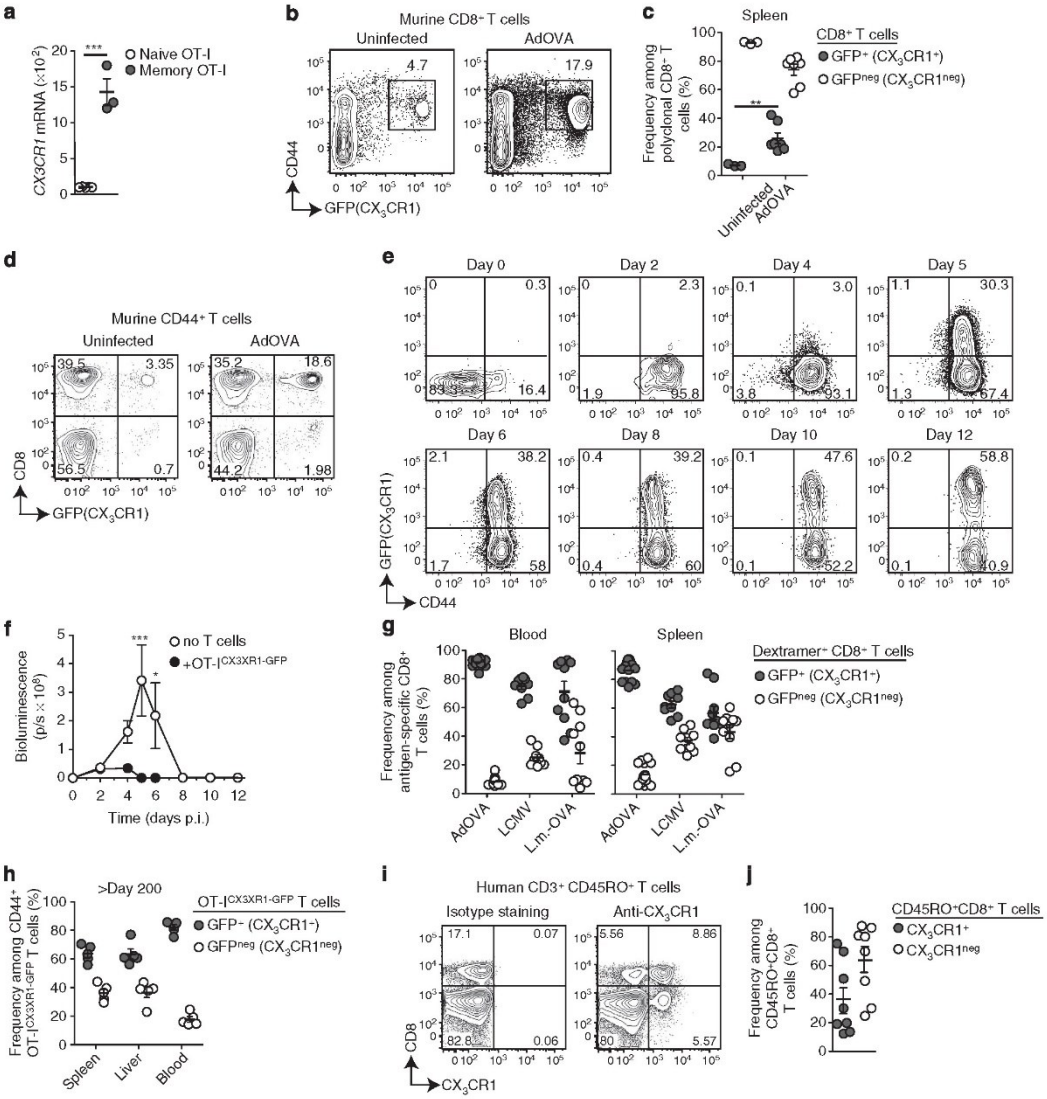

Figure 1 | CX_3CR1 expression on antigen-experienced memory T cells in mice and man. (**a**) Quantification of *Cx3cr1* mRNA levels on $CD44^{low}$ naive OT-I T cells ($n=5$) and $CD44^+$ memory OT-I T cells ($n=3$) at >d45 post *L.m.*-OVA infection. $^{***}P<0.001$, unpaired *t*-test. (**b**–**d**) Frequencies of GFP^+ T cells in untreated or AdOVA i.v infected $CX_3CR1^{+/GFP}$ reporter mice ($n=7$) at 60 d.p.i. isolated from the spleen (**b**,**c**) and the blood (**d**). $^{**}P<0.01$, unpaired *t*-test. (**e**) C57BL/6 mice that had received 3×10^5 naïve $CD44^{low}$ $CD45.1^+$ OT-$I^{CX3CR1\text{-}GFP}$ T cells 1 day before were infected with AdOVALUC at day 0 and analysed for $GFP(CX_3CR1)$/CD44 expression in OVA-specific $CD45.1^+$OT-$I^{CX3CR1\text{-}GFP}$ T cells at indicated time points. (**f**) *In vivo* bioluminescence activity of mice ($n=7$) from (**e**) demonstrating efficient OVA-specific T-cell immunity against virus-infected hepatocytes. C57BL/6 mice without adoptive T-cell transfer served as control. $^*P<0.05$ and $^{***}P<0.001$, two-way ANOVA. (**g**) $CX_3CR1^{+/GFP}$ mice were infected with AdOVA ($n=10$), *L.m.*-OVA ($n=9$) or LCMV WE ($n=10$). Frequencies of GFP^+ (CX_3CR1^+) and GFP^{neg} (CX_3CR1^{neg}) cells at 45–60 d.p.i. among splenic OVA-specific $CD44^+CD8^+$ T cells (AdOVA and *L.m.*-OVA infection) or gp33-specific $CD44^+$ $CD8^+$ T cells (LCMV infection) identified by Dextramer staining. (**h**) Frequencies of GFP^+ and GFP^{neg} $CD45.1^+$ cells at >200 days post AdOVA infection of C57BL/6 wild-type mice ($n=5$) that had received 10^3 naive $CD45.1^+$ OT-$I^{CX3CR1\text{-}GFP}$ cells before infection. (**i**) CX_3CR1 expression in human $CD45RO^+$ $CD3^+$ T cells isolated from the blood and (**j**) frequency of CX_3CR1^+ and CX_3CR1^{neg} cells among human $CD45RO^+$ $CD8^+$ T cells ($n=8$). In scatter plots, each circle represents one mouse or patient, fluorescence-activated cell sorting (FACS) plots show representative analysis for one mouse or patient per group. Data are representative for two or three independent experiments (**b**,**d**–**f**, mean and s.d.) or have been pooled from two independent experiments (**c**,**f**–**h**,**j**, mean and s.e.m.). In scatter plots, each circle represents one mouse or a different human donor, FACS plots show representative analysis for one mouse or human donor per group.

(Fig. 1h) arguing that both memory T-cell populations are long lived. Importantly, we confirmed CX_3CR1 expression on T cells in healthy human volunteers. Here, CX_3CR1 expression was also most prominent on antigen-experienced $CD45RO^+$ $CD8^+$ T cells with numbers varying among healthy individuals (Fig. 1i,j and Supplementary Fig. 1I). Taken together, these data indicated that CX_3CR1 is expressed in a population of murine and human memory $CD8^+$ T cells.

CX_3CR1 expression identifies cytotoxic memory $CD8^+$ T cells. As GFP (CX_3CR1) expression separates memory $CD8^+$ T cells into two populations (Fig. 1), we addressed the question whether antigen-specific GFP^+ (CX_3CR1^+) and GFP^{neg} (CX_3CR1^{neg}) memory $CD8^+$ T cells generated after viral or bacterial infections in $CX_3CR1^{+/GFP}$ reporter mice had distinct functional properties. The ability to produce the cytokine interleukin-2 (IL-2) is considered a hallmark of those memory T cells that have the potential to proliferate and generate T-cell progeny[22]. We found that GFP^{neg} (CX_3CR1^{neg}) memory $CD8^+$ T cells were the main producers of IL-2 upon re-stimulation, whereas GFP^+ (CX_3CR1^+) memory $CD8^+$ T cells failed to produce significant amounts of this cytokine (Fig. 2a and Supplementary Fig. 2A). To directly test the proliferative capacity of GFP^+ (CX_3CR1^+) versus GFP^{neg} (CX_3CR1^{neg}) memory $CD8^+$ T cells *in vivo*, we adoptively transferred both populations and analysed their numbers after viral or bacterial infections. Transferred GFP^{neg} (CX_3CR1^{neg}) memory $CD8^+$ T cells showed vigorous and antigen-specific proliferation upon pathogen challenge, whereas GFP^+ (CX_3CR1^+) memory $CD8^+$ T cells showed much less proliferative capacity (Fig. 2b). Similar results were obtained using transgenic OT-$I^{CX3CR1\text{-}GFP}$-derived memory $CD8^+$ T cells after re-challenge with AdOVA infection (Supplementary Fig. 2B).

Next, we investigated effector functions in GFP^+ (CX_3CR1^+) and GFP^{neg} (CX_3CR1^{neg}) memory $CD8^+$ T cells. In contrast to IL-2 expression, only GFP^+ (CX_3CR1^+) memory $CD8^+$ T cells at 60 d.p.i. (*L.m.*-OVA) constitutively expressed GzmB (Fig. 2c and Supplementary Fig. 2C), which is a hallmark of T cells with cytotoxic effector function[23]. Consequently, only GFP^+ (CX_3CR1^+) OT-$I^{CX3CR1\text{-}GFP}$ memory T cells showed potent cytotoxic effector function directly *ex vivo* (Fig. 2d). After adoptive transfer, GFP^+ (CX_3CR1^+) OT-$I^{CX3CR1\text{-}GFP}$ memory T cells but not GFP^{neg} (CX_3CR1^{neg}) T cells conferred immediate

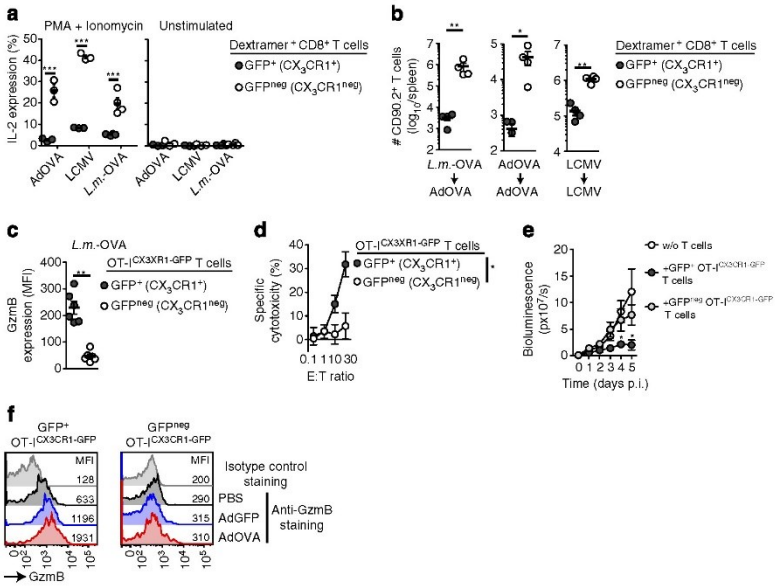

Figure 2 | CX_3CR1 expression separates memory $CD8^+$ T cells with distinct functions. (**a**,**b**) $CX_3CR1^{+/GFP}$ mice were infected with AdOVA ($n=3$), *L.m.*-OVA ($n=4$) or LCMV WE ($n=3$). At 45–60 d.p.i., spleen-derived GFP^+ (CX_3CR1^+) and GFP^{neg} (CX_3CR1^{neg}) memory T cells specific for OVA (after AdOVA and *L.m.*-OVA infection) or for LCMV gp33 were obtained by FACSorting. (**a**) *Ex vivo* IL-2 production after stimulation with PMA/ionomycin. $^{***}P<0.001$, unpaired *t*-test. (**b**) Adoptive transfer of sorted OVA-specific or LCMV-specific $CD8^+$ T cells (2×10^3) into $CD90.1^+$ mice ($n=4$) subsequently infected with AdOVA or LCMV. Determination of $CD90.2^+$ T-cell numbers at 8 d.p.i. in the spleen. $^*P<0.05$ and $^{**}P<0.01$, unpaired *t*-test. (**c**–**e**) Adoptive transfer of FACSsorted naive $CD45.1^+CD44^{low}$ OT-$I^{CX3CR1\text{-}GFP}$ T cells (5×10^2) into $CD45.2^+$ mice followed by *L.m.*-OVA infection. (**c**) At 45–60 d.p.i, $CD45.1^+$ Memory OT-$I^{CX3CR1\text{-}GFP}$ T cells from the spleen were analysed for intracellular GzmB expression ($n=6$). $^{**}P<0.01$, unpaired *t*-test. (**d**) OVA-specific cytotoxicity of sorted GFP^+ and GFP^{neg} memory OT-$I^{CX3CR1\text{-}GFP}$ T cells directly *ex vivo*. $^*P<0.05$, ANOVA. (**e**) Adoptive transfer of 3×10^5 sorted GFP^+ or GFP^{neg} memory OT-$I^{CX3CR1\text{-}GFP}$ T cells into mice ($n=6$) that were infected with AdOVALUC 4 h before. *In vivo* bioluminescence activity was determined to measure T-cell effector function against virus-infected luciferase-expressing hepatocytes over time. AdOVALUC-infected mice that did not receive T cells served as controls ($n=6$). Data are representative for —two or three independent experiments. $^*P<0.05$, two-way ANOVA. (**f**) Challenge of mice harbouring $CD45.1^+$ Memory OT-$I^{CX3CR1\text{-}GFP}$ T cells with AdGFP or AdOVA and 6 h later determination of GzmB expression in splenic GFP^+ and GFP^{neg} memory OT-$I^{CX3CR1\text{-}GFP}$ T cells. Data are representative for two independent experiments (**a**,**b**,**d**,**e**, mean and s.d.) or have been pooled from two independent experiments (**c**,**f**, mean and s.e.m.). In scatter plots of **a**–**c**, each dot represents data from one mouse. Fluorescence-activated cell sorting plots shown in **d** are representative for one mouse of a group of three or four mice per experiment.

in vivo protection by rapid control of hepatocyte infection with AdOVALUC (Fig. 2e). In contrast, GFP^{neg} (CX_3CR1^{neg}) T cells did not control infection (Fig. 2e), which is consistent with their lack of cytotoxic functions. Upon pathogen re-challenge, GFP^+ (CX_3CR1^+) OT-$I^{CX3CR1\text{-}GFP}$ memory T cells showed further rapid (6 h) increase of GzmB expression. Interestingly, GzmB expression was also triggered by AdGFP infection lacking the cognate antigen but was more pronounced upon AdOVA infection (Fig. 2f), indicating that antigen-specific restimulation was superior to virus-induced inflammation in augmenting GzmB expression. Strikingly, GFP^{neg} T cells remained GzmB negative under such conditions (Fig. 2f), providing a rationale for the failure of this population to confer protective immunity upon transfer (Fig. 2e). Interestingly, no difference in expression of interferon (IFN)-γ was observed between GFP^{neg} and GFP^+ T cells (Supplementary Fig. 2D). Having established the functional segregation of memory $CD8^+$ T cells based on CX_3CR1 expression, we next reconciled our data with previous work that employed the homing-related molecules CD62L and CCR7 to separate memory $CD8^+$ T cells into functionally distinct populations.

CX_3CR1 and CD62L identify four memory $CD8^+$ T-cell populations. Memory T cells have been divided into two populations based on the expression of CD62L and CCR7 that allows $CD62L^{hi}CCR7^+$ TCM to localize to lymphoid tissues, whereas $CD62L^{low}CCR7^{neg}$ TEM remain in the blood and peripheral tissues[5]. Although tissue localization correlates with expression of these markers, the separation of functional properties between TCM to generate T-cell progeny and TEM to show cytotoxic effector functions is less stringent[6,24,25]. This led us to analyse GFP (CX_3CR1) expression in $CD62L^{hi}CD127^+KLRG1^{neg}$ TCM, $CD62L^{low}CD127^+$ $KLRG1^{neg}$ TEM and $KLRG1^+CD8^+$ T cells derived from naïve OT-$I^{CX3CR1\text{-}GFP}$ T cells at 60 days after AdOVA infection. At this time point, all $KLRG1^+$ effector-like $CD8^+$ T cells showed high GFP (CX_3CR1) expression (Fig. 3a). However, 25% of TEM did not show GFP (CX_3CR1) expression (Fig. 3a) and 30% of TCM showed GFP (CX_3CR1) expression (Fig. 3a). Based on this data we reasoned that CX_3CR1 in combination with CD62L might enable a highly specific discrimination of memory T-cell subsets with distinct functional properties.

Indeed, using CD62L and CX_3CR1 in combination, four distinct populations of memory $CD8^+$ T cells could be discriminated in mice and healthy humans (Fig. 3b,g). At 60 days after AdOVA infection in mice, GzmB expression was exclusively found in GFP^+ (CX_3CR1^+) memory OT-$I^{CX3CR1\text{-}GFP}$ T cells irrespective of their CD62L expression level (Fig. 3c). In contrast, IL-2 production after restimulation was restricted to GFP^{neg} (CX_3CR1^{neg}) memory OT-$I^{CX3CR1\text{-}GFP}$ T cells, again irrespective of their CD62L expression levels (Fig. 3d). Along this line, only GFP^{neg} (CX_3CR1^{neg}) $CD62L^{hi}$ and GFP^{neg} (CX_3CR1^{neg})$CD62L^{low}$ memory OT-$I^{CX3CR1\text{-}GFP}$ T cells proliferated after adoptive transfer and AdOVA infection (Fig. 3e). Of note, progeny $CD8^+$ T cells were comprised of both, GFP^+ (CX_3CR1^+) and GFP^{neg} (CX_3CR1^{neg}) T cells (Fig. 3f), indicating that CX_3CR1-expressing $CD8^+$ T cells can arise from GFP^{neg} (CX_3CR1^{neg}) memory $CD8^+$ T cells during recall responses after viral infection.

Also in the polyclonal repertoire of human $CD45RO^+CD8^+$ T cells, staining for CD62L and CX_3CR1 identified four cell populations (Fig. 3g). CCR7 expression was observed in all $CD62L^{hi}$ memory T cells and thus did not discriminate CX_3CR1^+ from CX_3CR1^{neg} memory $CD8^+$ T cells (Supplementary Fig. 3A). The relative frequencies of these four populations varied between the 18 healthy individuals studied (Supplementary Fig. 3B,C). Only $CX_3CR1^+CD62L^{low}$ and $CX_3CR1^+CD62L^{hi}$ human memory $CD8^+$ T cells expressed GzmB (Fig. 3h,i). Accordingly, CD62L expression levels did not identify GzmB-positive cells among $CD45RO^+$ or $CD45RA^+$ $CD8^+$ T cells, whereas all GzmB-positive $CD8^+$ T cells stained positive for CX_3CR1 (Supplementary Fig. 3D). Furthermore, IL-2 production following restimulation was only observed in CX_3CR1^{neg} memory $CD8^+$ T cells, although we observed more prominent IL-2 production in $CX_3CR1^{neg}CD62L^{hi}$ compared with $CX_3CR1^{neg}CD62L^{low}$ $CD8^+$ T cells (Fig. 3i). In mice, several markers, such as CD27, CD28, CD127, and the activation-associated isoform of CD43 (1B11) have been reported to correlate with $CD8^+$ T-cell functionality[6,9]. As the expression of these markers has not been investigated within $CD62L^+$ TCM, especially not in humans, we evaluated their expression in comparison with our CX_3CR1-based separation on human memory T cells. In human memory T cells, CD43 expression was rather high in CX_3CR1^+ $CD8^+$ T cells, whereas CD27 showed higher expression on CX_3CR1^{neg} $CD8^+$ T cells (Supplementary Fig. 3E,F) indicating that the co-regulation of CD43 and CD27 on human memory $CD8^+$ T cells[9,26] does not allow for clear cut separation with regard to functionality as CX_3CR1-based separation. CD127 expression levels were slightly higher in CX_3CR1^{neg} T cells independent of CD62L expression levels (Supplementary Fig. 3E,F) consistent with previous reports on CD127 expression on long-lived central memory T cells[27–30]. Also, CD28 expression was slightly increased on CX_3CR1^{neg} T cells (Supplementary Fig. 3E,F) confirming the increased expression found previously on TCM[5,31]. Overall, beyond the resolution achieved by CD62L or other T-cell surface markers, CX_3CR1 expression precisely classifies memory $CD8^+$ T cells into two distinct populations in mice and humans independent of their tissue-homing properties, one with cytotoxic effector function but little proliferative capacity, the other with proliferative capacity but no cytotoxic function. To address this notion in an unbiased manner, we decided to apply transcriptomic and proteomic analyses of human memory $CD8^+$ T cells.

Core signature of human CX_3CR1^+ memory $CD8^+$ T cells. To further understand whether CX_3CR1 expression identifies distinct populations of $CD8^+$ T cells, we performed mRNA-sequencing of human naive $CD62L^{hi}CD45RA^+CD8^+$ T cells, $CX_3CR1^+CD62L^{hi}$ $CD45RO^+CD8^+$ T cells, CX_3CR1^+ $CD62L^{low}$ $CD45RO^+CD8^+$ T cells, $CX_3CR1^{neg}CD62L^{hi}$ $CD45RO^+CD8^+$ T cells and $CX_3CR1^{neg}CD62L^{low}CD45RO^+$ $CD8^+$ T cells, and assessed variable genes by an ANOVA model (Fig. 4a). Principal component analysis of variable genes within the data set clearly revealed one distinct population of $CX3CR1^+CD8^+$ T cells irrespective of their CD62L expression (Fig. 4b). Only in the $CX_3CR1^{neg}CD45RO^+CD8^+$ T cell populations, CD62L discriminated two separate populations, albeit they were more closely related to each other than to naïve $CD62L^{hi}$ $CD45RA^+CD8^+$ T cells and the CX_3CR1^+ $CD45RO^+CD8^+$ T-cell populations. Hierarchical clustering of variable genes shown as a heat map (Fig. 4c) confirmed these findings as naïve $CD45RA^+CD8^+$ T cells showed the most significant difference to the other four $CD45RO^+$ T-cell populations. $CX_3CR1^{neg}CD62L^{hi}CD8^+$ T cells and CX_3CR1^{neg} $CD62L^{low}CD8^+$ T cells had distinct gene expression patterns, whereas gene expression patterns of $CX_3CR1^+CD62L^{hi}CD8^+$ T cells and $CX_3CR1^+CD62L^{low}CD8^+$ T cells were almost identical. Consistent with these results and with the usefulness of CX_3CR1 as marker for functionally distinct T-cell populations, we found that CX_3CR1 expression was similar to CD43 expression,

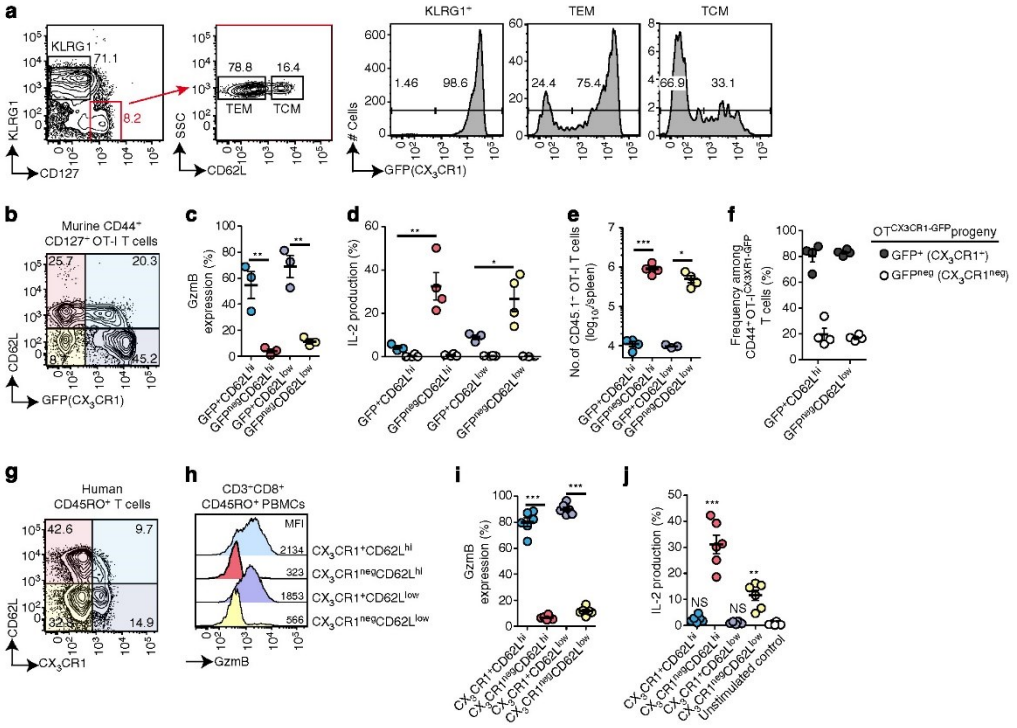

Figure 3 | CX_3CR1 and CD62L expression identifies four distinct memory CD8$^+$ T-cell populations. (**a**–**f**) Naive CD45.1$^+$ OT-I $^{CX3CR1\text{-}GFP}$ T cells (5×10^2) were adoptively transferred into CD45.2 mice subsequently infected with AdOVA. (**a**) At 60 d.p.i., CX3CR1 expression was determined in CD45.1$^+$ OT-I-derived KLRG1$^+$ T cells, CD62L^{low}CD127$^+$CD44$^+$ memory T cells (TEM) and CD62L^{hi}CD127$^+$CD44$^+$ memory T cells (TCM) isolated from the spleen. (**b**) Representative analysis of CD62L and GFP (CX_3CR1) expression in CD127$^+$ CD44$^+$ memory OT-I$^{CX3CR1\text{-}GFP}$ T cells from **a**. (**c**,**d**) Four populations of CD127$^+$ CD44$^+$ memory OT-I$^{CX3CR1\text{-}GFP}$ T cells after AdOVA infection separated by CD62L and GFP (CX_3CR1) expression levels were (**c**) analysed for GzmB expression or (**d**) sorted and analysed for IL-2 expression after PMA/ionomycine stimulation for 5 h. Unstimulated T cells from each population (empty circles) served as control. $n=3$ or 4 for each group; $^*P<0.05$, $^{**}P<0.01$, ANOVA. (**e**,**f**) Adoptive transfer of identical numbers (2×10^3 cells) of FACSorted CD45.1$^+$ cells from the four populations of memory T cells into CD45.2$^+$ mice ($n=4$) that were subsequently infected with AdOVA. (**e**) At 8 d.p.i., total numbers of CD45.1$^+$ T cells and (**f**) frequencies of CX_3CR1^+ cells among CD45.1$^+$ T-cell progeny was determined in the spleen. $^*P<0.05$, $^{***}P<0.001$, ANOVA. (**g**) Representative analysis showing CD62L and CX_3CR1 expression in human CD45RO$^+$CD3$^+$CD8$^+$ PBMCs. (**h**,**i**) Flow cytometric determination of expression of GzmB in the four cell populations stratified by CD62L and CX_3CR1 expression. $^{***}P<0.001$, ANOVA. (**j**) IL-2 expression in FACSorted cells from these four T-cell populations subjected to PMA/ionomycine stimulation for 5 h. $^{**}P<0.01$ and $^{***}P<0.001$, ANOVA. Fluorescence-activated cell sorting (FACS) plots are representative for three (**a**–**c**) or five (**g**,**h**) independent experiments. Data from one of three independent experiments are show in **c**–**f** each dot represents T cells from one mouse. (**i**,**j**) Pooled data for T cells from $n=6$ individual donors.

whereas other markers for memory T cells, such as CD27, CD28 or CD127, were downregulated in CX3CR1$^-$ CD8$^+$ T cells independent of their CD62L expression (Supplementary Fig. 3G). Focusing on differentially expressed genes as determined by the ANOVA model on present genes directly comparing CD62L$^+$ CX3CR1$^+$ CD8$^+$ T cells or CD62L$^-$ CX3CR1$^+$ CD8$^+$ T cells to naïve T cells and visualizing the results by ratio/ratio plots, further confirmed that CX_3CR1^-CD8$^+$ T cells had almost identical expression patterns irrespective of CD62L expression levels (Fig. 4d and Supplementary Data 1). In contrast, CD62L^{hi} and CD62L^{low} CD8$^+$ T cells lacking CX_3CR1 showed differential expression of a subset of genes (Fig. 4e and Supplementary Data 1). To determine a core signature for the CX_3CR1^+CD45RO$^+$ CD8$^+$ T cells, we performed an analytical approach combining the results of the ANOVA model with either co-regulation analysis or weighted network analysis and subtracted genes also enriched in CX3CR1$^-$ T cells to identify differentially expressed genes (Fig. 4f). This approach revealed a set of 363 signature genes (Supplementary Data 2) with high expression in CX3CR1$^+$ memory T cells, intermediate to low expression in CX3CR1$^-$ memory T cells and low to absent expression in naïve CD8$^+$ T cells (Supplementary Fig. 4). We visualized genes of this CX_3CR1-associated core signature belonging to functional categories including T-cell cytotoxicity markers, NK-cell markers, T-cell activation-associated molecules, adhesion molecules and transcription factors as heat maps of z-transformed expression values (Fig. 4g). This signature included known cytotoxic effector molecules such as FAS-L, perforin and GzmA/B/H, or transcription factors associated with effector function, such as TBX21, BATF, RUNX3 and EOMES, but also other molecules whose relation to CD8$^+$ T-cell effector has not been studied yet (Fig. 4g and Supplementary Data 2). Moreover, to better

NATURE COMMUNICATIONS | DOI: 10.1038/ncomms9306

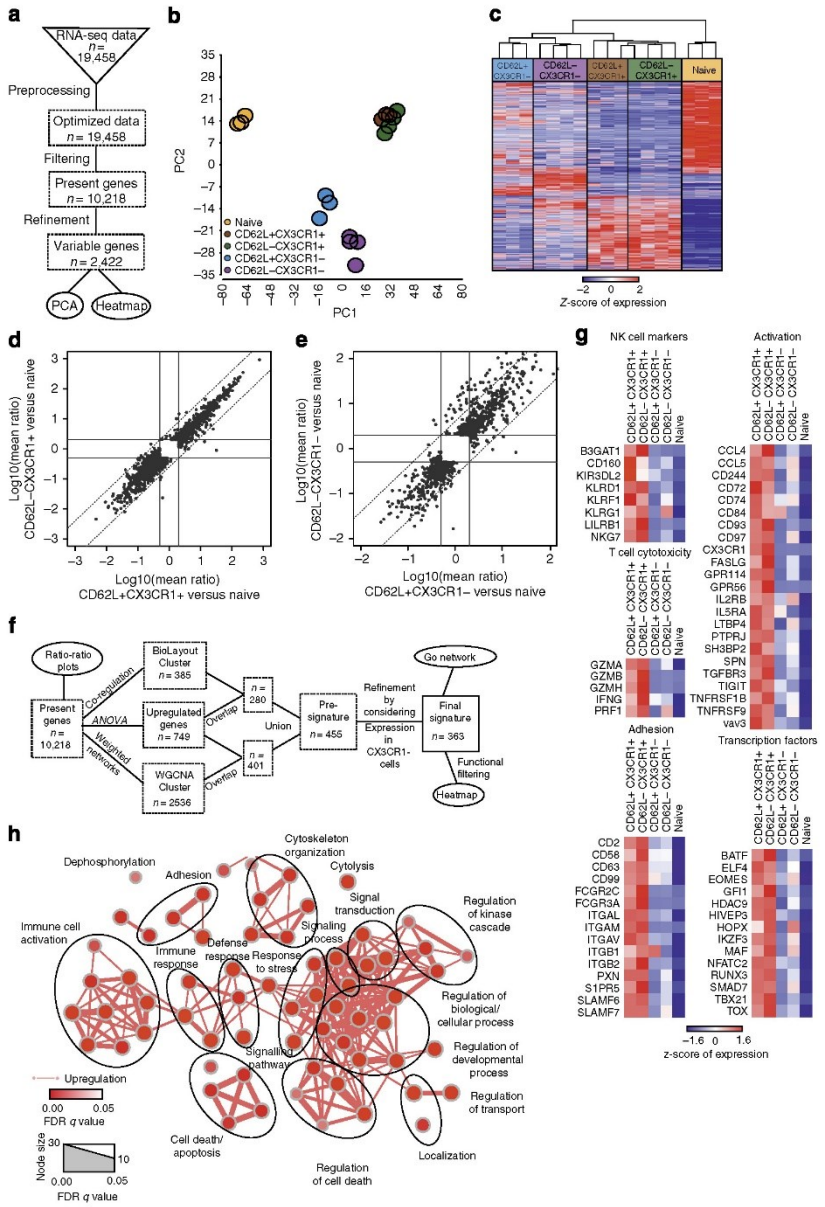

Figure 4 | Transcriptome analysis reveals a core signature of human CX_3CR1-expressing memory $CD8^+$ T cells with effector function. (**a**) Scheme describing the workflow for RNA-seq data preprocessing and filtering. (**b**) Principal component analysis (PCA) based on present and variable genes. (**c**) Heat map showing the z-transformed expression values of present and variable genes, coloured from blue to red. (**d**) Ratio-ratio plot of log10-transformed mean ratios of genes that are differentially expressed (fold change (FC) < -2 or > 2; FDR-corrected *P*-value < 0.05) comparing $CD62L^+$ $CX3CR1^+$ T cells versus naïve T cells (*x* axis) or $CD62L^-$ $CX3CR1^+$ T cells versus naïve T cells (*y* axis). (**e**) Ratio-ratio plot of log10-transformed mean ratios of genes being differentially expressed FC < -2 or > 2; FDR-corrected *P*-value < 0.05) comparing $CD62L^+$ $CX3CR1^-$ T cells versus naïve T cells (*x* axis) or $CD62L^-$ $CX3CR1^-$ T cells versus naïve T cells (*y* axis). (**f**) Schema describing the workflow for generating the transcriptome core signature for $CX3CR1^+$ T cells. (**g**) Heat map of selected genes out of the 363-gene core signature sorted by defined activity groups. Gene expression values were z-transformed for visualization and are coloured from blue to red. (**h**) Network visualization of Gene Ontology Enrichment Analysis based on the 363 core signature genes using BiNGO and EnrichmentMap. Enriched GO terms are depicted by red nodes, where colour and size represent the corresponding FDR-adjusted enrichment *P*-value (*q*-value). Overlap of genes between nodes is indicated by edge thickness.

understand which biological processes might be linked to the core signature of CX_3CR1^+ $CD45RO^+CD8^+$ T cells, we performed Gene Ontology Enrichment Analysis (GOEA) followed by network visualization (Fig. 4h). The major clusters of biological processes we obtained are compatible with an activated immune cell including Gene Ontology (GO) terms associated with immune cell activation, immune response, defense response, cytolysis, adhesion, response to stress, but also regulation of cell death and cell death/apoptosis. Taken together, the genome-wide analysis of gene expression defined a common gene signature that is shared by human $CX_3CR1^+CD45RO^+CD8^+$ T cells irrespective of their CD62L expression that have cytotoxic effector function.

Next, we performed proteome analysis of these T-cell populations to establish a global protein profile of the $CX3CR1^+$ memory $CD8^+$ T cells (Supplementary Data 3 and Supplementary Fig. 5A). Using the identical bioinformatical approach for data analysis (Fig. 5a), we observed a strong similarity between $CX_3CR1^+CD62L^{hi}$ and $CX_3CR1^+CD62L^{low}CD45RO^+CD8^+$ T-cell populations by principal component analysis, with CX_3CR1^{neg} $CD62L^{low}$ T cells being most closely related, whereas $CX_3CR1^{neg}CD62L^{hi}$ and naïve $CD8^+$ T-cell populations were more distinct (Fig. 5b). This was reflected by hierarchical clustering of variable proteins as both $CX_3CR1^+CD8^+$ T-cell populations showed close similarities, whereas CX_3CR1^{neg} $CD62L^{hi}$ and naïve $CD8^+$ T cells had clearly different gene expression patterns and CX_3CR1^{neg} $CD62L^{low}$ T cells revealed a pattern in-between both (Fig. 5c). Visualization of changes in gene or protein expression by volcano plots substantiated that separation of memory $CD8^+$ T cells into CX_3CR1^+ and CX_3CR1^{neg} cells is more powerful than separation into $CD62L^{hi}$ and $CD62L^{low}$ cells to identify genetically distinct populations (Supplementary Fig. 5B). We next investigated to which extent candidate molecules from the genome-wide transcriptome core signature were also present in the proteome. Similar to previous findings in other cell types, concordance of expression increased with elevated expression of mRNA and protein[32] (Fig. 5d). Of the 363 genes being part of the mRNA core signature, 189 were detected by proteome analysis (Supplementary Data 4). Using only those mRNA core signature genes and plotting fold-changes between $CX3CR1^+$ and naïve $CD8^+$ T cells on mRNA and protein levels revealed that the majority of these cell-type characterizing genes demonstrated concordant gene regulation (Fig. 5e).

To further validate these findings, we next generated a proteome-based signature for $CX3CR1^+$ $CD8^+$ T cells following the approach visualized in Fig. 4a, which resulted in 165 proteins (Supplementary Data 5). We then used these proteins to annotate the corresponding mRNA data for plotting fold-changes between $CX3CR1^+$ and naïve $CD8^+$ T cells on protein and mRNA levels (Fig. 5f). Again, except for seven genes, we found concordant gene regulation between proteome and transcriptome suggesting that post-transcriptional regulation is not highly relevant for these core signature genes in $CX3CR1^+$ T cells. Next, we determined the overlap of both approaches to reveal a set of 65 signature genes to be highly upregulated in $CX3CR1^+$ T cells both on mRNA and protein level (Supplementary Data 6). Functionally, these genes are best described by GOEA with the terms immune cell activation, immune response, defense response, cytolysis, cell adhesion and chemotaxis reminiscent with an activated immune cell (Fig. 5g). Taken together, this mathematical modelling of gene and protein expression demonstrates the value of CX_3CR1 as a marker to identify distinct populations of memory $CD8^+$ T cells that correlate with their functional properties. Furthermore, we establish a core gene and protein signature that identifies memory $CD8^+$ T cells with cytotoxic effector functions. Finally, we identify a close similarity between CX_3CR1-expressing memory T cells irrespective of their CD62L expression.

CX_3CR1^+ $CD62L^{hi}$ $CD8^+$ T cells are a resident effector memory population in lymph nodes. $CX_3CR1^+CD62L^{hi}CD8^+$ memory T cells closely resembled $CX_3CR1^+CD62L^{low}CD8^+$ memory T cells but were clearly distinct from CX_3CR1^{neg} $CD62L^{hi}CD8^+$ memory T cells in functional assays (Fig. 2) and transcriptome/proteome analyses (Figs 4 and 5). As indicated by their CD62L expression, we investigated whether CX_3CR1^+ $CD8^+$ memory T cells were present in lymph nodes of $CX_3CR1^{+/GFP}$ reporter mice. Sixty days after viral or bacterial infection, GFP^+ (CX_3CR1^+) $CD62L^{hi}CD8^+$ T cells constituted about 20–40% of antigen-specific memory $CD8^+$ T cells in lymph nodes (Fig. 6a,b and Supplementary Fig. 6A). Similarly, we detected GFP^+ (CX_3CR1^+) memory $CD8^+$ T cells in the white pulp of the spleen (Supplementary Fig. 6B). Although little is known about the heterogeneity of memory T cells present within lymph nodes, two distinct positioning and migration patterns have been described[8]. Therefore, we investigated whether CX_3CR1^+ and CX_3CR1^{neg} $CD8^+$ memory T cells differed in their positioning within the lymph node. Confirming our previous results[8], we found that $CD8^+$ memory T cells were not located in the deep paracortex as naïve T cells, but instead were found at the peripheral paracortex and the subcapsular sinus area. This differential positioning of memory versus naïve $CD8^+$ T cells was even further pronounced for CX_3CR1^+ memory $CD8^+$ T cells (Fig. 6c,d). $CX_3CR1^+CD8^+$ memory T cells had a lower velocity and scanned their environment more slowly than CX_3CR1^{neg} $CD8^+$ memory T cells, as analysed by intravital two-photon microscopy (Fig. 6e and Supplementary Movie 1). We did not observe $CX_3CR1^+CD8^+$ memory T cells exiting the lymph node, which prompted us to investigate the transit time of memory T-cell populations in the lymph node. We therefore blocked T-cell entry into lymph nodes by anti-CD62L-antibody application (Supplementary Fig. 6B,C). As a result, the numbers of naïve $CD8^+$ T cells and to a lesser extent of GFP^{neg} (CX_3CR1^{neg}) memory $CD8^+$ T cells declined in lymph nodes (Fig. 6f,g and Supplementary Fig. 6C,D). The numbers of GFP^+ (CX_3CR1^+) memory $CD8^+$ T cells, however, remained unaltered over a period of 6 days (Fig. 6f,g and Supplementary Fig. 6B,C). Taken together, CX_3CR1^+ memory $CD62L^{hi}CD8^+$ T cells represent a so far unrecognized lymph node-resident T-cell population positioned in vicinity of $CD169^+$ macrophages at the subcapsular sinus in anticipation of pathogens that invade via the lymphatic system. Having established CX_3CR1 as a marker that identifies memory $CD8^+$ T cells with cytotoxic function across tissues, we next aimed to analyse the abundance of such cells in the context of resolved and chronic viral infections.

Infection control correlates with $CX_3CR1^+CD8^+$ T-cells. We investigated the frequencies of virus-specific $CX_3CR1^+CD8^+$ T cells in patients suffering from chronic viral infection, such as chronic Hepatitis B and chronic Hepatitis C. As expected, we could only rarely detect virus-specific $CX_3CR1^+CD8^+$ T cells in the blood of these patients (Fig. 7a), in contrast to cytomegalovirus (CMV)-specific $CD8^+$ T cells from the same donors (Fig. 7a). In some but not all chronic Hepatitis C patients, we found few hepatitis C virus (HCV)-specific $CD8^+$ T cells that expressed CX_3CR1 and also co-expressed GzmB as well as perforin (Fig. 7b,c and Supplementary Fig. 7A), whereas CX_3CR1^{neg} HCV-specific $CD8^+$ T cells did not show GzmB or perforin expression (Fig. 7b,c). We did not detect GzmB or perforin

NATURE COMMUNICATIONS | DOI: 10.1038/ncomms9306 ARTICLE

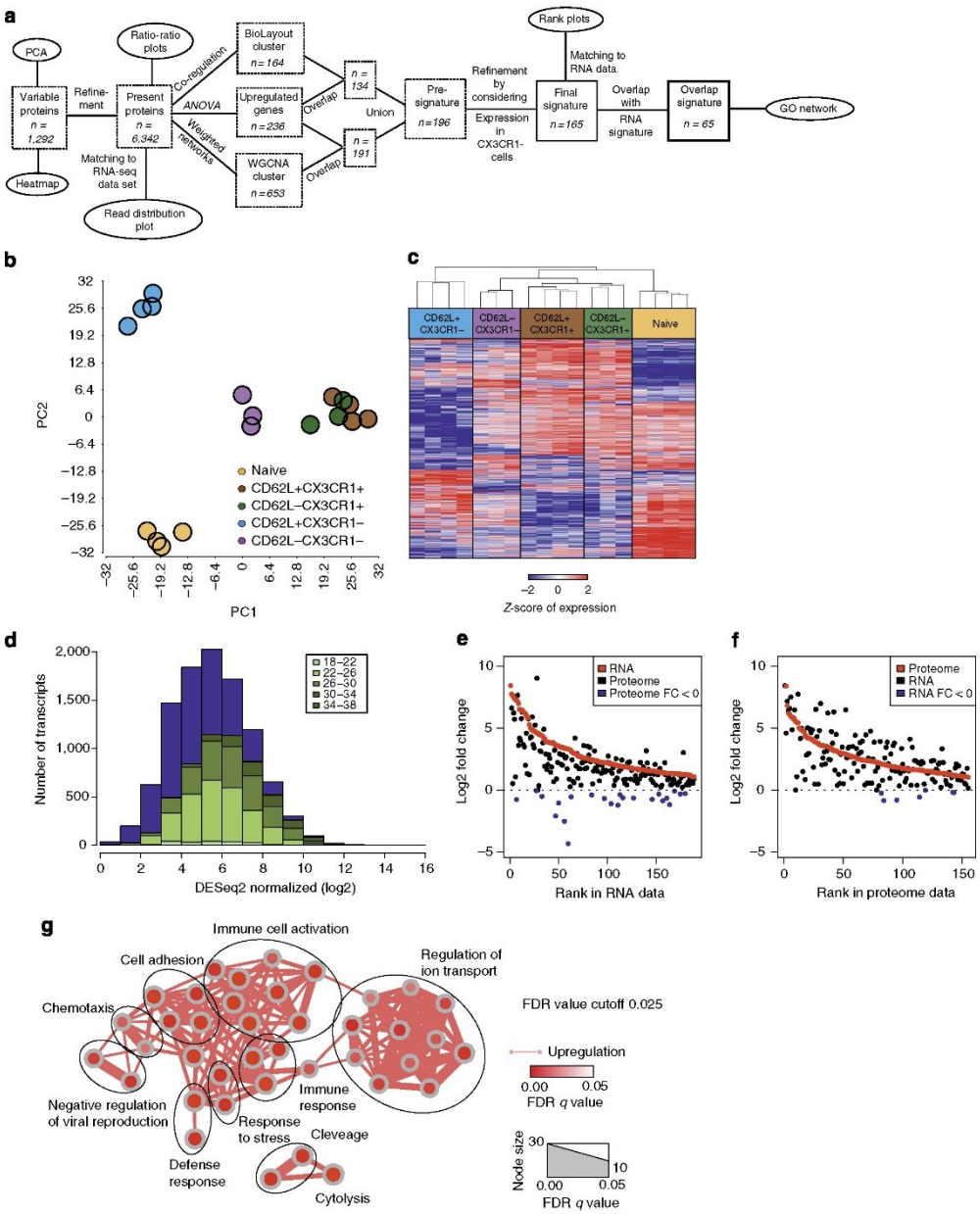

Figure 5 | Proteome signature of human CX_3CR1^+ memory $CD8^+$ T cells with effector function. (**a**) Scheme describing the workflow for analysis of proteome data. (**b**) Principal component analysis (PCA) based on present and variable proteins. (**c**) Heat map showing the z-transformed expression values of present and variable proteins, coloured from blue to red. (**d**) Histogram of normalized RNA-seq expression values of present genes subdivided according to the corresponding log2-transformed protein expression. Violet bars illustrate expression values and amounts of all present transcripts, whereas green-shaded bars represent expression values and amounts of transcripts matched to proteins. (**e**) Fold change rank plot of RNA-seq signature genes (red) with overlay of ranks of the corresponding proteins (black). Proteins having a log2-fold change lower than 0 are marked in blue. (**f**) Fold change rank plot of protein signature genes (red) with overlay of ranks of the corresponding RNA-seq genes (black). Genes having a log2-fold change lower than 0 are marked in blue. (**g**) Network visualization of Gene Ontology Enrichment Analysis using BiNGO and EnrichmentMap based on the 65 genes overlapping between the transcriptome and proteome signatures. Enriched GO terms are depicted by red nodes, where colour and size represent the corresponding FDR-adjusted enrichment *P*-value (*q*-value) < 0.025.

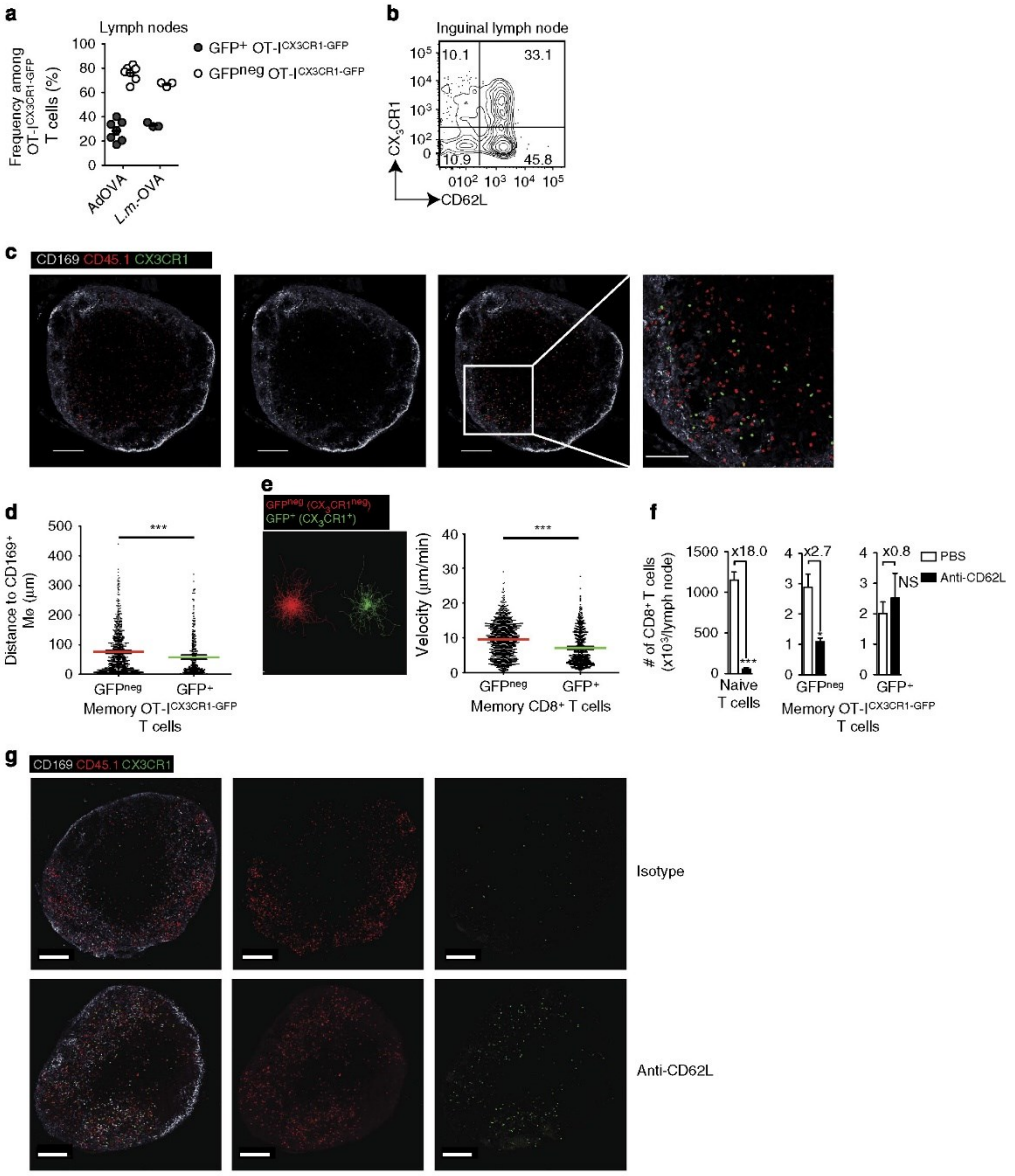

Figure 6 | CX_3CR1 identifies a distinct population of $CD8^+$ memory T cells in lymph nodes. (**a**) Quantification of GFP^+ and GFP^{neg} memory OT-$I^{CX3CR1\text{-}GFP}$ T cells within lymph nodes >45 d.p.i. with AdOVA ($n=7$) or *L.m.*-OVA ($n=3$). (**b**) Representative flow cytometric analysis of GFP and CD62L expression in memory OT-$I^{CX3CR1\text{-}GFP}$ T cells isolated from lymph nodes. (**c**) Confocal immunofluorescence images of popliteal lymph nodes from a mouse harbouring CX_3CR1^{neg} and CX_3CR1^+ memory OT-$I^{CX3CR1\text{-}GFP}$ T cells. Scale bar, 200 µm; zoom 100 µm). (**d**) Relative distance of CX_3CR1^{neg} and CX_3CR1^+ memory $CD8^+$ T cells from $CD169^+$ MΦ within popliteal lymph nodes. $^{***}P<0.001$, *t*-test. (**e**) Track length and average speed comparing CX_3CR1^{neg} and CX_3CR1^+ memory $CD8^+$ T cells in the steady state in the interfollicular area over 1 h. $^{***}P<0.001$, *t*-test. (**f**,**g**) At 60 days after adoptive transfer of naïve $CD45.1^+$ OT-$I^{CX3CR1\text{-}GFP}$ T cells (1×10^3) and AdOVA infection, mice were injected daily with anti-CD62L neutralizing antibody (100 µg per mouse i.p.) or PBS over a period of 6 days ($n=3$ per group). (**f**) Quantification of total numbers of endogenous naive $CD44^{low}CD8^+$ T cells, $GFP^{neg}CD44^+$ memory OT-$I^{CX3CR1\text{-}GFP}$ T cells and GFP^+CD44^+ memory OT-$I^{CX3CR1\text{-}GFP}$ T cells in inguinal lymph nodes. $^*P<0.05$, $^{***}P<0.001$ *t*-test. (**g**) Confocal immunofluorescence images of popliteal lymph nodes at 6 day after anti-CD62L antibody treatment. Scale bar, 200 µm. Data from one of at least two independent experiments are shown.

NATURE COMMUNICATIONS | DOI: 10.1038/ncomms9306

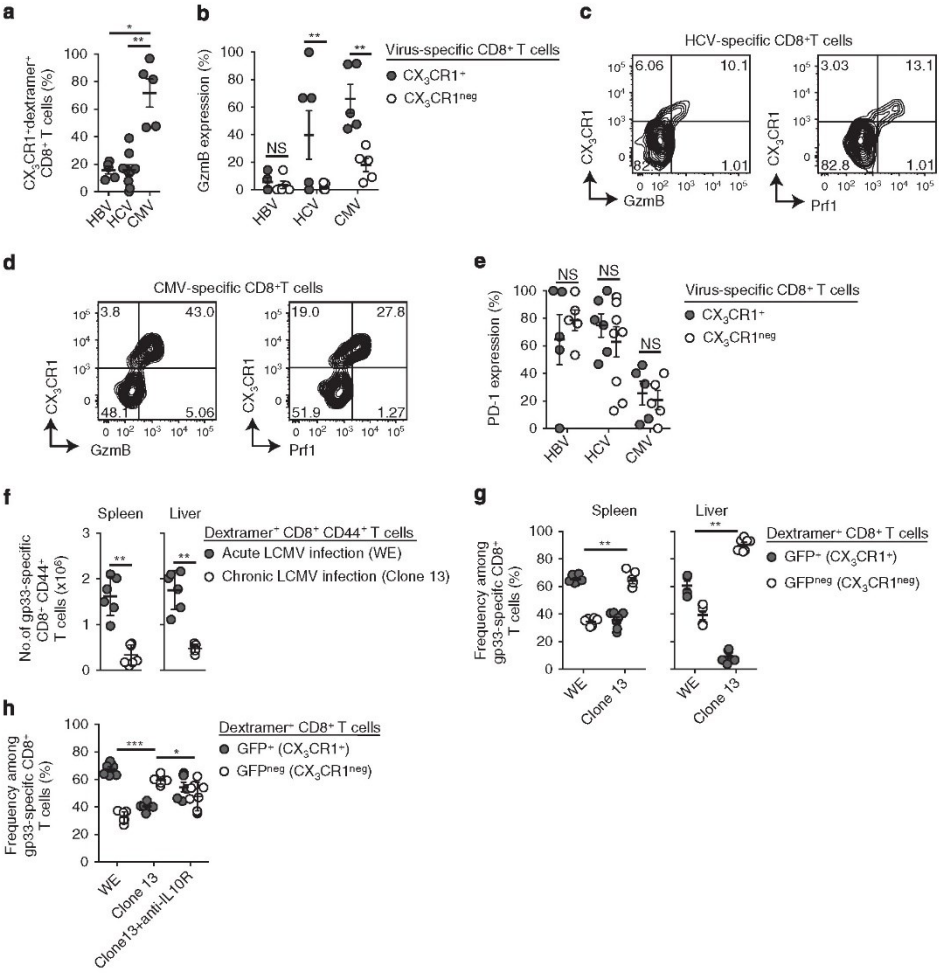

Figure 7 | Presence of CX_3CR1^+ $CD8^+$ T cells during acute resolved and chronic viral infection in man and mouse. (**a**–**e**) $CD8^+$ T cells isolated from the blood of human patients chronically infected with HBV or chronically infected with HCV were analysed for virus-specific $CD8^+$ T cells identified by tetramer staining. CMV-specific $CD8^+$ T cells from the same patients served as control. (**a**) Frequency of virus-specific CX_3CR1^+ $CD8^+$ T cells. $^*P<0.05$, $^{**}P<0.01$, *t*-test. (**b**) Flow cytometric analysis of intracellular GzmB expression in CX_3CR1^+ and CX_3CR1^{neg} virus-specific $CD8^+$ T cells. $^{**}P<0.01$, *t*-test. (**c**,**d**) Representative fluorescence-activated cell sorting (FACS) plots showing intracellular GzmB and perforin (Prf1) expression in (**c**) HCV-specific $CD8^+$ T cells and (**d**) CMV-specific $CD8^+$ T cells. (**e**) Flow cytometric analysis of PD-1 expression in CX_3CR1^+ and CX_3CR1^{neg} virus-specific $CD8^+$ T cells. (**f**–**h**) Analysis of LCMV gp33-specific $CD8^+$ T cells from $CX_3CR1^{+/GFP}$ mice 40 days after acute LCMV infection (WE strain; $n=6$) or chronic LCMV infection (Clone 13 strain, $n=7$). (**f**) Quantification of total gp33-specific $CD8^+$ T cells in the liver and spleen. $^{**}P<0.01$, *t*-test. (**g**) Frequency of GFP^+ (CX_3CR1^+) and GFP^{neg} (CX_3CR1^{neg}) cells among gp33-specific $CD8^+$ T cells. $^*P<0.05$, $^{**}P<0.01$, *t*-test. (**h**) Frequency of splenic GFP^+ (CX_3CR1^+) and GFP^{neg} (CX_3CR1^{neg}) gp33-specific $CD8^+$ T cells in response to anti-IL10R antibody treatment. $^*P<0.05$, $^{***}P<0.001$, ANOVA. **a**,**b**,**e** show data for at least five individual patients in each group, **c**,**d** show representative FACS plots for individual patients. Data in **f**–**h** is pooled from two to three independent experiments, error bars depict s.e.m.

expression in hepatitis B virus (HBV)-specific CD8 T cells in the blood of patients chronically infected with HBV (Fig. 7b). In contrast, we found many CMV-specific $CD8^+$ T cells from the same donors who co-expressed CX_3CR1^+ and GzmB and perforin (Fig. 7b,d). These results corroborated our findings that CX_3CR1^+ T cells have cytotoxic function and directly control viral infections. Of note, PD1 was similarly expressed in CX_3CR1^+ and CX_3CR1^{neg} virus-specific $CD8^+$ T cells in chronically infected patients (Fig. 7e), indicating that CX_3CR1 might more accurately reflect T-cell functionality than PD1 expression. These analyses revealed that virus-specific CX_3CR1^+ $GzmB^+$ $CD8^+$ T cells are found in controlled CMV infection and at low abundance during chronic viral infection in humans.

We next studied CX_3CR1 expression on virus-specific $CD8^+$ T cells during experimental infection with different LCMV clones in mice that is either resolved after acute infection (LCMV WE)

or develops into chronic infection (LCMV clone 13; Supplementary Fig. 7D). At 40 d.p.i., we detected significantly more LCMV-gp33-specific $CD8^+$ T cells in WE-infected compared with Clone 13-infected $CX_3CR1^{+/GFP}$ reporter mice in both the spleen and the liver (Fig. 7f). Among those, the frequency of GFP^+ (CX_3CR1^+) $CD8^+$ T cells was significantly increased in mice that successfully cleared acute LCMV WE infection compared with clone 13-infected mice (Fig. 7g). In chronically infected mice, GFP^{neg} (CX_3CR1^{neg}) $CD8^+$ T cells were abundant among LCMV-specific T cells at 40 d.p.i. (Fig. 7g). Next, we analysed whether successful therapeutic intervention would correlate with re-emergence of cytotoxic $CX_3CR1^+CD8^+$ T cells. To this end, we treated LCMV Clone13-infected mice with anti-IL-10 receptor antibodies. In line with published data[33,34], this treatment led to a two-log reduction in viral load (Supplementary Fig. 7E) and to an increase in the total numbers of LCMV-specific $CD8^+$ T cells (Supplementary Fig. 7F). This increase in LCMV-specific $CD8^+$ T cells was followed by an augmented frequency of GFP^+ (CX_3CR1^+) LCMV-specific $CD8^+$ T cells (Fig. 7h). Together, these results indicate that virus-specific CX_3CR1^+ memory T cells are also present during chronic viral infections albeit at much lower numbers than in resolved infection and that their numbers increase during successful therapeutic intervention.

Discussion

Discrete memory T-cell populations with complementary functions, executed in distinct anatomic locations, cooperate to mediate immune protection from repeated infection with intracellular pathogens. Lymphoid tissue homing receptors such as CD62L and CCR7 have been employed to distinguish between $CD62L^{hi}CCR7^+$ TCM that home to lymphoid tissues where they proliferate upon re-challenge and $CD62L^{low}CCR7^{neg}$ TEM that remain in the circulation and peripheral tissues where they mount immediate cytotoxic effector function[5]. We identify CX_3CR1 as the marker that differentiates memory $CD8^+$ T cells with direct cytotoxic effector function generated in response to viral or bacterial infections. CX_3CR1 expression allows their discrimination from memory T cells with proliferative potential. Using CX_3CR1 together with CD62L as markers, it is possible to stratify memory $CD8^+$ T cells in man and mouse into four populations. Genome-wide transcriptome and in-depth proteome analyses provided independent evidence that CX_3CR1 separates functionally distinct memory $CD8^+$ T-cell populations and allowed us to establish for the first time a core gene and protein signature of memory $CD8^+$ T cells with cytotoxic effector function. Based on these results, we identify a so far unrecognized memory $CX_3CR1^+CD62L^{hi}$ $CD8^+$ T-cell population with cytotoxic effector function that localizes to the subcapsular sinus of lymph nodes.

Human and mouse CX_3CR1^+ $CD8^+$ T cells co-expressed cytotoxic effector molecules (GzmB and perforin) and showed potent cytotoxicity but had no proliferative capacity. Expression of CX_3CR1 on virus-specific $CD8^+$ T cells appeared shortly after clearance of experimental infection, then steadily increased to reach a plateau 2 weeks and was still found up to 200 days after infection. This suggests that early effector T cells, which are generated during the initial phases of the pathogen-specific immune response[35], do not express CX_3CR1. However, CX_3CR1 is expressed shortly thereafter, presumably on both effector T cells and early memory T cells.

After clearance of infection, only long-lived memory $CD8^+$ T cells with immediate cytotoxic effector function expressed CX_3CR1. Some but not all CX_3CR1^+ memory T cells also showed expression of KLRG1, consistent with the reported expression of KRLG1 on some memory T cells[6]. $CX_3CR1^+CD8^+$ T cells found 60 days after infection showed a heterogeneous expression pattern of CD127, indicating that these cells may not exclusively depend on homeostatic survival signals delivered through the IL-7 receptor[27]. Instead CX_3CR1 itself may promote survival of memory $CD8^+$ T cells, similar to the dependence of survival myeloid cells on CX_3CR1 expression[36]. Expression of CX_3CR1 has been reported previously for myeloid cells, such as monocytes, macrophages and microglia[37,38], but also for $CD4^+$ helper T cells that cause persistent airway inflammation[17] and for terminally differentiated effector $CD8^+$ T cells[20,39]. Furthermore, CX_3CR1 is important for leukocyte migration and adhesion[40] and recruitment of cytotoxic T cells to sites of inflammation is achieved through CX_3CL1-expressing cells[20,39]. We did not find evidence for changes in the functional phenotype of CX_3CR1-deficient memory $CD8^+$ T cells, indicating that CX_3CR1-mediated signals are not the cause of direct cytotoxic effector functions in memory T cells.

Notwithstanding, CX_3CR1 expression accurately distinguished human and mouse memory T cells with direct cytotoxic effector functions from those with proliferative potential. Together with CD62L expression levels, four $CD45RO^+$ $CD8^+$ T-cell populations can be separated: CX_3CR1^{neg} $CD62L^{hi}CD8^+$, $CX_3CR1^{neg}CD62L^{low}$, $CX_3CR1^+CD62L^{hi}$ and CX_3CR1^+ $CD62L^{low}$ $CD8^+$ T cells. Transcriptome and proteome analysis of these cell populations revealed that CX_3CR1 was superior to CD62L to classify distinct memory $CD8^+$ T-cell populations based on functional properties. This allowed us to establish a core signature shared by memory $CD8^+$ T cells with cytotoxic function independent of their tissue localization. This core signature consists of 363 genes and contains granzymes, perforin, FASL and IFN-γ. The list further entails genes coding for transcription factors associated with effector function such as *Tbx21*, *Batf*, *Nfat*, *Runx3* (refs 41–43) and surface molecules found on NK cells such as CD57 (B3GAT1), CD160, killer cell lectin receptors and NKG7 (ref. 44) or signalling molecules such as SLAM genes that participate in NK cell function and T -ell differentiation[45]. Many of the core signature genes are also present in the proteome. Some proteins in the core signature, however, are not found in the gene signature such as s100 proteins, which exert alarm functions upon further oxidative modifications[46]. Although expression of these molecules known to be related to cytotoxic effector functions confirms the CX_3CR1-based core signature, this list will help to refine human immune monitoring to guide immune therapies and initiate research into molecular pathways not yet associated with cytotoxic memory T-cell function.

CX_3CR1 expression was found on $CD62L^{low}$ as well as $CD62L^{hi}$ memory $CD8^+$ T cells and transcriptome and proteome profiles of these two cell populations were almost identical. Based on these analyses both $CX_3CR1^+CD62^{low}$ T cells and $CX_3CR1^+CD62^{hi}$ memory T cells are best described as memory T cells with effector function. High CD62L expression suggested that some CX_3CR1^+memory T cells with effector function could localize to lymph nodes. Indeed, CX_3CR1^+ memory $CD8^+$ T cells were found in lymph nodes more than 60 days after viral and bacterial infection. These $CX_3CR1^+CD8^+$ T cells localized to the subcapsular sinus and showed prolonged and continuous interactions with $CD169^+$ macrophages, thus taking a strategic position where pathogens entering lymphoid tissues via afferent lymphatics are in first contact with immune cells[8]. It is possible that CX_3CR1^+ $CD8^+$ T cells in the lymph node may contribute to pathogen-specific immunity through immediate production of IFN-γ, that is required for rapid initiation of immune responses[8,47], after recognizing subcapsular

macrophages (cross)presenting microbial antigens. Such rapid induction of IFN-γ may initiate CXCL9-mediated recruitment of CXCR3-expressing memory T cells with proliferative potential[48] thereby causing timely induction of T-cell expansion upon local pathogen encounter in lymph nodes. They may further help to contain pathogens within this anatomic compartment through killing of infected macrophages[8]. $CX_3CR1^+CD62L^{hi}$ $CD8^+$ T cells may therefore complement innate lymphoid cells to rapidly mount immune responses in the lymph node[8]. Of note, CX_3CR1^+ $CD8^+$ T-cell numbers in lymph nodes did not decline despite blockade of lymphocyte re-entry with function-blocking CD62L antibodies, which suggested that these cells remained in lymph nodes for long periods of time. Alternatively, CX_3CR1^+ $CD8^+$ T cells might be superior to CX_3CR1^{neg} $CD8^+$ T cells in their ability to enter lymph nodes via alternative, CD62L-independent routes. The mechanisms determining positioning and retention of CX_3CR1^+ $CD8^+$ T cells in lymph nodes and the role of CX_3CR1^+ $CD8^+$ T cells in lymphoid tissues for induction of pathogen-specific immunity might be assisted by the CX_3C chemokine interface[39] but require further investigation.

Another memory T-cell population (TRM) with effector function is resident in epithelial tissues like the skin, gut and lung after local infection[49–51]. TRM develops locally through signalling by IL-15 and transforming growth factor-β from $KLRG1^{neg}$ T cells and are identified by expression of CD103 and CD69 (ref. 52). Both markers are absent from the core signature for memory $CD8^+$ T cells with direct cytotoxic function. Furthermore, the core signature of TRM[52] is distinct from the core signature of CX_3CR1^+ $CD8^+$ T cells. This suggests that TRM and CX_3CR1^+ memory $CD8^+$ T cells with cytotoxic effector function develop via separate pathways, which is supported by the expression in CX_3CR1^+ $CD8^+$ T cells of SMAD7 that regulates transforming growth factor-β-induced signalling[53]. Our finding of $CX_3CR1^{neg}CD62L^{low}CD8^+$ T cells, however, as memory T cells with proliferative potential that do not recirculate to lymphoid tissues and lack KLRG1 expression, may indicate that these cells are a source for TRM in epithelial tissues. As $CX_3CR1^{neg}CD62L^{hi}$ memory $CD8^+$ T cells in lymphoid tissue give rise to CX_3CR1^+ T cells with cytotoxic function, it is possible that $CX_3CR1^{neg}CD62L^{low}CD8^+$ T cells in response to local cues in epithelial tissues give rise to TRM, which provide local tissue protection independently from cytotoxicity by IFN-γ-mediated induction of anti-bacterial and anti-viral genes[54].

Chronic viral infection develops because of the immune system's inability to eliminate or control acute viral infection. Among the many factors contributing to such failure of immunity, deletion of virus-specific T cells and development of dysfunctional T cells with high expression of co-inhibitory receptors, such as PD1, TIM3 or CTLA4, leading to a dysregulated pattern of gene expression[55], are believed to be key for chronicity of viral infection[56–59]. In patients with chronic HCV infection, we found low numbers of circulating virus-specific $CX_3CR1^+CD8^+$ T cells that co-expressed GzmB and perforin. Only few virus-specific $CX_3CR1^+CD8^+$ T cells, which lacked GzmB expression, were detected in patients with chronic HBV infection, whereas high numbers of GzmB-expressing $CX_3CR1^+CD8^+$ T cells were found in CMV-specific $CD8^+$ T cells. PD1 expression was similar on both, CX_3CR1^+ and CX_3CR1^{neg} virus-specific $CD8^+$ T cells, indicating that CX_3CR1 expression may help to differentiate between PD1 as marker for recently activated T cells or as marker for dysfunctional T cells. Experimental LCMV infection studies in mice revealed a high ratio of virus-specific CX_3CR1^+ to CX_3CR1^{neg} $CD8^+$ T cells in resolved infection, whereas an inverted ratio was observed during chronic LCMV infection. It remains to be determined whether conversion from CX_3CR1^+ to CX_3CR1^{neg} $CD8^+$ T cells can occur and causes the observed decrease in $CX_3CR1^+CD8^+$ T cells in chronic infection. In contrast to the almost identical transcriptome and proteome profiles of $CD62L^{hi/low}CX_3CR1^+$ $CD8^+$ T cells, the profiles of $CX_3CR1^{neg}CD62L^{low}$ $CD8^+$ T cells and $CX_3CR1^{neg}CD62L^{hi}$ $CD8^+$ T cells were distinct. It is possible that $CX_3CR1^{neg}CD62L^{low}CD8^+$ T cells comprise a heterogeneous population of cells that contain T cells with proliferative potential that do not relocate to lymphoid tissues but also T cells that were previously CX_3CR1^+. Blockade of IL-10 signalling, which is known to strengthen anti-viral immunity during chronic infection[34], re-invigorated numbers of virus-specific $CX_3CR1^+CD8^+$ T cells and consequently lead to a two-log reduction in viral load, suggesting that $CX_3CR1^+CD8^+$ T cells might be sensitive to IL-10-mediated regulation *in vivo*.

Taken together, the use of CX_3CR1 as marker for identification of memory $CD8^+$ T cells with cytotoxic function will help to further our understanding of the principles of T-cell memory and immune protection. Detection of virus-specific CX_3CR1^+ $GzmB^+CD8^+$ T cells in patients with chronic viral infections suggests ongoing yet attenuated anti-viral immunity[4]. Identification of memory $CD8^+$ T cells with immediate cytotoxic function through the core signature defined here will foster the establishment of refined immune monitoring that will allow for improved guidance of immune therapies.

Methods

Mice. C57BL/6, CD90.1$^+$ C57BL/6, CX3CR1$^{+/GFP}$ (obtained from the Jung Lab), OT-I$^{CX3CR1\text{-}GFP}$ (CX3CR$^{+/GFP}$ x T-cell receptor transgenic OT-I), tdTomato OT-I$^{CX3CR1\text{-}GFP}$ and CD45.1$^+$ OT-I$^{CX3CR1\text{-}GFP}$ mice were bred under specific pathogen-free conditions in the central animal facility of the University Hospital Bonn. Mice were kept under specific pathogen-free conditions and *in vivo* experiments were approved by the Local Animal Care Commission of Northrhein Westphalia. Experiments were conducted with sex-matched female or male mice, aged 8–12 weeks at the start of each experiment.

Generation and analysis of murine memory CD8$^+$ T cells. To generate OT-I-derived memory T cells, low numbers (5×10^2 cells) of FACSorted naive CD44^{low} GFP^{neg} CD45.1$^+$ OT-I$^{CX3CR1\text{-}GFP}$ T cells were adoptively transferred into sex-matched CD45.2$^+$ recipient mice. Four hours later, mice were either infected with 5×10^3 colony-forming units *L.m.*-OVA by i.p. injection or infected with 5×10^6 plaque-forming units (PFUs) AdOVA. Memory OT-I cells were identified by the expression of the congenic marker CD45.1 in conjunction with a CD8$^+$CD44$^+$CD127$^+$ phenotype. TCM (CD62L^{hi}) and TEM (CD62L^{low}) were distinguished by CD62L expression. For functional analysis or adoptive transfer experiments, CD8$^+$ T cells were isolated from the spleen by enrichment with autoMACS (untouched CD8$^+$ T cell isolation kit, Miltenyi) followed by sorting for the respective markers on a BD Aria III. Experiments were performed with CD44$^+$CD127$^+$ memory CD8$^+$ T cells taken from the spleen at 45–70 d.p.i. if not indicated otherwise.

Infection models and *in vivo* bioluminescence imaging. *Listeria infection*. Mice were infected i.p. with *Listeria monocytogenes*-expressing OVA (*L.m.*- OVA) acquired from log phase of growth in BHI medium. 5×10^3 colony-forming units were used to generate memory T cells.

Adenovirus infection. Recombinant adenovirus expressing either OVA (AdOVA), GFP (AdGFP) or OVA and luciferase as fusion protein (AdOVALUC) were produced in 293 cells and purified by Cs-chlorid gradient ultracentrifugation as described previously[21]. Mice were infected with 5×10^6 PFU AdOVA by intravenous injection (i.v.) for generation of memory T cells. 1×10^7 PFU of AdOVA or AdGFP were used in re-challenge experiments to assess GzmB upregulation by memory T cells. Measurement of bioluminescence in livers of C57BL/6 mice was performed as described previously[21]. In brief, *in vivo* bioluminescence was analysed after intravenous infection with 1×10^7 PFU AdOVALUC using an IVIS 200 system (Caliper LifeSciences) 5 min after i.p. injection of Luciferin (50 mM in PBS, Caliper LifeSciences). Data analysis was performed with Living Image 2.50.1 software (Caliper LifeSciences).

LCMV infection. To generate gp-33-specific memory T cells, CX3CR1$^{+/GFP}$ mice were infected intravenously (i.v.) with 2×10^4 PFU of lymphocytic choriomeningitis virus WE-strain (LCMV WE). Mice were infected intravenously with 2×10^6 PFU of LCMV Clone13 or with 2×10^4 PFU of LCMV WE. Titres of virus were determined by plaque assay on Vero cells.

Isolation of human CD8$^+$ T cells. Peripheral blood mononuclear cells (PBMCs) were obtained from patients chronically infected with HBV, HCV, and healthy donors visiting the outpatient clinic of the University Hospital Freiburg. All donors gave written informed consent according to the local ethic committee's of the University hospital Freiburg ruling, federal laws and the Declaration of Helsinki. PBMCs were isolated using density-gradient centrifugation (Pancoll; PAN Biotech, Aidenbach, Germany).

For some experiments, CD8$^+$ T cells were isolated by autoMACS separation (Miltenyi) using anti-human CD8 Microbeads (Miltenyi). Virus-specific CD8$^+$ T cells were analysed using the following APC-labelled MHC class I-tetrameric complexes: HLA-A*02/HBV core18–27 (FLPSDFFPSV), HLA-A*02/HBV pol455–463 (GLSRYVARL), HLA-A*02/HCV NS31073–1081 (CINGVCWTV), HLA-A*02/HCV NS31406-1415 (KLVALGINAV), HLA-A*02/HCV NS5B2594–2602 (ALYDVVTKL), HLA-B*27/HCV NS5B2841–2849 (ARMILMTHF), HLA-A*02/CMV pp65495-503 (NLVPMVATV). PBMCs were stained with tetramer for 15 min at 37 °C and blocked with murine IgG1 before further staining for surface markers or intracellular cytotoxic proteins.

Analysis of memory T-cell functions and regulation of T-cell function *in vivo*. To analyse cytokine production, restimulation of FACSorted memory T cells was performed with phorbol myristate acetate (PMA) (5 ng ml^{-1}; Sigma-Aldrich) and Ionomycin (200 ng ml^{-1}, Sigma) for 4.5 h in the presence of Brefeldin A and Monensin (eBioscience). Restimulation of murine memory T cells from CX3CR1$^{+/GFP}$ mice (CD90.2$^+$) was performed in co-culture with CD90.1 splenocytes as feeder cells. Determination of antigen-specific cytotoxicity against peptide-loaded target cells was determined *in vitro* as described[60]. Analysis of intracellular GzmB expression was performed directly after isolation of memory T cells *ex vivo* without further stimulation.

Blockade of memory T-cell recirculation in vivo. To block access of circulating CD62L$^+$ memory T cells to lymph nodes, mice were injected with 100 µg of anti-CD62L antibody (clone MEL14) or PBS as control i.p. over a period of 6 days before analysis.

In vivo IL-10R blockade during chronic LCMV infection. Mice received i.p. five times 250 µg per mouse of IL-10R-specific antibody (clone 1B1.3a; Bio X Cell) or rat IgG isotype control antibody (clone KM1.GL113 Bio X Cell) each third day beginning at 25 d.p.i.

Flow cytometry and fluorescence-activated cell sorting. Flow cytometric analyses and assessment of mean fluorescence intensity were conducted with a LSR Fortessa (BD Biosciences). Data were analysed using FlowJo software (Tree Star). LIVE/DEAD Fixable Stain kit (Invitrogen) was used to exclude dead cells in all experiments with murine cells, anti-CD16/32 antibody (2.4G2) was used to block unspecific antibody binding via Fc receptors. Human cells were stained in PBS. The following antibodies (purchased from BioLegend or eBioscience) were used for murine samples: CD3 (17A2, dilution 1:200), CD8α (clone 53-6.7, 1:200), CD44 (IM7, 1:300), CD45.1 (A20, 1:200), CD62L (MEL-14, 1:300), CD90.1 (HIS51), 1:400, CD90.2 (HIS51, 1:400), CD127 (ebioSB/199, 1:200), IL-2 (JES6-5H4, 1:200) and IFN-γ (XMG1.2, 1:200). The following antibodies were used for human samples: CD3 (HIT3a, 1:50), CD8 (RPA-T8, 1:10), CD45RA (HI100, 1:25), CD45RO (UCHL1, 1:50), CD62L (DREG-56, 1:50), PD-1 (EH12.2H7, 1:25), CX3CR1 (2A9-1, 1:25), CCR7 (4B12, 1:25) and Perforin (dG9, 1:50). For intracellular staining of cytokines, cells were fixed in 4% PFA and intracellular staining by anti-IFN-γ or anti-IL-2 was performed in Permeabilization Buffer (eBioscience) for 30 min. Staining of Granzyme B (anti-human, cross-reactive with mouse, clone GB11, 1:100) was performed using the Foxp3/Transcription factor staining buffer set from eBioscience. All intracellular stainings in murine cells were done in combination with polyclonal anti-GFP antibody (Life Technologies, Invitrogen; dilution 1:500). Quantification of cell numbers was done with fluorochrome-labelled microbeads (CountBright absolute counting beads, Life Technologies, Invitrogen). Fluorescence-activated cell sorting of splenic naive (CD44^{low}GFP^{neg}) or memory (CD44^{hi}CD127$^+$) CD8$^+$ T cells was performed with an Aria III cell sorter (BD). Staining with the corresponding isotype antibody served as control. Antigen-specific endogenous memory T cells in mice were identified by staining with fluorochrome-conjugated H-2K$^{b:SIINFEKL}$ dextramers (AdOVA and L.m.-OVA infection; Immudex) or H-2D$^{b:KAVYNFATC}$ dextramers (LCMV infection; Immudex) according to the manufacturer's protocol.

Immunofluorescence staining. Lymph node and spleens were harvested and fixed using PLP buffer (0.05 M phosphate buffer containing 0.1 M L-lysine (pH 7.4), 2 mg ml^{-1} $NaIO_4$ and 10 mg ml^{-1} paraformaldehyde) for 12 h, then dehydrated in 30% sucrose before embedding in OCT freezing media (Sakura Finetek). Thirty-micrometre sections were cut on a CM3050S cryostat (Leica), adhered to Superfrost Plus slides (VWR), stained, mounted with Fluormount G (Southern Biotech) and acquired on a 710 confocal microscope (Carl Zeiss Microimaging). Frozen sections were permeabilized and blocked in 0.1 M Tris (AppliChem) containing 0.3% Triton X-100 (GERBU Biotechnik), 1% FCS (Biochrom AG), 1% GCWFS (Sigma Aldrich) and 1% normal mouse serum (Life Technologies). Serial lymph node sections were prepared, each section was visually inspected using epifluorescent light microscopy, and several representative sections from different lymph node (LN) areas were acquired using confocal microscopy for detailed analysis. The following antibodies were used for staining: anti-CD8 (5H10; Invitrogen), anti-CD169 (c3D6.112; AbDSerotec), ER-TR7 (Santa Cruz Biotechnology), anti-B220 (RA3–6B2; Life Technologies), anti-F4/80 (BM8; BioLegend), anti-CD45.1 (A20; eBioscience). Unconjugated primary antibodies were stained with AF-conjugated secondary antibodies (Life Technologies). For CX_3CR1 detection, staining with a secondary rabbit anti-GFP (Life Technologies) was used to increase the signal. Primary antibodies were used at a concentration of 1:200, secondary antibodies at a concentration of 1:1,000.

Intravital two-photon imaging. Mice were anaesthetized with isoflurane (Abbott, Wiesbaden; 2.5% for induction, 1–1.5% for maintenance, vapourized in an 80:20 mixture of O_2 and air), popliteal LNs were exposed and intravital microscopy was performed using a protocol modified from a previous report[61]. For imaging of td-Tomato and GFP (CX_3CR1)-transgenic CD8$^+$ T cells, we used a Zeiss 780 microscope equipped with a Chameleon laser (Coherent) tuned to 930 nm and a ×20 water dipping lens (numerical aperture = 1.0, Zeiss, Jena). The microscope was enclosed in an environmental chamber, in which anaesthetized mice were warmed by heated air, and the surgically exposed lymph node was kept at 36–37 °C with warmed PBS. For dynamic imaging, we recorded a z-stack of 57 µm using 3 µm step size in the interfollicular area and acquired every 40 s. Raw imaging data were processed and analysed with Imaris software (Bitplane).

Analysis of microarray-based gene expression profiling data. We used a previously generated data set to identify genes associated with memory T cells (GSE63118). Genome Studio (Illumina) was used to profile the raw expression data, where probesets having missing bead types were excluded from the analysis. Processed data of 23 samples were imported into Partek Genomics Suite (PGS) software (v6.6; Partek Inc., log2-transformed and normalized using quantile normalization. Using a background log2-intensity of 6.7886, probesets showing a mean expression lower than this threshold in all five investigated groups were excluded, resulting in 20,515 defined present genes. Their expression values were standardized to a mean of zero and standard deviation of one, and the genes were clustered into 25 groups by using 20,000 training iterations to obtain a self-organizing map. For each condition, the clusters were visualized as heat map based on their eigenvalues, where increased values are shown in red, decreased values in blue and intermediate values in green.

RNA isolation and purification for RNA-seq analysis. Total RNA was extracted with QIAzol Lysis Reagent (Qiagen) and then purified using the miRNeasy Mini Kit (Qiagen) according to the manufacturers' recommendations. The RNA integrity (RNA Integrity Score ≥6.8) and quantity were determined on the Agilent 2100 Bioanalyzer (Agilent) per the manufacturer's recommendation and subjected to cDNA synthesis.

cDNA library preparation and RNA sequencing. To generate cDNA libraries, 1,000 pg total RNA were amplified and converted to cDNA using NuGEN's Ovation RNA-Seq kit V2. In brief, the mRNA was reverse transcribed to synthesize the first-strand cDNA by using a combination of random hexamers and a poly-T chimeric primer. Double-stranded DNA is generated by fragmentation of the mRNA template strand using RNA-dependent DNA polymerase. The double-stranded DNA was purified using Agencourt RNAClean XP beads. The DNA is amplified linearly using a SPIA process in which RNase H degrades RNA in DNA/RNA heteroduplex at the 5′-end of the double-stranded cDNA, after which the SPIA primer binds to the cDNA and the polymerase starts replication at the 3′-end of the primer by displacement of the existing forward strand. Finally, random hexamers were used to amplify the second-strand cDNA linearly. Following amplification, 5.0 µg cDNA was fragmented to ~200 bp using the Covaris S2 and the fragmentation parameters described in the Encore SP Rapid DR Multiplex library preparation protocol (NuGEN). The remainder of the library preparation followed the manufacturer's protocol as described in Encore SP Rapid DR Multiplex System. Paired-end sequencing of bar-coded cDNA libraries at 101 cycles (100 bases each end) was carried out on a HiSeq 1000. The raw sequence data have been deposited to GEO with accession number GSE63147.

Sample preparation for MS analysis. Cell pellets were washed in PBS and lysed in 6 M Guanidinium chloride (GdmCl), 10 mM HEPES (pH 8) and 10 mM dithiothreitol. Cells were heated for 10 min at 95 °C and sonicated for 15 min at 4 °C (level 5, Bioruptor, Diagenode). Cysteine residues were alkylated in the dark for 30 min with 55 mM iodacetamide. Lysates were diluted 1:3 with 50 mM ammoniumbicarbonate for a proteolytic digest with LysC (1:50, w/w, Wako) for 3 h. Samples were further diluted to 0.6 M GdmCl and digested with trypsin (1:50, w/w, Promega) at room temperature overnight. Buffer exchange was performed on C18 material (Empore, IVA-Analysetechnik). Peptide mixtures were eluted in 80% acteonitrile (ACN) and the organic solvent was removed by centrifugal evaporation. Cleaned peptides were resuspended in 2% ACN, 0.1% trifluoroacetic acid and 0.5% acetic acid.

LC-MS/MS. Peptides were separated on an EASY-nLC 1000 HPLC system (Thermo Fisher Scientific) coupled online to the Q Exactive mass spectrometer via a nanoelectrospray source (Thermo Fisher Scientific). Peptides were loaded in buffer A (0.5% formic acid) on in house packed columns (75 μm inner diameter, 50 cm length and 1.9 μm C18 particles from Dr Maisch GmbH). Peptides were eluted with a nonlinear 240 min gradient of 5–60% buffer B (80% ACN, 0.5% formic acid) at a flow rate of 250 nl min^{-1} and a column temperature of 50 °C. Operational parameters were real-time monitored by the SprayQC software. The Q Exactive was operated in a data-dependent acquisition mode with a survey scan range of 300–1,700 *m/z* and a resolution of 70,000 at *m/z* 200. Up to the five most abundant isotope patterns with a charge ≥2 were isolated with a 2.2 Thomson (Th) isolation window and subjected to higher-energy collisional dissociation fragmentation at a normalized collision energy of 25. Fragmentation spectra were acquired with a resolution of 17,500 at *m/z* 200. Dynamic exclusion of sequenced peptides was set to 45 s. Thresholds for ion injection time and ion target values were set to 20 ms and 3E6 for the survey scans and 120 ms and 1E5 for the MS/MS scans, respectively. Data were acquired using the Xcalibur software (Thermo Scientific).

MS data analysis. MaxQuant software (version 1.3.10.18) was used to analyse MS raw files[62]. MS/MS spectra were searched against the human Uniprot FASTA database (Version May 2013, 88'847 entries) and a common contaminants database (247 entries) by the Andromeda search engine. Cysteine carbamidomethylation was applied as fixed and N-terminal acetylation and methionine oxidation as variable modification. Enzyme specificity was set to trypsin with a maximum of two missed cleavages and a minimum peptide length of seven amino acids. A false discovery rate (FDR) of 1% was applied on peptide and protein level. Peptide identification was performed with an allowed initial precursor mass deviation of up to 7 p.p.m. and an allowed fragment mass deviation of 20 p.p.m. Nonlinear retention time alignment of all measured samples was performed in MaxQuant. Peptide identifications were matched across different replicates within a time window of 1 min of the aligned retention times. In addition, single shot runs were match against a T-cell peptide library built from single shot MS measurements of primary human T cells at various activation stages. Protein identification required at least 1 razor peptide. A minimum ratio count of 1 was required for valid quantification events via MaxQuant's Label Free Quantification algorithm (MaxLFQ). Data were filtered for common contaminants and peptides only identified by side modification were excluded from further analysis. In addition, a minimum of three valid quantifications in at least one group of biological replicates was required. Remaining missing values were imputed with random numbers from a normal distribution (mean-shift = 1.8; width = 0.3), to simulate low abundance values below the noise level.

Bioinformatics of RNA-seq data. RNA-Seq reads were aligned against the human reference genome hg19 using TopHat v2.0.11. To obtain transcript and gene information, the aligned reads were mapped against the hg19 RefSeq database Release 66 (ref. 63) using Partek Genomics Suite (PGS) software (v6.6; Partek Inc.). Annotated data were normalized using the DESeq2 package within the statistical software R version 3.0.2. In addition, normalized read counts lower than 1 were set equal to 1 to avoid spurious fold changes later on. The genes were filtered to those being present within the data set, defined as having a mean normalized read count larger than 10 in at least one of the investigated groups. Of those, the genes being variable ($P<0.05$) across the data set were visualized via principal component analysis and via a heat map based on z-transformed data using PGS. The list of present genes was then further analysed by three different methods to obtain a core signature for $CX3CR1^+$ $CD8^+$ T cells. Genes commonly and significantly upregulated in $CD62L^+$ $CX3CR1^+$ and $CD62L^-$ $CX3CR1^+$ T cells were identified by using an ANOVA model (FC > 2, FDR-corrected *P*-value < 0.05). Ratio/ratio plots were used to compare different cell populations on the single-gene level. Clusters of co-regulated genes were determined by applying the Markov Clustering (MCL) algorithm within BioLayout $Express^{3D}$ version 3.2 (ref. 64) with standard criteria on those genes showing a Pearson correlation of at least 0.85. Weighted correlation network analysis was performed in R using a power of 7, a minModuleSize of 30 and a MEDissThres of 0.3 resulting in 20 clusters. For the last two methods, the one cluster representing genes being highly expressed in $CX3CR1^+$ and only moderately expressed in $CX3CR1^-$ and naïve T cells were chosen. Each of these clusters was then intersected with the list of significantly upregulated genes, and the union of the two intersection lists containing 455 genes was considered as a pre-signature. To refine this signature, genes showing a fold change lower than 1.5 as well as an absolute expression value difference lower than 50 between $CX3CR1^+$ and $CX3CR1^-$ cells were removed. After finally excluding known polymorph MHCII genes, a signature of 363 genes remained. The distribution of expression values of those genes was displayed separately for all five conditions via boxplots. Sixty-five specific genes were visualized in form of a heat map based on z-transformed data. Finally, all 363 signature genes were linked to prior knowledge by performing GOEA using the $Cytoscape^{65}$ plug-in BiNGO (v2.44) with an FDR threshold of 0.05 to include only significant results. The Cytoscape plugins Enrichment Map (v1.1) with a Jaccard coefficient of 0.25 and an FDR *Q*-value cutoff of 0.025 as well as Word Cloud were used to visualize the GO network.

Bioinformatics of proteome data. Proteins being variable ($P<0.05$) across the data set were visualized via principal component analysis and via a heat map based on z-transformed data using PGS. To link the RNA-seq expression data to the protein data, the data sets were matched by using the UniProt database. The distribution of normalized RNA-seq expression values of present genes was visualized in the form of a histogram splitted into different protein expression classes. To obtain a core signature for CX_3CR1^+ $CD8^+$ T cells based on protein data, the same approach as used for the RNA-seq data was applied, harbouring only a few changes in terms of the used parameters. The MCL algorithm in BioLayout $Express^{3D}$ was applied on proteins showing a Pearson correlation of at least 0.8. For weighted correlation network analysis, a power of 18 and a MEDissThres of 0.5 were used. Collating the intersections of each CX_3CR1^+ cell representing cluster with the significantly and commonly upregulated proteins resulted in a pre-signature of 192 proteins. After excluding proteins encoded by known polymorph MHCII genes as wells as those proteins having an absolute expression difference of <1e + 06 between CX_3CR1^+ and CX_3CR1^- cells, a refined signature of 165 proteins remained. Fold change rank plots were used to map their change of expression to their corresponding change in the RNA-seq data set, as well as the same vice versa for the defined RNA-seq signature. Overlapping the transcriptome and proteome signatures resulted in 65 CX_3CR1^+-associated proteins, which generated a clearly refined GO network based on the same enrichment parameters as used for the transcriptome-based signature network.

Statistical analysis. The two-tailed Student's *t*-test was used for the statistical analysis of differences between two groups. Comparison of multiple groups was done using two-way ANOVA.

References

1. Harty, J. T., Tvinnereim, A. R. & White, D. W. CD8+ T cell effector mechanisms in resistance to infection. *Annu. Rev. Immunol.* **18,** 275–308 (2000).
2. Welsh, R. M., Selin, L. K. & Szomolanyi-Tsuda, E. Immunological memory to viral infections. *Annu. Rev. Immunol.* **22,** 711–743 (2004).
3. Kaech, S. M. & Cui, W. Transcriptional control of effector and memory CD8+ T cell differentiation. *Nat. Rev. Immunol.* **12,** 749–761 (2012).
4. Utzschneider, D. T. *et al.* T cells maintain an exhausted phenotype after antigen withdrawal and population reexpansion. *Nat. Immunol.* **14,** 603–610 (2013).
5. Sallusto, F., Lenig, D., Forster, R., Lipp, M. & Lanzavecchia, A. Two subsets of memory T lymphocytes with distinct homing potentials and effector functions. *Nature* **401,** 708–712 (1999).
6. Olson, J. A., McDonald-Hyman, C., Jameson, S. C. & Hamilton, S. E. Effector-like CD8(+) T cells in the memory population mediate potent protective immunity. *Immunity* **38,** 1250–1260 (2013).
7. Heath, W. R. & Carbone, F. R. The skin-resident and migratory immune system in steady state and memory: innate lymphocytes, dendritic cells and T cells. *Nat. Immunol.* **14,** 978–985 (2013).
8. Kastenmuller, W., Torabi-Parizi, P., Subramanian, N., Lammermann, T. & Germain, R. N. A spatially-organized multicellular innate immune response in lymph nodes limits systemic pathogen spread. *Cell* **150,** 1235–1248 (2012).
9. Hikono, H. *et al.* Activation phenotype, rather than central- or effector-memory phenotype, predicts the recall efficacy of memory CD8+ T cells. *J. Exp. Med.* **204,** 1625–1636 (2007).
10. Jameson, S. C. & Masopust, D. Diversity in T cell memory: an embarrassment of riches. *Immunity* **31,** 859–871 (2009).
11. Mueller, S. N., Gebhardt, T., Carbone, F. R. & Heath, W. R. Memory T cell subsets, migration patterns, and tissue residence. *Annu. Rev. Immunol.* **31,** 137–161 (2013).
12. Böttcher, J. P. *et al.* Liver-primed memory T cells generated under noninflammatory conditions provide anti-infectious immunity. *Cell Rep.* **3,** 779–795 (2013).
13. Jung, S. *et al.* Analysis of fractalkine receptor CX(3)CR1 function by targeted deletion and green fluorescent protein reporter gene insertion. *Mol. Cell. Biol.* **20,** 4106–4114 (2000).
14. Yona, S. *et al.* Fate mapping reveals origins and dynamics of monocytes and tissue macrophages under homeostasis. *Immunity* **38,** 79–91 (2013).
15. Bar-On, L. *et al.* CX3CR1+ CD8alpha+ dendritic cells are a steady-state population related to plasmacytoid dendritic cells. *Proc. Natl Acad. Sci. USA* **107,** 14745–14750 (2010).
16. Staumont-Salle, D. *et al.* CX(3)CL1 (fractalkine) and its receptor CX(3)CR1 regulate atopic dermatitis by controlling effector T cell retention in inflamed skin. *J. Exp. Med.* **211,** 1185–1196 (2014).
17. Mionnet, C. *et al.* CX3CR1 is required for airway inflammation by promoting T helper cell survival and maintenance in inflamed lung. *Nat. Med.* **16,** 1305–1312 (2010).

18. Wirth, T. C. *et al.* Repetitive antigen stimulation induces stepwise transcriptome diversification but preserves a core signature of memory CD8(+) T cell differentiation. *Immunity* **33,** 128–140 (2010).
19. Best, J. A. *et al.* Transcriptional insights into the CD8(+) T cell response to infection and memory T cell formation. *Nat. Immunol.* **14,** 404–412 (2013).
20. Nishimura, M. *et al.* Dual functions of fractalkine/CX3C ligand 1 in trafficking of perforin+/granzyme B+ cytotoxic effector lymphocytes that are defined by CX3CR1 expression. *J. Immunol.* **168,** 6173–6180 (2002).
21. Stabenow, D. *et al.* Bioluminescence imaging allows measuring CD8 T cell function in the liver. *Hepatology (Baltimore, MD)* **51,** 1430–1437 (2010).
22. Feau, S., Arens, R., Togher, S. & Schoenberger, S. P. Autocrine IL-2 is required for secondary population expansion of CD8(+) memory T cells. *Nat. Immunol.* **12,** 908–913 (2011).
23. Heusel, J. W., Wesselschmidt, R. L., Shresta, S., Russell, J. H. & Ley, T. J. Cytotoxic lymphocytes require granzyme B for the rapid induction of DNA fragmentation and apoptosis in allogeneic target cells. *Cell* **76,** 977–987 (1994).
24. Wherry, E. J. *et al.* Lineage relationship and protective immunity of memory CD8 T cell subsets. *Nat. Immunol.* **4,** 225–234 (2003).
25. Bachmann, M. F., Wolint, P., Schwarz, K., Jager, P. & Oxenius, A. Functional properties and lineage relationship of CD8+ T cell subsets identified by expression of IL-7 receptor alpha and CD62L. *J. Immunol.* **175,** 4686–4696 (2005).
26. Badovinac, V. P. & Harty, J. T. Manipulating the rate of memory CD8+ T cell generation after acute infection. *J. Immunol.* **179,** 53–63 (2007).
27. Kaech, S. M. *et al.* Selective expression of the interleukin 7 receptor identifies effector CD8 T cells that give rise to long-lived memory cells. *Nat. Immunol.* **4,** 1191–1198 (2003).
28. Huster, K. M. *et al.* Selective expression of IL-7 receptor on memory T cells identifies early CD40L-dependent generation of distinct CD8+ memory T cell subsets. *Proc. Natl Acad. Sci. USA* **101,** 5610–5615 (2004).
29. Boettler, T. *et al.* Expression of the interleukin-7 receptor alpha chain (CD127) on virus-specific CD8+ T cells identifies functionally and phenotypically defined memory T cells during acute resolving hepatitis B virus infection. *J. Virol.* **80,** 3532–3540 (2006).
30. Sarkar, S. *et al.* Functional and genomic profiling of effector CD8 T cell subsets with distinct memory fates. *J. Exp. Med.* **205,** 625–640 (2008).
31. Topp, M. S. *et al.* Restoration of CD28 expression in CD28- CD8+ memory effector T cells reconstitutes antigen-induced IL-2 production. *J. Exp. Med.* **198,** 947–955 (2003).
32. Nagaraj, N. *et al.* Deep proteome and transcriptome mapping of a human cancer cell line. *Mol. Syst. Biol.* **7,** 548 (2011).
33. Ejrnaes, M. *et al.* Resolution of a chronic viral infection after interleukin-10 receptor blockade. *J. Exp. Med.* **203,** 2461–2472 (2006).
34. Brooks, D. G. *et al.* Interleukin-10 determines viral clearance or persistence in vivo. *Nat. Med.* **12,** 1301–1309 (2006).
35. Joshi, N. S. *et al.* Inflammation directs memory precursor and short-lived effector CD8(+) T cell fates via the graded expression of T-bet transcription factor. *Immunity* **27,** 281–295 (2007).
36. Landsman, L. *et al.* CX3CR1 is required for monocyte homeostasis and atherogenesis by promoting cell survival. *Blood* **113,** 963–972 (2009).
37. Auffray, C., Sieweke, M. H. & Geissmann, F. Blood monocytes: development, heterogeneity, and relationship with dendritic cells. *Annu. Rev. Immunol.* **27,** 669–692 (2009).
38. Cardona, A. E. *et al.* Control of microglial neurotoxicity by the fractalkine receptor. *Nat. Neurosci.* **9,** 917–924 (2006).
39. Kim, K. W. *et al.* In vivo structure/function and expression analysis of the CX3C chemokine fractalkine. *Blood* **118,** e156–e167 (2011).
40. Imai, T. *et al.* Identification and molecular characterization of fractalkine receptor CX3CR1, which mediates both leukocyte migration and adhesion. *Cell* **91,** 521–530 (1997).
41. Kurachi, M. *et al.* The transcription factor BATF operates as an essential differentiation checkpoint in early effector CD8+ T cells. *Nat. Immunol.* **15,** 373–383 (2014).
42. Agnellini, P. *et al.* Impaired NFAT nuclear translocation results in split exhaustion of virus-specific CD8+ T cell functions during chronic viral infection. *Proc. Natl Acad. Sci. USA* **104,** 4565–4570 (2007).
43. Cruz-Guilloty, F. *et al.* Runx3 and T-box proteins cooperate to establish the transcriptional program of effector CTLs. *J. Exp. Med.* **206,** 51–59 (2009).
44. Lopez-Verges, S. *et al.* CD57 defines a functionally distinct population of mature NK cells in the human CD56dimCD16+ NK-cell subset. *Blood* **116,** 3865–3874 (2010).
45. Cannons, J. L., Tangye, S. G. & Schwartzberg, P. L. SLAM family receptors and SAP adaptors in immunity. *Annu. Rev. Immunol.* **29,** 665–705 (2011).
46. Lim, S. Y., Raftery, M. J., Goyette, J., Hsu, K. & Geczy, C. L. Oxidative modifications of S100 proteins: functional regulation by redox. *J. Leukoc. Biol.* **86,** 577–587 (2009).
47. Kastenmuller, W. *et al.* Peripheral prepositioning and local CXCL9 chemokine-mediated guidance orchestrate rapid memory CD8+ T cell responses in the lymph node. *Immunity* **38,** 502–513 (2013).
48. Sung, J. H. *et al.* Chemokine guidance of central memory T cells is critical for antiviral recall responses in lymph nodes. *Cell* **150,** 1249–1263 (2012).
49. Masopust, D., Vezys, V., Wherry, E. J., Barber, D. L. & Ahmed, R. Cutting edge: gut microenvironment promotes differentiation of a unique memory CD8 T cell population. *J. Immunol.* **176,** 2079–2083 (2006).
50. Wakim, L. M., Woodward-Davis, A. & Bevan, M. J. Memory T cells persisting within the brain after local infection show functional adaptations to their tissue of residence. *Proc. Natl Acad. Sci. USA* **107,** 17872–17879 (2010).
51. Gebhardt, T. *et al.* Different patterns of peripheral migration by memory CD4+ and CD8+ T cells. *Nature* **477,** 216–219 (2011).
52. Mackay, L. K. *et al.* The developmental pathway for CD103(+)CD8+ tissue-resident memory T cells of skin. *Nat. Immunol.* **14,** 1294–1301 (2013).
53. Hayashi, H. *et al.* The MAD-related protein Smad7 associates with the TGFbeta receptor and functions as an antagonist of TGFbeta signaling. *Cell* **89,** 1165–1173 (1997).
54. Ariotti, S. *et al.* T cell memory. Skin-resident memory CD8(+) T cells trigger a state of tissue-wide pathogen alert. *Science* **346,** 101–105 (2014).
55. Doering, T. A. *et al.* Network analysis reveals centrally connected genes and pathways involved in CD8+ T cell exhaustion versus memory. *Immunity* **37,** 1130–1144 (2012).
56. Barber, D. L. *et al.* Restoring function in exhausted CD8 T cells during chronic viral infection. *Nature* **439,** 682–687 (2006).
57. Blackburn, S. D. *et al.* Coregulation of CD8+ T cell exhaustion by multiple inhibitory receptors during chronic viral infection. *Nat. Immunol.* **10,** 29–37 (2009).
58. Wherry, E. J. T cell exhaustion. *Nat. Immunol.* **12,** 492–499 (2011).
59. Jin, H. T. *et al.* Cooperation of Tim-3 and PD-1 in CD8 T-cell exhaustion during chronic viral infection. *Proc. Natl Acad. Sci. USA* **107,** 14733–14738 (2010).
60. Diehl, L. *et al.* Tolerogenic maturation of liver sinusoidal endothelial cells promotes B7-homolog 1-dependent CD8+ T cell tolerance. *Hepatology (Baltimore, MD)* **47,** 296–305 (2008).
61. Bajenoff, M. *et al.* Stromal cell networks regulate lymphocyte entry, migration, and territoriality in lymph nodes. *Immunity* **25,** 989–1001 (2006).
62. Cox, J. & Mann, M. MaxQuant enables high peptide identification rates, individualized p.p.b.-range mass accuracies and proteome-wide protein quantification. *Nat. Biotechnol.* **26,** 1367–1372 (2008).
63. Pruitt, K. D. *et al.* RefSeq: an update on mammalian reference sequences. *Nucleic Acids Res.* **42,** D756–D763 (2014).
64. Theocharidis, A., van Dongen, S., Enright, A. J. & Freeman, T. C. Network visualization and analysis of gene expression data using BioLayout Express(3D). *Nat. Protoc.* **4,** 1535–1550 (2009).
65. Smoot, M. E., Ono, K., Ruscheinski, J., Wang, P. L. & Ideker, T. Cytoscape 2.8: new features for data integration and network visualization. *Bioinformatics (Oxford, England)* **27,** 431–432 (2011).

Acknowledgements

We thank Elmar Endl and Andreas Dolf from the core facility flow cytometry and cell sorting for excellent technical assistance and the DFG SFB 704, SFB TR36 and SFB TR57 and the Excellence Cluster ImmunoSensation for their support. We thank Caetano Reis e Sousa, Immunobiology Laboratory, Francis Crick Institute, for critical reading of the manuscript.

Author contributions

J.P.B., M.B., F.M., Z.A., B.H., S.E., J.C.R., C.R., T.B., T.F., D.G., D.E. performed the experiments and analysed the data; M.B., F.M., J.C.R., J.S. and J.L.S. performed the bioinformatic analyses; F.M. and J.C.R. performed and analysed the proteomics measurements; J.P.B., M.B., F.M., S.J., D.H.B., U.P., R.T., M.M., C.K., J.L.S., W.K. and P.K. designed the experiments and provided essential reagents as well as essential analysis technology; J.P.B., M.B., F.M., J.L.S., C.K., W.K. and P.A.K. wrote the manuscript.

Additional information

Accession codes: GSE63147.

Supplementary Information accompanies this paper at http://www.nature.com/naturecommunications

Competing financial interests: The authors declare no competing financial interests.

Reprints and permission information is available online at http://npg.nature.com/reprintsandpermissions/

How to cite this article: Böttcher, J. P. *et al.* Functional classification of memory $CD8^+$ T cells by CX_3CR1 expression. *Nat. Commun.* 6:8306 doi: 10.1038/ncomms9306 (2015).

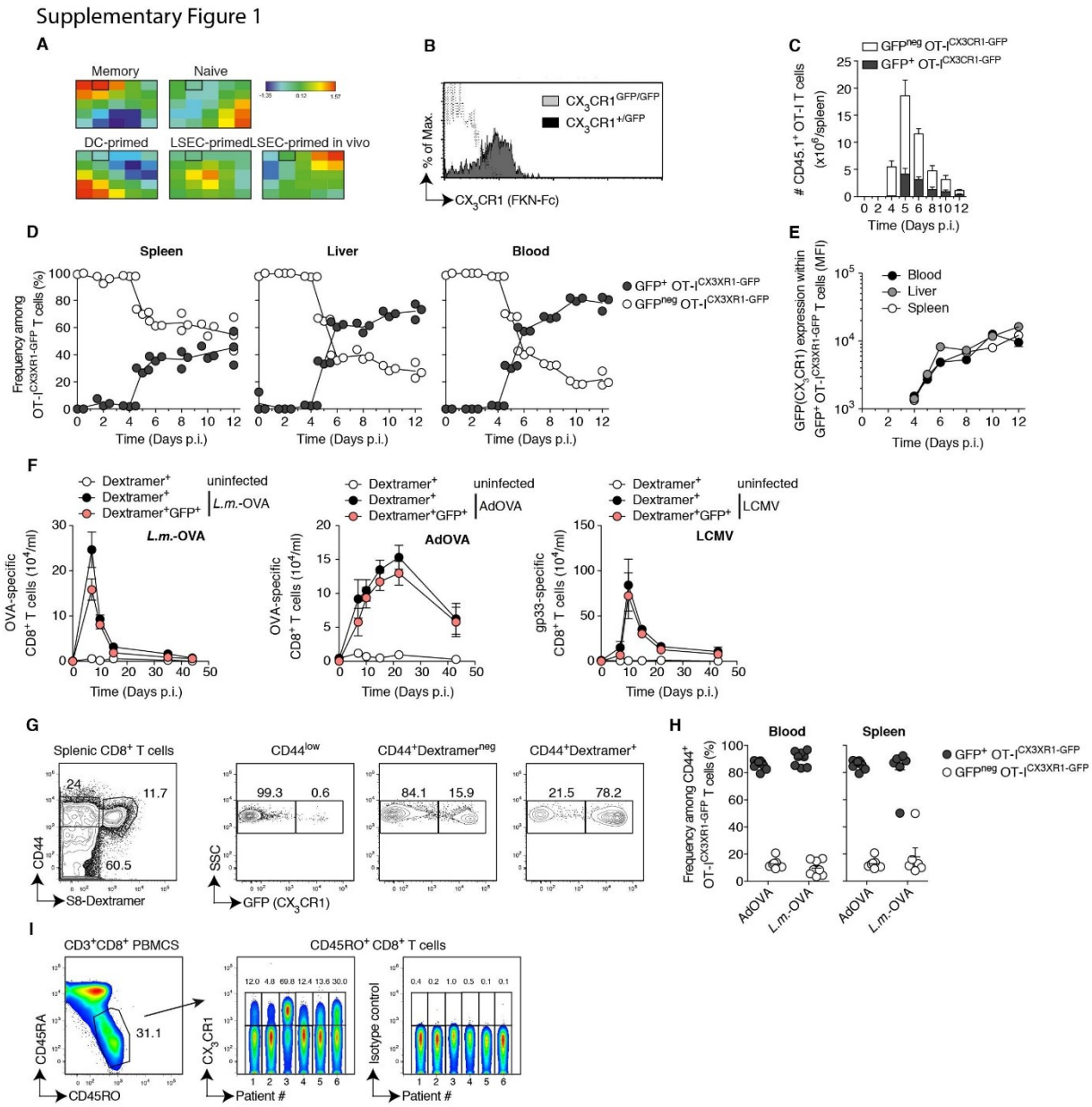

Supplementary Figure 1 *CX_3CR1 expression on $CD8^+$ T cells in man and mouse*
(A) Self-Organizing Map (SOM) clustering based on present genes obtained from gene expression data from memory, naive as well as LSEC-, DC-, and *in vivo* LSEC-primed $CD8^+$ T cells (*1*) was used to identify genes specific for memory $CD8^+$ T cells. The gene cluster containing *CX_3CR1* is marked with a frame. **(B)** GFP^+CD8^+ T cells from CX_3CR1 reporter mice were analyzed for CX_3CR1 protein expression using CX_3CL1-Fc detected with a secondary antibody. **(C-E)** C57BL/6 mice, that had received $3x10^5$ naive $CD44^{low}CD45.1^+$ OT-$I^{CX3CR1-GFP}$, were infected with AdOVALUC (see Fig. 1 H, I). Time kinetics for **(C)** total numbers of GFP^+ and GFP^{neg} $CD45.1^+$ OT-$I^{CX3CR1-GFP}$ T cells in spleen, **(D)** frequencies of GFP^+ and GFP^{neg} T cells among $CD45.1^+$ OT-$I^{CX3CR1-GFP}$ cells in spleen, liver and blood and **(E)** Mean fluorescence intensity (MFI) of the GFP signal in GFP^+ $CD45.1^+$ OT-$I^{CX3CR1-GFP}$ T cells. **(F)** Time kinetics after infection of $CX_3CR1^{+/GFP}$ mice with AdOVA, *L.m.*-OVA or LCMV (WE strain) for numbers of total and OVA-specific GFP^+CD44^+ $CD8^+$ T cells (after AdOVA and *L.m.*-OVA infection) or LCMV gp33-specific $CD44^+$ $CD8^+$ T cells isolated from blood. OVA-specific or gp33-specific T cells were identified by Dextramer-staining. Uninfected $CX_3CR1^{+/GFP}$ mice served as control. **(G)** Flow cytometric analysis of CX_3CR1 expression in splenic OVA-specific $CD44^+$ $CD8^+$ T cells from $CX_3CR1^{+/GFP}$ mice at d60 after AdOVA infection. OVA-specific T cells were identified by staining with H2-$K^{b:SIINFEKL}$ Dextramers (S8-Dextramer). **(H)** C57BL/6 mice were infected with AdOVA or *L.m.*-OVA after adoptive transfer of 500 FACSsorted naive $CD44^{low}CD8^+$ OT-$I^{CX3CR1-GFP}$ T cells into $CD45.2^+$ mice. After >45 days, determination of the frequencies of GFP^+ and GFP^{neg} cells among $CD45.1^+$ OT-$I^{CX3CR1-GFP}$ cells in blood and spleen. **(I)** Flow cytometric analysis of CX_3CR1 expression in $CD3^+CD45RO^+CD8^+$ PBMCs from blood of 6 healthy humans.

Supplementary Figure 2

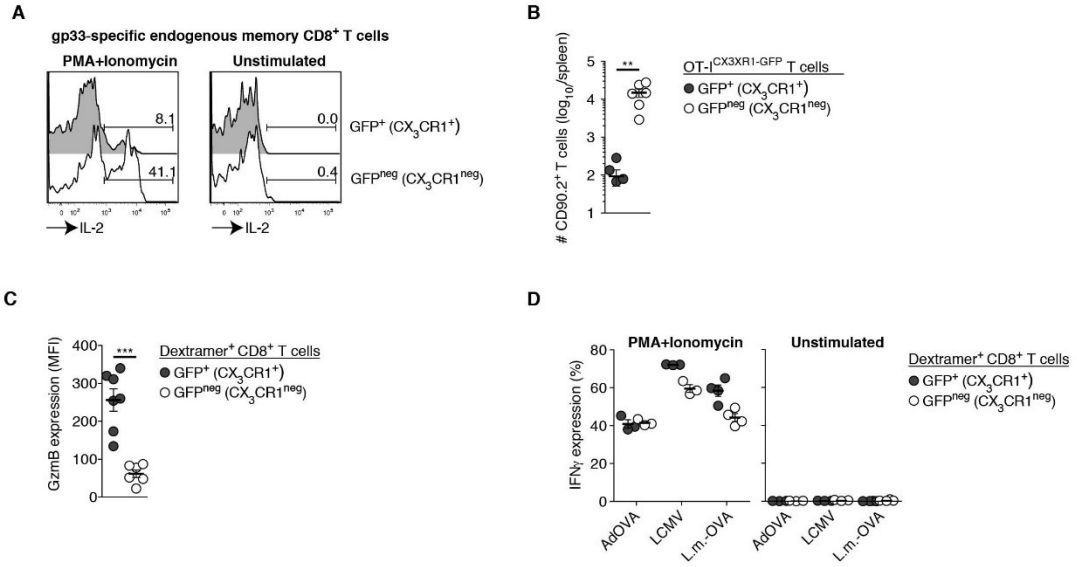

Supplementary Figure 2 *CX_3CR1 expression separates $CD8^+$ T cells with effector function from T cells with proliferative capacity*

(A) Representative analysis of intracellular IL-2 expression in GFP^+ and GFP^{neg} gp33-specific memory T cells isolated from spleen of $CX_3CR1^{+/GFP}$ mice that were infected with LCMV 60 days before. **(B)** $5x10^2$ GFP^+ or GFP^{neg} memory OT-$I^{CX3CR1-GFP}$ T cells ($CD90.2^+$) were adoptively transferred into CD90.1 mice followed by infection with AdOVA. Determination of numbers of $CD90.2^+$ T cells at d8 p.i. in the spleen. **$p<0.01$, t-test. **(C)** Quantification of GzmB expression in (CX_3CR1^+) and GFP^{neg} (CX_3CR1^{neg}) OVA-specific memory T cells from spleen of $CX_3CR1^{+/GFP}$ mice that were infected with *L.m.*-OVA >45 days before. ***$p<0.001$, t-test. **(D)** $CX_3CR1^{+/GFP}$ mice were infected with AdOVA, *L.m.*-OVA or LCMV (WE strain). 45-60 days later, IFNγ production by GFP^+ (CX_3CR1^+) and GFP^{neg} (CX_3CR1^{neg}) memory $CD8^+$ T cells specific for OVA (after AdOVA and *L.m.*-OVA infection) or LCMV gp33 was determined after PMA/Ionomycin stimulation *ex vivo.*

Supplementary Figure 3

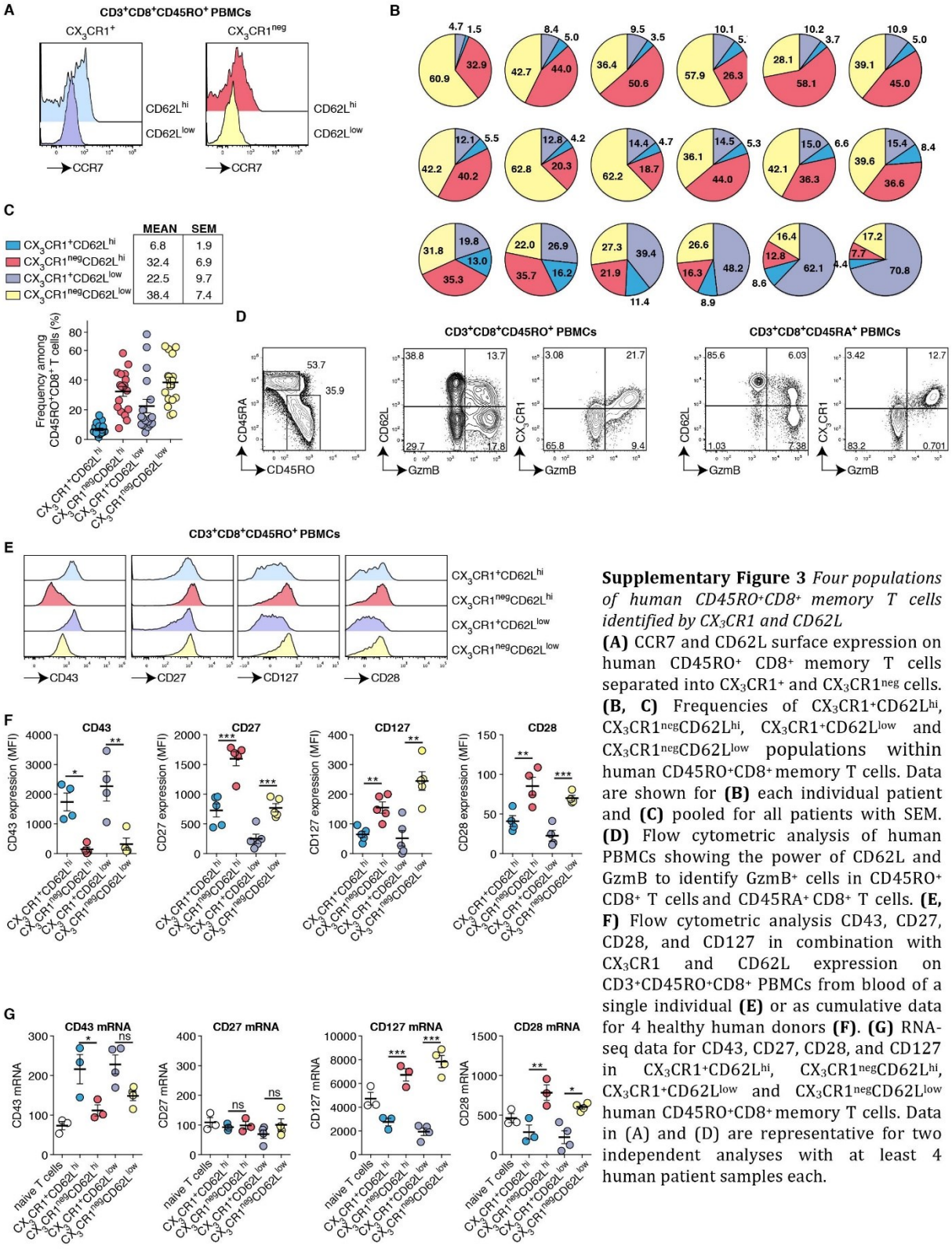

Supplementary Figure 3 *Four populations of human CD45RO+CD8+ memory T cells identified by CX3CR1 and CD62L*

(A) CCR7 and CD62L surface expression on human CD45RO+ CD8+ memory T cells separated into CX3CR1+ and CX3CR1neg cells. **(B, C)** Frequencies of CX3CR1+CD62Lhi, CX3CR1negCD62Lhi, CX3CR1+CD62Llow and CX3CR1negCD62Llow populations within human CD45RO+CD8+ memory T cells. Data are shown for **(B)** each individual patient and **(C)** pooled for all patients with SEM. **(D)** Flow cytometric analysis of human PBMCs showing the power of CD62L and GzmB to identify GzmB+ cells in CD45RO+ CD8+ T cells and CD45RA+ CD8+ T cells. **(E, F)** Flow cytometric analysis CD43, CD27, CD28, and CD127 in combination with CX3CR1 and CD62L expression on CD3+CD45RO+CD8+ PBMCs from blood of a single individual **(E)** or as cumulative data for 4 healthy human donors **(F)**. **(G)** RNA-seq data for CD43, CD27, CD28, and CD127 in CX3CR1+CD62Lhi, CX3CR1negCD62Lhi, CX3CR1+CD62Llow and CX3CR1negCD62Llow human CD45RO+CD8+ memory T cells. Data in (A) and (D) are representative for two independent analyses with at least 4 human patient samples each.

Supplementary Figure 4

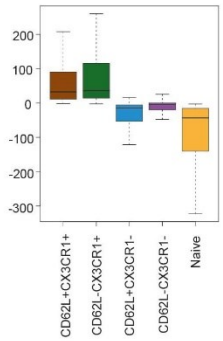

Supplementary Figure 4 *Identification of a core signature for human cytotoxic T cells*

Boxplots representing the distribution of correlation values for each CD8+ T cell subpopulation of the Biolayout cluster used in combination with the ANOVA model to identify the core signature of CX3CR1+ CD8+ T cells.

Supplementary Figure 5

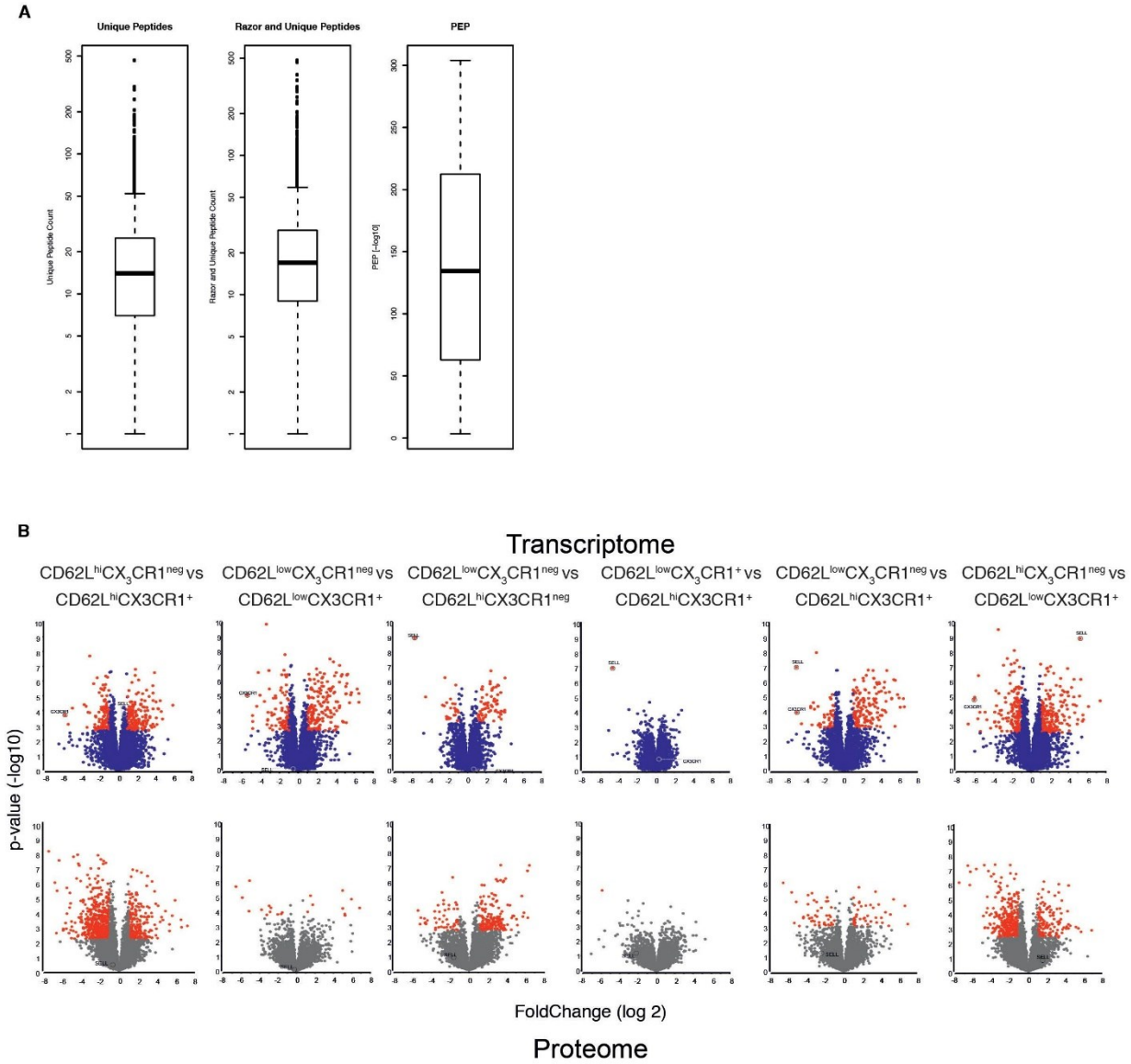

Supplementary Figure 5 *Proteomics identification measures and volcano plot analysis of differences in transcriptome and proteome between memory CD8⁺ T cell populations*
(A) Quality measures of protein group identifications. Numbers of unique peptides per identified protein group, numbers of razor and unique peptides per identified protein group and protein posterior error probability (PEP) for each protein group are shown. Boxplots show median with 5%–95% percentile. All numbers derive from the complete proteome data set including the peptide library. **(B)** Volcano plots displaying log2-fold-change against -log10-p-value of the comparisons of the different CD8⁺ memory T-cell populations as indicated. Upper row: RNA-seq data, Lower row: proteome data

Supplementary Figure 6

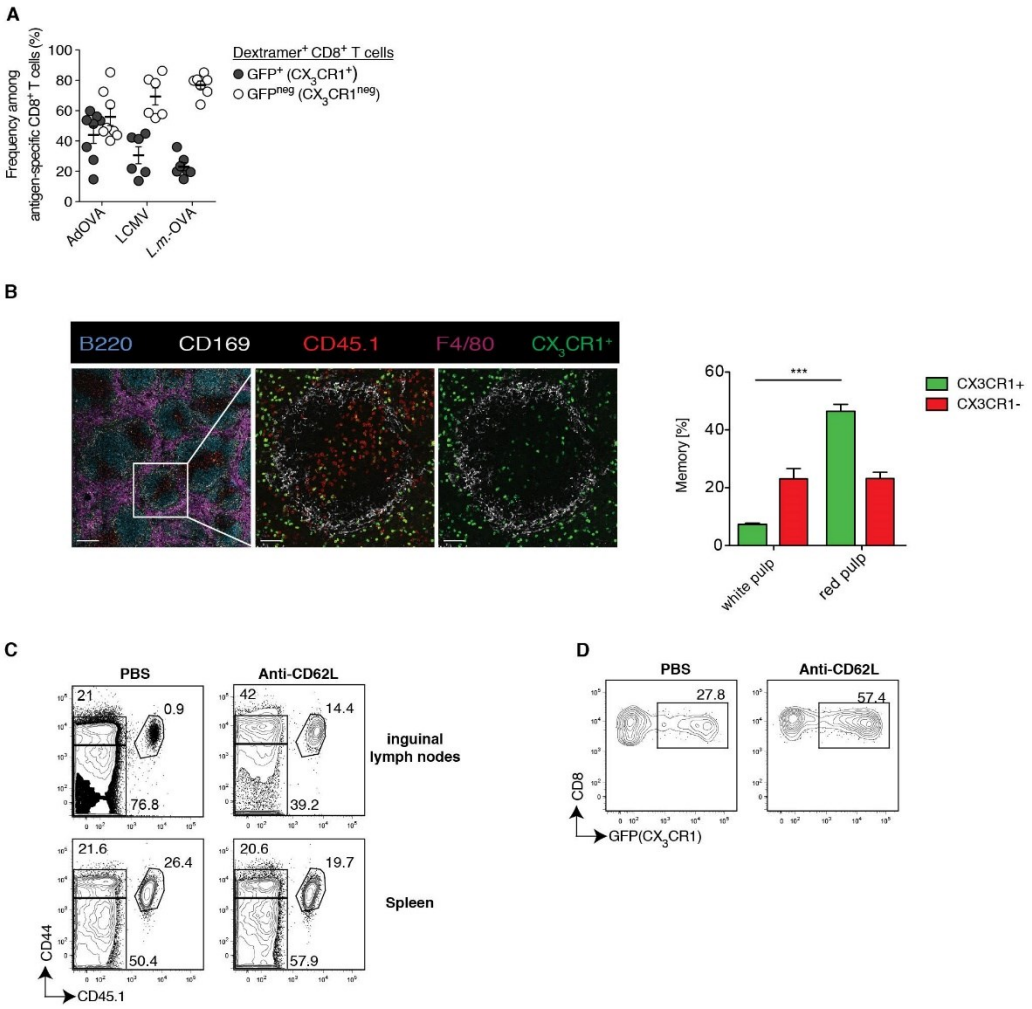

Supplementary Figure 6 *Localization of CX_3CR1 expressing memory $CD8^+$ T cells to lymphoid tissue*
(A) $CX_3CR1^{+/GFP}$ mice were infected with AdOVA, *L.m.*-OVA or LCMV (WE strain). At d45-60 p.i., the frequency of GFP^+ (CX_3CR1^+) and GFP^{neg} (CX_3CR1^{neg}) cells was determined among OVA-specific $CD44^+$ $CD8^+$ T cells (after AdOVA and L.m.-OVA infection) or gp33-specific $CD44^+$ $CD8^+$ T cells (after LCMV infection) identified by Dextramer staining in pooled lymph nodes. **(B)** Detection GFP^+ (CX_3CR1^+) CD45.1+ T cells in spleen. **(C, D)** Mice harboring $CD45.1^+$ memory OT-$I^{CX3CR1\text{-}GFP}$ T cells were injected daily with anti-CD62L neutralizing antibody (100µg/mouse i.p.) or PBS over a period of 6 days. **(C)** Frequency of endogenous (CD45.1 negative) polyclonal naive $CD44^{low}$ $CD8^+$ T cells, $CD44^+$ $CD8^+$ T cells and $CD45.1^+$ memory OT-$I^{CX3CR1\text{-}GFP}$ T cells in inguinal lymph nodes and spleen. **(D)** Frequency of GFP^+ and GFP^{neg} cells among $CD45.1^+$ memory OT-$I^{CX3CR1\text{-}GFP}$ T cells in inguinal lymph nodes. Data is representative for three independent experiments with 3 mice per group

Supplementary Figure 7

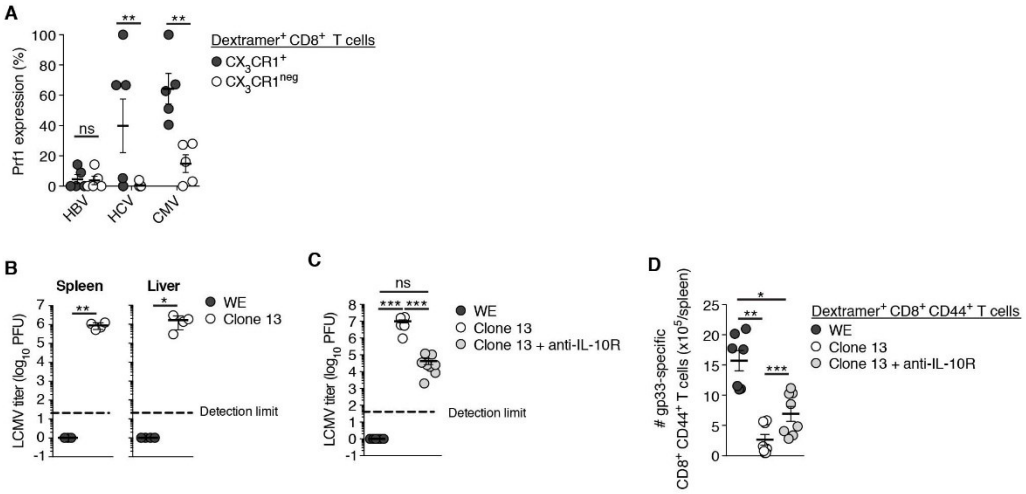

Supplementary Figure 7. *CX_3CR1 identifies cytotoxic virus-specific $CD8^+$ T cells in chronic viral infection*
(A) Analysis of Perforin (Perf1) expression among CX_3CR1^+ and CX_3CR1^{neg} virus-specific $CD8^+$ T cells isolated from blood of patients chronically infected with HBV or HCV (see Figure 7A, B). CMV-specific $CD8^+$ T cells from the same donors served as control. **p<0.01, t-test. **(B)** Determination of viral titers in liver and spleen of $CX_3CR1^{+/GFP}$ mice 40 days after infection with either LCMV WE or LCMV Clone 13. *p<0.05, **p<0.01, t-test. **(C)** Effect of anti-IL10R treatment on viral titers of LCMV Clone 13-infected $CX_3CR1^{+/GFP}$ mice 40 days after infection. ***p<0.001, ANOVA. **(D)** Quantification of splenic gp33-specific $CD8^+$ T cells of $CX_3CR1^{+/GFP}$ mice 40 days p.i. with LCMV WE, LCMV Clone 13 or after infection with LCMV Clone 13 followed by treatment with anti-IL10R antibody. Each dot represents T cells from one mouse. *p<0.05, **p<0.01***p<0.001, ANOVA.

3 Conclusion

3.1 Towards single cell immune proteomes

Mass spectrometry (MS)-based proteomics has evolved to a high-throughput technology to study complex biological systems[177,286]. Due to its continuous improvements, it is now possible to measure the complete proteome of model organisms such as yeast in just one hour[287]. Especially, improved sample handing accompanied with the use of high-pressure high-performance liquid chromatography considerable improved reproducibility and peptide identification rates[288]. New hardware components of mass spectrometers increased their speed, accuracy, and sensitivity[216]. For instance, new orbitrap analyzer can acquire a survey mass spectrum followed by ten fragment spectra in less than one second at a resolution of 15,000 at m/z 200[221,227]. In addition, sophisticated bioinformatic programs[232] and quantification strategies[241], laid the foundation for analyzing complete mammalian proteomes[289] such as those from human immune cells[290].

This thesis extends the journey of complete, accurate and ubiquitous cell proteomes to the immune system[291]. It demonstrates that proteomics can deliver high quality and deep proteome profiles not only form individual immune cells, but also from time-resolved immune responses as well as multicellular immune systems. The quantitative shotgun proteomics workflow was applied to identify functional difference in CD8 T cell subsets[292]. Furthermore, the human CD4 T cell response was investigated, shedding new light on the morphological and functional alterations that occur during the first four days of T cell activation. More than 30% of all measured proteins significantly change after 3 days, including proteins involved in arginine and proline metabolism[293]. Finally, this thesis provides a proteome atlas containing proteome profiles of 28 distinct human hematopoietic cell types at a depth of >10,000 proteins, covering 80% of immune related proteins. A new version of the orbitrap mass analyzer provided the last puzzle piece to execute a single shot strategy[221], which reached average protein quantification rates of 7,500 proteins from primary human immune cells using 3h gradient single shot measurements[294].

When viewed in the context of large research consortia such as ImmGen[295] or the Human Cell Atlas[35], which primarily characterize cell types at the gene and transcript level, this thesis and other studies[296,297] create a desire for these consortia to also develop roadmaps for measuring complete proteomes of all human immune cell types. This idea is not unfeasible since new technology developments have enabled the first comprehensive datasets of single cell

proteome measurements[298,299]. On the one hand, MS-based imaging technologies can analyze single cells on protein level already at high throughput, but rely on labelled antibodies and usually are limited to only a few proteins that can be measured in parallel[300]. On the other hand, single-shot MS-based proteomics, has the promise to quantify all proteins in a cell. To this end three different approaches are being followed. First, Single-Cell ProtEomics by Mass Spectrometry (SCoPE-MS)[301] and Improved Boosting to Amplify Signal with Isobaric Labeling (iBASIL)[302] use isobaric tags to create booster channels to overcome peptide detection limits and sample loss. With this approach the proteome heterogeneity of monocyte and macrophages cell lines was analyzed covering more than 1,000 single cells at a depth of 3,000 proteins[301]. Second, nanoliter-scale oil-air-droplet (OAD) chip[303] or nanodroplet processing in one pot for trace samples (nanoPOTS)[304] use advanced microfluidic devices to reduce sample loss and when coupled to a mass spectrometer can reach single cell resolution. Third, the true single cell proteome (T-SCP) pipeline uses a novel trapped ion mobility mass spectrometer combined with new acquisition methods and miniaturized sample preparation, which allowed the quantification of more than 1,000 proteins in single HeLa cells[305]. Although, these new technologies are in their infancy, they already display great potential to capture the vast variety of cellular immune networks at the protein level.

It is evident that proteomics is a versatile “omic” technology that offers the study of biological systems from different angles[177] and will continue to push its technological boundaries to increase our knowledge of biological systems that ultimately translate to better disease management.

3.2 Multi-dimensional immune networks for personalized medicine

This thesis constructed three different immune networks - (1) a functional intracellular transcriptome and proteome murine CD8 memory T cell network[306], (2) an intracellular and time-resolved proteome and metabolome network of the human CD4 T cell immune response[307], and (3) an intra- and intercellular proteome and secretome network of the human hematopoietic system[294].

In the first network, transcriptome and proteome analysis identified a novel protein marker that functionally differentiates distinct memory T cell populations. Together with protein

cluster enrichment analysis, this new marker distinguishes four functionally different memory T cell subsets based on migration and cytotoxic potential, leading to a new memory T cell population with effector functions and the ability to migrate to the subcapsular sinus of lymph nodes. In the second network, the proteomic and metabolic changes during T cell activation were investigated. Integrative metabolic network analysis revealed that T cells heavily consume L-arginine and convert it to downstream metabolites. Perturbation of the metabolic network by providing additional L-arginine resulted in a shift from glycolysis to OXPHOS and an increased numbers of T cells with a central memory phenotype. Global protein-metabolite interaction network analysis was conducted to further elucidate L-arginine mediated functional changes in T cells. Moreover, this network study discovered that T cells with elevated L-arginine levels exhibit enhanced survival and anti-tumor activity. The third network aimed to conduct a global assessment of the immune system by measuring the proteomes of all major human hematopoietic immune cells in their native and selected activated states. It reached 70% coverage for all immune-relevant signaling molecules including transcription factors, adaptor molecules, cell surface receptors, and secreted molecules, making it the most comprehensive immune proteome resource to date. Together with selected secretome data and bioinformatic algorithms, an immune cell network based on receptor-ligand and receptor-receptor interaction data was constructed. Containing more than 150,000 edges, this cell communication network exceeded the scientific literature knowledge network obtained from natural language processing and discovered previously unknown outgoing and ingoing connections. In addition, the network architecture revealed that immune cell signaling is more diverse inter- than intracellularly in comparison with other organs and that antigen-presenting cells increase, while cytotoxic cells decrease their hierarchy height upon activation. Furthermore, the network was extended to other organs and tissues of the body and found that myeloid immune cells establish more connections with non-immune tissues than lymphoid immune cells. Together, this cell-cell network highlights the different communication structures between myeloid and lymphoid immune cells on the level of proteins and provides a snapshot of cell-type and context-dependent secretion patterns of innate immune cells.

These described networks contribute to the greater picture of network medicine. For instance, understanding functional differences of T memory sub populations will enhance our understanding of immune protection and enable improved immunotherapies such as vaccines. Manipulating T cell fitness by metabolic perturbation can be beneficial for adaptive T cell therapies. Finally, global networks such as the hematopoietic proteome network can serve as a

reference map for future perturbation studies to identify disease specific network nodes or edges that can be targeted by established immune therapies. In general, diverse network medicine techniques have led to some central biological findings. The human disease network constructed from publicly available disease repositories provided a global view of the relationship between disorders and their disease genes[308]. This approach allowed to study all human disease at ones and highlights that most disease genes are non-essential genes and constitute nodes at the network periphery[271]. Using protein-protein interactions maps and mathematical algorithms diseases relationships could be explained by overlapping disease network modules[309]. Furthermore, disease-gene networks extended to disease-drug networks allowed the prediction of adverse events and therapeutic effects for drug repurposing using network proximity measures[310].

While personalized medicine is most advanced in the field of oncology, it still faces many challenges to be universally applied in clinical practice[311]. One puzzle piece includes the interpretation of large “omic” data sets and the development of algorithms that can stratify patient groups based on biomarkers and are able to recommend treatment strategies from such multi-layered networks[206]. Based on the success stories of immunotherapies[130], it is evident that the immune system plays a fundamental role in many diseases and disorders. Thus, systems-immunology approaches, such as those discussed in this thesis, are only beginning to improve the main immunological metrics used in medicine[312]. It will be fascinating to see how the many areas of expertise - from unique human tissue models[313] to innovative data privacy approaches[314] - evolve in order to make personalized medicine become standard of care.

4 Abbreviations

AMPK	adenosine monophosphate-activated protein kinase
APC	antigen presenting cell
AP-MS	affinity purification followed by mass spectrometry
CTLA-4	cytotoxic T-lymphocyte-associated protein 4
DC	dendritic cell
DDA	data dependent acquisition
FAO	fatty acid oxidation
FO B	follicular B cells
FRC	fibroblastic reticular cells
HEV	high endothelial venules
IFN	interferon
IL	interleukin
LPS	lipopolysaccharide
LXR	liver X receptors
MALDI	matrix-assisted laser desorption ionization
MHC	histocompatibility complex
MQ	macrophage
MS	mass spectrometry/mass spectrometer
mTOR	mechanistic target of rapamycin
MZ B	marginal zone B cells
NK	natural killer
OXPHOS	oxidative phosphorylation
PAMP	pathogen associated molecular pattern
PD-1	programmed cell death protein 1
PD-L1	programmed death-ligand 1
PI3K	phosphatidylinositol 3-kinase
SREBP	sterol regulatory element-binding proteins
TCM	central memory T cells
TCR	T cell receptor
TEM	effector memory T cells
Th	T-helper

TNF	tumor necrosis factor
TOF	time of flight
TPA	total protein abundance approach

5 References

1. Kaufmann, S. H. E. Immunology's coming of age. *Front. Immunol.* **10**, 1–13 (2019).
2. Kaufmann, S. H. E. Immunology's foundation: The 100-year anniversary of the Nobel Prize to Paul Ehrlich and Elie Metchnikoff. *Nature Immunology* vol. 9 705–712 (2008).
3. Forsdyke, D. R. Almroth Wright, opsonins, innate immunity and the lectin pathway of complement activation: a historical perspective. *Microbes and Infection* vol. 18 450–459 (2016).
4. Lahaie, Y. M. & Watier, H. Contribution of physiologists to the identification of the humoral component of immunity in the 19th century. *mAbs* vol. 9 774–780 (2017).
5. Landsteiner, K. Individual differences in human blood. *Science* vol. 73 403–409 (1931).
6. Edelman, G. M. ANTIBODY STRUCTURE AND MOLECULAR IMMUNOLOGY. *Ann. N. Y. Acad. Sci.* **190**, 5–25 (1971).
7. Porter, R. R. Structural studies of immunoglobulins. *Science* vol. 180 713–716 (1973).
8. Claman, H. N. On discovering thymus-marrow synergism. *Front. Immunol.* **5**, 588 (2014).
9. Cosimi, A. B. Nobel prizes in medicine in the field of transplantation. *Transplantation* **82**, 1558–1562 (2006).
10. Billingham, R. E., Brent, L. & Medawar, P. B. 'Actively acquired tolerance' of foreign cells. *Nature* **172**, 603–606 (1953).
11. Burnet, F. M. A Modification of Jerne's Theory of Antibody Production using the Concept of Clonal Selection. *CA. Cancer J. Clin.* **26**, 119–121 (1976).
12. Tonegawa, S. Somatic generation of immune diversity. *Vitr. Cell. Dev. Biol.* **24**, 253–265 (1988).
13. Beutler, B. Microbe sensing, positive feedback loops, and the pathogenesis of inflammatory diseases. *Immunological Reviews* vol. 227 248–263 (2009).
14. Hoffmann, J. A. & Reichhart, J. M. Drosophila innate immunity: An evolutionary perspective. *Nature Immunology* vol. 3 121–126 (2002).
15. Steinman, R. M. & Hemmi, H. Dendritic cells: Translating innate to adaptive immunity. *Current Topics in Microbiology and Immunology* vol. 311 17–58 (2006).
16. Feldman, M., Taylor, P., Paleolog, E., Brennan, F. M. & Maini, R. N. Anti-TNFα

therapy is useful in rheumatoid arthritis and Crohn's disease: Analysis of the mechanism of action predicts utility in other diseases. in *Transplantation Proceedings* vol. 30 4126–4127 (1998).

17. Wei, S. C., Duffy, C. R. & Allison, J. P. Fundamental mechanisms of immune checkpoint blockade therapy. *Cancer Discovery* vol. 8 1069–1086 (2018).
18. Germain, R. N., Meier-Schellersheim, M., Nita-Lazar, A. & Fraser, I. D. C. Systems biology in immunology: a computational modeling perspective. *Annu. Rev. Immunol.* **29**, 527–85 (2011).
19. Davis, M. M. Systems immunology. *Curr. Opin. Immunol.* **65**, 79 (2020).
20. Fulton, K. M. & Walker, J. M. *Immunoproteomics*. vol. 1061 (Humana Press, 2013).
21. Arstila, T. P. *et al.* A direct estimate of the human αβ T cell receptor diversity. *Science (80-.).* **286**, 958–961 (1999).
22. Sun, B. L. *et al.* Lymphatic drainage system of the brain: A novel target for intervention of neurological diseases. *Prog. Neurobiol.* **163**–**164**, 118–143 (2018).
23. Feola, M., Merklin, R., Cho, S. & Brockman, S. K. The Terminal Pathway of the Lymphatic System of the Human Heart. *Ann. Thorac. Surg.* **24**, 531–536 (1977).
24. Swartz, M. A. The physiology of the lymphatic system. *Adv. Drug Deliv. Rev.* **50**, 3–20 (2001).
25. Dranoff, G. Cytokines in cancer pathogenesis and cancer therapy. *Nat. Rev. Cancer* **4**, 11–22 (2004).
26. Brinkmann, V. *et al.* Neutrophil Extracellular Traps Kill Bacteria. *Science (80-.).* **303**, 1532–1535 (2004).
27. Murray, P. J. & Wynn, T. A. Protective and pathogenic functions of macrophage subsets. *Nat. Rev. Immunol.* **11**, 723–737 (2011).
28. Hamilos, D. L. Antigen presenting cells. *Immunol. Res.* **8**, 98–117 (1989).
29. Mathers, A. R. & Larregina, A. T. Professional antigen-presenting cells of the skin. *Immunologic Research* vol. 36 127–136 (2006).
30. Panja, A. & Mayer, L. Antigen presentation in the intestine. *Baillieres. Clin. Gastroenterol.* **10**, 407–425 (1996).
31. Cooper, M. A., Fehniger, T. A. & Caligiuri, M. A. The biology of human natural killer-cell subsets. *Trends Immunol.* **22**, 633–640 (2001).
32. Andersen, M. H., Schrama, D., Thor Straten, P. & Becker, J. C. Cytotoxic T cells. *Journal of Investigative Dermatology* vol. 126 32–41 (2006).
33. Sallusto, F. Heterogeneity of Human CD4+ T Cells Against Microbes. *Annu. Rev.*

Immunol. **34**, 317–334 (2016).

34. Wang, Y., Liu, J., Burrows, P. D. & Wang, J. Y. B Cell Development and Maturation. in *Advances in Experimental Medicine and Biology* vol. 1254 1–22 (Springer, 2020).
35. Regev, A. *et al.* The human cell atlas. *Elife* **6**, (2017).
36. Borish, L. C. & Steinke, J. W. 2. Cytokines and chemokines. *Journal of Allergy and Clinical Immunology* vol. 111 S460–S475 (2003).
37. Parkin, J. & Cohen, B. An overview of the immune system. *Lancet* vol. 357 1777–1789 (2001).
38. Silk, A. W. & Margolin, K. Cytokine Therapy. *Hematology/Oncology Clinics of North America* vol. 33 261–274 (2019).
39. Epstein, J., Eichbaum, Q., Sheriff, S. & Ezekowitz, R. A. B. The collectins in innate immunity. *Curr. Opin. Immunol.* **8**, 29–35 (1996).
40. Medzhitov, R. & Janeway, C. Innate immunity. *N. Engl. J. Med.* **343**, 338–44 (2000).
41. Bianchi, M. E. DAMPs, PAMPs and alarmins: all we need to know about danger. *J. Leukoc. Biol.* **81**, 1–5 (2007).
42. Bluestone, J. A., MacKay, C. R., O'Shea, J. J. & Stockinger, B. The functional plasticity of T cell subsets. *Nat. Rev. Immunol.* **9**, 811–816 (2009).
43. Parker, D. C. T cell-dependent B cell activation. *Annual Review of Immunology* vol. 11 331–360 (1993).
44. Melchers, F. *et al.* Repertoire selection by pre-B-cell receptors and B-cell receptors, and genetic control of B-cell development from immature to mature B cells. *Immunol. Rev.* **175**, 33–46 (2000).
45. Kaech, S. M., Wherry, E. J. & Ahmed, R. Effector and memory T-cell differentiation: implications for vaccine development. *Nat. Rev. Immunol.* **2**, 251–62 (2002).
46. O'Shea, J. J., Ma, A. & Lipsky, P. Cytokines and autoimmunity. *Nature Reviews Immunology* vol. 2 37–45 (2002).
47. Goodnow, C. C., Sprent, J., Barbara, B. F. & Vinuesa, C. G. Cellular and genetic mechanisms of self tolerance and autoimmunity. *Nature* vol. 435 590–597 (2005).
48. Kumar, B. V., Connors, T. J. & Farber, D. L. Human T Cell Development, Localization, and Function throughout Life. *Immunity* vol. 48 202–213 (2018).
49. Cohen, I. R. Activation of benign autoimmunity as both tumor and autoimmune disease immunotherapy: A comprehensive review. *Journal of Autoimmunity* vol. 54 112–117 (2014).
50. Rosenberg, S. A. Entering the mainstream of cancer treatment. *Nat. Rev. Clin. Oncol.*

11, 630–632 (2014).

51. Junt, T. *et al.* Subcapsular sinus macrophages in lymph nodes clear lymph-borne viruses and present them to antiviral B cells. *Nature* **450**, 110–114 (2007).
52. Mueller, S. N. & Germain, R. N. Stromal cell contributions to the homeostasis and functionality of the immune system. *Nature Reviews Immunology* vol. 9 618–629 (2009).
53. Friedman, R. S., Jacobelli, J. & Krummel, M. F. Surface-bound chemokines capture and prime T cells for synapse formation. *Nat. Immunol.* **7**, 1101–1108 (2006).
54. Castellino, F. *et al.* Chemokines enhance immunity by guiding naive CD8+ T cells to sites of CD4+ T cell-dendritic cell interaction. *Nature* **440**, 890–895 (2006).
55. Sallusto, F., Lenig, D., Förster, R., Lipp, M. & Lanzavecchia, A. Two subsets of memory T lymphocytes with distinct homing potentials and effector functions. *Nature* **401**, 708–712 (1999).
56. Mueller, S. N., Gebhardt, T., Carbone, F. R. & Heath, W. R. Memory T cell subsets, migration patterns, and tissue residence. *Annu. Rev. Immunol.* **31**, 137–161 (2013).
57. Masopust, D., Vezys, V., Marzo, A. L. & Lefrançois, L. Preferential localization of effector memory cells in nonlymphoid tissue. *J. Immunol.* **192**, 845–849 (2014).
58. Reinhardt, R. L., Khoruts, A., Merica, R., Zell, T. & Jenkins, M. K. Visualizing the generation of memory CD4 T cells in the whole body. *Nature* **410**, 101–105 (2001).
59. Sallusto, F., Geginat, J. & Lanzavecchia, A. Central memory and effector memory T cell subsets: Function, generation, and maintenance. *Annu. Rev. Immunol.* **22**, 745–763 (2004).
60. Gebhardt, T. *et al.* Memory T cells in nonlymphoid tissue that provide enhanced local immunity during infection with herpes simplex virus. *Nat. Immunol.* **10**, 524–530 (2009).
61. Masopust, D. *et al.* Dynamic T cell migration program provides resident memory within intestinal epithelium. *J. Exp. Med.* **207**, 553–564 (2010).
62. Masopust, D., Murali-Krishna, K. & Ahmed, R. Quantitating the Magnitude of the Lymphocytic Choriomeningitis Virus-Specific CD8 T-Cell Response: It Is Even Bigger than We Thought. *J. Virol.* **81**, 2002–2011 (2007).
63. Moon, J. J. *et al.* Naive CD4+ T Cell Frequency Varies for Different Epitopes and Predicts Repertoire Diversity and Response Magnitude. *Immunity* **27**, 203–213 (2007).
64. Van Heijst, J. W. J. *et al.* Recruitment of antigen-specific cd8+ t cells in response to infection is markedly efficient. *Science (80-.).* **325**, 1265–1269 (2009).

65. Gett, A. V., Sallusto, F., Lanzavecchia, A. & Geginat, J. T cell fitness determined by signal strength. *Nat. Immunol.* **4**, 355–360 (2003).

66. Stemberger, C. *et al.* A Single Naive CD8+ T Cell Precursor Can Develop into Diverse Effector and Memory Subsets. *Immunity* **27**, 985–997 (2007).

67. Teixeiro, E. *et al.* Different T cell receptor signals determine CD8+ memory versus effector development. *Science (80-.).* **323**, 502–505 (2009).

68. Obar, J. J. *et al.* Pathogen-Induced Inflammatory Environment Controls Effector and Memory CD8 + T Cell Differentiation . *J. Immunol.* **187**, 4967–4978 (2011).

69. Pearce, E. L. & Shen, H. Generation of CD8 T Cell Memory Is Regulated by IL-12. *J. Immunol.* **179**, 2074–2081 (2007).

70. Pipkin, M. E. *et al.* Interleukin-2 and Inflammation Induce Distinct Transcriptional Programs that Promote the Differentiation of Effector Cytolytic T Cells. *Immunity* **32**, 79–90 (2010).

71. Cui, W., Liu, Y., Weinstein, J. S., Craft, J. & Kaech, S. M. An interleukin-21-interleukin-10-STAT3 pathway is critical for functional maturation of memory CD8 + T cells. *Immunity* **35**, 792–805 (2011).

72. Yang, C. Y. *et al.* The transcriptional regulators Id2 and Id3 control the formation of distinct memory CD8 + T cell subsets. *Nat. Immunol.* **12**, 1221–1229 (2011).

73. Tomura, M. *et al.* Monitoring cellular movement in vivo with photoconvertible fluorescence protein 'Kaede' transgenic mice. *Proc. Natl. Acad. Sci. U. S. A.* **105**, 10871–10876 (2008).

74. Stein, J. V. *et al.* The CC chemokine thymus-derived chemotactic agent 4 (TCA-4, secondary lymphoid tissue chemokine, 6Ckine, exodus-2) triggers lymphocyte function- associated antigen 1-mediated arrest of rolling T lymphocytes in peripheral lymph node high endothelial venules. *J. Exp. Med.* **191**, 61–75 (2000).

75. Tubo, N. J., McLachlan, J. B. & Campbell, J. J. Chemokine receptor requirements for epidermal T-cell trafficking. *Am. J. Pathol.* **178**, 2496–503 (2011).

76. Matsumoto, M. *et al.* CD43 Collaborates with P-Selectin Glycoprotein Ligand-1 to Mediate E-Selectin-Dependent T Cell Migration into Inflamed Skin. *J. Immunol.* **178**, 2499–2506 (2007).

77. Hamann, A., Andrew, D. P., Jablonski-Westrich, D., Holzmann, B. & Butcher, E. C. Role of alpha 4-integrins in lymphocyte homing to mucosal tissues in vivo. *J. Immunol.* **152**, 3282–93 (1994).

78. Ray, S. J. *et al.* The Collagen Binding α1β1 Integrin VLA-1 Regulates CD8 T Cell-

Mediated Immune Protection against Heterologous Influenza Infection. *Immunity* **20**, 167–179 (2004).

79. Moser, B. & Loetscher, P. Lymphocyte traffic control by chemokines. *Nature Immunology* vol. 2 123–128 (2001).
80. Buck, M. D., O'Sullivan, D. & Pearce, E. L. T cell metabolism drives immunity. *J. Exp. Med.* **212**, 1345–1360 (2015).
81. Pui, J. C. *et al.* Notch1 expression in early lymphopoiesis influences B versus T lineage determination. *Immunity* **11**, 299–308 (1999).
82. Janas, M. L. *et al.* Thymic development beyond beta-selection requires phosphatidylinositol 3-kinase activation by CXCR4. *J. Exp. Med.* **207**, 247–61 (2010).
83. Maciver, N. J., Michalek, R. D. & Rathmell, J. C. Metabolic regulation of T lymphocytes. *Annu. Rev. Immunol.* **31**, 259–283 (2013).
84. Wieman, H. L., Wofford, J. A. & Rathmell, J. C. Cytokine stimulation promotes glucose uptake via phosphatidylinositol-3 kinase/Akt regulation of Glut1 activity and trafficking. *Mol. Biol. Cell* **18**, 1437–46 (2007).
85. Akashi, K., Kondo, M., von Freeden-Jeffry, U., Murray, R. & Weissman, I. L. Bcl-2 rescues T lymphopoiesis in interleukin-7 receptor-deficient mice. *Cell* **89**, 1033–41 (1997).
86. Peschon, J. J. *et al.* Early lymphocyte expansion is severely impaired in interleukin 7 receptor-deficient mice. *J. Exp. Med.* **180**, 1955–60 (1994).
87. Fox, C. J., Hammerman, P. S. & Thompson, C. B. Fuel feeds function: energy metabolism and the T-cell response. *Nat. Rev. Immunol.* **5**, 844–52 (2005).
88. Surh, C. D. & Sprent, J. Homeostasis of naive and memory T cells. *Immunity* **29**, 848–62 (2008).
89. Heiden, M. G. V., Cantley, L. C. & Thompson, C. B. Understanding the warburg effect: The metabolic requirements of cell proliferation. *Science* vol. 324 1029–1033 (2009).
90. Pearce, E. L., Poffenberger, M. C., Chang, C. H. & Jones, R. G. Fueling immunity: Insights into metabolism and lymphocyte function. *Science (80-.).* **342**, 1242454 (2013).
91. Frauwirth, K. A. *et al.* The CD28 signaling pathway regulates glucose metabolism. *Immunity* **16**, 769–777 (2002).
92. Laplante, M. & Sabatini, D. M. MTOR signaling in growth control and disease. *Cell* vol. 149 274–293 (2012).

93. Wang, R. *et al.* The Transcription Factor Myc Controls Metabolic Reprogramming upon T Lymphocyte Activation. *Immunity* **35**, 871–882 (2011).

94. Michalek, R. D. *et al.* Estrogen-related receptor-α is a metabolic regulator of effector T-cell activation and differentiation. *Proc. Natl. Acad. Sci. U. S. A.* **108**, 18348–18353 (2011).

95. Doedens, A. L. *et al.* Hypoxia-inducible factors enhance the effector responses of CD8 + T cells to persistent antigen. *Nat. Immunol.* **14**, 1173–1182 (2013).

96. Kopf, H., de la Rosa, G. M., Howard, O. M. Z. & Chen, X. Rapamycin inhibits differentiation of Th17 cells and promotes generation of FoxP3+ T regulatory cells. *Int. Immunopharmacol.* **7**, 1819–1824 (2007).

97. Michalek, R. D. *et al.* Cutting Edge: Distinct Glycolytic and Lipid Oxidative Metabolic Programs Are Essential for Effector and Regulatory CD4 + T Cell Subsets . *J. Immunol.* **186**, 3299–3303 (2011).

98. Lee, K. *et al.* Mammalian target of rapamycin protein complex 2 regulates differentiation of Th1 and Th2 cell subsets via distinct signaling pathways. *Immunity* **32**, 743–753 (2010).

99. MacIver, N. J., Michalek, R. D. & Rathmell, J. C. Metabolic regulation of T lymphocytes. *Annu. Rev. Immunol.* **31**, 259–83 (2013).

100. Pearce, E. L. *et al.* Enhancing CD8 T-cell memory by modulating fatty acid metabolism. *Nature* **460**, 103–107 (2009).

101. Jones, R. G. & Thompson, C. B. Revving the Engine: Signal Transduction Fuels T Cell Activation. *Immunity* vol. 27 173–178 (2007).

102. Araki, K. *et al.* mTOR regulates memory CD8 T-cell differentiation. *Nature* **460**, 108–112 (2009).

103. van der Windt, G. J. W. *et al.* Mitochondrial Respiratory Capacity Is a Critical Regulator of CD8 + T Cell Memory Development. *Immunity* **36**, 68–78 (2012).

104. Fraser, K. A., Schenkel, J. M., Jameson, S. C., Vezys, V. & Masopust, D. Preexisting High Frequencies of Memory CD8+ T Cells Favor Rapid Memory Differentiation and Preservation of Proliferative Potential upon Boosting. *Immunity* **39**, 171–183 (2013).

105. Jacobs, S. R. *et al.* Glucose Uptake Is Limiting in T Cell Activation and Requires CD28-Mediated Akt-Dependent and Independent Pathways. *J. Immunol.* **180**, 4476–4486 (2008).

106. Cham, C. M., Driessens, G., O'Keefe, J. P. & Gajewski, T. F. Glucose deprivation inhibits multiple key gene expression events and effector functions in CD8+ T cells.

Eur. J. Immunol. **38**, 2438–2450 (2008).

107. Macintyre, A. N. *et al.* The glucose transporter Glut1 is selectively essential for CD4 T cell activation and effector function. *Cell Metab.* **20**, 61–72 (2014).
108. Pearson, C., Silva, A. & Seddon, B. Exogenous amino acids are essential for interleukin-7 induced cd8 t cell gowth. *PLoS One* **7**, (2012).
109. Sinclair, L. V. *et al.* Control of amino-acid transport by antigen receptors coordinates the metabolic reprogramming essential for T cell differentiation. *Nat. Immunol.* **14**, 500–508 (2013).
110. Carr, E. L. *et al.* Glutamine Uptake and Metabolism Are Coordinately Regulated by ERK/MAPK during T Lymphocyte Activation. *J. Immunol.* **185**, 1037–1044 (2010).
111. Hayashi, K., Jutabha, P., Endou, H., Sagara, H. & Anzai, N. LAT1 Is a Critical Transporter of Essential Amino Acids for Immune Reactions in Activated Human T Cells. *J. Immunol.* **191**, 4080–4085 (2013).
112. Han, J. M. *et al.* Leucyl-tRNA synthetase is an intracellular leucine sensor for the mTORC1-signaling pathway. *Cell* **149**, 410–424 (2012).
113. Powell, J. D. Slc7a5 helps T cells get with the program. *Nature Immunology* vol. 14 422–424 (2013).
114. Ananieva, E. A., Patel, C. H., Drake, C. H., Powell, J. D. & Hutson, S. M. Cytosolic branched chain aminotransferase (BCATc) regulates mTORC1 signaling and glycolytic metabolism in CD4- T cells. *J. Biol. Chem.* **289**, 18793–18804 (2014).
115. Nakaya, M. *et al.* Inflammatory T cell responses rely on amino acid transporter ASCT2 facilitation of glutamine uptake and mTORC1 kinase activation. *Immunity* **40**, 692–705 (2014).
116. Rath, M., Müller, I., Kropf, P., Closs, E. I. & Munder, M. Metabolism via arginase or nitric oxide synthase: Two competing arginine pathways in macrophages. *Frontiers in Immunology* vol. 5 (2014).
117. Fletcher, M. *et al.* L-Arginine depletion blunts antitumor T-cell responses by inducing myeloid-derived suppressor cells. *Cancer Res.* **75**, 275–283 (2015).
118. Cobbold, S. P. *et al.* Infectious tolerance via the consumption of essential amino acids and mTOR signaling. *Proc. Natl. Acad. Sci. U. S. A.* **106**, 12055–12060 (2009).
119. Angelini, G. *et al.* Antigen-presenting dendritic cells provide the reducing extracellular microenvironment required for T lymphocyte activation. *Proc. Natl. Acad. Sci. U. S. A.* **99**, 1491–1496 (2002).
120. Lochner, M., Berod, L. & Sparwasser, T. Fatty acid metabolism in the regulation of T

cell function. *Trends in Immunology* vol. 36 81–91 (2015).

121. Kidani, Y. *et al.* Sterol regulatory element-binding proteins are essential for the metabolic programming of effector T cells and adaptive immunity. *Nat. Immunol.* **14**, 489–499 (2013).
122. Bensinger, S. J. *et al.* LXR Signaling Couples Sterol Metabolism to Proliferation in the Acquired Immune Response. *Cell* **134**, 97–111 (2008).
123. Thurnher, M. & Gruenbacher, G. T lymphocyte regulation by mevalonate metabolism. *Science Signaling* vol. 8 (2015).
124. Berod, L. *et al.* De novo fatty acid synthesis controls the fate between regulatory T and T helper 17 cells. *Nat. Med.* **20**, (2014).
125. Wang, R. & Green, D. R. Metabolic checkpoints in activated T cells. *Nature Immunology* vol. 13 907–915 (2012).
126. O'Sullivan, D. & Pearce, E. L. Targeting T cell metabolism for therapy. *Trends Immunol.* **36**, 71–80 (2015).
127. Mellman, I., Coukos, G. & Dranoff, G. Cancer immunotherapy comes of age. *Nature* **480**, 480–9 (2011).
128. Rosenberg, S. A. Cancer immunotherapy comes of age. *Nature Clinical Practice Oncology* vol. 2 115 (2005).
129. Farkona, S., Diamandis, E. P. & Blasutig, I. M. Cancer immunotherapy: The beginning of the end of cancer? *BMC Med.* **14**, 73 (2016).
130. Chen, D. S. & Mellman, I. Oncology meets immunology: The cancer-immunity cycle. *Immunity* **39**, 1–10 (2013).
131. Motz, G. T. & Coukos, G. Deciphering and Reversing Tumor Immune Suppression. *Immunity* vol. 39 61–73 (2013).
132. Pardoll, D. M. & Topalian, S. L. The role of CD4+ T cell responses in antitumor immunity. *Curr. Opin. Immunol.* **10**, 588–94 (1998).
133. Palucka, K. & Banchereau, J. Dendritic-cell-based therapeutic cancer vaccines. *Immunity* **39**, 38–48 (2013).
134. Rammensee, H.-G., Weinschenk, T., Gouttefangeas, C. & Stevanović, S. Towards patient-specific tumor antigen selection for vaccination. *Immunol. Rev.* **188**, 164–76 (2002).
135. Kasuga, K. Comprehensive analysis of MHC ligands in clinical material by immunoaffinity-mass spectrometry. *Methods Mol. Biol.* **1023**, 203–18 (2013).
136. Palucka, K. & Banchereau, J. Cancer immunotherapy via dendritic cells. *Nat. Rev.*

Cancer **12**, 265–277 (2012).

137. Kantoff, P. W. *et al.* Sipuleucel-T immunotherapy for castration-resistant prostate cancer. *N. Engl. J. Med.* **363**, 411–22 (2010).
138. Hinrichs, C. S. & Rosenberg, S. A. Exploiting the curative potential of adoptive T-cell therapy for cancer. *Immunol. Rev.* **257**, 56–71 (2014).
139. Gattinoni, L. *et al.* Removal of homeostatic cytokine sinks by lymphodepletion enhances the efficacy of adoptively transferred tumor-specific CD8+ T cells. *J. Exp. Med.* **202**, 907–912 (2005).
140. Rosenberg, S. A. *et al.* Durable complete responses in heavily pretreated patients with metastatic melanoma using T-cell transfer immunotherapy. *Clin. Cancer Res.* **17**, 4550–4557 (2011).
141. Qian, X., Wang, X. & Jin, H. Cell transfer therapy for cancer: past, present, and future. *Journal of immunology research* vol. 2014 525913 (2014).
142. Alexandrov, L. B. *et al.* Signatures of mutational processes in human cancer. *Nature* **500**, 415–421 (2013).
143. Yee, C. Adoptive T-cell therapy for cancer: Boutique therapy or treatment modality? *Clin. Cancer Res.* **19**, 4550–4552 (2013).
144. Morgan, R. A., Dudley, M. E. & Rosenberg, S. A. Adoptive cell therapy: genetic modification to redirect effector cell specificity. *Cancer J.* **16**, 336–41 (2010).
145. Gross, G., Waks, T. & Eshhar, Z. Expression of immunoglobulin-T-cell receptor chimeric molecules as functional receptors with antibody-type specificity. *Proc. Natl. Acad. Sci. U. S. A.* **86**, 10024–10028 (1989).
146. Kochenderfer, J. N. & Rosenberg, S. A. Treating B-cell cancer with T cells expressing anti-CD19 chimeric antigen receptors. *Nat. Rev. Clin. Oncol.* **10**, 267–76 (2013).
147. Ribas, A. Releasing the Brakes on Cancer Immunotherapy. *N. Engl. J. Med.* **373**, 1490–2 (2015).
148. Leach, D. R., Krummel, M. F. & Allison, J. P. Enhancement of antitumor immunity by CTLA-4 blockade. *Science* **271**, 1734–6 (1996).
149. Robert, C. *et al.* Ipilimumab plus dacarbazine for previously untreated metastatic melanoma. *N. Engl. J. Med.* **364**, 2517–26 (2011).
150. Hodi, F. S. *et al.* Improved survival with ipilimumab in patients with metastatic melanoma. *N. Engl. J. Med.* **363**, 711–23 (2010).
151. Keir, M. E., Butte, M. J., Freeman, G. J. & Sharpe, A. H. PD-1 and its ligands in tolerance and immunity. *Annu. Rev. Immunol.* **26**, 677–704 (2008).

152. Chemnitz, J. M., Parry, R. V, Nichols, K. E., June, C. H. & Riley, J. L. SHP-1 and SHP-2 associate with immunoreceptor tyrosine-based switch motif of programmed death 1 upon primary human T cell stimulation, but only receptor ligation prevents T cell activation. *J. Immunol.* **173**, 945–54 (2004).

153. Topalian, S. L. *et al.* Safety, Activity, and Immune Correlates of Anti–PD-1 Antibody in Cancer. *N. Engl. J. Med.* **366**, 2443–2454 (2012).

154. Herbst, R. S. *et al.* A study of MPDL3280A, an engineered PD-L1 antibody in patients with locally advanced or metastatic tumors. *J. Clin. Oncol.* **31**, 3000–3000 (2013).

155. Brahmer, J. R. *et al.* Safety and activity of anti-PD-L1 antibody in patients with advanced cancer. *N. Engl. J. Med.* **366**, 2455–65 (2012).

156. Sznol, M. *et al.* Survival and long-term follow-up of safety and response in patients (pts) with advanced melanoma (MEL) in a phase I trial of nivolumab (anti-PD-1; BMS-936558; ONO-4538). *J. Clin. Oncol.* **31**, CRA9006–CRA9006 (2013).

157. Sakuishi, K. *et al.* Targeting Tim-3 and PD-1 pathways to reverse T cell exhaustion and restore anti-tumor immunity. *J. Exp. Med.* **207**, 2187–2194 (2010).

158. Jacobs, J. F. M., Nierkens, S., Figdor, C. G., de Vries, I. J. M. & Adema, G. J. Regulatory T cells in melanoma: the final hurdle towards effective immunotherapy? *Lancet. Oncol.* **13**, e32-42 (2012).

159. West, E. E. *et al.* PD-L1 blockade synergizes with IL-2 therapy in reinvigorating exhausted T cells. *J. Clin. Invest.* **123**, 2604–2615 (2013).

160. Goding, S. R. *et al.* Restoring Immune Function of Tumor-Specific CD4 + T Cells during Recurrence of Melanoma . *J. Immunol.* **190**, 4899–4909 (2013).

161. Gajewski, T. F., Fuertes, M., Spaapen, R., Zheng, Y. & Kline, J. Molecular profiling to identify relevant immune resistance mechanisms in the tumor microenvironment. *Current Opinion in Immunology* vol. 23 286–292 (2011).

162. Wolchok, J. D. *et al.* Nivolumab plus Ipilimumab in Advanced Melanoma. *N. Engl. J. Med.* **369**, 122–133 (2013).

163. Ge, Y., Xi, H., Ju, S. & Zhang, X. Blockade of PD-1/PD-L1 immune checkpoint during DC vaccination induces potent protective immunity against breast cancer in hu-SCID mice. *Cancer Lett.* **336**, 253–259 (2013).

164. Duraiswamy, J., Kaluza, K. M., Freeman, G. J. & Coukos, G. Dual blockade of PD-1 and CTLA-4 combined with tumor vaccine effectively restores T-cell rejection function in tumors. *Cancer Res.* **73**, 3591–3603 (2013).

165. Liu, C. *et al.* BRAF inhibition increases tumor infiltration by T cells and enhances the

antitumor activity of adoptive immunotherapy in mice. *Clin. Cancer Res.* **19**, 393–403 (2013).

166. Ménard, C., Martin, F., Apetoh, L., Bouyer, F. & Ghiringhelli, F. Cancer chemotherapy: not only a direct cytotoxic effect, but also an adjuvant for antitumor immunity. *Cancer Immunol. Immunother.* **57**, 1579–87 (2008).
167. Le, D. T. & Jaffee, E. M. Regulatory T-cell modulation using cyclophosphamide in vaccine approaches: a current perspective. *Cancer Res.* **72**, 3439–44 (2012).
168. Sevko, A. *et al.* Antitumor effect of paclitaxel is mediated by inhibition of myeloid-derived suppressor cells and chronic inflammation in the spontaneous melanoma model. *J. Immunol.* **190**, 2464–71 (2013).
169. Schumacher, T. N., Kesmir, C. & van Buuren, M. M. Biomarkers in cancer immunotherapy. *Cancer Cell* vol. 27 12–14 (2015).
170. Van Allen, E. M. *et al.* Genomic correlates of response to CTLA-4 blockade in metastatic melanoma. *Science (80-.).* **350**, 207–211 (2015).
171. Rizvi, N. A. *et al.* Mutational landscape determines sensitivity to PD-1 blockade in non-small cell lung cancer. *Science (80-.).* **348**, 124–128 (2015).
172. Llosa, N. J. *et al.* The vigorous immune microenvironment of microsatellite instable colon cancer is balanced by multiple counter-inhibitory checkpoints. *Cancer Discov.* **5**, 43–51 (2015).
173. Chan, T. A. *et al.* Development of tumor mutation burden as an immunotherapy biomarker: Utility for the oncology clinic. *Annals of Oncology* vol. 30 44–56 (2019).
174. Sharma, P. & Allison, J. P. The future of immune checkpoint therapy. *Science (80-.).* **348**, 56–61 (2015).
175. Powderly, J. D. *et al.* Biomarkers and associations with the clinical activity of PD-L1 blockade in a MPDL3280A study. *J. Clin. Oncol.* **31**, 3001–3001 (2013).
176. Melero, I. *et al.* Evolving synergistic combinations of targeted immunotherapies to combat cancer. *Nature Reviews Cancer* vol. 15 457–472 (2015).
177. Aebersold, R. & Mann, M. Mass-spectrometric exploration of proteome structure and function. *Nature* **537**, 347–355 (2016).
178. Nyman, T. A., Lorey, M. B., Cypryk, W. & Matikainen, S. Mass spectrometry-based proteomic exploration of the human immune system: focus on the inflammasome, global protein secretion, and T cells. *Expert Rev. Proteomics* **14**, 395–407 (2017).
179. Hein, M. Y. *et al.* A Human Interactome in Three Quantitative Dimensions Organized by Stoichiometries and Abundances. *Cell* **163**, 712–723 (2015).

180. Yang, J., Wagner, S. A. & Beli, P. Illuminating Spatial and Temporal Organization of Protein Interaction Networks by Mass Spectrometry-Based Proteomics. *Front. Genet.* **6**, 344 (2015).

181. He, W. T. *et al.* Gasdermin D is an executor of pyroptosis and required for interleukin-1β secretion. *Cell Res.* **25**, 1285–1298 (2015).

182. He, Y., Zeng, M. Y., Yang, D., Motro, B. & Núñez, G. NEK7 is an essential mediator of NLRP3 activation downstream of potassium efflux. *Nature* **530**, 354–357 (2016).

183. D'Souza, R. C. J. *et al.* Time-resolved dissection of early phosphoproteome and ensuing proteome changes in response to TGF-β. *Sci. Signal.* **7**, (2014).

184. Humphrey, S. J., Azimifar, S. B. & Mann, M. High-throughput phosphoproteomics reveals in vivo insulin signaling dynamics. *Nat. Biotechnol.* **33**, 990–995 (2015).

185. Gfeller, D., Bassani-Sternberg, M., Schmidt, J. & Luescher, I. F. Current tools for predicting cancer-specific T cell immunity. *Oncoimmunology* **5**, e1177691 (2016).

186. Hoppes, R., Ekkebus, R., Schumacher, T. N. M. & Ovaa, H. Technologies for MHC class I immunoproteomics. *J. Proteomics* **73**, 1945–1953 (2010).

187. Bassani-Sternberg, M. *et al.* Direct identification of clinically relevant neoepitopes presented on native human melanoma tissue by mass spectrometry. *Nat. Commun.* **7**, (2016).

188. Alpízar, A. *et al.* A molecular basis for the presentation of phosphorylated peptides by HLA-B antigens. *Mol. Cell. Proteomics* **16**, 181–193 (2017).

189. Liepe, J. *et al.* A large fraction of HLA class I ligands are proteasome-generated spliced peptides. *Science (80-.).* **354**, 354–358 (2016).

190. Lun, X. K. & Bodenmiller, B. Profiling Cell Signaling Networks at Single-cell Resolution. *Molecular and Cellular Proteomics* vol. 19 744–756 (2020).

191. Schwamborn, K. & Caprioli, R. M. MALDI imaging mass spectrometry--painting molecular pictures. *Mol. Oncol.* **4**, 529–38 (2010).

192. Bodenmiller, B. Multiplexed Epitope-Based Tissue Imaging for Discovery and Healthcare Applications. *Cell Syst.* **2**, 225–238 (2016).

193. Giesen, C. *et al.* Highly multiplexed imaging of tumor tissues with subcellular resolution by mass cytometry. *Nat. Methods* **11**, 417–422 (2014).

194. Angelo, M. *et al.* Multiplexed ion beam imaging of human breast tumors. *Nat. Med.* **20**, 436–442 (2014).

195. Itzhak, D. N., Tyanova, S., Cox, J. & Borner, G. H. H. Global, quantitative and dynamic mapping of protein subcellular localization. *Elife* **5**, (2016).

196. Meissner, F., Scheltema, R. A., Mollenkopf, H. J. & Mann, M. Direct proteomic quantification of the secretome of activated immune cells. *Science (80-.).* **340**, 475–478 (2013).

197. Greening, D. W., Xu, R., Gopal, S. K., Rai, A. & Simpson, R. J. Proteomic insights into extracellular vesicle biology–defining exosomes and shed microvesicles. *Expert Review of Proteomics* vol. 14 69–95 (2017).

198. Li, M. *et al.* Quantitative proteomic analysis of exosomes from HIV-1-infected lymphocytic cells. *Proteomics* **12**, 2203–2211 (2012).

199. Kowal, J. *et al.* Proteomic comparison defines novel markers to characterize heterogeneous populations of extracellular vesicle subtypes. *Proc. Natl. Acad. Sci. U. S. A.* **113**, E968–E977 (2016).

200. Luber, C. A. *et al.* Quantitative Proteomics Reveals Subset-Specific Viral Recognition in Dendritic Cells. *Immunity* **32**, 279–289 (2010).

201. Worah, K. *et al.* Proteomics of Human Dendritic Cell Subsets Reveals Subset-Specific Surface Markers and Differential Inflammasome Function. *Cell Rep.* **16**, 2953–2966 (2016).

202. Riaz, T., Sollid, L. M., Olsen, I. & De Souza, G. A. Quantitative proteomics of gut-derived Th1 and Th1/Th17 clones reveal the presence of CD28+ NKG2D-Th1 cytotoxic CD4+ T cells. *Mol. Cell. Proteomics* **15**, 1007–1016 (2016).

203. Hukelmann, J. L. *et al.* The cytotoxic T cell proteome and its shaping by the kinase mTOR. *Nat. Immunol.* **17**, 104–112 (2016).

204. Tyanova, S. *et al.* Proteomic maps of breast cancer subtypes. *Nat. Commun.* **7**, (2016).

205. Guo, T. *et al.* Rapid mass spectrometric conversion of tissue biopsy samples into permanent quantitative digital proteome maps. *Nat. Med.* **21**, 407–413 (2015).

206. Amit, I., Regev, A. & Hacohen, N. Strategies to discover regulatory circuits of the mammalian immune system. *Nat. Rev. Immunol.* **11**, 873–880 (2011).

207. Meissner, F. & Mann, M. Quantitative shotgun proteomics: Considerations for a high-quality workflow in immunology. *Nat. Immunol.* **15**, 112–117 (2014).

208. Wiśniewski, J. R., Zougman, A., Nagaraj, N. & Mann, M. Universal sample preparation method for proteome analysis. *Nat. Methods* **6**, 359–362 (2009).

209. Rappsilber, J., Ishihama, Y. & Mann, M. Stop And Go Extraction tips for matrix-assisted laser desorption/ionization, nanoelectrospray, and LC/MS sample pretreatment in proteomics. *Anal. Chem.* **75**, 663–670 (2003).

210. Michalski, A., Cox, J. & Mann, M. More than 100,000 detectable peptide species elute

in single shotgun proteomics runs but the majority is inaccessible to data-dependent LC-MS/MS. *J. Proteome Res.* **10**, 1785–1793 (2011).

211. Köcher, T., Swart, R. & Mechtler, K. Ultra-high-pressure RPLC hyphenated to an LTQ-orbitrap velos reveals a linear relation between peak capacity and number of identified peptides. *Anal. Chem.* **83**, 2699–2704 (2011).
212. Jorgenson, J. W. Capillary liquid chromatography at ultrahigh pressures. *Annu. Rev. Anal. Chem.* **3**, 129–150 (2010).
213. Cristobal, A. *et al.* In-house construction of a UHPLC system enabling the identification of over 4000 protein groups in a single analysis. *Analyst* **137**, 3541–3548 (2012).
214. Fenn, J. B., Mann, M., Meng, C. K., Wong, S. F. & Whitehouse, C. M. Electrospray ionization for mass spectrometry of large biomolecules. *Science (80-.).* **246**, 64–71 (1989).
215. Mann, M. & Wilm, M. Electrospray mass spectrometry for protein characterization. *Trends Biochem. Sci.* **20**, 219–224 (1995).
216. Perry, R. H., Cooks, R. G. & Noll, R. J. Orbitrap mass spectrometry: Instrumentation, ion motion and applications. *Mass Spectrom. Rev.* **27**, 661–699 (2008).
217. Xian, F., Hendrickson, C. L. & Marshall, A. G. High resolution mass spectrometry. *Anal. Chem.* **84**, 708–719 (2012).
218. Scigelova, M., Hornshaw, M., Giannakopulos, A. & Makarov, A. Fourier transform mass spectrometry. *Molecular and Cellular Proteomics* vol. 10 (2011).
219. Makarov, A. Electrostatic axially harmonic orbital trapping: A high-performance technique of mass analysis. *Anal. Chem.* **72**, 1156–1162 (2000).
220. Michalski, A. *et al.* Ultra high resolution linear ion trap orbitrap mass spectrometer (orbitrap elite) facilitates top down LC MS/MS and versatile peptide fragmentation modes. *Mol. Cell. Proteomics* **11**, (2012).
221. Scheltema, R. A. *et al.* The Q exactive HF, a benchtop mass spectrometer with a pre-filter, high-performance quadrupole and an ultra-high-field orbitrap analyzer. *Mol. Cell. Proteomics* **13**, 3698–3708 (2014).
222. Lange, O., Damoc, E., Wieghaus, A. & Makarov, A. Enhanced Fourier transform for Orbitrap mass spectrometry. *Int. J. Mass Spectrom.* **369**, 16–22 (2014).
223. Makarov, A. *et al.* Performance evaluation of a hybrid linear ion trap/orbitrap mass spectrometer. *Anal. Chem.* **78**, 2113–2120 (2006).
224. Scigelova, M. & Makarov, A. Orbitrap mass analyzer - Overview and applications in

proteomics. in *Proteomics* vol. 1 16–21 (Proteomics, 2006).

225. Olsen, J. V. *et al.* Higher-energy C-trap dissociation for peptide modification analysis. *Nat. Methods* **4**, 709–712 (2007).
226. Mitchell Wells, J. & McLuckey, S. A. Collision-induced dissociation (CID) of peptides and proteins. *Methods in Enzymology* vol. 402 148–185 (2005).
227. Michalski, A. *et al.* Mass spectrometry-based proteomics using Q exactive, a high-performance benchtop quadrupole orbitrap mass spectrometer. *Mol. Cell. Proteomics* **10**, M111.011015 (2011).
228. Domon, B. & Aebersold, R. Options and considerations when selecting a quantitative proteomics strategy. *Nature Biotechnology* vol. 28 710–721 (2010).
229. James, A. & Jorgensen, C. Basic design of MRM assays for peptide quantification. *Methods Mol. Biol.* **658**, 167–185 (2010).
230. Gillet, L. C. *et al.* Targeted data extraction of the MS/MS spectra generated by data-independent acquisition: A new concept for consistent and accurate proteome analysis. *Mol. Cell. Proteomics* **11**, (2012).
231. Cox, J. *et al.* Andromeda: A peptide search engine integrated into the MaxQuant environment. *J. Proteome Res.* **10**, 1794–1805 (2011).
232. Cox, J. & Mann, M. MaxQuant enables high peptide identification rates, individualized p.p.b.-range mass accuracies and proteome-wide protein quantification. *Nat. Biotechnol.* **26**, 1367–1372 (2008).
233. Elias, J. E. & Gygi, S. P. Target-decoy search strategy for increased confidence in large-scale protein identifications by mass spectrometry. *Nat. Methods* **4**, 207–214 (2007).
234. Bantscheff, M., Lemeer, S., Savitski, M. M. & Kuster, B. Quantitative mass spectrometry in proteomics: Critical review update from 2007 to the present. *Analytical and Bioanalytical Chemistry* vol. 404 939–965 (2012).
235. Bantscheff, M., Lemeer, S., Savitski, M. M. & Kuster, B. Quantitative mass spectrometry in proteomics: Critical review update from 2007 to the present. *Anal. Bioanal. Chem.* **404**, 939–965 (2012).
236. Ong, S. E. *et al.* Stable isotope labeling by amino acids in cell culture, SILAC, as a simple and accurate approach to expression proteomics. *Mol. Cell. Proteomics* **1**, 376–386 (2002).
237. Gygi, S. P. *et al.* Quantitative analysis of complex protein mixtures using isotope-coded affinity tags. *Nat. Biotechnol.* **17**, 994–999 (1999).

238. Thompson, A. *et al.* Tandem mass tags: A novel quantification strategy for comparative analysis of complex protein mixtures by MS/MS. *Anal. Chem.* **75**, 1895–1904 (2003).

239. Liu, H., Sadygov, R. G. & Yates, J. R. A model for random sampling and estimation of relative protein abundance in shotgun proteomics. *Anal. Chem.* **76**, 4193–4201 (2004).

240. Ishihama, Y. *et al.* Exponentially modified protein abundance index (emPAI) for estimation of absolute protein amount in proteomics by the number of sequenced peptides per protein. *Mol. Cell. Proteomics* **4**, 1265–1272 (2005).

241. Cox, J. *et al.* Accurate proteome-wide label-free quantification by delayed normalization and maximal peptide ratio extraction, termed MaxLFQ. *Mol. Cell. Proteomics* **13**, 2513–2526 (2014).

242. Zeiler, M., Straube, W. L., Lundberg, E., Uhlen, M. & Mann, M. A protein epitope signature tag (PrEST) library allows SILAC-based absolute quantification and multiplexed determination of protein copy numbers in cell lines. *Mol. Cell. Proteomics* **11**, O111.009613 (2012).

243. Beynon, R. J., Doherty, M. K., Pratt, J. M. & Gaskell, S. J. Multiplexed absolute quantification in proteomics using artificial QCAT proteins of concatenated signature peptides. *Nat. Methods* **2**, 587–589 (2005).

244. Schwanhüusser, B. *et al.* Global quantification of mammalian gene expression control. *Nature* **473**, 337–342 (2011).

245. Wiśniewski, J. R. *et al.* Extensive quantitative remodeling of the proteome between normal colon tissue and adenocarcinoma. *Mol. Syst. Biol.* **8**, 611 (2012).

246. Kidd, B. A., Peters, L. A., Schadt, E. E. & Dudley, J. T. Unifying immunology with informatics and multiscale biology. *Nat. Immunol.* **15**, 118–127 (2014).

247. Subramanian, N., Torabi-Parizi, P., Gottschalk, R. A., Germain, R. N. & Dutta, B. Network representations of immune system complexity. *Wiley Interdiscip. Rev. Syst. Biol. Med.* **7**, 13–38 (2015).

248. Arda, H. E. & Walhout, A. J. M. Gene-centered regulatory networks. *Briefings Funct. Genomics Proteomics* **9**, 4–12 (2009).

249. Park, P. J. ChIP-seq: Advantages and challenges of a maturing technology. *Nature Reviews Genetics* vol. 10 669–680 (2009).

250. Gilchrist, M. *et al.* Systems biology approaches identify ATF3 as a negative regulator of Toll-like receptor 4. *Nature* **441**, 173–178 (2006).

251. Calvano, S. E. *et al.* A network-based analysis of systemic inflammation in humans.

Nature **437**, 1032–1037 (2005).

252. Arnit, I. *et al.* Unbiased reconstruction of a mammalian transcriptional network mediating pathogen responses. *Science (80-.).* **326**, 257–263 (2009).
253. Spooner, C. J., Cheng, J. X., Pujadas, E., Laslo, P. & Singh, H. A Recurrent Network Involving the Transcription Factors PU.1 and Gfi1 Orchestrates Innate and Adaptive Immune Cell Fates. *Immunity* **31**, 576–586 (2009).
254. Xue, J. *et al.* Transcriptome-Based Network Analysis Reveals a Spectrum Model of Human Macrophage Activation. *Immunity* **40**, 274–288 (2014).
255. Chevrier, N. *et al.* Systematic discovery of TLR signaling components delineates viral-sensing circuits. *Cell* **147**, 853–867 (2011).
256. Parnas, O. *et al.* A Genome-wide CRISPR Screen in Primary Immune Cells to Dissect Regulatory Networks. *Cell* **162**, 675–686 (2015).
257. Lee, M. N. *et al.* Identification of regulators of the innate immune response to cytosolic DNA and retroviral infection by an integrative approach. *Nat. Immunol.* **14**, 179–185 (2013).
258. Subramanian, N., Natarajan, K., Clatworthy, M. R., Wang, Z. & Germain, R. N. The adaptor MAVS promotes NLRP3 mitochondrial localization and inflammasome activation. *Cell* **153**, 348–361 (2013).
259. Makela, S. M., Strengell, M., Pietila, T. E., Osterlund, P. & Julkunen, I. Multiple signaling pathways contribute to synergistic TLR ligand-dependent cytokine gene expression in human monocyte-derived macrophages and dendritic cells. *J. Leukoc. Biol.* **85**, 664–672 (2009).
260. Bauernfeind, F. G. *et al.* Cutting Edge: NF-κB Activating Pattern Recognition and Cytokine Receptors License NLRP3 Inflammasome Activation by Regulating NLRP3 Expression. *J. Immunol.* **183**, 787–791 (2009).
261. Rivera, A., Siracusa, M. C., Yap, G. S. & Gause, W. C. Innate cell communication kick-starts pathogen-specific immunity. *Nat. Immunol.* **17**, 356–63 (2016).
262. Shalek, A. K. *et al.* Single-cell transcriptomics reveals bimodality in expression and splicing in immune cells. *Nature* **498**, 236–240 (2013).
263. Ornatsky, O. *et al.* Highly multiparametric analysis by mass cytometry. *Journal of Immunological Methods* vol. 361 1–20 (2010).
264. Mullassery, D., Horton, C. A., Wood, C. D. & White, M. R. H. Single live-cell imaging for systems biology. *Essays Biochem.* **45**, 121–133 (2008).
265. Frankenstein, Z., Alon, U. & Cohen, I. R. The immune-body cytokine network defines

a social architecture of cell interactions. *Biol. Direct* **1**, 32 (2006).

266. Ramilowski, J. A. *et al.* A draft network of ligand-receptor-mediated multicellular signalling in human. *Nat. Commun.* **6**, 7866 (2015).
267. Kastenmüller, W., Torabi-Parizi, P., Subramanian, N., Lämmermann, T. & Germain, R. N. A spatially-organized multicellular innate immune response in lymph nodes limits systemic pathogen spread. *Cell* **150**, 1235–1248 (2012).
268. Kumar, R. & Nanduri, B. HPIDB - a unified resource for host-pathogen interactions. *BMC Bioinformatics* **11**, (2010).
269. Urban, M. *et al.* PHI-base: A new interface and further additions for the multi-species pathogen-host interactions database. *Nucleic Acids Res.* **45**, D604–D610 (2017).
270. Durmuş Tekir, S. D. & Ülgen, K. Ö. Systems biology of pathogen-host interaction: Networks of protein-protein interaction within pathogens and pathogen-human interactions in the post-genomic era. *Biotechnology Journal* vol. 8 85–96 (2013).
271. Barabasi, A.-L., Gulbahce, N. & Loscalzo, J. Network medicine: a network-based approach to human disease. *Nat. Rev. Genet.* **12**, 56–68 (2011).
272. Schadt, E. E., Friend, S. H. & Shaywitz, D. A. A network view of disease and compound screening. *Nat. Rev. Drug Discov.* **8**, 286–295 (2009).
273. Hotson, A. N. *et al.* Coordinate actions of innate immune responses oppose those of the adaptive immune system during Salmonella infection of mice. *Sci. Signal.* **9**, ra4 (2016).
274. Dobrin, R. *et al.* Multi-tissue coexpression networks reveal unexpected subnetworks associated with disease. *Genome Biol.* **10**, R55 (2009).
275. Shen-Orr, S. S. *et al.* Towards a cytoklne-cell interaction knowledgebase of the adaptive immune system. in *Pacific Symposium on Biocomputing 2009, PSB 2009* 439–450 (NIH Public Access, 2009). doi:10.1142/9789812836939_0041.
276. Schaab, C., Geiger, T., Stoehr, G., Cox, J. & Mann, M. Analysis of high accuracy, quantitative proteomics data in the MaxQB database. *Mol. Cell. Proteomics* **11**, (2012).
277. Bergthaler, A. & Menche, J. The immune system as a social network. *Nat. Immunol.* **18**, 481–482 (2017).
278. O'Neill, L. A. J., Kishton, R. J. & Rathmell, J. A guide to immunometabolism for immunologists. *Nature Reviews Immunology* vol. 16 553–565 (2016).
279. Sukumar, M. *et al.* Mitochondrial Membrane Potential Identifies Cells with Enhanced Stemness for Cellular Therapy. *Cell Metab.* **23**, 63–76 (2016).
280. Sukumar, M. *et al.* Inhibiting glycolytic metabolism enhances CD8+ T cell memory

and antitumor function. *J. Clin. Invest.* **123**, 4479–4488 (2013).

281. Bronte, V. & Zanovello, P. Regulation of immune responses by L-arginine metabolism. *Nat. Rev. Immunol.* **5**, 641–654 (2005).
282. Grohmann, U. & Bronte, V. Control of immune response by amino acid metabolism. *Immunological Reviews* vol. 236 243–264 (2010).
283. Kishton, R. J., Sukumar, M. & Restifo, N. P. Arginine Arms T Cells to Thrive and Survive. *Cell Metab.* **24**, 647–648 (2016).
284. Welsh, R. M., Selin, L. K. & Szomolanyi-Tsuda, E. Immunological memory to viral infections. *Annual Review of Immunology* vol. 22 711–743 (2004).
285. Heath, W. R. & Carbone, F. R. The skin-resident and migratory immune system in steady state and memory: Innate lymphocytes, dendritic cells and T cells. *Nature Immunology* vol. 14 978–985 (2013).
286. Nilsson, T. *et al.* Mass spectrometry in high-throughput proteomics: Ready for the big time. *Nat. Methods* **7**, 681–685 (2010).
287. Hebert, A. S. *et al.* The one hour yeast proteome. *Mol. Cell. Proteomics* **13**, 339–347 (2014).
288. Kulak, N. A., Pichler, G., Paron, I., Nagaraj, N. & Mann, M. Minimal, encapsulated proteomic-sample processing applied to copy-number estimation in eukaryotic cells. *Nat. Methods* **11**, 319–324 (2014).
289. Nagaraj, N. *et al.* Deep proteome and transcriptome mapping of a human cancer cell line. *Mol. Syst. Biol.* **7**, 548 (2011).
290. Luber, C. A. Pattern recognition receptors are subset specific in dendritic cells In vivo quantitative proteomic investigations using. *PhD Thesis* (2009).
291. Mann, M., Kulak, N. A., Nagaraj, N. & Cox, J. The Coming Age of Complete, Accurate, and Ubiquitous Proteomes. *Mol. Cell* **49**, 583–590 (2013).
292. Böttcher, J. P. *et al.* Functional classification of memory CD8 + T cells by CX 3 CR1 expression. *Nat. Commun.* **6**, 8306 (2015).
293. Geiger, R. *et al.* L-Arginine Modulates T Cell Metabolism and Enhances Survival and Anti-tumor Activity. *Cell* **167**, 829-842.e13 (2016).
294. Rieckmann, J. C. *et al.* Social network architecture of human immune cells unveiled by quantitative proteomics. *Nat. Immunol.* **18**, 583–593 (2017).
295. Benoist, C. *et al.* Consortium biology in immunology: The perspective from the Immunological Genome Project. *Nat. Rev. Immunol.* **12**, 734–740 (2012).
296. Kim, M. S. *et al.* A draft map of the human proteome. *Nature* **509**, 575–581 (2014).

297. Wilhelm, M. *et al.* Mass-spectrometry-based draft of the human proteome. *Nature* **509**, 582–587 (2014).
298. Marx, V. A dream of single-cell proteomics. *Nat. Methods* **16**, 809–812 (2019).
299. Slavov, N. Unpicking the proteome in single cells. *Science* vol. 367 512–513 (2020).
300. Hartmann, F. J. *et al.* Single-cell metabolic profiling of human cytotoxic T cells. *Nat. Biotechnol.* **39**, 186–197 (2020).
301. Specht, H. *et al.* Single-cell proteomic and transcriptomic analysis of macrophage heterogeneity using SCoPE2. *Genome Biol.* **22**, (2021).
302. Tsai, C. F. *et al.* An Improved Boosting to Amplify Signal with Isobaric Labeling (iBASIL) Strategy for Precise Quantitative Single-cell Proteomics. *Mol. Cell. Proteomics* **19**, 828–838 (2020).
303. Li, Z. Y. *et al.* Nanoliter-Scale Oil-Air-Droplet Chip-Based Single Cell Proteomic Analysis. *Anal. Chem.* **90**, 5430–5438 (2018).
304. Zhu, Y. *et al.* Nanodroplet processing platform for deep and quantitative proteome profiling of 10-100 mammalian cells. *Nat. Commun.* **9**, (2018).
305. Brunner, A.-D. *et al.* Ultra-high sensitivity mass spectrometry quantifies single-cell proteome changes upon perturbation. *bioRxiv* 2020.12.22.423933 (2020) doi:10.1101/2020.12.22.423933.
306. Böttcher, J. P. *et al.* Functional classification of memory CD8 + T cells by CX 3 CR1 expression. *Nat. Commun.* **6**, (2015).
307. Geiger, R. *et al.* L-Arginine Modulates T Cell Metabolism and Enhances Survival and Anti-tumor Activity. *Cell* **167**, 829-842.e13 (2016).
308. Goh, K. *et al.* The human disease network. *Proc. Natl. Acad. Sci. U. S. A.* **104**, 8685–90 (2007).
309. Menche, J. *et al.* Disease networks. Uncovering disease-disease relationships through the incomplete interactome. *Science (80-.).* **347**, 1257601 (2015).
310. Guney, E., Menche, J., Vidal, M. & Barábasi, A.-L. Network-based in silico drug efficacy screening. *Nat. Commun.* **7**, 10331 (2016).
311. Delhalle, S., Bode, S. F. N., Balling, R., Ollert, M. & He, F. Q. A roadmap towards personalized immunology. *npj Syst. Biol. Appl.* **4**, 9 (2018).
312. Davis, M. M., Tato, C. M. & Furman, D. Systems immunology: Just getting started. *Nature Immunology* vol. 18 725–732 (2017).
313. Moysidou, C. M., Barberio, C. & Owens, R. M. Advances in Engineering Human Tissue Models. *Frontiers in Bioengineering and Biotechnology* vol. 8 620962 (2021).

314. Sheller, M. J. *et al.* Federated learning in medicine: facilitating multi-institutional collaborations without sharing patient data. *Sci. Rep.* **10**, (2020).

6 Acknowledgement

I would like to thank those who supported me and contributed to this work:

Matthias Mann for patience, advice, support, and inspiration. Great lab retreats, and happy hours.

Felix Meissner for mentoring, freedom to explore, guidance when needed, patience, and support.

Daniel Hornburg for friendship and support, tackling R together, inspiration.

Sen Office (Tar, Annika, Meera, Lars, Jennifer, Steven, Martin, Alex) for friendship, fun work atmosphere, support, great discussions, great music, and pizza Friday's.

Jürgen Cox for bioinformatic support and great software solutions.

Korbinian Mayr, Igor Paron, Mario Orosh and Gaby Sowa for mass spec and technical support.

Alison Dalfovo and Theresa Schneider for countless administrative support.

Mann Lab for a great atmosphere with many inspiring characters.

Roger Geiger for mentoring, friendship, introducing me to the world of T cells.

Lanzavecchia Lab (Roger, David, Tobias, etc.) for a great time in "Belli" and sharing buffy coats with me.

Shen-Orr Lab for great discussion around networks and collaboration.

IMPRS coordination office for support and organization of many PhD retreats, seminars, and BBQs.

My family for unconditional support.